

STELLAR AND SUBSTELLAR ASTROPHYSICS WITH EXTREME ADAPTIVE OPTICS

by

Logan A. Pearce

Copyright © Logan A. Pearce 2024

A Dissertation Submitted to the Faculty of the

DEPARTMENT OF ASTRONOMY

In Partial Fulfillment of the Requirements

For the Degree of

DOCTOR OF PHILOSOPHY

In the Graduate College

THE UNIVERSITY OF ARIZONA

2024

THE UNIVERSITY OF ARIZONA
GRADUATE COLLEGE

As members of the Dissertation Committee, we certify that we have read the dissertation prepared by: Logan A. Pearce titled:

and recommend that it be accepted as fulfilling the dissertation requirement for the Degree of Doctor of Philosophy.



Jared Males

Date: Jul 30, 2024



Laird Close

Date: Jul 30, 2024



Chad Bender

Date: Jul 30, 2024



Alycia J Weinberger (Aug 8, 2024 15:14 EDT)

Alycia J Weinberger

Date: Aug 8, 2024



Natasha Batalha (Jul 30, 2024 10:35 PDT)

Natasha Batalha

Date: Jul 30, 2024

Final approval and acceptance of this dissertation is contingent upon the candidate's submission of the final copies of the dissertation to the Graduate College. 

I hereby certify that I have read this dissertation prepared under my direction and recommend that it be accepted as fulfilling the dissertation requirement.



Jared Males

Date: Jul 30, 2024

Steward Observatory, Department of Astronomy

ACKNOWLEDGMENTS

I wish to acknowledge Dr. Adam Kraus for enthusiastically taking me on as a student when I barely knew how to launch python and giving me a challenging project which forced me to learn important things. I also want to acknowledge the REU program at Northern Arizona University, particularly Drs. Will Grundy and Jennifer Hanley, for giving me my first research experience. And Dr. Andrew Vanderburg for being an evangelist for my *Gaia* orbit fitting method and inviting my input to numerous papers, growing my network and collaborations, many of which have been quite fruitful. And finally the Extreme Wavefront Control Lab research group, a supportive, fun, and wicked smart group of people who made my grad school experience great, in spite of 2 years of COVID-19.

This material is based upon work supported by the National Science Foundation Graduate Research Fellowship Program under Grant No. DGE-1746060 and the NSF INTERN program described in DCL NSF 23-024.

MagAO was developed with support from the NSF (#0321312, #1206422, #1506818, #9618852). We thank the LCO and Magellan staffs for their outstanding assistance throughout our commissioning runs. We also thank the teams at the Steward Observatory Mirror Lab/CAAO (University of Arizona), Microgate (Italy), and ADS (Italy) for their contributions to the ASM. MagAO-X was developed with support from the NSF MRI Award #1625441. The Phase II upgrade program is made possible by the generous support of the Heising-Simons Foundation. We thank the LCO and Magellan staffs for their outstanding assistance throughout our observing runs.

The author wishes to recognize and acknowledge the very significant cultural role and reverence that the summit of Maunakea has always had within the indigenous Hawaiian community. We are most fortunate to have the opportunity to conduct observations from this mountain.

This research has made use of the NASA Exoplanet Archive, which is operated by the California Institute of Technology, under contract with the National Aeronautics and Space Administration under the Exoplanet Exploration Program.

This research has made use of the Washington Double Star Catalog maintained at the U.S. Naval Observatory.

This work has made use of data from the European Space Agency (ESA) mission *Gaia* (<https://www.cosmos.esa.int/gaia>), processed by the *Gaia* Data Processing and Analysis Consortium (DPAC, <https://www.cosmos.esa.int/web/gaia/dpac/consortium>).

LAND ACKNOWLEDGMENT

We respectfully acknowledge the University of Arizona is on the land and territories of Indigenous peoples. Today, Arizona is home to 22 federally recognized tribes, with Tucson being home to the O'odham and the Yaqui. Committed to diversity and inclusion, the University strives to build sustainable relationships with sovereign Native Nations and Indigenous communities through education offerings, partnerships, and community service.

DEDICATION

Dedicated to my parents who have enthusiastically supported every crazy thing I've wanted to do. Because of their support I have been able to pursue all of my dream jobs, including this one.

TABLE OF CONTENTS

LIST OF FIGURES	12
LIST OF TABLES	32
ABSTRACT	33
CHAPTER 1 Introduction	34
1.1 Setting the Stage – the Scientific Context	35
1.2 Direct Imaging is the Future of Exoplanet Science	35
1.3 Direct Detection of Exoplanets	40
<i>1.3.1 Thermal Emission</i>	40
<i>1.3.2 Reflected Light</i>	42
1.4 How We Accomplish High-Contrast Imaging	44
1.5 This Work	48
CHAPTER 2 Concepts	50
2.1 Image Post-processing	51
<i>2.1.1 Image Reduction Algorithms: Observing Strategy</i>	51
<i>2.1.2 Applying the Model</i>	55
2.2 RUWE and Other Indicators of Binarity	59
<i>2.2.1 RUWE Definition</i>	63
<i>2.2.2 Interpreting RUWE Value</i>	64
<i>2.2.3 Other Causes of RUWE Excess Besides Multiplicity</i>	67
<i>2.2.4 Other Tests for Binarity</i>	68
<i>2.2.5 Conclusion</i>	70

2.3	Accelerating Stars and Proper Motion Anomaly	70
CHAPTER 3 Boyajian’s Star B: The Co-Moving Companion to KIC 8462852 A		76
3.1	Introduction	77
3.2	Analysis	78
3.2.1	<i>Observations</i>	78
3.2.2	<i>Astrometry</i>	79
3.2.3	<i>Stellar Parameters</i>	82
3.3	Results	84
3.3.1	<i>KIC 8462852 B</i>	84
3.3.2	<i>KIC 8462852 cc1</i>	88
3.3.3	<i>KIC 8462852 cc2</i>	89
3.4	Discussion	89
3.5	Conclusion	92
CHAPTER 4 Companion Mass Limits for 17 Binary Systems Obtained with Binary Differential Imaging and MagAO/Clio		94
4.1	Introduction	95
4.2	Motivation: Substellar Companions in Wide Binaries	97
4.3	Binary Systems in our Survey	99
4.4	Methods	102
4.4.1	<i>Observations</i>	102
4.4.2	<i>Data Reduction</i>	102
4.4.3	<i>KLIP PSF Subtraction</i>	104
4.4.4	<i>Contrast and mass limits</i>	105
4.5	Results	109
4.5.1	<i>Factors Affecting Contrast and Mass Limits</i>	109
4.5.2	<i>Notable System Results</i>	110
4.5.3	<i>Completeness</i>	114
4.6	Discussion	115
4.6.1	<i>BDI Performance Compared to Other Observing Modes.</i>	115

4.6.2	<i>The Scientific Context of Our Survey</i>	115
4.7	Conclusion	116
CHAPTER 5 HIP 67506 C: MagAO-X Confirmation of a New Low-Mass Stellar Companion to HIP 67506 A		
5.1	Introduction	123
5.2	Stellar Properties	124
5.2.1	<i>Indicators of a Companion to HIP 67506 A</i>	124
5.3	Observations and Analysis	129
5.3.1	<i>Observations</i>	129
5.3.2	<i>MagAO-X Photometry</i>	131
5.3.3	<i>Astrometry</i>	134
5.4	Results	137
5.4.1	<i>Photometry</i>	137
5.4.2	<i>Astrometry</i>	139
5.5	Conclusion	139
CHAPTER 6 The ExAO Pup Search I: Five New (Candidate) Sirius-Like WD+MS Star Systems		
6.1	Introduction	141
6.1.1	<i>White Dwarf Pollution and Wide Stellar Companions.</i>	141
6.1.2	<i>The ExAO Pup Search: Extreme AO and WD Pollution</i>	144
6.2	Observations	145
6.2.1	<i>Target Selection</i>	145
6.2.2	<i>Imaging Data</i>	145
6.2.3	<i>Data Reduction</i>	147
6.3	Results	149
6.3.1	<i>Detections</i>	149
6.3.2	<i>Non-Detections</i>	163
6.3.3	<i>Survey Completeness</i>	168
6.4	Discussion	170

6.4.1	<i>Our Survey Compared to Previous Surveys</i>	170
6.4.2	<i>Towards Probes of Companion Influence on Pollution Through Orbit Studies</i>	173
6.4.3	<i>Revisiting the Missing White Dwarf Problem</i>	174
6.5	Conclusion	177
CHAPTER 7	Ongoing Project: Reflected Light Exoplanet Observations with MagAO-X and GMagAO-X	178
7.1	Introduction	179
7.1.1	<i>Observing Exoplanets in Reflected Light</i>	179
7.1.2	<i>Breaking the Phase-Radius Degeneracy</i>	182
7.1.3	<i>Preparing for Reflected Light Observations</i>	182
7.2	Methods	183
7.2.1	<i>Modeling Reflected Light Observations</i>	183
7.2.2	<i>Modeling Gas Giant Planets: GJ 876 b/c</i>	189
7.2.3	<i>Modeling Terrestrial Planets: Proxima Centauri b</i>	194
7.2.4	<i>Predicting S/N</i>	196
7.3	Results	201
7.3.1	<i>GJ 876 b</i>	201
7.3.2	<i>GJ 876 c</i>	202
7.3.3	<i>Proxima Centauri b</i>	204
7.4	Future Work	205
7.5	Conclusion	209
CHAPTER 8	Conclusion	211
APPENDIX A	Appendix to Chapter 4	215
A.1	Binary System Details	216
APPENDIX B	Appendix to Chapter 5	223
B.1	HIP 67506 B is not a wide binary companion to HIP 67506 A	224
APPENDIX C	Appendix to Chapter 6	227

REFERENCES 234

LIST OF FIGURES

1.1	All currently known exoplanets in the Exoplanet Archive as of this writing (grey dots) with literature occurrence rates overlaid, colored by occurrence rate. The region direct imaging is most sensitive to ($\sim 10\text{s}–1000\text{s}$ of au and $\sim 1–1000 M_{\text{Jup}}$) has exceedingly low occurrence rates. An interactive version of this plot is available at www.loganpearce.com . References: Bowler (2016); Bowler and Nielsen (2018); Bryan et al. (2016); Cassan et al. (2012); Fernandes et al. (2019); Fulton et al. (2021); Galicher et al. (2016); Lafrenière et al. (2014); Lannier et al. (2016); Meshkat et al. (2017); Naud et al. (2017); Nielsen et al. (2019); Poleski et al. (2021); Rameau et al. (2015); Vigan et al. (2021)	36
1.2	Two plots from Hardegree-Ullman et al. (submitted) comparing the detection of oxygen in an Earth-like exoplanet via transit spectroscopy and direct detection with an ELT. In the most optimistic case, a transit spectroscopy survey with a GMT-size telescope will take hundreds of years to detect one Earth-like oxygen signature. Via direct detection, a GMT-size telescope can make approximately 5 detections in 10 years.	38
1.4	The Pillars of Creation as imaged by JWST NIRCам. New stars are forming the dense clumps of the molecular cloud.	38
1.3	Illustration of the contrasts involved in directly imaging exoplanets, reproduced from Follette (2023)	39
1.6	Diagram illustrating the definition of phase angle α	42

- 1.5 Top: Blackbody radiation as a function of wavelength for objects are four different temperatures, 5000 K (yellow), 3000 K (red), 2000 K (dark red), and 1000 K (brown). The curves have been normalized such that their peak flux is equal to one, to emphasize the location of the peak for each curve. As objects cool, the peak of their emission shifts to longer and redder wavelengths. Filter curves for several common filters are shown in grey. Bottom: Thermal emission model spectra from PICASO (Batalha et al., 2019) exoplanet atmosphere modeling code for planets as they age and cool (effective temperature decreasing and surface gravity increases). 43
- 1.7 Simplified diagrams of adaptive optics and coronagraph systems. See text for details. 45
- 1.8 Reproduction of Figure 5 from Currie et al. (2023) showing the effects of adding different stages of a high-contrast imaging system (in this case SPHERE on VLT). Left: no AO correction, seeing-limited distorted starlight. Center left: AO correction applied, diffraction-limited point spread function, with diffraction effects and speckles visible. Center right: AO + coronagraph, a “dark hole” in which speckles are suppressed is visible in a ring surrounding the central obscured star; the faint off-axis companion is visible just to the lower right. Right: AO + coronagraph + PSF subtraction applied, now the starlight is almost entirely removed and the faint companion is clear. 46
- 1.9 A schematic of MagAO-X rendered by Joseph Long using the solid model of Close et al. 2018. Red: light from the telescope first encounters the woofer DM, then the 2k tweeter DM. Light is then split by a beam splitter (purple circle) into a path to the science cameras and a path to the pyramid wavefront sensor (orange). Green: light to the science cameras first enters the coronagraph system and the NCPC DM. Blue: finally light arrives at the two science cameras. See text for more detail. . . . 47

- 1.10 Stills from a movie recorded during the 2024A observing semester of the star π Pupis taken in the z' filter. Left: with the AO off the star is distorted and the faint companion, indicated by the red arrow, is not visible. The star's signal bounces around on the detector. Right: with the AO on, the star signal becomes fixed on the detector and diffraction-limited, and the faint companion is now easily seen (red arrow). The other symmetrical point-like signals are speckles caused by the diffraction from the tweeter and NCPC DMs. 49
- 2.1 Illustration of classical RDI. A science target with a hidden companion (red) and a reference star are observed. The PSF model is constructed as the median image of the reference star images, then subtracted from every science image. The final image is taken as the derotated and medianed (or summed) image of subtracted science images. 52
- 2.2 Illustration of classical ADI, reproduced from AstroBites article by Jessica Donaldson (<https://astrobites.org/2013/06/09/lowest-mass-exoplanet-discovered-via-direct-imaging/>). As the star is observed, the field rotates, and the companion signal (red) rotates through the fixed optical artifacts (white). A PSF reference is made from the median of the entire observation – since the companion moves through the field it is not contained in the median image. The PSF model is then subtracted from each image in the dataset, removing fixed artifacts but leaving the companion signal, and the final image is taken as the median of the derotated and subtracted images. 53
- 2.3 Stills from an animation produced by the SCExAO/CHARIS team of slices from a datacube produced by the CHARIS IFU (Currie et al., 2019). As the wavelength gets longer diffracted optical features move outward (left to right) but the companion signal (red arrow) does not, distinguishing a genuine astrophysical signal from nearby speckles. 54

- 2.4 Left: Figure 5 from Gaia Collaboration et al. (2016), displaying a schematic of the Gaia focal plane CCD. The along-scan and across-scan directions are indicated in the top left corner. Stars move across the focal plane from left to right in the diagram, illustrated by the yellow star and arrow, to the summing well and transfer gate. This translates the PSF into a Line Spread Function (LSF). If more than one source falls on the detector, multiple peaks will be present in the LSF, and the amount of blending of those peaks depends on the position angle of the two sources relative to the along-scan direction. Right: Figure 7 from El-Badry (2024) showing *Gaia*'s view of an astrometric binary with components of different masses and luminosities. Both objects orbit the center of mass (plus) and the photocenter traces out the dashed line, the wobble *Gaia* would detect. 61
- 2.5 Figure 1 of Belokurov et al. 2020 showing an HRD for 4M Gaia DR2 objects from their selection criteria (see Sec 2.1) color coded by RUWE. Two distinct regions of elevated RUWE are evident, corresponding to main sequence (MS) multiples and white dwarf - M dwarf binaries (WD+MD). The supports the claim that RUWE can be used to probe multiplicity. 65
- 2.6 Left: Figure 1 (bottom) from Stassun and Torres 2021 showing the absolute fractional parallax difference between Gaia and EB parallaxes on the y-axis vs \log RUWE. Blue halos mark EBs with known tertiary companions. The largest parallax difference and largest RUWE values (top right) are entirely populated by these systems. The red dashed line (added for this work) marks the nominal "good" value of $\text{RUWE} = 1.4$. Right: Figure 3 from Stassun and Torres 2021 showing the same data as Figure 1, plotted as a function of the amount of angular photocenter shift (a''_{phot}), with the relation of Equation 5 plotted in black line. 66
- 2.7 Selected plot from Figure 5 of Belokurov et al. 2020 relating RUWE to separation of binaries in Washington Double Star Catalog. Extremely high RUWE values are common for binaries with separation less than 1.5". 68

- 2.8 Reproduction of Figure 1 from El-Badry (2024) showing *Gaia* ’s parameter space of binarity probed by different metrics. Objects in the red hashed region will be spatially resolved by *Gaia* , proper motion anomaly (described in Section 2.3) probes the green region, *Gaia* ’s spectroscopic binary pipeline catches objects in the teal region, and RUWE probes the pink hashed region, with some sources having full astrometric orbits (yellow region). 70
- 2.9 Reproduction of Figure 1 Kervella et al. (2019) illustrating proper motion anomaly. The luminous object observed by *Hipparcos* and *Gaia* is labeled A and the less luminous object, which contributes negligibly to the photometry, is labeled B. The observed proper motions of A are shown as $\mu_{G2/H}$, μ_{HG} is the proper motion difference vector from *Hipparcos* and *Gaia* DR2 astrometric position (α, δ, ϖ) , and $\Delta\mu_{G2/H}$ is the PMa vector where $\Delta\mu_{G2/H} = \mu_{G2/H} - \mu_{HG}$. The motion A makes through space is given by the dashed black line, while it would have followed the dotted blue line if it did not have the unseen companion. $\Delta\mu$ thus corresponds to the projected velocity vector of the photocenter around the barycenter. 72
- 2.10 A proper motion anomaly sensitivity plot for a XOOMIES target. 75
- 3.1 Keck/NIRC2 adaptive optics image of KIC 8462852 A, B, and candidate companions, shown in log stretch to emphasize the faint candidate companions. The primary, KIC 8462852 A, is shown inside a linear stretched box to avoid saturation. The secondary, labeled B, is located 2'' to the east. The two candidate companions are labeled cc1 for the brighter companion, 3.8'' southwest, and cc2, 2.8'' southwest. 82
- 3.2 Data, model, and residual map of the primary (labeled "A"), companion (labeled "B"), and candidate companions ("cc1" and "cc2") for one image from the 2019 dataset. The model shown is built using the mean values of the parameter chains from the MCMC fit for that image, and is shown with a square root stretch to emphasize the faint residuals. 83

- 3.3 Left: Change in relative astrometry for KIC 8462852 B in separation (y-axis) and angular direction (x-axis) in individual images (circles) and mean values for each epoch (crosses). Epochs 2016 and 2019 dither positions are reported as separate observations. Thick crosses show statistical uncertainty, thin crosses show systematic uncertainty. Crosses to the left display the median error in individual image measurements. We measure a total relative velocity of $\mu = 0.14 \pm 0.44 \text{ mas yr}^{-1}$, which is consistent with zero. Right: Observed position of KIC 8462852 B (circles, error bars smaller than marker size) with expected motion if it were a background star (black track, crosses indicate expected position at observation times). KIC 8462852 B displays common proper motion with KIC 8462852 A, consistent with a bound companion. 88
- 3.4 Orbital parameter posterior distributions for KIC 8462852 B. Posterior distributions on eccentricity, inclination, and argument of periastron are similar to priors shown in orange. Semi-major axis and longitude of nodes have no prior due to the scale-and-rotate process of OFTI (see Blunt et al. 2017), while T_0 , periastron, and apastron are derived from orbital parameters. 89
- 3.5 The absolute proper motions of KIC 8462852 A, B, cc1, and cc2, and objects in *Gaia* DR2 in a 0.5° cone search around the position of KIC 8462852 A. The proper motion for cc1 and cc2 are consistent with the motion of nearby stars with chance alignment. 90
- 3.6 Left: Relative astrometry for KIC 8462852 cc1 in individual images (circles) and mean values in each epoch (crosses). Thick crosses show statistical uncertainty, thin crosses show systematic uncertainty. Crosses to the left display the median error in individual image measurements. We measure a total relative velocity of $\mu = 5.0 \pm 0.7 \text{ mas yr}^{-1}$. Epochs 2016 and 2019 dither positions are reported separately. Right: Observed position of KIC 8462852 cc1 (circles) with expected motion if it were a background star (black track, crosses indicate expected position at observation times). The relative motion of KIC 8462852 cc1 is not consistent with being a bound companion. It is likely a star with similar space velocity and chance alignment. 90

- 3.7 Left: Relative astrometry for KIC 8462852 cc2 in individual images (circles) and mean values in each epoch (crosses). Statistical uncertainty dominates systematic uncertainty for this object. Crosses to the left display the median error in individual image measurements. We measure a total relative velocity of $\mu = 11.9 \pm 2.5 \text{ mas yr}^{-1}$. Right: Observed position of KIC 8462852 cc2 (circles) with expected motion if it were a background star (black track, crosses indicate expected position at observation times). The relative motion of KIC 8462852 cc2 is consistent with an unbound field object. 91
- 4.1 Illustration of our BDI implementation of the KLIP methodology. This process is repeated for Star B using Star A as the eigenbasis. 103
- 4.2 Illustration of our method for determining signal to noise ratio (S/N) based on Mawet et al. (2014). The image is a post-BDI reduction of HD 82984 A with a fake signal injected right at the $5\text{-}\sigma$ S/N limit at separation $r = 7\lambda/D$ and position angle 270° East of North. HD 82984 A is behind the mask and marked with an orange star. The sum of the pixels within the red aperture, with diameter $= 1\lambda/D$, is \bar{x}_1 in Eqn 4.1; the mean and standard deviation of the sum of the pixels in the white apertures are \bar{x}_2 and s_2 respectively; n_2 is the number of white apertures. This computation was repeated for all $N = 2\pi r$ apertures along the ring of radius r , and for rings of radius $r = n\lambda/D$, where n is an integer. 105
- 4.3 Results of BDI-KLIP reduction of HD 37551. Top: reduced image of HD 37551 A reduced with HD 37551 B as reference (left) and vice versa (right) using 15 KLIP modes. North is up and East is to the left in both images. Middle: Contrast limits (left) and mass limits (right) as a function of separation for HD 37551 A (purple) and HD 37551 B (red). These are the deepest contrast and mass limits in our survey, reaching as low as $5M_{\text{Jup}}$ in to 40 AU for both A and B. Bottom: Survey completeness maps for both stars for a grid of (semi-major axis, mass) pairs. Color map indicates fraction of simulated companions which would have been detected at each grid point. Contours indicate 10% (white), 50%, and 90% (inner-most contour) of simulated companions detected. 117

- 4.4 Contrast for TWA 13 A as a function of number of basis modes (N_{KLIP}). The deepest contrast is achieved at $N_{\text{KLIP}} = 10$ for this system. Optimal number of basis modes varies between datasets and is reported in Table 4.3. 118
- 4.5 Top: A selected image of HD 36705 A (left) and HD 36705 B (right) from our 2017 dataset, shown with a ZScale stretch to emphasize the faint PSF features, with gray scale showing pixel counts. The image of the two stars appear significantly different due to their large relative contrast ($\Delta\text{mag} \approx 2$) and the brightness of HD 36705 A in the MagAO [3.95] filter, with many features visible on A lost in the noise for B. This resulted in contrast limits when used to perform BDI due to insufficient starlight subtraction. Bottom: A selected image from the 2015 epoch HD 222259 observation, shown with a ZScale stretch. The HD 222259 A PSF (left) contains a glint (bottom left corner), HD 222259 B (right) contains a different glint (bottom of frame); both PSF cores are elongated. These features show up prominently in the BDI reduction. 118
- 4.6 Top: BDI reduction of HD 36705 using 20 KLIP modes. North is up and East is to the left in both images. HD 36705 A is significantly brighter than HD 36705 B, and PSF features visible in A are lost to noise in B, resulting in poor starlight subtraction and contrast limits, particularly for A. Bottom: BDI reduction of HD 222259 using 24 KLIP modes. North is up and East is to the left in both images. Regions of bright and dark pixels in the upper northeast corner are due to the ghosts visible in Figure 4.5, as are bright and dark areas in the central regions. 119
- 4.7 Top: BDI reduction of HIP 67506 (labeled A) and TYC 7797-34-2 (labeled B) using 30 KLIP modes. North is up and East is to the left in both images. The candidate companion signal is located $\sim 0.2''$ ($\sim 2\lambda/D$) to the east of HIP 67506 (behind mask), indicated by the red circle. The candidate signal rotated with the sky rotation, unlike the azimuthally broadened features at similar separation. Middle: contrast curves for HIP 67506 and TYC 7797-34-2. We show mass limits for TYC 7797-34-2 using a young age (500 Myr) and a field age (5 Gyr). Bottom: Completeness map for HIP 67506 and TYC 7797-34-2. Contours show 10%, 50%, and 90% completeness. 120

- 4.8 Completeness map for every star in our survey as a function of mass and semi-major axis. Colormap and contours give the number of stars for which a given (sma, mass) pair is complete. 121
- 5.1 MKO L' KLIP-reduced image of HIP 67506 A from our Binary Differential Imaging survey described in Pearce et al. (2022). The central star is masked in the reduction, and the candidate signal is marked with a red circle $\sim 2''$ ($2.0 \lambda/D$) to the east. This was identified as a candidate signal due to the fact that it did not appear to smear azimuthally with derotation like the other residual structures at similar separation, and the other indications described in Section 5.2.1 125
- 5.2 Gaia EDR3 BP minus RP vs absolute G magnitude color-magnitude diagram of Praesepe Cluster members identified in Deacon and Kraus 2020 (orange). Objects they flagged as possible overluminous binaries are outlined in blue up-pointing triangles, and purple down-pointing triangles are objects they flagged with elevated astrometric noise, following their Figure 4. The position of HIP 67506 is marked with a red star in the main and inset axis, which shows a close view of the region surrounding HIP 67506 A. HIP 67506 A falls on the overluminous region above the main sequence, pointing to the presence of an unresolved stellar companion. . . 126
- 5.3 MagAO-X images of HIP 67506 A and HIP 67506 C in the four photometric filters g' , r' , i' , z' , shown with log stretch. HIP 67506 A is centered in each image, and HIP 67506 C, located $0.1''$ to the south east, is marked by the white pointers. North is up and East is left, and the stretch and spatial scale is same for each image. . . . 127
- 5.4 Results of our grid search of $[x, y, c]$ values for a model which minimizes HIP 67506 C residuals post-KLIP processing for the 2015 MagAO/Clio epoch. Each parameter is plotted versus the difference in RMS between KLIP-reduced image with and without the model subtracted. Each parameter was fit with a Gaussian function while keeping the others fixed at their peak value. 132

- 5.5 Top: Data, model, and residual of the $[x, y, c]$ that minimizes residuals in 2015 MagAO/Clio observation. Data and residual images are post-KLIP processing, and shown with a log stretch; model image shows the signal with peak values in Figure 5.4 that was subtracted from images prior to KLIP processing. Middle and bottom: Data, model, and residuals from the 2D Gaussian model in the 2022 MagAO-X z' image for HIP 67506 A (middle) and HIP 67506 C (bottom). 132
- 5.6 The lowest χ^2 of all MIST model fits occurred for age \sim 14 Myr when ages were constrained to be the same for both objects. This figure shows the map of the reduced χ^2 surface in $\log(T_{\text{eff}})$ and $\log(L)$ for HIP 67506 A (top) and HIP 67506 C (bottom) for age = 14 Myr and the best-fitting values of metallicity and rotation for each. The lowest reduced χ^2 value for each is marked with an orange star. Contours denote $\chi^2 = 25, 50, \text{ and } 100$. Inset axis: χ^2 of model verses model star mass for fits of models with age = 14 Myr. The lowest χ^2 values occurred at $M_A = 1.13 M_{\odot}$ and $M_C = 0.39 M_{\odot}$ 134
- 5.7 Color-magnitude diagram (CMD) of Sloan $r'-i'$ vs. Sloan g' absolute magnitude. Points are photometry from the CARMENES sample of well-characterized M- and L dwarfs (Cifuentes et al., 2020) and a selection of Hipparcos stars with SDSS photometry and T_{eff} estimates from McDonald et al. 2012. Our photometry of HIP 67506 A (star) and HIP 67506 C (diamond) and uncertainties (black errorbars) are overplotted. A and C are colored according to the T_{eff} of the best-fit MIST model shown in Figure 5.6. The best-fitting MIST models correspond to T_{eff} values consistent with nearby objects on the CMD. 135

- 5.8 Relative astrometry of HIP 67506 C relative to A for the MagAO 2015 epoch (purple) and the MagAO-X 2022 epoch (orange). The abscissa and ordinate axes display position of HIP 67506 C relative to A in mas in right ascension (RA) and declination (Dec). The motion of a non-moving background object at the position of HIP 67506 C is given by the black track; the predicted position in 2015, given then 2022 position, is an open diamond. The observed position and uncertainty in each epoch is shown as filled circles (uncertainties are smaller than the marker for the 2022 epoch). The observed motion of the HIP 67506 C is not consistent with a background object, and is likely due to orbital motion. 138
- 6.1 Left: Pup Search targets in RA/Dec. Targets accessible to MagAO-X from Las Campanas Observatory are plotted in blue, targets accessible to northern hemisphere instruments are in magenta. Targets outlined by the purple star were observed in fall 2022, and the yellow star in spring 2024. Right: Pup Search targets color magnitude diagram in *Gaia* absolute G magnitude vs *Gaia* bp - rp color. The red points mark the 84 wide candidate WDMS systems identified in Sec 6.2.1. The grey points are the 10,000 nearest high-quality solutions ($\text{ruwe} < 1.1$) in *Gaia* DR3, with approximate spectral type ranges marked in blue (adapted from the spectral type-color relations in Pecaute and Mamajek 2013). The inset axis shows a zoomed view of the region of interest. The blue region marks the approximate location of the giant branch. All of our target MS stars fall within the AFGK region, and $\sim 60\%$ are in the giant star region. 146
- 6.2 Color-magnitude diagram of the confirmed and candidate companions from Table 6.2 shown in SDSS $r' - z'$ color and SDSS i' absolute magnitude. Colored markers give measured photometry in MagAO-X filters converted to SDSS filters using color conversion table; host stars are marked with stars, companions are marked by circles. Grey dots are the same *Gaia* sample from Figure 6.1 converted to SDSS colors using *GaiaXPY* (Ruz-Mieres and zuzannakr, 2023) to generate synthetic photometry from *Gaia* DR3 spectra. 151

- 6.3 MagAO-X images of the confirmed and candidate companion signals in this work, including the 2022 and 2024 detections of PupS-1B. All images are North up/ East left; the filter, host star, and observation date are as indicated. Scale bars show 0.5'' and corresponding physical scales. The companion is marked by a red circle. 156
- 6.4 Model fit results for PupS-1B to Bergeron et al. (1995) synthetic photometry. Top: χ^2 map with model effective temperature on the X-axis and $\log(g)$ on the Y-axis with value interpolated between grid points. There is a degeneracy between T_{eff} and $\log(g)$. The best fitting model is marked with an orange star, with the orange solid and dotted contours showing 1- and 2σ surfaces from that minimum χ^2 value. Bottom: the absolute magnitude in the three filters for all models within 1σ of the best fitting model ($\text{mean } \chi^2 < \min[\chi^2] + \sigma_{\min[\chi^2]}$, solid markers) and 2σ ($\text{mean } \chi^2 < \min[\chi^2] + 2\sigma_{\min[\chi^2]}$, transparent markers) compared to our observations (teal open circles) and uncertainties (teal bars; thick bars are 1σ and thin bars are 2σ uncertainties) at the mean *Gaia* DR3 parallax for the primary. The colors show the T_{eff} of the model and the marker shape shows the $\log(g)$. The best fitting model is $T_{\text{eff}} = 11,000\text{K}$, $\log(g) = 8.0$ ($\chi^2 = 4.5 \pm 4.4$), followed by $T_{\text{eff}} = 10,500\text{K}$, $\log(g) = 8.0$ ($\chi^2 = 5.2 \pm 4.2$), $T_{\text{eff}} = 8500\text{K}$, $\log(g) = 7.5$ ($\chi^2 = 5.6 \pm 4.6$), $T_{\text{eff}} = 17,000\text{K}$, $\log(g) = 8.5$ ($\chi^2 = 7.2 \pm 4.8$), $T_{\text{eff}} = 16,500\text{K}$, $\log(g) = 8.5$ ($\chi^2 = 9.6 \pm 5.8$), and $T_{\text{eff}} = 30,000\text{K}$, $\log(g) = 9.0$ ($\chi^2 = 11.4 \pm 6.2$). 157
- 6.5 Common proper motion plot for PupS-1B. The offset from TYC 4831-473-1 in RA and Dec are given on the x- and y-axis respectively, with our observed position in 2022 and 2024 are given by the blue and red circles. If PupS-1B were an unmoving background star, it would follow the black track relative to TYC 4831-473-1, given by the host star's proper motion and parallax; we would have observed PupS-1B at the location of the red diamond in 2024. Our observed location is highly discrepant with this predicted location and moving in the opposite direction in RA. We conclude that PupS-1B is not a background star, and posit that the apparent motion of PupS-1B is due to orbital motion. More observations are required to begin to pin down orbital parameters. 158

- 6.6 Proper motion anomaly (PMA) plot for 33 Sex (host of PupS-cc2; top) and TYC 5518-135-1 (host of PupS-cc7; bottom) using the methodology of Kervella et al. (2022). This plot describes the (minimum) mass of an object as a function of separation that would produce the observed proper motion anomaly between the *Hipparcos* and *Gaia* observations. Left: The orange vertical line marks the separation of cc2 from 33 Sex, and the horizontal orange line marks the approximate mass of a mid-M dwarf. This suggests the cc2 is either not in a face-on orbit (as assumed by the sensitivity function), or another object is contributing to the observed PMA and cc2 is not responsible for the observed acceleration. Right: The orange vertical line marks the separation of cc7 from host, and the horizontal vertical line marks the approximate mass of a white dwarf. cc7's position above the sensitivity curve indicates it is either on an inclined or eccentric orbit, there is another object in the system and cc7 is not responsible for the observed acceleration. 159
- 6.7 Color-magnitude diagram of the candidate companion signal to TYC 5518-135-1, PupS-cc7. Since we do not have r' photometry we show it here in SDSS $i' - z'$ color vs SDSS i' absolute magnitude. cc7 clearly falls in the WD regime, however the exact position in the WD sequence is not well constrained with only i' and z' colors. 161
- 6.8 Proper motion anomaly plot for TYC 368-1591-1. See text of Figure 6.6 for explanation. The orange region marks where our imaging is sensitive. The inset axes shows the flux contrast corresponding to those minimum masses (purple) and our imaging 3σ contrast limit (red). The grey vertical lines mark where they cross, the grey horizontal line marks the minimum mass at that limit. Our contrast curves rule out at 3σ companions within the orange region outside of the grey line, which is objects $>0.35 M_{\odot}$ ($\sim M_{3.5V}$) at >160 mas. 169
- 6.9 Map of completeness to hydrogen-dominated white dwarf companions in our survey. . . . 170

- 6.10 Pup Search confirmed and candidate companions in this work plotted (orange stars and diamond) against known SLS from Zuckerman 2014 (red), Holberg et al. 2013 (and references there-in; blue), WDMS systems in *Gaia* DR3 from Noor et al. 2024 (purple), wide post-common envelope binaries in *Gaia* from Yamaguchi et al. 2024 (magenta), and two SLS detected via astrometric acceleration and AO imaging in Bowler et al. 2021 (yellow), plotted with separation in arcseconds on the x-axis and physical separation in au on the y-axis. The orange diamond marks the location of PupS-cc8, which is not confirmed to be a white dwarf companion. We illustrate the approximate limits of MagAO-X search space between 48 mas ($2 \lambda/D$ in i') and 3" (half the detector FOV) by grey dashed lines. The contours give an adaptation of Willems and Kolb 2004 Figure 10 (right) to our parameter space. See text for details. 171
- 6.11 Reproduction of Figure 1 from El-Badry (2024) showing the sensitivity regimes of various multiplicity metrics for a two-solar mass binary. We have added the purple rectangle to indicate the regime of the new candidate companions in our survey. They fall outside the regime for which RUWE and PMA are most sensitive, and are too faint to be resolved in *Gaia*, illustrating that these metrics are useful but incomplete for assessing WD multiplicity. 173
- 6.12 Number of WDs expected and observed within 100 pc local volume. The dashed blue line is the number of WDs predicted by theory (see text for details), the purple line is the 100 pc *Gaia* sample from Jiménez-Esteban et al. 2023, the magenta line is the 100 pc WD+MS sample from Rebassa-Mansergas et al. 2021, corrected for their 80% completeness of their sample and the 9% completeness of their sample from the underlying WD+MS population, the orange line is the new WD+MS from Nayak et al. 2024, and the black line is the sum. We did not include WD+MS surveys for which the objects are resolved in *Gaia*, since they would be captured in the Jiménez-Esteban et al. (2023) catalog. The dotted grey line shows the approximate detection limit for *Gaia* for a WD at 100 pc, assuming a detection limit of $G = 20$ mag; the dashed grey line shows the approximate detection limit for the Pup Search for a WD companion to a G0 star at 100 pc, assuming a noise floor of 5×10^{-5} , the best case in our initial survey results. 176

- 7.1 100s of the nearest known radial velocity detected exoplanets in separation (in λ/D for a 6.5 m mirror at 800 nm) vs Lambertian contrast. The dashed grey line marks a typical resolution limit of $2\lambda/D$. Proxima Centauri b and GJ 876 b/c are marked with red circles. An interactive version of this plot with details for each planet is available here: <http://www.loganpearcescience.com/reflected-light-calculations.html> 180
- 7.2 Empirical mass-radius relation for planets derived from references given and compiled at <https://jaredmales.github.io/mxlib-doc/> 181
- 7.3 Nayak et al. (2017) Figure 1 illustrating the phase-radius degeneracy for reflected light planets. Small radius planets at full phase will appear at the same brightness as large radius planets at larger phase angles, necessitating additional information (estimates of planet radius or phase) to distinguish these cases for a flux measurement. 183
- 7.4 Figure 3 of Batalha et al. (2019) illustrating how PICASO solves 1D radiative transfer for exoplanet atmospheres. The observer sees emitted radiation I_0^+ as a function of angle relative to surface normal (μ). The stellar radiation F_0 is incident at angle μ_0 at the top atmosphere layer T_0 . The atmosphere is modeled as a series of plane-parallel layers T_i . Incident radiation is attenuated by optical depth in the layer δT_i 184
- 7.5 Points at which PICASO computes intensities for different phase angles – full phase, 60° , and 90° . Each example uses 10 vertical Chebyshev angles and 10 horizontal Gauss angles, following the formality of Horak and Little (1965). The number of angles for each is user-specified, with more angles requiring longer computation times. PICASO automatically takes advantage of symmetry where possible to speed up calculation times. 186
- 7.6 The effect of varying f_{sed} (top) and K_{zz} (bottom) on Earth-like atmosphere spectrum with water clouds. For each of the two pairs of plots, the named parameter is varied and the remaining parameters are kept constant. The left-hand plots show the resulting albedo spectrum compared to an Earth-like model in Feng et al. (2018) (black) and a cloud-free model (black dashed); the right-hand plots show the cloud vertical extent (y-axis) and optical depth (x-axis). 188

- 7.7 Phase angle sampling as a function of orbit for GJ 876 b modeling. We produced models for all points marked with a black x. Black circle marks inferior conjunction (brightest phase) and black diamond marks superior conjunction (faintest phase). The solid grey lines mark $1\lambda/D$ for MagAO-X ($D = 6.5$ m, $\lambda = 800$ nm) and GMagAO-X ($D = 24.5$ m, $\lambda = 800$ nm); the dashed grey lines mark $1\lambda/D$ for MagAO-X and GMagAO-X. The colormap shows the viewing phase at each point in the orbit. Left: the orbit projected on the plane of the sky (longitude of nodes arbitrarily set to 90° as it is unconstrained); Middle: the separation in the plane of the sky as a function of the orbital phase (parameterized by mean anomaly, where $\text{meananom} = 0\pi$ is periastron and the orbit proceeds through $\text{meananom} = 2\pi$); Right: separation in the orbital plane, which sets the equilibrium temperature for the models and controls the chemistry. GJ 876 b remains within $2\lambda/D$ for MagAO-X throughout its orbit, but is entirely outside $2\lambda/D$ for GMagAO-X, even at its brightest phase. The orbital separation changes by less than 0.02 au throughout the orbit, so the model PT profile and chemistry do not change as a function of separation. 191
- 7.8 Pressure-temperature profile for GJ 876 b models plotted with condensation curves for chemical species. The thick lines give PT profile for the three C/O ratios modeled; the PT profile is not meaningfully affected by C/O ratio or orbital phase. The inset shows the region where the PT profile crosses with S_8 (sulfur hazes) and water curves showing where in the atmosphere those species condense into clouds. 192
- 7.9 Phase angle sampling as a function of orbit for GJ 876 c modeling. See Figure 7.7 for explanation. The orbital separation changes significantly throughout the orbit, so the model PT profile and chemistry will change as a function of separation. Left: the red dashed line marks the line of nodes, with $\text{phase} > 90$ being towards the observer and $\text{phase} < 90$ being away from the observer 193
- 7.10 Pressure-temperature profile for GJ 876 c models plotted with condensation curves for chemical species. See Figure 7.8 caption for explanation. 193
- 7.11 Left: Projected orbit for four inclination values with phase sampling marked as before. Right: same orbits in plane-of-sky separation as a function of orbital phase. 195

7.12 Contrast as a function of wavelength for various surface materials for the airless Prox Cen b models, with filter profiles shown below.	196
7.13 The fractional contribution of atmospheric speckles (I_{as}) for a linear predictive wavefront controller at 800 nm as a function of separation and guide star magnitude (colors), azimuthally averaged from the maps of Males et al. (2021).	200
7.14 S/N as a function of exposure time for the GJ 876 b/c REFLECTX models in the filters listed for a 24.5 m primary, computed using Eqn 7.23. The models used here are at quadrature with $f_{sed} = 0.03$ and $K_{zz} = 1 \times 10^9$ (the brightest cloud configuration, see Figure 7.15). We estimated the throughput as 0.1, $\tau_{as} = 0.02$ (Males et al., 2021, Fig 10), I_{as} and Strehl ratio from the tables from Males et al. (2021), The grey shaded region marks $S/N = 5$, a typical detection threshold. The mid-M host star is brightest in longer wavelengths, giving shorter exposure times to detection on those filters.	200
7.15 Planet-star contrast spectrum from models of GJ 876 b at quadrature with $C/0 = 1.0$ for three cloud configurations, $f_{sed} = 0.3$, $K_{zz} 1 \times 10^{-9}$ (light blue), $f_{sed} = 6$, $K_{zz} 1 \times 10^{-9}$ (dark purple), and cloud-free (light pink). Molecular absorption lines are marked for the $f_{sed} = 6$ case. Filter curves used in this analysis are shown in grey below. The atmosphere is H_2 and He dominant, with water, methane, and ammonia the next most prevalent molecules. As cloud opacity decreases molecular absorption lines appear, as well as an upward slope to the blue end from Rayleigh scattering.	201
7.16 Broadband colors for GJ 876 b quadrature models for cloud free (black), cloudy with $K_{zz} = 1 \times 10^9$ (circles, solid line) and varying f_{sed} (colors), and cloudy with $K_{zz} = 1 \times 10^{11}$ (triangles, dashed line) and varying f_{sed} . Left: Planet-star flux contrast as a function of wavelength, with broadband filter profiles for g, r, i, z, J, H, K filters shown below in grey. Right: broadband $i - H$ vs J contrast colors. Cloud properties are broadly distinguishable in color-magnitude space.	202
7.17 Phase curves for selected cloud models for r and J band.	203

7.18	Left: Models in color-magnitude space as a function of phase; error bars are for $S/N = 5$. The cloudy spectra behave differently as a function of phase. Right: Selected cloud models in color-magnitude space as a function of phase for three C/O ratio values. Broadband photometry is not sufficient for distinguishing C/O ratio above uncertainty.	203
7.19	204
7.20	Left: Phase curves for GJ 876 c models for cloudy and cloud-free models in z' band. Some cloud configurations exhibit brightening trend at higher phase angles. Right: Models in J vs $H - i$ color space where some cloud configurations exhibit surprising behavior with phase due to the (lack of) condensation of water clouds.	205
7.21	Top: GJ 876 c physical separation as a function of orbital phase and viewing phase. Orbit points within the purple regions are too hot for water clouds to condense under the assumptions of this model. Bottom left: Reflectance spectrum for four phases. Right: cloud opacity as a function of altitude (parameterized by pressure). For the smaller phase angles water clouds form between 0–0.1 bars which are absent at higher phase angles.	206
7.22	Color-magnitude diagram for airless (red) and Earth-like atmosphere models. The airless and Earth-like models are well separated from each other, and for the most part from the different cases within each group, by several magnitudes, just as with the gas giant models.	207
7.23	Top: Earth-like Proxima Centauri b cloudless albedo spectrum for inclination = 60° and phase = 90° , with molecular absorption features labeled. Bottom: Earth-like atmosphere albedo model under the same configurations with 100% and 50% cloud cover; the flux contrast (F_p/F_s), the stellar spectrum model, and the planet flux spectrum. More cloud cover leads to brighter planets but fewer spectral features for constraining composition.	208

- B.1 Relative astrometry of HIP 67506 A and HIP 67506 B (WDS J13500-4303 A and B). The abscissa and ordinate axes display position of HIP 67506 B relative to HIP 67506 A in mas in right ascension (RA) and declination (Dec). The motion of a non-moving background object at the position of HIP 67506 B is shown by the black track for the Gaia DR3 proper motion and parallax given for HIP 67506 B, with the predicted position at WDS observation epochs marked by colored diamonds. The blue track shows the track over the same time span given by the Gaia DR3 proper motion and parallax of HIP 67506 B. The observed WDS positions shown in Table B.1 are marked by filled circles with corresponding epoch colors. The observed motion of HIP 67506 B relative to HIP 67506 A is consistent with the Gaia DR3 proper motion and not with a common proper motion pair. We conclude that the order-of-magnitude higher distance for HIP 67506 B than HIP 67506 A given by Gaia DR3 is correct. 225
- C.1 Reduced images for the systems without companion detection. Each system was reduced using the method indicated. White circles in TYC 5480-589-1 and TYC 1262-1500-1 mark speckles that aren't candidate signals. See the text for details for each system. 228
- C.2 Contrast curves for non-detections. The colored regions mark the 1-, 2-, 3-, and 5- σ limits as a function of separation for each system and reduction method given. Separation is given in both λ/D units (bottom) and milliarcseconds (top); contrasts are given in flux contrast units. The black line gives the 1- σ noise floor for each observation. The classical ADI reduction got lower limits for TYC 5512-916-1 than KLIP ADI. Contrast curves were computed using the method described in Section 6.3.2 229
- C.3 Completeness maps for non-detections. See text for details. a: TYC 5518-135-1, b: TYC 5480-589-1, c: TYC 5512-916-1, d: TYC 6712-1511-1, e: TYC 877-681-1, f: TYC 1447-1616-1, g: TYC 368-1591-1, h: TYC 1262-1500-1, i: TYC 169-1942-1 230

C.4	Fit results for PupS-cc2 to Phoenix models. Top left: χ^2 surface for models in the $(T_{\text{eff}}, M/H)$ space with $\log(g)$ fixed at 4.0. The location of the lowest χ^2 is marked by the orange star, and the error bars show models within the uncertainty on that χ^2 value. Top right: χ^2 surface for models in the $(T_{\text{eff}}, \log(g))$ space with M/H fixed at -4.0. Both $\log(g)$ and M/H are not constrained by our photometry. Bottom left: Models within 1σ of the lowest χ^2 model, with our photometry and uncertainty overplotted in teal. Bottom right: Violin plots for each model showing the distribution of χ^2 values for the model from our bootstrap simulation with $M/H = -3.5, \log(g) = 0$	231
C.5	Model fit results for PupS-cc3. See caption of Figure 6.4 for plot explanation.	231
C.6	Model fit results for PupS-cc4. See caption of Figure 6.4 for plot explanation.	232
C.7	Model fit results for PupS-cc5. See caption of Figure 6.4 for plot explanation.	232
C.8	Fit results for PupS-cc6 to Phoenix models. Top left: χ^2 surface for models in the $(T_{\text{eff}}, M/H)$ space with $\log(g)$ fixed at 0.0. The location of the lowest χ^2 is marked by the orange star, and the error bars show models within the uncertainty on that χ^2 value. Top right: χ^2 surface for models in the $(T_{\text{eff}}, \log(g))$ space with M/H fixed at -3.5. Both $\log(g)$ and M/H are not constrained by our photometry. Bottom: Models within 1σ of the lowest χ^2 model, with our photometry and uncertainty overplotted in teal.	233
C.9	Model fit results for PupS-cc7. See caption of Figure 6.4 for plot explanation.	233

LIST OF TABLES

3.1	Keck/NIRC2 NGS AO Astrometry for KIC 8462852 candidate companions	80
3.2	System and Stellar Properties for KIC 8462852 AB	84
4.2	Summary of Binary Systems	100
4.2	Summary of Binary Systems (continued)	101
4.3	Summary of Observations and Results by Binary System	107
4.3	Summary of Observations and Results by Binary System (continued)	108
4.4	Gaia EDR3 Multiplicity Metrics for HIP 67506	112
5.1	Multiplicity Metrics for HIP 67506 A	128
5.2	Stellar Properties of HIP 67506 A	130
5.3	Properties of HIP 67506 C	130
6.1	Observations and Data Reduction	150
6.2	Companion Detections	164
6.2	Companion Detections Cont.	165
6.3	Non-Detections	166
7.1	GJ 876 Star and Planet Parameters	190
7.2	Proxima Centauri Star and Planet Parameters	194
7.3	Inclination, Mass, and Radius for Prox Cen b used in our models	195
B.1	WDS catalog entry for HIP 67506 A and HIP 67506 B (WDS J13500-4303 A and B)	226

ABSTRACT

To date the majority of planets known to exist outside of our solar system (exoplanets) have been discovered indirectly, yet the direct detection of exoplanets is the future of exoplanet characterization. Searching for signs of life (biosignatures) on worlds beyond our solar system through the next generation of ground-based extremely large telescopes is one of the top priorities for the next decade of astronomy. Yet this is extremely challenging from a technological perspective in that planets are very close to their host stars and very faint, making it difficult to disentangle the faint planet signal from the star. The Extreme Wavefront Control Lab at Steward Observatory is developing technology and methodology for this challenging science through the MagAO-X instrument, an extreme high-contrast imaging instrument on the 6.5 m Magellan Clay Telescope and a pathfinder for the high contrast imager GMagAO-X which will be part of the upcoming 24.5 m Giant Magellan Telescope planned for the 2030s. In my PhD work at the University of Arizona I have employed the capabilities of MagAO-X, and its predecessor MagAO, for stellar and substellar astrophysical research. In this work I will describe how we achieve high-contrast imaging with MagAO-X, a survey I analyzed using binary stars for data reduction, a survey I designed using the power of MagAO-X for exoplanet science through white dwarf stars in binaries, and simulation work I am conducting preparing for exoplanet detections through reflected light with MagAO-X and GMagAO-X.

Chapter 1

Introduction

“Dad, do you think there’s people on other planets?”

“I don’t know, Sparks. But I guess I’d say if it is just us... seems like an awful waste of space.”

Ted Arroway (Carl Sagan)

Contact (1997)

1.1 Setting the Stage – the Scientific Context

I remember being a freshman in high school in 1995, sitting in my band uniform in the football stands, talking to my peers, who probably couldn't care less, about how the first planet beyond our solar system had just been discovered. In my lifetime we've gone from knowing about the existence of 9 planets (later downgraded to 8 of course) to knowing about the existence of 5,616 + 8 planets (as of April 21, 2024). These are plotted as the grey dots in Figure 1.1, with our solar system planets overplotted. We have uncovered an array of diversity of what planetary systems can look like.

With this diversity of planets we have never been closer to being able to tackle the question of life on other worlds. Searching for biosignatures on exoplanets through ground-based ELT adaptive optics is the future of exoplanet science. The Astro2020 Decadal Survey, "Pathways to Discovery in Astronomy and Astrophysics for the 2020s" ([National Academies of Sciences, Engineering, and Medicine, 2021](#)), which identifies the top priorities for the next decade of astronomy, calls for "a step-by-step program to identify and characterize Earth-like extrasolar planets [exoplanets], with the ultimate goal of obtaining imaging and spectroscopy of potentially habitable worlds" ["Pathways to Habitable Worlds" pg 2], and identifies investment in a large US Extremely Large Telescope (ELT) program, including the Giant Magellan Telescope (GMT) and Thirty Meter Telescope (TMT), as the top priority for ground based astronomy, citing the power of 20-40 mirrors with diffraction-limited observing via adaptive optics (AO) for addressing every important science case.

My work documented here encompasses astrophysics with current ground-based AO technology and preparations for exoplanet detection and characterization with ground-based ELT AO.

1.2 Direct Imaging is the Future of Exoplanet Science

To date, the vast majority of exoplanets have been detected indirectly, through observing their host star and the influence they have on it. Only a small fraction have been directly detected by collecting photons emitted by the planet. As of this writing in the NASA Exoplanet Archive¹ there are 70 directly imaged planets of the 5600 known exoplanets, or ~1%. Figure 1.1 shows

¹<https://exoplanetarchive.ipac.caltech.edu/>

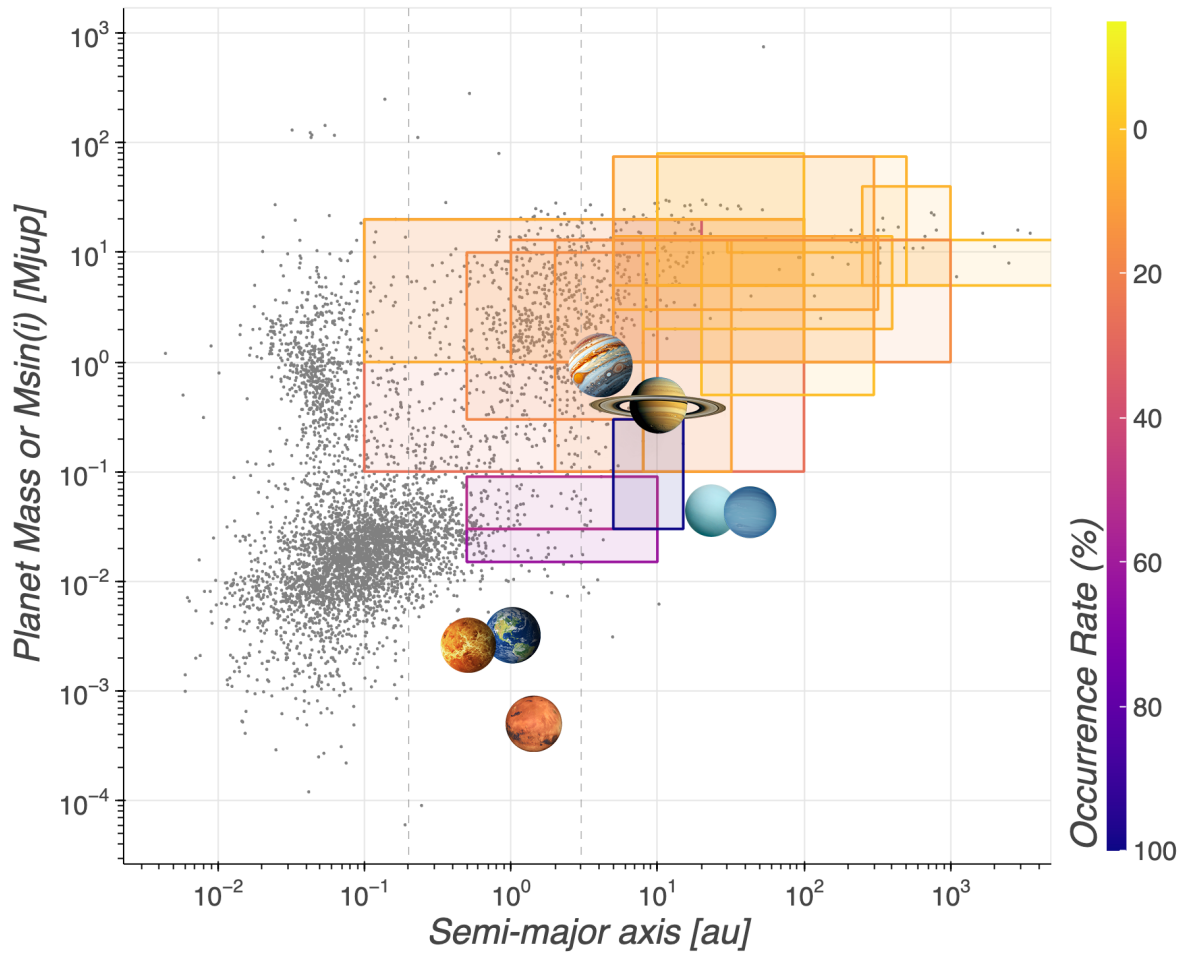


Figure 1.1: All currently known exoplanets in the Exoplanet Archive as of this writing (grey dots) with literature occurrence rates overlaid, colored by occurrence rate. The region direct imaging is most sensitive to (~ 10 s– 1000 s of au and ~ 1 – $1000 M_{\text{Jup}}$) has exceedingly low occurrence rates. An interactive version of this plot is available at www.loganpearce.com. References: [Bowler \(2016\)](#); [Bowler and Nielsen \(2018\)](#); [Bryan et al. \(2016\)](#); [Cassan et al. \(2012\)](#); [Fernandes et al. \(2019\)](#); [Fulton et al. \(2021\)](#); [Galicher et al. \(2016\)](#); [Lafrenière et al. \(2014\)](#); [Lannier et al. \(2016\)](#); [Meshkat et al. \(2017\)](#); [Naud et al. \(2017\)](#); [Nielsen et al. \(2019\)](#); [Poleski et al. \(2021\)](#); [Rameau et al. \(2015\)](#); [Vigan et al. \(2021\)](#)

the occurrence rates of planets from literature in the region direct imaging is sensitive to (colored boxes); most are less than 10%, meaning that of all the stars surveyed in a given survey, less than 1 in 10 had a detectable planet signal in the regime the survey was sensitive to.

Yet direct imaging is the best way to characterize exoplanets. Directly collecting photons from the planet offers access to parameters unavailable to other detection methods such as transit and

radial velocity detections². The most readily available observations are the astrometry (relative and absolute position) and photometry (brightness in different wavelength ranges), which provides orbit, brightness, and variability information; coupled with precise distance and age information, evolutionary models can provide mass and formation process constraints. Precise astrometric measurements of companion position relative to the star, along with the star's absolute astrometry, especially covering a long time baseline, can be used to determine companion mass without any model dependence, which can in turn provide feedback to evolutionary models. Population level studies and occurrence rates can identify population level trends informing formation processes. Orbit studies can also inform formation processes through (mis)alignment of any of planet orbit/binary star orbit/host star spin axis/planet spin axis, and planet impact on observed disk features. Direct detection of planet photons from thermal emission through the atmosphere or from starlight reflecting off the atmosphere directly probes atmosphere composition through molecular absorption or emission lines and continuum shape, which probes cloud properties, pressure-temperature profiles, and chemical processes, in both broadband and low- and high-resolution spectroscopy; compared to transit spectroscopy which only probes the upper atmosphere haze along the edge of the planetary disk. (Follette, 2023)

Direct imaging with ELTs will also be essential for biosignature detection. Figure 1.2 shows two plots from Hardegree-Ullman et al. (submitted) examining detection of the biosignature O₂ with transit spectroscopy. Transit spectroscopy involves observing the spectrum of a star as a planet transits across the disk of the star. During the transit, light from the star will pass through the edges of the atmosphere (on the terminator) and encode information about the composition of the atmosphere. Detection of O₂ via transit spectroscopy will take a survey of hundreds of years with current planned ELTs in the most optimistic scenario (Figure 1.2 left). Meanwhile a 10 year survey for O₂ via direct spectroscopy with the European ELT or GMT will deliver 5–15 O₂ detections (Figure 1.2 right). And direct spectroscopy integrates the detection over the entire planet disk (for thermal emission) or a portion of the disk (reflected light) rather than just light passing through the atmosphere at the terminator. Direct imaging is the most efficient and information-rich probe of Earth-like planets and biosignatures.

²Transit: observing the period dimming of a star's light as a planet passes in front and obscures a portion of the star's disk. Radial velocity: observing the cyclic motion of a star towards and away from the observer due to the gravitational influence of the planet

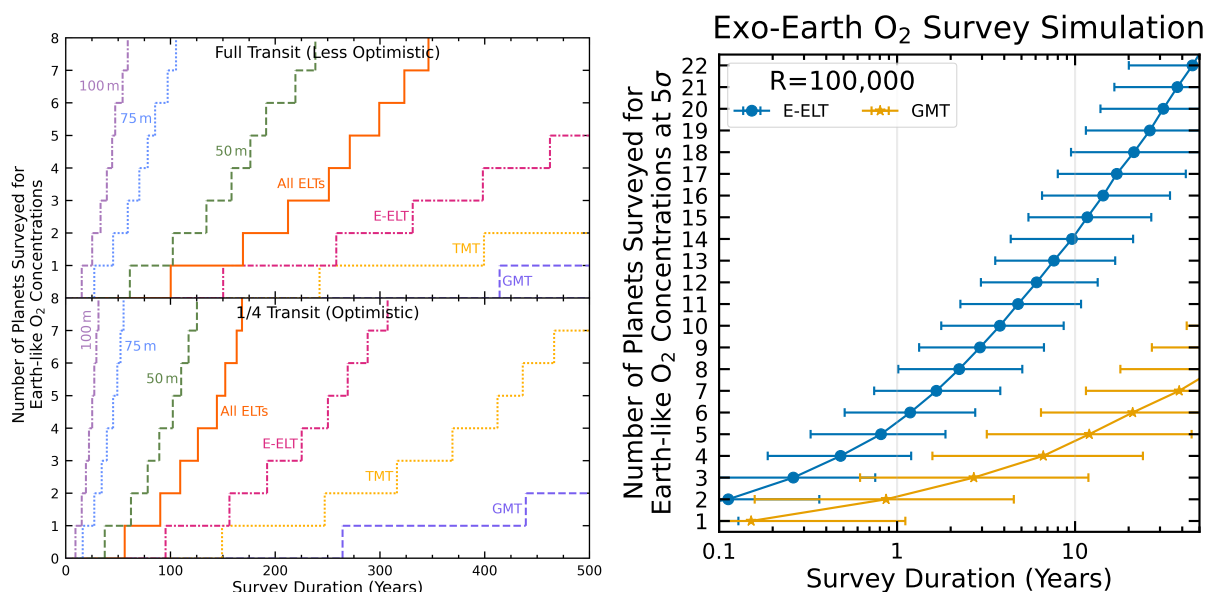


Figure 1.2: Two plots from Hardegree-Ullman et al. (submitted) comparing the detection of oxygen in an Earth-like exoplanet via transit spectroscopy and direct detection with an ELT. In the most optimistic case, a transit spectroscopy survey with a GMT-size telescope will take hundreds of years to detect one Earth-like oxygen signature. Via direct detection, a GMT-size telescope can make approximately 5 detections in 10 years.

Direct detection of planets, however, is extremely hard, and it's easy to see why. Stars are bright and planets are not. Figure 1.3 illustrates the contrasts (the ratio of planet flux to star flux) involved. The contrast of a young Jupiter to a Sun-like star is similar to contrast of a firefly to a lighthouse; for a mature Jupiter it is similar to bioluminescent algae to the lighthouse! We are trying to tease out a signal of something that is 1 million to 10 billion times fainter than the thing right next to it. In Figure 1.1, the directly imaged planets (grey dots in the yellow boxes) all have masses $\gtrsim 10 M_{\text{JUP}}$, meaning pretty much all are several times larger than Jupiter, because they glow more brightly in thermal emission than lower mass planets and thus have lower contrasts (more below)



Proximity to the star is an additional challenge. In Figure 1.1, the directly imaged planets are all at separations $\gtrsim 10$ au and out to 1000's of au, meaning most are beyond the orbit of Saturn in our solar system and even well beyond the Kuiper Belt out to the distance of the Oort Cloud. However, in Figure 1.1, there are thousands of planets closer to the

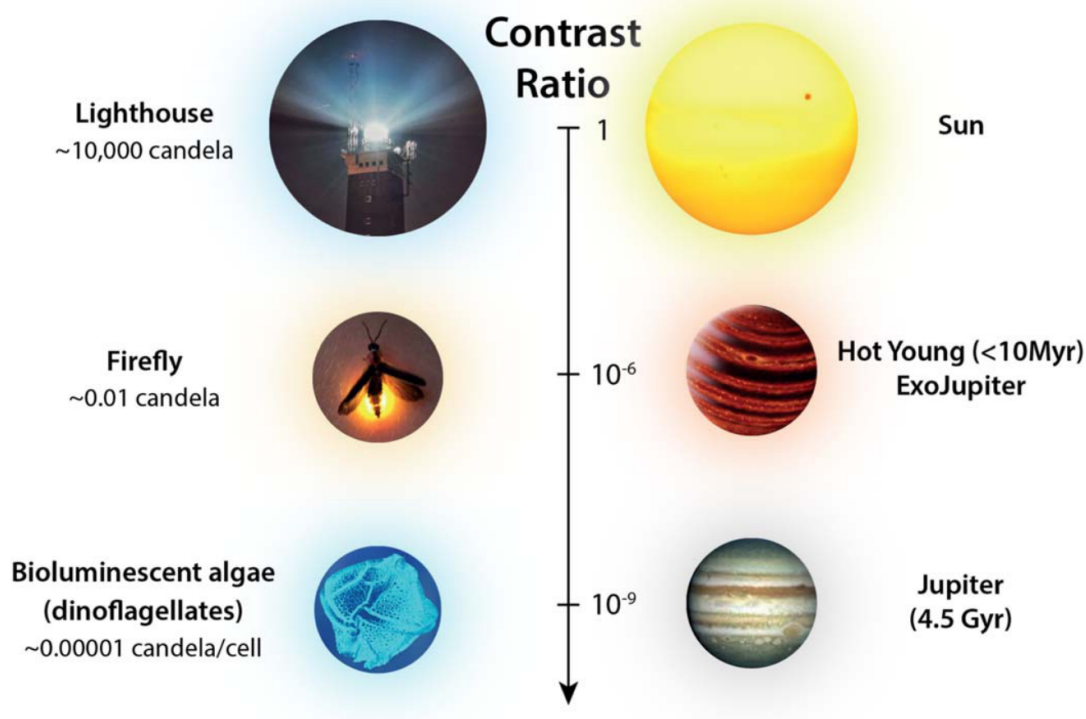


Figure 1.3: Illustration of the contrasts involved in directly imaging exoplanets, reproduced from [Follette \(2023\)](#)

their host stars than the Earth is from the Sun; there are even entire exo-solar systems closer to their star than Mercury is from our Sun (e.g., the Trappist-1 system, [Gillon et al., 2017](#)). This is mainly due to detection capabilities – detection methods like transits and radial velocity are more sensitive to close in planets, while direct imaging is more sensitive to widely-separated planets.

So the most basic nature of the problem in direct imaging is to push technology to detect fainter objects (higher contrast) at closer separations. The MagAO-X instrument at Steward Observatory is a technology development platform for driving direct imaging technology and capabilities. **The ultimate science goal of MagAO-X is to detect nearby**

terrestrial planets in reflected light, and the team is developing innovative technology and observing strategies for getting there. It is also a platform for building towards GMagAO-X, the planned high-contrast imaging instrument for the GMT.

The next sections outline how we directly detect exoplanets and how we accomplish high-contrast imaging.

1.3 Direct Detection of Exoplanets

1.3.1 Thermal Emission

Stars form from the gravitational collapse of molecular gas and dust in giant molecular clouds. Figure 1.4 shows a JWST NIRCcam image of the famous “Pillars of Creation”, where young stars are in the process of forming in the dense regions of the cloud, assisted from intense high-energy radiation from some nearby very hot stars just outside the image to the upper right. Planets are also forming around those stars, and are believed to form through two mechanisms:

1. A top-down formation in which a smaller amount of gas and dust from the same molecular cloud undergo gravitational collapse in a manner similar to the star. Massive giant planets and brown dwarfs are believed to form in this manner.
2. A bottom-up formation in which small debris left over (pebbles) from the star’s formation coalesce and accrete gas and dust as they slowly build up mass. Terrestrial and gas giant planets are believed to form in this way.³

Regardless of how it is accreted, as material accretes it falls down the gravitational potential well of the protoplanet, exchanging gravitational potential energy for heat energy, so young forming objects are heated as they grow. These objects don’t have enough mass to attain the temperatures

³There is a bit of disagreement about what constitutes a “planet” on the high-mass end versus a brown dwarf. Brown dwarfs are substellar objects too small to ignite hydrogen fusion but larger than a planet, but where is the planet/brown dwarf line? The accepted dividing line is $13 M_{\text{Jup}}$ — objects above $13 M_{\text{Jup}}$ can fuse deuterium in their cores when they are young. But this is imperfect. Is a $10 M_{\text{Jup}}$ object that formed via gravitational collapse a planet, since it’s below $13 M_{\text{Jup}}$, but it formed like a brown dwarf? But formation mechanism is hard to determine observationally whereas mass is easier. Is a free-floating $10 M_{\text{Jup}}$ object a planet even though it has no host star? Maybe there shouldn’t be a distinguishing line at all, it’s all one large mass function all the way down. But surely bottom-up vs top-down formation matters? All of this is a still very much an open question to date, and one I find very interesting. Since this work doesn’t address this question, I will use the term “planet” or substellar object or planetary mass companion and not worry too much about it here.

necessary to ignite hydrogen fusion in their cores, and they radiate their heat of formation away with no heat source to replace it. So planets and brown dwarfs are hot when they are young, but cool as they age.

Objects glow at different wavelengths of light corresponding to their temperatures, a function in physics known as black body radiation⁴. The temperature of the black body describes the shape of the emitted energy as a function of wavelength. At the effective temperature of the Sun's atmosphere (~ 5700 K), the peak of the emitted light is around the color yellow (which is why the Sun can be described as yellow); for a cooler star, the black body peak shifts to longer wavelengths and the star appears redder. Figure 1.5 (top) shows emission curves for a black body at four different temperatures (normalized to the peak flux being one, to emphasize the location of the peak for each curve). As an object cools its peak emission shifts to longer and redder wavelengths. The grey curves show several common telescope filter transmission as a function of wavelength, g , r , i , and z in visible wavelengths, J , H , and K in near-infrared wavelengths. For a Sun-like star its flux will be highest in visible filters r and i , whereas for a cooler object the flux will peak in the near-IR. Figure 1.5 (bottom) shows model spectra⁵ of thermal emission as a planet cools as it ages; the planet flux drops by ~ 12 orders of magnitude as it cools from 2300 K to 230 K.

Young high-mass planets and brown dwarfs ($\lesssim 300$ Myr) thus will glow brightest in near-IR wavelengths, and get fainter and redder as they cool. By the time objects are several Gyr old, their heat from formation is long gone, and equilibrium temperatures are now set by thermal flux from interior processes and by incident radiation from their star.

All of the direct imaging planet and brown dwarf companion detections to date have been through thermal emission of hot young objects. Direct imaging planet searches traditionally have targeted young star forming clusters where the age and cluster membership is relatively well constrained and young planets can be expected to be brightest in the 2–10 μm range (e.g. Nielsen et al., 2019, and other references in Figure 1.1). Objects $\lesssim 10$'s of Myr have contrasts of 10^{-3} – 10^{-4} in the 3–5 μm range because their temperatures are ~ 500 – 1500 K. Chapter 4 of this work analyzes data from a young-star survey with images in a filter centered at 3.9 μm .

⁴An common example is the coil on an electric stove glowing red when its hot

⁵as shown in the Picaso tutorials found here: https://natashabatalha.github.io/picaso/notebooks/workshops/SaganSchool2021/3_Chemistry.html

As we saw in Figure 1.1, the regimes accessible to thermal emission surveys have yielded low occurrence rates, requiring a shift in observing strategy to regimes we know have a lot of planets, namely older (and therefore cooler) and closer systems. Several researchers at UA are designing surveys in the $10\mu\text{m}$ wavelength region, which presents challenges from optics and also from thermal emission from the Earth's atmosphere, which is bright at those wavelengths. Another strategy is to abandon thermal emission and shift to detecting planets in reflected light.

1.3.2 Reflected Light

This will be discussed in detail in Chapter 7, but I lay out the basics here. Just as the Moon reflects the Sun's light, we can also detect exoplanets via the light they reflect from their host star. Reflected light exoplanet detections do not depend on age, and contrasts are lower at closer separations, and so allow probing the regions where we know there are already thousands of planets detected via other methods. However, the contrasts involved in reflected light are several orders of magnitude higher (fainter) than young massive planet thermal emission.

The reflected light contrast depends on: 1. planet radius, 2. planet/star separation, 3. planet viewing phase, 4. planet atmosphere properties (albedo).

Contrast as a function of wavelength and phase for a diffusively scattering⁶ surface is given by

$$C(\alpha, \lambda) = A_g(\lambda) \left(\frac{R_p}{r} \right)^2 \left[\frac{\sin \alpha + (\pi - \alpha) \cos \alpha}{\pi} \right] \quad (1.1)$$

where λ is the wavelength, $A_g(\lambda)$ is the geometric albedo as a function of wavelength, R_p is the planet radius, r is the star-planet separation, and α is the viewing phase angle (Cahoy et al., 2010, 2017).

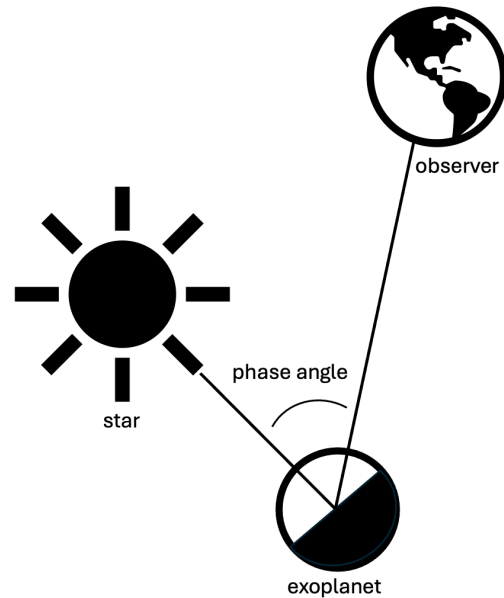


Figure 1.6: Diagram illustrating the definition of phase angle α

⁶scatters isotropically, like a matte surface, as opposed to specular reflection like a mirror

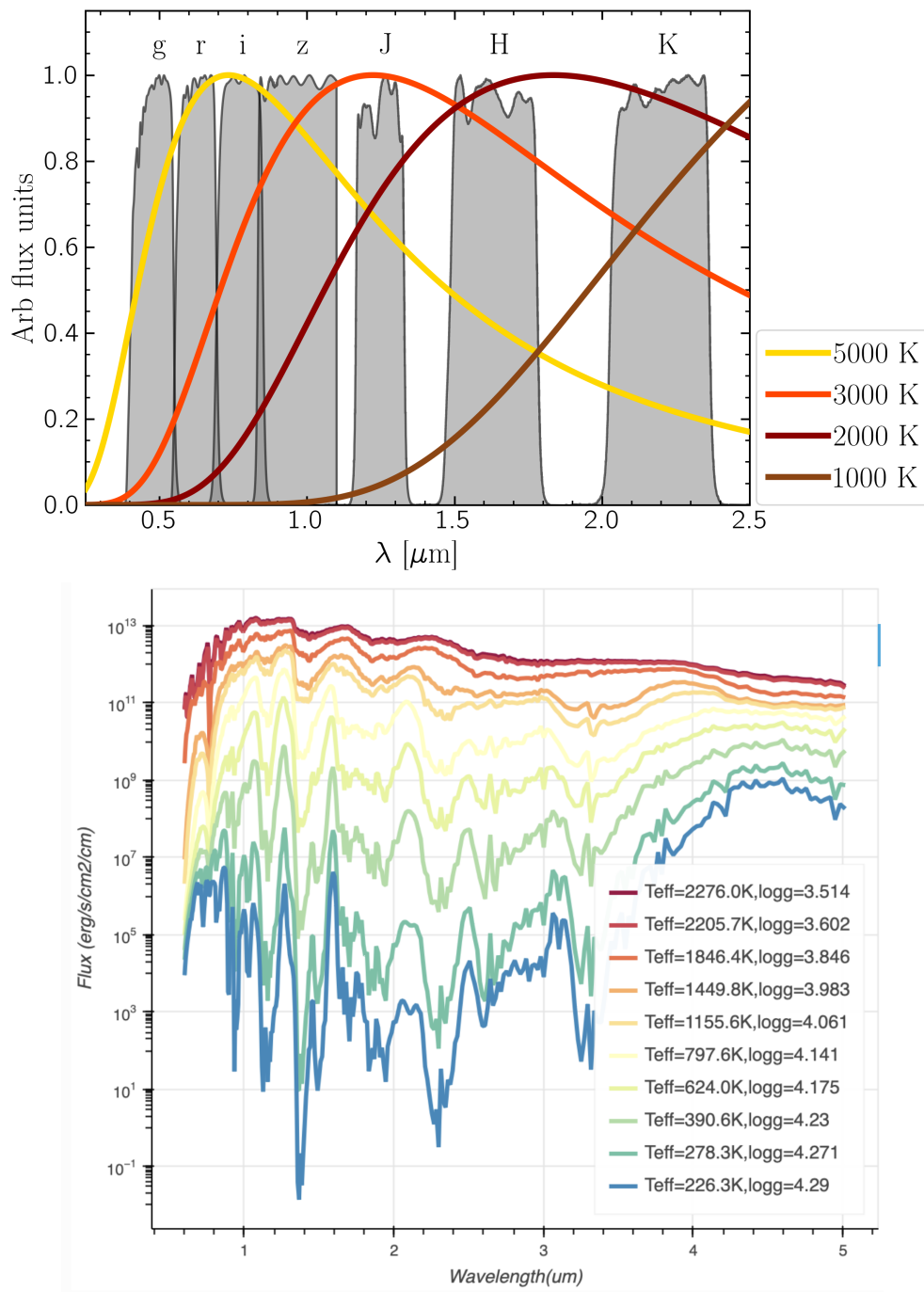


Figure 1.5: Top: Blackbody radiation as a function of wavelength for objects are four different temperatures, 5000 K (yellow), 3000 K (red), 2000 K (dark red), and 1000 K (brown). The curves have been normalized such that their peak flux is equal to one, to emphasize the location of the peak for each curve. As objects cool, the peak of their emission shifts to longer and redder wavelengths. Filter curves for several common filters are shown in grey. Bottom: Thermal emission model spectra from PICASO (Batalha et al., 2019) exoplanet atmosphere modeling code for planets as they age and cool (effective temperature decreasing and surface gravity increases).

Geometric albedo is defined as the ratio of the reflected light to light reflected by an idealized flat diffuse reflecting surface of the same area: $A_g(\lambda) = \frac{F_R(\alpha=0^\circ, \lambda)}{F_I(\lambda)}$, where $F_I(\lambda)$ is the incident flux from the star and $F_R(\alpha = 0^\circ, \lambda)$ is the reflected flux at full phase ($\alpha = 0$). Exoplanet atmospheres and surfaces will have different albedos at different wavelengths, translating to varying observed contrasts enabling characterization.

The classical phase function $\Phi(\alpha)$ describes the fraction of light reflected relative to full phase, from 0.0–1.0; in the Lambertian scattering example Eqn 1.1 above $\Phi(\alpha) = \left[\frac{\sin \alpha + (\pi - \alpha) \cos \alpha}{\pi} \right]$. The phase angle α is defined as the angle between the light source (the star) and the observer, illustrated in Figure 1.6, with full phase at $\alpha = 0^\circ$, quarter phase (quadrature) at $\alpha = 90^\circ$ and new phase at $\alpha = 180^\circ$.

Contrast also goes as R_p^2 , giving a degeneracy between planet radius and phase – a small planet at full phase can have the same contrast as a large planet at large phase angle. This will be discussed in detail in Chapter 7.

In Chapter 7 of this work I go into detail on reflected light observations, discuss how we are preparing for reflected light planet detections with current and future instruments, and the initial modeling work I am conducting for these observations.

1.4 How We Accomplish High-Contrast Imaging

High-contrast imaging (HCI) refers to a suite of techniques employed towards suppressing the light from the bright thing (star) to reveal light from a nearby faint thing (like a planet or disk); the contrast (the ratio of flux from the faint thing to flux from the bright thing, $\text{contrast} = \frac{F_{\text{source}}}{F_{\text{star}}}$) between the star and planet is extremely high, with planets being from about 1 million to 10 billion times fainter than their nearby stars.

Figure 1.7 displays simplified diagrams of the adaptive optics and coronagraph systems in a basic high-contrast imaging system. Starlight is a flat plane wave by the time it reaches the top of the atmosphere and is distorted by turbulence before it hits the primary mirror. The light is sent from the telescope to a deformable mirror, which reflects light into a beam splitter which sends some light to a wavefront sensor and the rest to the coronagraph system. The WFS senses the distortion and sends a control signal to the DM which pushes and pulls on actuators, deforming the surface of the DM to correct out the distortions and return the light to a flat plane wave – this is the

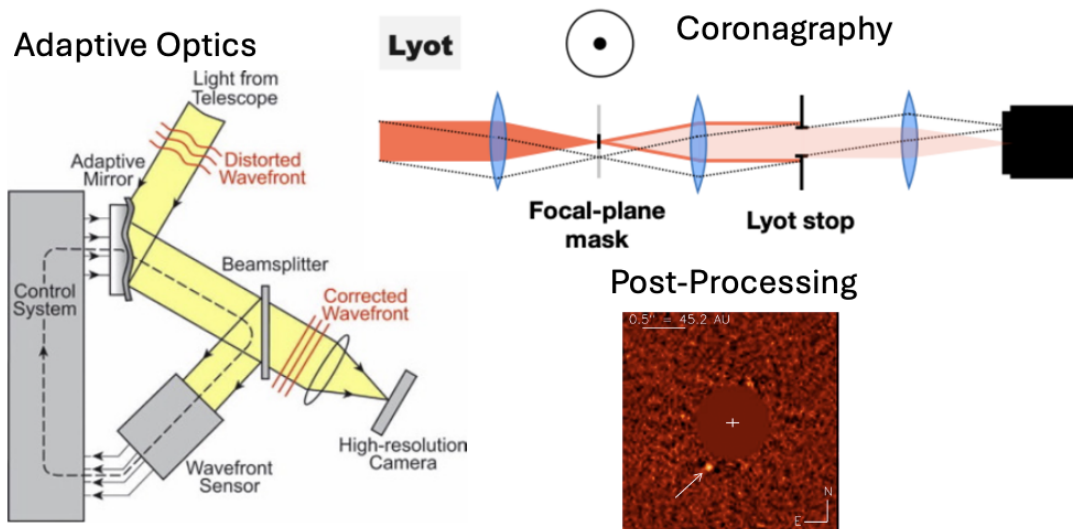


Figure 1.7: Simplified diagrams of adaptive optics and coronagraph systems. See text for details.

adaptive optics (AO) system. The light then travels to the coronagraph system. A Lyot coronagraph is an obstruction that blocks the on-axis light (starlight, red) allowing off-axis light (such as a faint companion, black dashed line) to pass through to the detector. Finally we remove residual starlight in the image using post-processing techniques to reveal the faint companion (white arrow).

Figure 1.8 illustrates the effect of adding each stage of high-contrast imaging on the resulting image. With no AO correction applied, the atmosphere causes the light from the star to spread out and bounce around on the detector – this is a term astronomers call “seeing”, how much the light from a point is spread out in an image. The image is “seeing-limited” – the parameter that sets the size of the point spread function (how light from a point source [star] is spread out on the detector; PSF) is the amount of turbulence and distortion from the atmosphere. When the AO system is turned on, the DM restores the starlight to as close as possible to a flat plane wave. The parameter that sets the size of the image on the detector is now set by the fact that light is a wave and is diffracted by the telescope pupil and other obstructions. The image is now “diffraction limited”. Even though we’ve corrected the distortion, we still have to deal with the fact that light is a wave, and as it interacts with the telescope pupil and obstructions it will diffract, creating an “Airy” pattern with a tight central core and rings of decreasing amplitude extending radially. The full-width at half maximum (FWHM) of a diffraction-limited PSF is $\approx \frac{\lambda}{D}$ where λ is the wavelength and D is the telescope primary mirror diameter, and θ describes the radius of the diffraction limited core. The ability to distinguish two point sources close together (the resolution) is now set by the

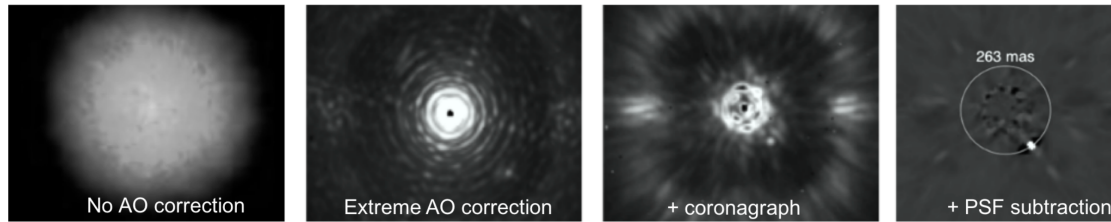


Figure 1.8: Reproduction of Figure 5 from Currie et al. (2023) showing the effects of adding different stages of a high-contrast imaging system (in this case SPHERE on VLT). Left: no AO correction, seeing-limited distorted starlight. Center left: AO correction applied, diffraction-limited point spread function, with diffraction effects and speckles visible. Center right: AO + coronagraph, a “dark hole” in which speckles are suppressed is visible in a ring surrounding the central obscured star; the faint off-axis companion is visible just to the lower right. Right: AO + coronagraph + PSF subtraction applied, now the starlight is almost entirely removed and the faint companion is clear.

telescope mirror and the wavelength of light you’re observing in. The diffraction limited resolution of a 6.5m telescope in the “red” r' filter ($\lambda_0 = 0.613\mu\text{m}$) is $0.02''$, compared to a good seeing-limited observation at Las Campanas Observatory in Chile of $0.5''$. A larger diameter primary mirror, such as the GMT’s 25.4 m mirror, provides much higher spatial resolution compared to the Magellan Clay Telescope’s 6.5 m mirror or even the James Webb Space Telescope’s 6.5 m mirror, so large-primary ground-based telescopes are essential for probing close-in regimes. Additionally, detecting planets in bluer (shorter) wavelengths also provides higher spatial resolution, since the size of the Airy pattern scales with wavelength. Detecting planets in reflected visible light (where they are brightest) allows for closer-in planets than thermal emission because they are detected in visible rather than IR wavelengths. This will be discussed in detail in Chapter 7.

Additionally, imperfections in the optics and imperfect AO correction cause coherent scattered starlight called speckles, which act as copies of the PSF which increase noise and can be mistaken for astrophysical signals (giving a false positive planet detection). The addition of a coronagraph blocks the central starlight but allows off-axis light from, for example a planet, to pass through. The combination of AO and a coronagraph creates a “dark hole” – a region where scattered and diffracted starlight is suppressed and detectable contrast is much higher. There are several different coronagraph types and techniques which are beyond the scope of this work. Finally, post-processing techniques remove instrument and optical artifacts and leave behind genuine astrophysical signals. Post-processing will be covered in more detail in Chapter 2.

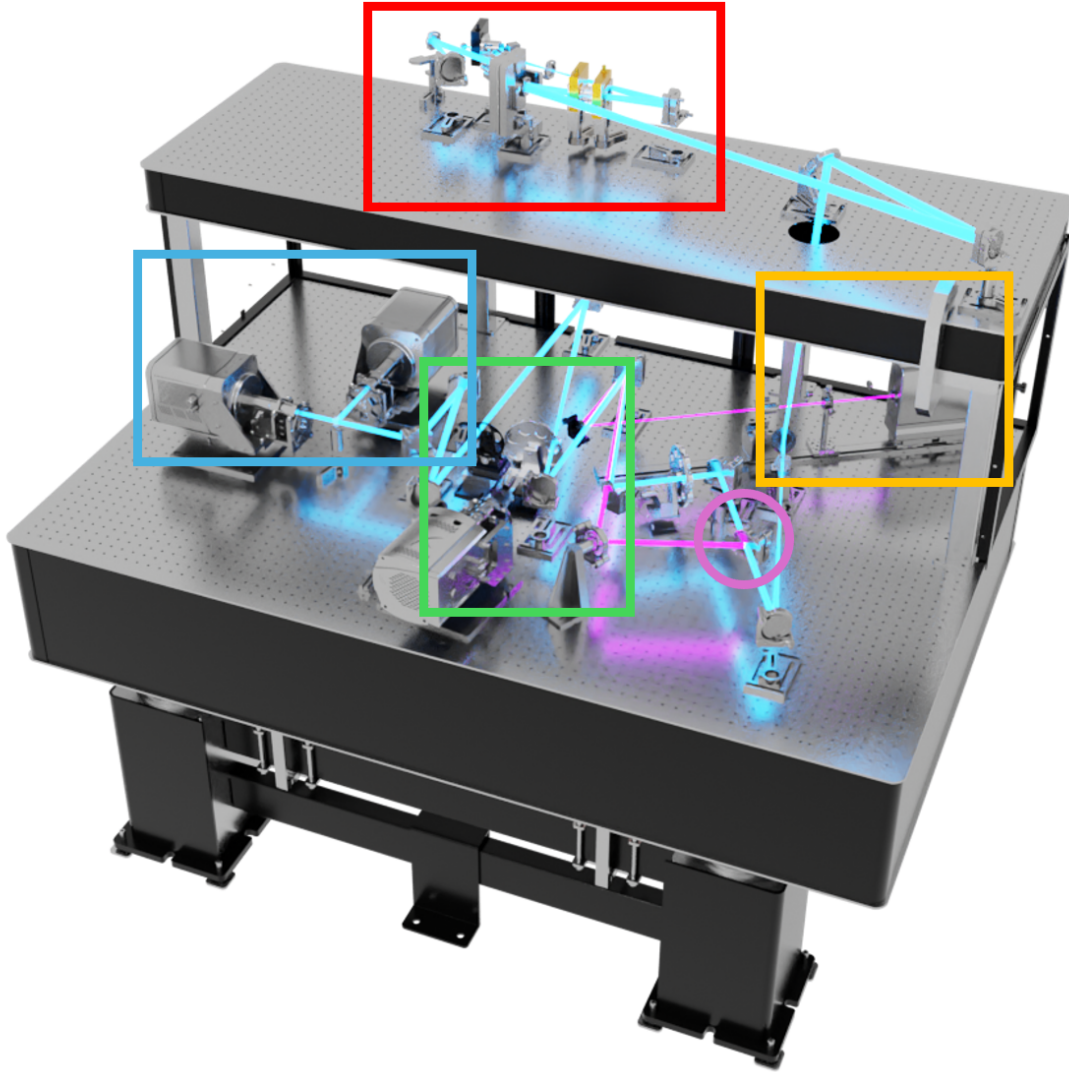


Figure 1.9: A schematic of MagAO-X rendered by Joseph Long using the solid model of [Close et al. 2018](#). Red: light from the telescope first encounters the woofer DM, then the 2k tweeter DM. Light is then split by a beam splitter (purple circle) into a path to the science cameras and a path to the pyramid wavefront sensor (orange). Green: light to the science cameras first enters the coronagraph system and the NCPC DM. Blue: finally light arrives at the two science cameras. See text for more detail.

MagAO-X is an Extreme Adaptive Optics (ExAO) instrument built by the Extreme Wavefront Control Lab (XWCL) at Steward Observatory at the University of Arizona ([Males et al., 2022](#)). ExAO improves upon the simple diagram above by improvements in DMs (more actuators, faster correction speeds), coronagraphs, and cameras. It sits on the Nasmyth platform of the Magellan Clay telescope, a 6.5 m telescope at Las Campanas Observatory in Chile.

A schematic of MagAO-X is shown in Figure 1.9. Starlight entering MagAO-X is reimaged via off-axis parabolic mirror to the two DMs marked by the red box: the 97 actuator “woofer”

DM which corrects for large spatial scale aberrations followed by the 2K actuator “tweeter” DM which corrects for small spatial scale aberrations, similar to low- and high-frequency woofer and tweeter speakers in a stereo system. Light then enters the beamsplitter where some of it is sent off to the pyramid WFS (orange box) and the rest is sent to the coronagraph system (green box). Before the coronagraph there is an additional DM, called the non-common path corrector (NCPC) DM, an innovation in MagAO-X which corrects for light going to the science camera that takes a different path than light to the WFS. Finally the light arrives simultaneously at the two science cameras (blue box), which enables simultaneous observations in two filter bands. Finally, there is an integral field unit spectrograph, VIS-X (not pictured), which exploits MagAO-X’s resolution and extreme wavefront control for high-resolution spectroscopy. For more detail on the mechanical design of MagAO-X see [Close et al. 2018](#).

Figure 1.10 illustrates the effect of turning MagAO-X’s HCI system on a bright star with a hidden companion.

Unlike other HCI instruments targeting thermal emission, for reflected light we need to observe the planets where the star is brightest, in optical wavelengths. MagAO-X uses four broadband optical filters: g' ($\lambda_0 = 0.527\mu\text{m}$, $\Delta\lambda_{\text{eff}} = 0.044\mu\text{m}$), r' ($\lambda_0 = 0.614\mu\text{m}$, $\Delta\lambda_{\text{eff}} = 0.109\mu\text{m}$), i' ($\lambda_0 = 0.762\mu\text{m}$, $\Delta\lambda_{\text{eff}} = 0.126\mu\text{m}$), and z' ($\lambda_0 = 0.908\mu\text{m}$, $\Delta\lambda_{\text{eff}} = 0.130\mu\text{m}$), as well as two narrowband filters for the hydrogen Balmer α line ($\lambda_0 = 0.656\mu\text{m}$, $\Delta\lambda_{\text{eff}} = 0.009\mu\text{m}$) and continuum ($\lambda_0 = 0.668\mu\text{m}$, $\Delta\lambda_{\text{eff}} = 0.009\mu\text{m}$), and methane ($\lambda_0 = 0.875\mu\text{m}$, $\Delta\lambda_{\text{eff}} = 0.026\mu\text{m}$) and continuum ($\lambda_0 = 0.923\mu\text{m}$, $\Delta\lambda_{\text{eff}} = 0.023\mu\text{m}$)⁷. MagAO-X has a diffraction-limited resolution of 29 mas in z' and 20 mas in r' , with 5.9 mas per pixel (Long et al., submitted).

1.5 This Work

In this dissertation I will describe how I have made use of AO instruments past (Keck/NIRC2 and MagAO), present (MagAO-X), and future (GMagAO-X) for stellar and substellar detection and characterization. One common theme in all my work has been (sub)stellar binarity and dynamics.

⁷Filter specifications and filter curves can be found in the MagAO-X instrument handbook at <https://magao-x.org/docs/handbook/index.html>

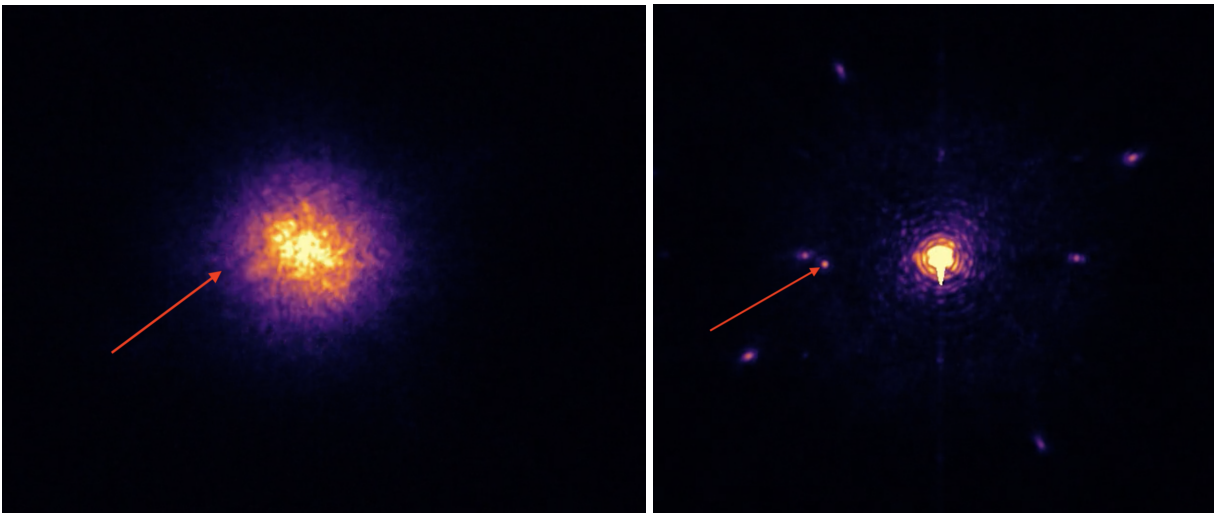


Figure 1.10: Stills from a movie recorded during the 2024A observing semester of the star pi Pupis taken in the z' filter. Left: with the AO off the star is distorted and the faint companion, indicated by the red arrow, is not visible. The star's signal bounces around on the detector. Right: with the AO on, the star signal becomes fixed on the detector and diffraction-limited, and the faint companion is now easily seen (red arrow). The other symmetrical point-like signals are speckles caused by the diffraction from the tweeter and NCPC DMs.

Chapter 2

Concepts

“Looking up into the night sky is looking into infinity – distance is incomprehensible and therefore meaningless.”

Douglas Adams
Hitchhiker's Guide to the Galaxy

“Well, I mean, yes idealism, yes the dignity of pure research, yes the pursuit of truth in all its forms, but there comes a point I'm afraid where you begin to suspect that the entire multidimensional infinity of the Universe is almost certainly being run by a bunch of maniacs.”

Douglas Adams
Hitchhiker's Guide to the Galaxy

In this section I will go a bit deeper into concepts underlying my work and which are used in my analyses.

2.1 Image Post-processing

As outlined in Chapter 1, high-contrast imaging is enabled by starlight and speckle suppression upstream of the science camera, and by post-processing after the images have been obtained. Here I will briefly discuss post-processing algorithms, especially the ones employed in my analyses in this work.

2.1.1 Image Reduction Algorithms: Observing Strategy

The goal of post-processing is to remove the star's point-spread function (PSF), scattered starlight, and speckles without removing any of the signal of a true astrophysical source such as a planet or disk. This is accomplished by constructing a model containing the stellar PSF and all speckles and optical artifacts, but does not contain any companion signal, and subtracting it from the science target images; there are several clever observing tricks to play to obtain an accurate PSF model to fully remove unwanted signal and fully retain wanted signal.

Reference Differential Imaging

Reference Differential Imaging (RDI) involves observing another star, using that star's PSF as a model PSF, and subtracting it from your science target images ([Smith and Terile, 1984](#)). Reference images can either be obtained concurrently with science observations by observing another nearby star of similar magnitude, or constructed from a large library of high-quality images of reference stars (e.g [Sanghi et al., 2022](#)). RDI is especially advantageous for disk imaging and for objects at small angular separations ([Ruane et al., 2019](#)). A disadvantage is that the reference and science images aren't obtained simultaneously so differences in conditions, either spatially or temporally, between science and reference nearly always hinder PSF subtraction. [Figure 2.1](#) illustrates classical RDI with an observed nearby star.

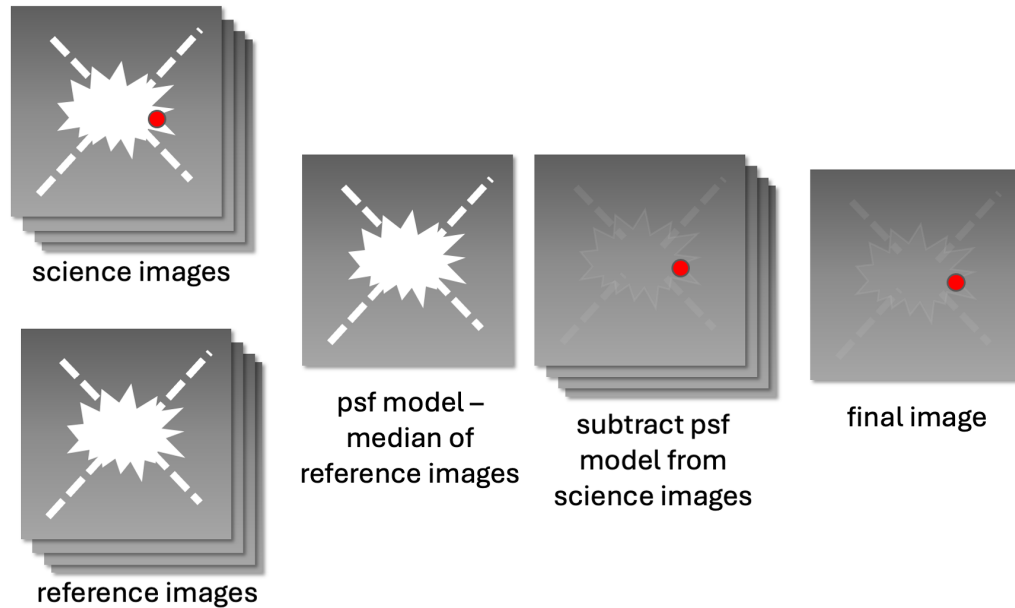


Figure 2.1: Illustration of classical RDI. A science target with a hidden companion (red) and a reference star are observed. The PSF model is constructed as the median image of the reference star images, then subtracted from every science image. The final image is taken as the derotated and medianed (or summed) image of subtracted science images.

Angular Differential Imaging

Angular Differential Imaging (ADI, [Marois et al., 2006](#)) exploits the Earth's rotation to obtain differentiation between images of the science target to allow PSF reconstruction without observing another star. For an AltAz telescope, using pupil-tracking mode, the sky is allowed to rotate throughout the observation while the pupil is fixed with respect to the detector. As the field rotates, optical artifacts such as speckles and diffraction spikes remain fixed on the detector while true astrophysical signals like a companion rotate. Given enough rotation angle, a reference PSF can be constructed from the fixed features that don't move over time, distinguishing speckles, which are copies of the PSF, from PSFs caused by genuine signals. When the images are PSF-subtracted and derotated, the star signal is removed but the companion signal remains. Related to ADI is roll-subtraction for space-based imaging, where PSF references are derived from different satellite roll angles of the same star (e.g [Schneider et al., 2014](#)). Figure 2.2 illustrates the ADI process.

A disadvantage of ADI is the potential for source self-subtraction, especially for extended sources like disks and sources at small angular separations. Without sufficient rotation throughout

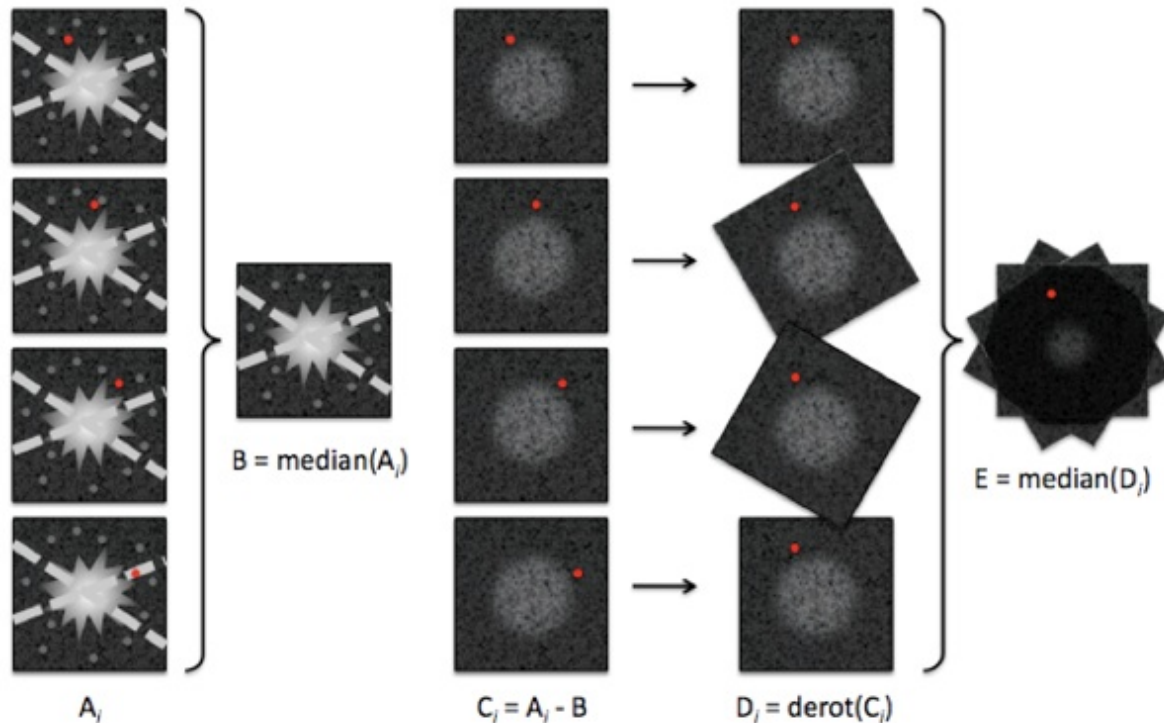


Figure 2.2: Illustration of classical ADI, reproduced from AstroBites article by Jessica Donaldson (<https://astrobites.org/2013/06/09/lowest-mass-exoplanet-discovered-via-direct-imaging/>). As the star is observed, the field rotates, and the companion signal (red) rotates through the fixed optical artifacts (white). A PSF reference is made from the median of the entire observation – since the companion moves through the field it is not contained in the median image. The PSF model is then subtracted from each image in the dataset, removing fixed artifacts but leaving the companion signal, and the final image is taken as the median of the derotated and subtracted images.

the dataset, the signal of interest will not be sufficiently separated in subsequent observations as to not be included in the model PSF, resulting in negative lobes on either side where the source has subtracted itself. Additional perturbations outside of the optics, including wind-driven halo, also will not be subtracted by ADI.

Spectral Differential Imaging

Spectral (and/or Simultaneous) Differential Imaging (SDI) exploits differences between the star and planet spectrum at different wavelengths, and the fact that optical artifacts scale with wavelength while astrophysical signals do not, as the source of differentiation separating optical artifacts from astrophysical signals.

One common use of SDI is in imaging young accreting protoplanets. As a young planet is forming, material accreting onto the growing planet is heated as it exchanges gravitational potential energy for heat, exciting electrons into higher energy states. As the electrons decay back down they emit light at specific wavelengths (λ) corresponding to the difference in energy levels. The hydrogen Balmer α line ($H\alpha$, $\lambda = 0.656 \mu\text{m}$) corresponds to the electron transition from the $n = 3$ to $n = 2$ energy level, so young forming gas giant planets emit strongly at that wavelength. Using a narrow photometric filter centered at the $H\alpha$ wavelength and another centered just off the $H\alpha$ line (the continuum filter), we can scale the continuum image to model the stellar PSF and subtract from the $H\alpha$ image and reveal sources emitting at the wavelength (called simultaneous differential imaging, e.g. [Close et al., 2014](#); [Wagner et al., 2018](#); [Close, 2020](#))

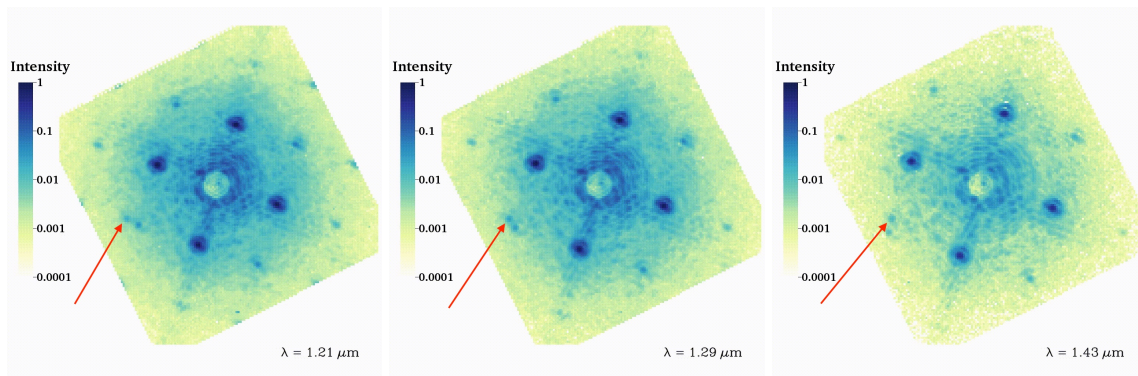


Figure 2.3: Stills from an animation produced by the SCE_xAO/CHARIS team of slices from a datacube produced by the CHARIS IFU ([Currie et al., 2019](#)). As the wavelength gets longer diffracted optical features move outward (left to right) but the companion signal (red arrow) does not, distinguishing a genuine astrophysical signal from nearby speckles.

An integral field unit spectrograph (IFU or IFS) also enables SDI. IFUs disperse light using a microlens array, fiber bundles, or image slicer, producing spectral information at points in the image plane. A data cube is then produced of the source at varying spatial points and spectral wavelengths. This enables SDI through extracting spectral features of signals of interest in a way similar to narrowband filters (e.g. [Haffert et al., 2019](#)).

Wavelength differences can also be used to distinguish genuine astrophysical signals from optical features like speckles. Because the PSF scales with λ/D , speckles and diffracted optical features will scale as you move through the IFU datacube, while astrophysical signals will not. This is illustrated in [Figure 2.3](#) with slices from a datacube produced by SCE_xAO/CHARIS IFU

(Currie et al., 2019). As wavelengths increases, the speckles move outward while the companion signal (red arrow) does not.

SDI is frequently employed in concert with ADI (often called ASDI) to obtain a better PFS subtraction and signal detection.

2.1.2 *Applying the Model*

Once the observation strategy of choice has been employed, optimally constructing the model and subtracting the stellar PSF involves selecting an appropriate algorithm. For all algorithms, signal recovery can be enhanced with the application of frame selecting (using only the highest-quality frames), a high- or low-pass filter, gaussian smoothing, and unsharp masks to suppress low spatial frequency structures and retain high frequency structures (point sources, disk features).

At its most simple, or “classical”, a PSF model can be constructed, in the case of RDI or ADI, by making a median image of the reference dataset, subtracting the median image PSF model from each image in the science target dataset, derotating the PSF subtracted images, and summing or median-combining the derotated and subtracted cube.

The LOCI algorithm (Locally Optimized Combination of Images, Lafrenière et al. 2007; Currie et al. 2012; Marois et al. 2014) makes use of the ADI cube or a large library of reference images to construct an optimal model PSF from a linear combination of reference images with coefficients optimized for sections of the image independently. Lafrenière et al. (2007) found that LOCI can outperform classical ADI at small angles, with only marginal reduction in off-axis companion light.

Currently the most widely used algorithm for PSF reconstruction is Karhunen-Loève Image Processing (KLIP, Soummer et al., 2012), an application of Principal Component Analysis (PCA) to imaging data (which is mathematically identical to LOCI but with the addition of modal truncation, Males, personal communication). PCA is a dimensionality reduction technique in which data are used to construct a set of principal components which correspond to the largest dimensions of variability – i.e., the first principal component describes the axis of largest variability, the second describes the axis of most variability of what is left when the first component is removed, and so on. The principle components comprise a new orthonormal basis set which are linearly uncorrelated; these are eigenvectors of the data’s covariance matrix. Dimensionality reduction is achieved

by selecting the top n principal components to use in model construction, where n is an integer less than the principal component dimensionality. The data can be projected onto the truncated new basis set.

With KLIP, images in the reference dataset are decomposed into principal components, and the science image is projected onto the new orthonormal basis up to n components (“modes”) to create a PSF model, which is subtracted from the science image. Assuming there is no companion signal in the reference set (either a reference star or the ADI image stack) the companion signal will not be present in the KLIP basis, and so won’t be present in the reconstructed PSF model. (However, there usually is a companion signal, especially for ADI, resulting in self subtraction).

The math behind KLIP is given in [Soummer et al. \(2012, Sec 2.2\)](#), but I reproduce here a simplified explanation to help enable constructing a KLIP algorithm, including how this can be coded in python (there are several ways to go about translating the math into code, this is how I did it for the analysis in Chapter 4 of this work).

First construct a reference image dataset of K images R_K from the reference library or observation (RDI), or by removing the image of interest from the image stack (ADI). Then for each science target image T :

1. Reshape R_K and T into a linear vector. Construct a mean image of the T and subtract so that T has a zero mean value; Construct a mean image of R_K and subtract from each R_K image.

```

1  import numpy as np
2  # reshape science image and reference datacube:
3  shape=scienceimage.shape
4  p = shape[0]*shape[1]
5  N = refdatacube[0]
6  T = np.reshape(scienceimage, (p))
7  R = np.reshape(refdatacube, (N,p))
8  # subtract mean from reference images:
9  immean = np.nanmean(R, axis=0)
10 R_meansub = R - immean[None,:]
11 # subtract mean from science image
12 immean = np.nanmean(T)
13 T_meansub = T - immean[None,:]
14

```

2. Construct a PCA basis set from the reference images such that¹

$$Z_k^{KL} = \frac{1}{\sqrt{\Lambda_k}} \sum_{p=1}^K c_k(\psi_p) R_p \quad (2.1)$$

where Z is the Karhunen-Loève (KL) basis set, $c_k(\psi_p)$ are the eigenvectors of the covariance matrix and Λ_k are the eigenvalues for $k = [1 \dots K]$. Select the maximum number of modes to use in PSF reconstruction, K_{klip}

```

1   # compute covariance matrix:
2   cov = np.cov(R_meansub)
3   # compute eigenvalues (lambda) and corresponding eigenvectors (c)
4   # of covariance matrix. Compute only the eigenvalues/vectors up to
5   # the desired number of bases K_klip.
6   from scipy.linalg import eigh
7   lamb,c = eigh(cov, eigvals = (N-np.max(K_klip),N-1))
8   # np.cov returns eigenvalues/vectors in increasing order, so
9   # we need to reverse the order:
10  index = np.flip(np.argsort(lamb))
11  # sort corresponding eigenvalues:
12  lamb = lamb[index]
13  # sort eigenvectors in order of descending eigenvalues:
14  c = c.T
15  c = c[index]
16  # np.cov normalizes the covariance matrix by N-1. We have to correct
17  # for that because it's not in the Soummer 2012 equation:
18  lamb = lamb * (p-1)
19  # Take the dot product of the reference image with corresponding
20  # eigenvector:
21  Z = np.dot(R.T, c.T)
22  # Multiply by 1/sqrt(eigenvalue):
23  Z = Z * np.sqrt(1/lamb)

```

¹Note – for RDI this step can be done once, but for ADI this step must be repeated for each science image, since for ADI the basis is formed from the other images in the same dataset.

3. Compute the PSF estimator \hat{I} by projecting the science image T onto the basis set Z up to desired number of KLIP modes K_{klip} by taking the inner product of T with Z

$$\hat{I} = \sum_{k=1}^{K_{\text{klip}}} \langle T, Z \rangle Z \quad (2.2)$$

```

1  # Make K_klip number of copies of science image
2  # to use fast vectorized math:
3  T_meansub = np.tile(T_meansub, (np.max(K_klip), 1))
4  # Project science target onto KL Basis:
5  projection_sci_onto_basis = np.dot(T_meansub, Z)
6  # This produces a (K_klip, K_klip) sized array of identical
7  # rows of the projected science target. We only need one row:
8  projection_sci_onto_basis = projection_sci_onto_basis[0]
9  # This fancy math let's you use fewer modes to subtract:
10 lower_triangular = np.tril(np.ones([np.max(K_klip), np.max(K_klip)]))
11 projection_sci_onto_basis_tril = projection_sci_onto_basis *
    lower_triangular
12 # Create the final psf estimator by multiplying by the basis modes:
13 Ihat = np.dot(projection_sci_onto_basis_tril[K_klip-1, :], Z.T)
14

```

4. Finally compute the final image by subtracting the PSF estimator from T and reshape final image back into image shape

$$F = T - \hat{I} \quad (2.3)$$

```

1  # Truncate the science image to the number of requested modes to use:
2  T_trunc = T_meansub[:np.size(K_klip), :]
3  # Subtract estimated psf from science image:
4  F = T_trunc - Ihat
5  # Reshape to
6  F = np.reshape(F, (np.size(K_klip), *shape))
7

```

Repeat that procedure for every science image in the dataset, derotate and combine the subtracted images into a final image (in Chapter 4 I used a sigma-clipped mean).

The number of KLIP modes for a given reduction is a tunable parameter. KLIP algorithms such as `pyKLIP` (Wang et al., 2015, which I make use of in Chapter 6) include additional tunable parameters and parallel computational efficiencies beyond what I have shown here.

There are further observing and PSF subtraction algorithms such as polarization differential imaging (PDI, Kuhn et al., 2001), coherence differential imaging (CDI, Bottom et al., 2017), and applying KLIP to pixel time series vectors (TRAP, Samland et al., 2021; Long et al., 2023) which are innovative but beyond the scope of this work.

In Chapter 4 of this work I describe an application of RDI called Binary Differential Imaging (BDI), in which a \sim equal-magnitude stellar binary is imaged with both stars on the detector at the same time, so science target and reference image can be as close to identical as possible. In Chapter 6 of this work I make use of classical ADI, KLIP ADI, and classical RDI in reduction of various datasets imaged with MagAO-X.

2.2 RUWE and Other Indicators of Binarity

The European Space Agency’s *Gaia* satellite, launched in 2013, is revolutionizing astronomy. Its mission is to measure the astrometry (the distance, position, and velocity) of \sim 1.7 billion stars with extreme precision. Knowing the distance to an astrophysical object is the key to unlocking essentially everything about it – e.g. size, luminosity, galactic position; knowing its velocity unlocks, for example, dynamical history, group membership, the presence of hidden companions. Having a sample of 1.7 billion object in and near our galaxy with extremely precise astrometric measurements, I don’t think it’s too much to say, will forever change our access to knowledge about the universe.

As of this writing *Gaia* has had three data releases (DRs), each with progressively more numbers of objects with high and higher-quality astrometric solutions, and a few objects with complete orbital solutions. Future data releases promise to include thousands of objects with orbits, astrometrically-detected planets, and even the time-series astrometry for objects. Currently *Gaia* DR3 provides a single time-stamp position, parallax, proper motion, and a host of other measure-

ments (including T_{eff} , luminosity, radial velocity, and even radius estimates for a small subset of objects).

As I am interested in stellar and substellar multiplicity, *Gaia* provides a set of unique tools to leverage towards disentangling the presence and dynamical effect of companions, both hidden and known. In [Pearce et al. \(2020\)](#) I developed an orbit-fitting package, called `lofti`, for stellar binaries for which both objects are resolved by *Gaia*. It is based on the Orbits for the Impatient algorithm ([Blunt et al., 2017](#)) and uses the *Gaia* proper motion of one object relative to the other as constraints for fitting the orbit, and returns a (loosely constrained) set of orbital elements consistent with that motion. `lofti` has been used to show a trend towards alignment of wide stellar companion and planet orbits for transiting planet-hosting stars ([Christian et al., 2022](#)), misalignment between a stellar and planetary orbit (which are aligned) and the circumbinary disk ([Barber et al., submitted to Nature](#)) and in several other transiting planet discoveries with wide companions (e.g. [Vanderburg et al., 2020, 2019](#); [Venner et al., 2021](#); [Newton et al., 2019](#); [Hagelberg et al., 2020](#)).

However the *Gaia* astrometric solution assumes a single star model for astrometric motion. Despite the fact that a large fraction of stars are in multiple systems, only $\sim 10\%$ of stars have noticeably non-linear motions over the relatively short time-span covered by the *Gaia* observation window ($\delta t_{DR2} = 668$ days, $\delta t_{EDR3} = 1038$ days) ([Lindgren et al., 2021](#), Sec. 3.1). Wide multiples may have periods too long to show significant curvature during the observation window; close multiples may have periods so short that deviations in the photocenter (the center of light of the two objects) position average out over the observation window.

The angular resolution (the minimum separation between sources with different source ids) is $0.18''$ by design, however sources separated by $\lesssim 0.6''$ generally only have 2-parameter solutions in DR3 (see [Lindgren et al., 2021](#), Sec 5.2 & Fig 6). The resolving power depends on relative magnitude between components, and is $\sim 0.5''$ for equal magnitude stars, up to $\sim 1.2''$ for $\Delta G = 5$ ([Gaia Collaboration et al., 2021](#)). However it also depends on the positioning of a given binary on the CCD at the time of the observation. Sources with separation $\gtrsim 1.2''$ can be observed individually, but for separations $< 1.2''$, depending on the position angle both stars may fall on the detector simultaneously and cause confusion in the peak finding.

Figure 2.4 displays a schematic of the *Gaia* astrometric CCD from [Gaia Collaboration et al. 2016](#), Fig 5 illustrating how sources are registered. Point spread functions (PSFs) of sources are

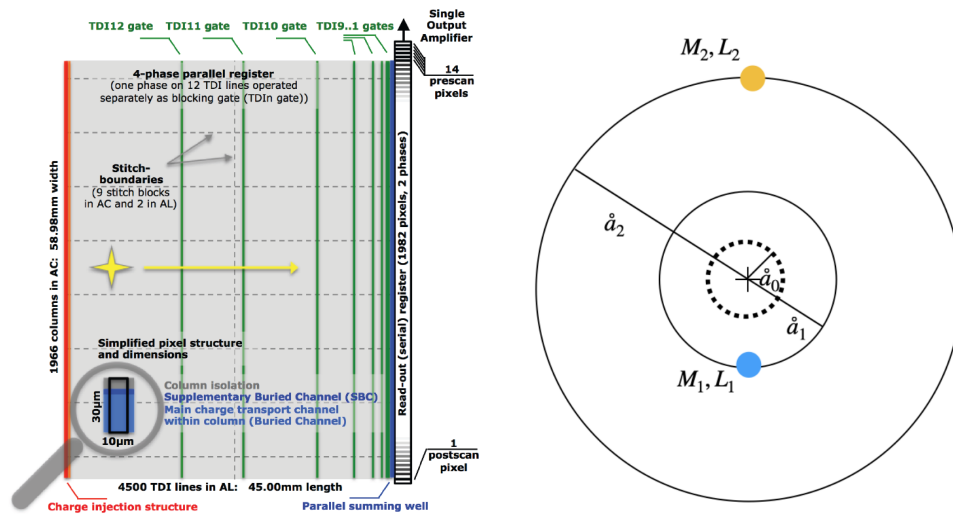


Figure 2.4: Left: Figure 5 from [Gaia Collaboration et al. \(2016\)](#), displaying a schematic of the Gaia focal plane CCD. The along-scan and across-scan directions are indicated in the top left corner. Stars move across the focal plane from left to right in the diagram, illustrated by the yellow star and arrow, to the summing well and transfer gate. This translates the PSF into a Line Spread Function (LSF). If more than one source falls on the detector, multiple peaks will be present in the LSF, and the amount of blending of those peaks depends on the position angle of the two sources relative to the along-scan direction. Right: Figure 7 from [El-Badry \(2024\)](#) showing *Gaia*'s view of an astrometric binary with components of different masses and luminosities. Both objects orbit the center of mass (plus) and the photocenter traces out the dashed line, the wobble *Gaia* would detect.

read in the along-scan (AL) direction to the parallel summing well, which translates the PSF into a line-spread function (LSF). If more than one source falls on the detector, multiple peaks will be present in the LSF, and the amount of blending of those peaks depends on the position angle of the two sources relative to the across-scan (AC) direction and their relative magnitudes. For example, if the position angle is something like 30° with respect to the AC direction at the first observation (t_1), and at some time later (t_2) the pair is observed with PA something like 80° , the photocenter of the LSF will shift from t_1 to t_2 , especially if one component is fainter than the other. [Kervella et al. \(2022\)](#) coined the term “Gaiacenter” for the epoch pointing of Gaia (after “Hippacenter” for Hipparcos observations of double stars from [Martin et al. 1997](#)). For binaries from 0.1”-1.2”, the “Gaiacenter” will be closer to the primary as a function of the two stars’ relative magnitude, and will vary as a function of position angle on the detector. Thus the astrometric solution will be perturbed, and we should expect significant astrometric error.

Summarizing [Penoyre et al. 2021](#) Sec 2, they showed that astrometric identification is most sensitive to binary periods up to the length of time spanned by the data collection period. If the observation period spans only a fraction of the orbit, the deviation is approximately linear and can be lost in the proper motion; if the binary period is small the astrometric deviation is small. This establishes a period sensitivity range of months $\lesssim P \lesssim 10$ years. Binaries outside this period range are generally probed via other methods. Periods $\gtrsim 10$ years are more likely to be visually resolvable and identified as two separate astrometric sources with proper motions consistent with being bound (see [El-Badry et al., 2021](#)); periods \lesssim months are tight binaries which can cause measurable variation in the light curve or even transits. Photometric detection of binaries relies on an overbrightness of source luminosity than that expected for a single star, but relies on the dimmer source being bright enough to be detectable above uncertainty in the spectrum of the brighter (we will see this in the discussion of M-dwarf-white dwarf binaries in Chapter 6). And spectroscopic binaries, which can be observed over a wide range of periods, are limited to time spanned by observations and the existence of spectroscopic features in both stars. Observing a single system with multiple methods is a powerful probe of multiplicity and a necessary tool for breaking degeneracies in parameters derived from observation (we will see this in Chapter 5).

2.2.1 RUWE Definition

The Gaia Renormalized Unit Weight Error (RUWE) is a single number designed to encapsulate all sources of error in the astrometric solution. RUWE is the square root of the normalized chi-square of the astrometric fit to the along-scan (AL) observations, $UWE = [\chi^2 / (n - n_p)]^{1/2}$, where n is the number of good CCD observations of the source, and n_p is the number of fit parameters, either 5 [parallax (ϖ), RA (α), Dec (δ), proper motion in RA ($\mu_{\alpha*} = \mu_\alpha \cos \delta$), and Dec (μ_δ)] or 6 (5 parameters plus pseudo-color for those without high-quality color information) in DR3 (Lindegren et al., 2021, Sec 3.1). UWE close to 1.0 is expected for well-behaved solutions of single stars. However sources of extreme colors or magnitude can show UWEs larger than 1.0 even if the solution appears reliable, so it is necessary to scale (renormalize) UWE by a factor depending on the magnitude and color of the source; this is the RUWE. RUWE encapsulates all sources of error in the fit to the astrometric model, and is easier to interpret than other indicators such as astrometric excess noise, number of bad along-scan observations, or goodness of fit along-scan. RUWE then is:

$$RUWE = \frac{UWE}{UWE_0(G, C)} \quad (2.4)$$

where $UWE_0(G, C)$ is the reference UWE value as a function of G magnitude and color of the source. Lindegren (2018b) Sec 4 details the derivation of the normalizing factor. RUWE allows establishment of a single value for assessment of the quality of astrometric solution, for distinguishing between “good” and “bad” solutions (Lindegren (2018b), Sec 1). $RUWE \sim 1.0$ for well-behaved single star solutions; often a threshold of $RUWE \lesssim 1.4$ is used to indicate well-behaved solutions (Lindegren, 2018b; Lindegren et al., 2021). Sources whose observations are inconsistent with the astrometric 5-parameter model could be caused by unequal-magnitude binarity (Lindegren, 2018b, Sec 2) or other factors which cause the photocenter of the source to wobble during the Gaia observation window.

RUWE is related to the chi-squared of the single-source astrometric fit. Equation (1) from Belokurov et al. (2020):

$$RUWE^2 \approx \chi^2 = \frac{1}{\nu} \sum_{i=1}^N \frac{R_i^2}{\sigma_i^2} \quad (2.5)$$

where $\nu = N - 5$ is the number of degrees of freedom, $N = \text{astrometric_n_good_obs_all}$ which is the number of good observations along scan, 5 is the number of parameters in the DR2 (for which this paper was written, EDR3 and DR3 include 6 parameter fits for some sources). R_i, σ_i are model residuals from fit and corresponding centroiding errors for a given observation of a source. Anything that causes the photocenter to wobble – move differently than the center of mass which moves as a single source – such as unresolved subsystems, will increase χ^2 of the fit and thus the RUWE.

2.2.2 Interpreting RUWE Value

RUWE = 1.4 is often used as a cutoff threshold for “good” vs “bad”, but the reality is much more complex and less straightforward than RUWE > 1.4 = multiple, RUWE < 1.4 = single star, and should never be relied on in that way. [Maíz Apellániz et al. \(2021\)](#), in their validation of EDR3 using globular clusters, found that the distribution of parallaxes for sources within $1.4 < \text{RUWE} < 2.0$ had an average normalized parallax average of 0, and standard deviation < 4, and so were generally safe to use after introducing an additional uncertainty term. RUWE > 2 deviated from a normalized average of zero and so have larger biases.

[Belokurov et al. \(2020\)](#) conducted a detailed study of RUWE relation to unresolved binary systems in Gaia DR2 for RUWE < 2. Figure 2.5 shows Figure 1 from their paper, an HR diagram of Gaia DR2 sources from their selection criteria (Sec 2.1), color-coded by RUWE. Two distinct regions of elevated RUWE are evident, corresponding to main sequence (MS) multiples and white dwarf - M dwarf binaries (WD+MD), evidence for a relation between multiplicity and RUWE. They used the known binary systems of the SB9 spectroscopic binary catalog ([Pourbaix et al., 2004](#)) to test RUWE and photocenter wobble correlation.

They parameterized the amplitude of the photocenter perturbation as

$$R_i = R_i^{ss} + \delta\theta_i \quad (2.6)$$

where $\delta\theta$ is perturbation in arcsec. Converting to perturbation in physical units:

$$\frac{\delta a}{AU} = \frac{\delta\theta}{mas} \frac{D}{kpc}. \quad (2.7)$$

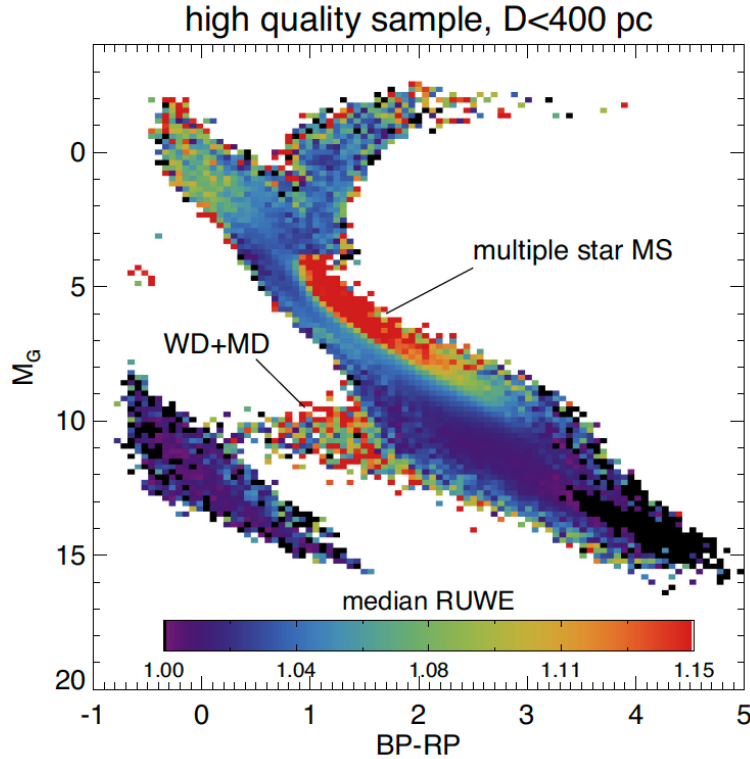


Figure 2.5: Figure 1 of [Belokurov et al. 2020](#) showing an HRD for 4M Gaia DR2 objects from their selection criteria (see Sec 2.1) color coded by RUWE. Two distinct regions of elevated RUWE are evident, corresponding to main sequence (MS) multiples and white dwarf - M dwarf binaries (WD+MD). The supports the claim that RUWE can be used to probe multiplicity.

They determine that, as predicted, the angular centroid wobble decreases inversely with distance, and that Gaia is sensitive to perturbations for sources less than 2-3 kpc distant. Gaia’s sensitivity is a function of mass and luminosity ratios. They estimate that for systems less than 1-2 kpc, systems with semi-major axis between 0.1 - 10 AU can be detected. Wider binaries do not produce significant RUWE excess because the centroid perturbation is quasi-linear and absorbed into the proper motion; these can still be detected through the proper motion anomaly (PMA; see [Kervella et al. 2022](#); [Brandt 2021](#) for PMA between Hipparcos and Gaia epochs). Their binary fractions, while limited in ability, are not too far off from those in literature for SB9 and WD binary samples they compare to, indicating that **RUWE can be a reliable indication of the presence of an unresolved companion.**

However, [Stassun and Torres \(2021\)](#) also found strong evidence of correlation between RUWE and unresolved subsystems, even for RUWE values **less than** 1.4. They used a sample of benchmark eclipsing binaries (EBs) to probe the mean offset of Gaia EDR3 parallaxes from the bench-

mark sample, using RUWE as their primary astrometric goodness-of-fit indicator. Figure 2.6 (left) displays Figure 1 (bottom) from their paper showing the absolute fractional parallax difference between Gaia and EB parallaxes as a function of $\log \text{RUWE}$, with systems with known subsystems highlighted in blue halos. The largest parallax difference and largest RUWE values (top right) are entirely populated by these systems. They report a high probability of correlation between parallax difference and RUWE using statistical tests.

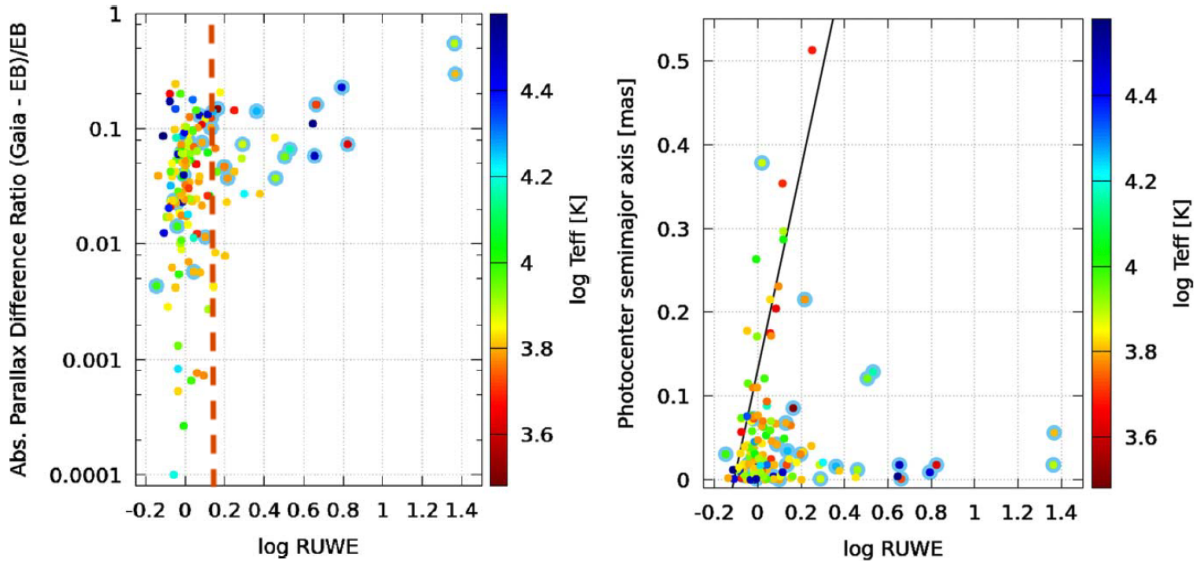


Figure 2.6: Left: Figure 1 (bottom) from [Stassun and Torres 2021](#) showing the absolute fractional parallax difference between Gaia and EB parallaxes on the y-axis vs $\log \text{RUWE}$. Blue halos mark EBs with known tertiary companions. The largest parallax difference and largest RUWE values (top right) are entirely populated by these systems. The red dashed line (added for this work) marks the nominal “good” value of $\text{RUWE} = 1.4$. Right: Figure 3 from [Stassun and Torres 2021](#) showing the same data as Figure 1, plotted as a function of the amount of angular photocenter shift (a''_{phot}), with the relation of Equation 5 plotted in black line.

The red dashed line (added for this work) marks the nominal “good” value of $\text{RUWE} = 1.4$, below which the correlation persists. [Stassun and Torres \(2021\)](#) find that even below $\text{RUWE} = 1.4$, the RUWE values are very strongly correlated with photocenter motion. Figure 2.6 (right) displays Figure 3 of their paper showing this correlation for $\text{RUWE} < 1.4$. They determine a strong correlation ($r^2 = 0.82$) for $1.0 \lesssim \text{RUWE} \lesssim 1.4$ (which may extend out to $\text{RUWE} \sim 1.8$) of

$$a_{\text{phot}}[\text{mas}] = 1.204 \times \log_{10} \text{RUWE} + 0.13 \quad (2.8)$$

shown by the black line in Figure 2.6 (right). This shows that RUWE is highly sensitive to unresolved companions and **strongly correlated with photocenter motion**, even within the “good” range of 1.0–1.4, and can actually serve as a quantitative predictor of motion.

Penoyre et al. (2020) sought to quantify the effect of photocenter wobble of a single source through numerical modeling. The motion induced by the companion increases the χ^2 of the measurement by a factor of $\chi_{\text{binary}}^2 = \delta\theta^2/\sigma_{\text{ast}}^2$, where $\delta\theta$ is the angular perturbation and σ_{ast}^2 is the astrometric scatter in the measurement. Then, UWE predicted from these quantities is

$$\text{UWE}_{\text{pred}} = \sqrt{\frac{\chi_{\text{total}}^2}{N_{\text{obs}} - 5}} \simeq \sqrt{1 + \left(\frac{\delta\theta}{\sigma_{\text{ast}}}\right)^2} \quad (2.9)$$

They conclude that for shorter period binaries (where period is less than the observational time baseline), the photocenter motion gives increased error, which provides a lower limit to the on-sky angular separation of the binary (there is the possibility that some of the binary motion is absorbed into the center-of-mass motion errors). However it might be difficult or impossible to establish this for any one given system. Periods significantly longer than observational baseline will just cause a constant offset.

High RUWE values have been shown to also explain relative velocity vectors for wide stellar binaries that appear to exceed escape velocity, apparent non-Newtonian motion, which has been used as a test of alternative gravity theories. Clarke (2020) and Belokurov et al. (2020) showed that contamination by sources with unresolved subsystems, and resulting high RUWE values, reproduce the high-velocity tail exceeding escape velocity observed by Pittordis and Sutherland (2019).

2.2.3 Other Causes of RUWE Excess Besides Multiplicity

Marginally resolved sources. If the stellar image is perturbed from a single PSF but Gaia identifies it as a single source, it creates a large centroiding error. Belokurov et al. (2020) shows extremely high values of RUWE for known visual binaries with separation $\rho < 1.5''$, reproduced here in Figure 2.7. However **there is no correlation between RUWE and ρ** — at small separations even faint companions can cause significant centroid displacement. They find that BP/RP excess points to brighter companions and high variability, and that the bulk of semi-resolved double stars could be filtered out by applying cuts to those parameters (see Figure 5 of their paper).

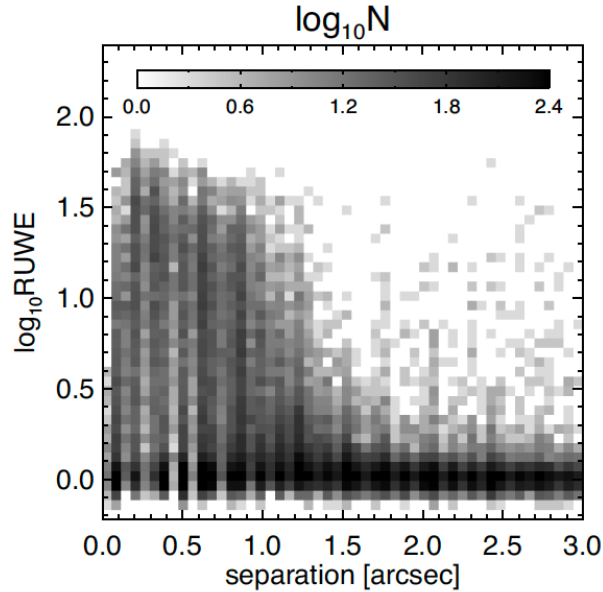


Figure 2.7: Selected plot from Figure 5 of [Belokurov et al. 2020](#) relating RUWE to separation of binaries in Washington Double Star Catalog. Extremely high RUWE values are common for binaries with separation less than 1.5”.

Variability. [Belokurov et al. \(2020\)](#) also report a correlation between RUWE and variability with RR Lyrae, Cepheids, and long period variable sources, particularly for the brightest ($5 < G < 14$) RR Lyrae stars, while there is little correlation for fainter stars ($G > 14$). This correlation arises from the normalization of RUWE on these stars. The variable object will be measured at a range of magnitudes and colors and thus can’t be normalized using a single value of u_o .

Source misidentification is also possible for sources in crowded fields or fast-moving sources. If the position of one source is recorded as belonging to another for a few observations it can introduce significant excess noise.

Unmodeled noise such as random changes in the source, telescope, data pipeline, underestimation of astrometric error, etc ([Penoyre et al., 2021](#), , Sec 4.1).

Disks Elevated RUWE has also been shown to result from the presence of a disk for young sources ($\tau \lesssim 10$ Myr; [Fitton et al. 2022](#))

2.2.4 Other Tests for Binarity

Additional Gaia quantities can be useful for testing for unresolved binarity. Prior to the astrometric solution, the data passes the image parameter determination (IPD) stage, where the standard

stellar model is fit to the image locations. Goodness-of-fit (gof) statistics from the IPD stage are sensitive to deviations from the simple single point source model, as well as modelling and calibration errors.

Here I summarize (Lindegren et al., 2021, Sec 5.3) on other multiplicity metrics. `ipd_gof_harmonic_ampli` measures the amplitude of the variation of goodness of fit as a function of the position angle of the scan direction. It is normally small but can become large for elongated PSF images such as unresolved binaries. `ipd_frac_multi_peak` is the percentage of windows used for astrometric processing that contained more than one peak, so it is sensitive to resolved binaries that produce multiple peaks in the window in some scan directions. `astrometric_excess_noise` quantifies how much motion of the image center deviates from the standard astrometric model in angular units (mas) per AL observation, while the `astrometric_excess_noise_sig` gives the S/N of the excess noise;

`astrometric_excess_noise_sig` $\lesssim 2$ is considered insignificant (essentially zero). `astrometric_excess_noise/astrometric_excess_noise_sig` may be used as an estimate of the uncertainty in the excess noise source. However, Belokurov et al. (2020) note that for their subsample of Gaia DR2 solutions, only \approx half of sources with $\text{RUWE} > 1.1$ have excess noise > 0 , that excess noise “saturates” to zero, and that it is susceptible to systematic trends as a function of color and magnitude; thus RUWE is a better metric to test for binarity than excess noise. . All of these are at play in Chapters 4 and 5.

Finally overluminosity in *Gaia* colors can indicate an unresolved multiple. Deacon and Kraus (2020) examined known members of three young clusters and selected unresolved multiples using their position above the main sequence, along with *Gaia* astrometric excess noise, to select likely binaries; in Chapter 5 I use the position of HIP 67506 A among their candidate binaries as indication of a hidden luminous companion. Rebassa-Mansergas et al. (2021) used the position of *Gaia* sources between the main sequence and the white dwarf sequence to select for white dwarf + M dwarf binaries.

RUWE is one metric among many probing multiplicity. Figure 2.8 shows the parameter space of binarity for which different *Gaia* metrics are sensitive.

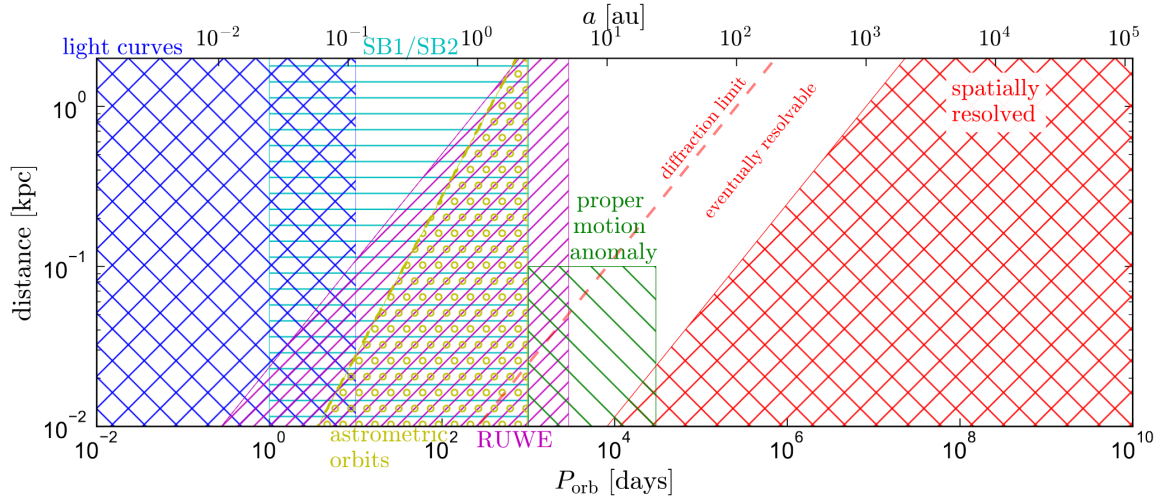


Figure 2.8: Reproduction of Figure 1 from El-Badry (2024) showing *Gaia*'s parameter space of binarity probed by different metrics. Objects in the red hashed region will be spatially resolved by *Gaia*, proper motion anomaly (described in Section 2.3) probes the green region, *Gaia*'s spectroscopic binary pipeline catches objects in the teal region, and RUWE probes the pink hashed region, with some sources having full astrometric orbits (yellow region).

2.2.5 Conclusion

RUWE is a very valuable parameter for testing the quality of *Gaia* solutions, but can't be interpreted in any straightforward way and requires careful examination. Throughout this work I have made use of the parameter as a signpost for multiplicity, one clue among many. For example, in Chapter 4 and 5 I use it as one clue pointing to a candidate companion signal likely being real and meriting followup; in Chapter 6 I use it to help prioritize observing targets. It is especially useful when deciding to rely on the information provided by the *Gaia* astrometric solution for a given source, such as if a `lofti` fit result is reliable (`lofti` includes a warning if either sources have $\text{RUWE} > 1.2$). Until future data releases with more metrics and time series astrometry, understanding RUWE is crucial but is not a cut-and-dry multiplicity metric.

2.3 Accelerating Stars and Proper Motion Anomaly

On the topic of astrometry and multiplicity, it's worth spending a few pages talking about accelerating stars. Before *Gaia* was the 1991 *Hipparcos* astrometric satellite mission. While not as precise as *Gaia*, having a 1991 astrometric measurement and a 2016 astrometric measurement for a single star means you can detect long-period accelerations, longer than what would perturb *Gaia*'s

measurement and so missed in quality metrics, but just right if you're interested in low-luminosity objects on wide orbits accessible to direct imaging, such as a wide giant planet or brown dwarf. This is the latest revolution in direct imaging surveys. Uninformed “blind” surveys of young stellar clusters, the primary mode of direct imaging surveys of the past decade, have returned very low occurrence rates of wide orbit companions, illustrated in Figure 1.1, where the region from ~ 10 au to 1000's of au have occurrence rates in the single digits. These types of surveys are no longer operationally feasible, and a new survey design is warranted.

The *Hipparcos* (Esa, 1997) satellite was an astrometric mission launched in 1989. Stars observed in both *Gaia* (epoch 2016.0) and *Hipparcos* (epoch 1991.25) thus have two velocity measurements spanning ~ 25 years. For single star, or an equal-luminosity binary, the proper motion vector observed by *Hipparcos* and *Gaia* will be constant, however if the luminosity ratio $p = L_2/L_1 < 1$ and is less than the mass ratio $q = m_2/m_1$, the center of mass will shift and the photocenter follows a “virtual orbit” (Kervella et al., 2019). This proper motion anomaly (PMA) points to the presence of a low luminosity object exerting gravitational pull on the star. In 2018 Brandt (2018) produced a well-vetted and calibrated catalog of accelerating stars called the Hipparcos-Gaia Catalog of Accelerations (HGCA). Kervella et al. (2019) also independently produced a catalog of accelerating stars.

The Kervella et al. (2019) and Brandt (2018) catalogs represent the objects most likely to have companions accessible to direct imaging and a ready source for developing optimized target lists, which is the direction the whole field has moved for direct imaging surveys (e.g. Currie et al., 2021). Sebastiaan Haffert and I have developed the XOOMIES survey for the extreme AO instrument MagAO-X targeting accelerating stars in the Scorpius-Centaurus star forming region. As of this writing we have detected 3 XOOMIES companions out of 3 targeted, a 100% yield rate (Haffert et al. in prep). PMA is a powerful tool for direct imaging surveys.

The math for **long period accelerations** (period longer than *Hipparcos–Gaia* time baseline of 25.24 yrs) is shown below. Figure 2.9 illustrates the derivation of the proper motion anomaly. The acceleration of a star in the HGCA is given by

$$a_{\alpha,\delta}[t_a] = \frac{\Delta\mu_{\text{HG}}}{(t_{\text{Gaia}} - t_{\text{Hip}})/2} \quad (2.10)$$

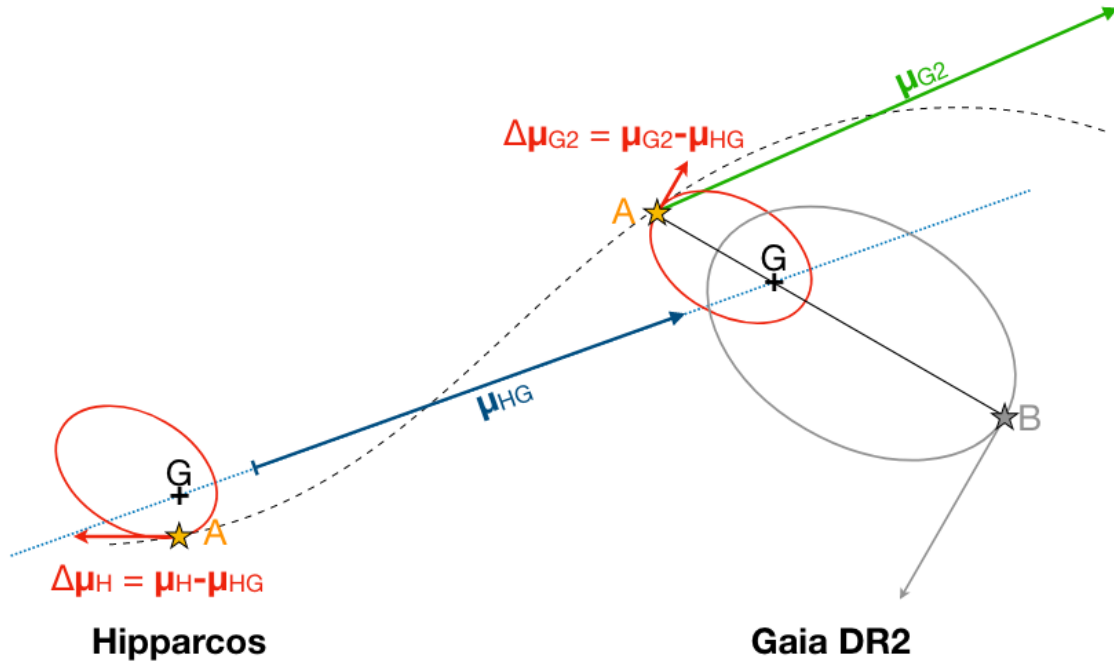


Figure 2.9: Reproduction of Figure 1 [Kervella et al. \(2019\)](#) illustrating proper motion anomaly. The luminous object observed by *Hipparcos* and *Gaia* is labeled A and the less luminous object, which contributes negligibly to the photometry, is labeled B. The observed proper motions of A are shown as $\mu_{G2/H}$, μ_{HG} is the proper motion difference vector from *Hipparcos* and *Gaia* DR2 astrometric position (α, δ, ϖ) , and $\Delta\mu_{G2/H}$ is the PMA vector where $\Delta\mu_{G2/H} = \mu_{G2/H} - \mu_{HG}$. The motion A makes through space is given by the dashed black line, while it would have followed the dotted blue line if it did not have the unseen companion. $\Delta\mu$ thus corresponds to the projected velocity vector of the photocenter around the barycenter.

(Eqn 9 in [Brandt et al., 2019](#)), where $\Delta\mu_{HG}$ is the difference in proper motion between the *Gaia* epoch and the *Hipparcos*–*Gaia* scaled positional difference, which is the most sensitive acceleration measurement ([Brandt et al., 2019](#)), and

$$t_a = \frac{3t_{\text{Gaia}} + t_{\text{Hip}}}{4} \quad (2.11)$$

(Eqn 10 in [Brandt et al., 2019](#)) is the weighted linear combination of the two reductions derived in [Brandt \(2018\)](#). The plane-of-sky acceleration then is related to the mass of the object by

$$a_{\alpha\delta} = \frac{GM_B}{r^2} \cos \phi \quad (2.12)$$

(Eqn 4 in [Brandt et al., 2019](#)) where G is the gravitational constant, r is the true physical separation in the orbit plane, ϕ is the angle between r and the sky plane, with $\rho = r\pi \cos(\phi)$, where ρ is the projected sky plane separation and π is the parallax. Acceleration in the line-of-sight direction, a_{RV} , is

$$a_{\text{RV}} = \frac{GM_B}{r^2} \sin \phi \quad (2.13)$$

(Eqn 5 in [Brandt et al., 2019](#)), so with simultaneous measurements of a_{RV} , $a_{\alpha\delta}$, and ρ , there is a unique solution for companion mass:

$$M_B = \frac{\rho^2 (a_{\alpha\delta}^2 + a_{\text{RV}}^2)^{3/2}}{\pi^2 G a_{\alpha\delta}^2} \quad (2.14)$$

(Eqn 7 in [Brandt et al., 2019](#)).

For **short period orbits**, these proper motions do not correspond to instantaneous accelerations ([Brandt, 2024](#)), but companion masses can be well constrained when combined with astrometric and/or RV measurements that span a large fraction of the orbit (e.g. [Xuan and Wyatt, 2020](#); [Venner et al., 2021](#); [Balmer et al., 2023](#)).

Without the line-of-sight acceleration or projected separation, the acceleration only constrains m_2/r^2 , so it scales with companion mass and physical separation – a less massive object close in can cause the same observed PMA as a larger object at a wider separation. ([Kervella et al., 2019](#)) derives the following relation for a face-on orbit with $M_B \ll M_A$:

$$\frac{M_B}{\sqrt{r}} = \sqrt{\frac{M_A}{G}} v_1 = \sqrt{\frac{M_A}{G}} \left(\frac{\Delta\mu[\text{mas a}^{-1}]}{\pi[\text{mas}]} \times 4740.470 \right) \quad (2.15)$$

where the multiple term converts the given units to velocity in m s^{-1} . This gives a **minimum mass estimate for the object causing the PMA** as a function of separation, since it only accounts for the plane-of-sky acceleration. They estimate from geometrical and simulation arguments that the projected minimum mass is $\eta = 87_{-32}^{+12}\%$ of the 3d orbital PMA and estimate the deprojected companion mass as

$$\frac{M_B^\dagger}{\sqrt{r}} = \sqrt{\frac{M_A}{G}} \left(\frac{\Delta\mu[\text{mas a}^{-1}]}{\eta \pi[\text{mas}]} \times 4740.470 \right) \quad (2.16)$$

with appropriately propagated uncertainties.

Their final relation for the mass as a function of separation (r) is

$$M_B^\dagger(r) = \frac{\sqrt{r}}{\gamma[P(r)/\delta t]} \sqrt{\frac{M_A}{G}} \frac{\delta v}{\eta \zeta} \quad (2.17)$$

where δt is the observing window for the astrometric mission, since the velocities reported are the time averaged velocity over the observing window, where $\delta t = 1227$ d for *Hipparcos* (Perryman et al., 1997) and $\delta t = 668$ d for *Gaia* DR2 (Gaia Collaboration et al., 2018); ζ is a term correcting for bias in orbital periods longer than the 24.25 yr baseline; γ is the sensitivity variation of PMA due to smearing of shorter period companions where period is less than observing window; and the period is $P(r) = \sqrt{\frac{4\pi^2 r^3}{GM_A}}$.

All of this is wrapped up in a python script provided by the authors for producing a PMA sensitivity curve from a Hip-Gaia PMA. Figure 2.10 shows an example curve for one of the XOOMIES targets. The peaks interior of $\sim 0.03''$ are caused by period aliasing with the observing window; the curve is linear with separation beyond $\sim 0.1''$. This is a good survey target because the minimum mass given by this curve is in the giant planet regime.

I have made use of these curves in Chapters 3 and 5 of this work, in addition to developing the XOOMIES target list. Another powerful use of PMA has been dynamical mass measurements. Brown dwarf atmospheres and evolution are notoriously hard to model, and parameters derived from models carry a lot of uncertainty. If the mass of the host star is well known, and the orbit can be well constrained, a dynamical mass independent of any modeling can be obtained for brown dwarf and giant planet companions, enabling characterization and benchmarking evolutionary models (e.g Brandt et al., 2019; Bowler et al., 2021; Franson et al., 2022; Sepulveda and Bowler, 2022; Rickman et al., 2024)

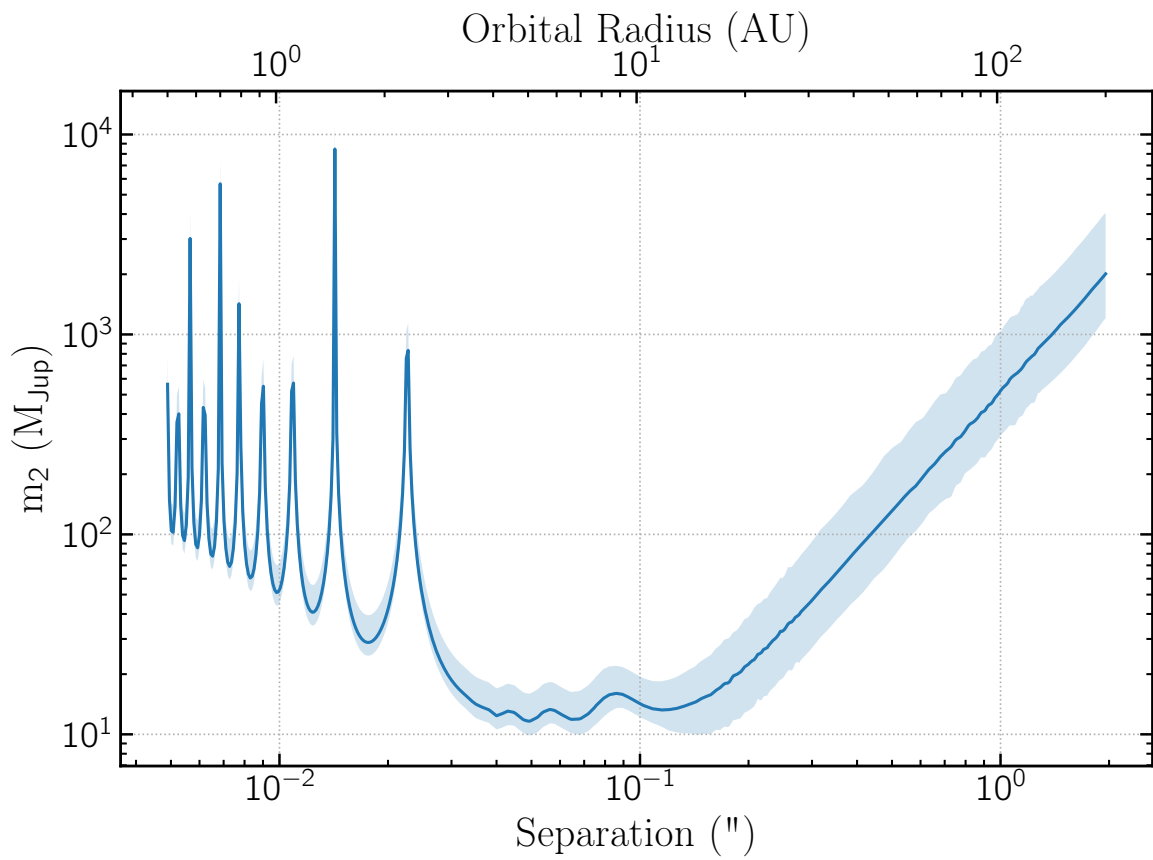


Figure 2.10: A proper motion anomaly sensitivity plot for a XOOMIES target.

Chapter 3

Boyajian's Star B: The Co-Moving Companion to KIC 8462852 A

“Scientists have resolved the mystery of bizarrely dimming star Boyajian’s star saying that the ”alien megastructure” is not alone... As per astrologers, KIC 8462852, also known as Boyajian’s star, seems to have a binary companion that could be contributing to its irregular dips in its brightness. ”

WION News covering this paper

This chapter is reproduced from [Pearce et al. 2021](#)

3.1 Introduction

Many possible causes have been posited to explain the unusual light curve of KIC 8462852 (a.k.a “Boyajian’s Star”) discovered in [Boyajian et al. 2016](#) (hereafter B16). KIC 8462852 exhibits large, possibly aperiodic dips in a variety of shapes, inconsistent with an exoplanet explanation (B16). There has been significant interest in the system, with many suggested explanations from the beginning of a Late Heavy Bombardment-like period ([Bodman and Quillen, 2016](#)), to interstellar clouds or an intervening object ([Wright and Sigurdsson, 2016](#)), to uneven circumstellar material ([Wyatt et al., 2018](#)), to alien megastructures ([Wright et al., 2016](#)). Some explanations such as recent cataclysmic dust-generating events ([Marengo et al., 2015](#)), massive debris disks ([Thompson et al., 2016](#)), close-in obscuring material or YSO-like behavior ([Lisse et al., 2015](#)), and instrumental effects (B16) have already been ruled out as explanations.

The break-up of exocomets or planetesimals on eccentric orbits was preferred given the observations ([Thompson et al., 2016](#)), although [Bodman and Quillen \(2016\)](#) showed this idea does not fully explain all the dips, nor the apparent long term dimming trend ([Montet and Simon, 2016](#)). [Simon et al. \(2018\)](#) showed the long-term dimming trend may be part of a more complicated episodic dimming and brightening. [Boyajian et al. \(2018\)](#) report post-*Kepler* observations that show consistency with optically thin dust and intrinsic variations of the star, while [Martinez Gonzalez et al. \(2019\)](#) found no clear evidence of comets and evidence for clumps of thick material within the thin dust.

A faint possible companion star was observed at separation $\rho = 1.95''$, position angle $PA = 96 \pm 6$, and $\Delta H = 3.840 \pm 0.017$ mag by B16, but given their single epoch of imaging, were unable to determine if the two were physically associated. B16 determined that blending with the object was not a cause of the anomalous light curve, as its optical faintness means even a 100% drop in its flux could not explain the deepest dips seen in the Kepler light curve. The object’s separation translates to 880 ± 10 AU at the distance of 451 ± 5 pc ([Gaia Collaboration et al., 2018](#)), meaning it would not be currently affecting the observed behavior of KIC 8462852 via tides or strong gravitational interactions with bodies at small orbital radii. If it were a bound

companion however, it might affect other bound objects via long-term perturbations, and could trigger a barrage of occulting objects inward towards the host star.

[Clemens et al. 2018](#) observed the system with the Mimir near-infrared wide-field imager on the 1.8-m Perkins telescope in 2017, and compared the relative astrometry of the candidate companion to the 2014 Keck/NIRC2 observations reported in [B16](#). They reported a tangential speed of $44.9 \pm 4.9 \text{ km s}^{-1}$ for the candidate companion relative to KIC 8462852, and concluded it is not a bound companion. However, the seeing-limited resolution of their second-epoch imaging was 1.3–1.5", so the companion was only resolved at ≤ 1.5 times the observational FWHM. This challenging observational fit could have been prone to a separation/contrast degeneracy that affected the measured change in position.

In this work we use three epochs of Keck/NIRC2 astrometry spanning five years to revisit the status of the close companion to KIC 8462852, and show that they are a common proper motion pair and a gravitationally bound binary system. We analyze two other faint objects in our images and show that they are unassociated. In [Section 3.2](#) we outline our astrometric methods. In [Section 3.3](#) we report relative proper motions and demonstrate common (or lack of common) proper motion for the three candidate companions from our astrometry and assess the probability of binarity. In [Section 3.4](#) we discuss implications of the presence of a wide stellar companion for the KIC 8462852 system.

3.2 Analysis

3.2.1 Observations

We obtained observations of the KIC 8462852 system using the near-infrared imaging camera NIRC2 coupled with the natural guide star adaptive optics system ([Wizinowich et al., 2000](#)) on the Keck-II telescope in 2014 (28 images), 2016 (13 images), and 2019 (10 images). The observations in 2014 (PI M. Liu) were obtained in K , H , and J bands, and were used by [B16](#) to confirm the existence of KIC 8462852 B as a candidate companion. The observations in 2016 and 2019 were obtained by our team (PIs Mann and Huber) in the K' -band filter, with the aim of testing whether KIC 8462852 B is co-moving. In both 2016 and 2019, we obtained observations with KIC 8462852 placed at two distinct orientations and dither positions. We deliberately duplicated the 2016 orien-

tations and positions in 2019, with the goal of enabling cross-epoch measurements of motion that are independent of residual errors in the correction of the camera’s static geometric distortion. In our subsequent analysis, we henceforth treat each of the two dither positions in 2016 and 2019 as an independent observation, denoted as 2016-1/2019-1 and 2016-2/2019-2, respectively.

All images used the narrow camera, with adaptive optics in natural guide star mode, in position angle tracking mode. We linearized each science and calibration frame in Python using the methodology of the IDL task `linearize_nirc2.pro`¹, then dark-subtracted and flat-fielded science frames in the standard manner. We adopted bad pixel identifications from Kraus et al. (2016) and replaced with the median of surrounding pixels, then detrended spatially correlated readnoise from the mirrored positions of each quadrant (Kraus et al., in prep).

Figure 3.1 displays a NIRC2 image from the 2019 epoch, with the comoving binary companion marked as B, located 1.95” to the east, and the two candidate companions marked as cc1, 3.8” southwest, and cc2, 2.8” southwest. KIC 8462852 B was visible at sufficient signal-to-noise for astrometric analysis in all datasets; cc1 was sufficiently visible only in the K and K' bands at all three epochs; and cc2 was sufficiently visible only in the K' band in the 2016 and 2019 datasets.

3.2.2 Astrometry

We used the Gaussian PSF fitting routine described in Pearce et al. (2019) to precisely measure the (x, y) pixel position and uncertainty of the four components in each image. Details of the modeling and acceptance criterion are described in Pearce et al. (2019) and applied in the same manner to this data set. Briefly, we modeled the PSF of the primary and candidate companion as the sum of two 2-dimensional Gaussian functions and varied the model parameters through a custom Gibbs Sampler Markov Chain Monte Carlo (MCMC) routine. We performed astrometric calibrations for the primary and each of the three candidate companions for each step along the MCMC chains, including optical distortion and plate scale error (Yelda et al., 2010; Service et al., 2016), and differential aberration and atmospheric refraction, then computed separation and position angle from primary for each (x, y) position in the chains for each candidate companion. We took the mean and standard deviation of the separation and position angle chains as the final value and uncertainty in an image. Positions in each image are given in Figures 3.3, 3.6, and 3.7 as filled circles, with the

¹<http://www.astro.sunysb.edu/metchev/ao.html>

Table 3.1: Keck/NIRC2 NGS AO Astrometry for KIC 8462852 candidate companions

Epoch	MJD	Filter	N_{images}	N_{coadds}	t_{int} (sec)	Separation ^a (mas)	Position Angle ^b (deg)	Δm^c (mag)
B								
2014.79	56946.30	<i>J</i>	9	10	0.726	1952.78 ± 0.77	96.064 ± 0.014	3.884 ± 0.057
2014.79	56946.30	<i>H</i>	9	10	0.726	1952.69 ± 0.36	96.059 ± 0.010	3.704 ± 0.034
2014.79	56946.30	<i>K</i>	10	10	0.726	1952.61 ± 0.40	96.058 ± 0.013	3.525 ± 0.020
2016.72 Dither 1	57651.23	<i>K'</i>	2	10	1.0	1950.64 ± 0.14	96.064 ± 0.004	3.640 ± 0.004
2016.72 Dither 2	57651.23	<i>K'</i>	11	10	1.0	1951.07 ± 0.07	96.063 ± 0.004	3.638 ± 0.012
2019.44 Dither 1	58646.50	<i>K'</i>	2	20	1.0	1951.63 ± 0.09	96.069 ± 0.004	3.632 ± 0.006
2019.44 Dither 2	58646.50	<i>K'</i>	8	20	1.0	1951.88 ± 0.06	96.062 ± 0.004	3.626 ± 0.009
cc1								
2014.79	56946.30	<i>K</i>	10	10	0.726	3871.5 ± 2.6	256.377 ± 0.042	5.77 ± 0.38
2016.72 Dither 1	57651.23	<i>K'</i>	2	10	1.0	3863.2 ± 1.3	256.380 ± 0.015	6.11 ± 0.03
2016.72 Dither 2	57651.23	<i>K'</i>	11	10	1.0	3862.0 ± 0.7	256.401 ± 0.007	6.07 ± 0.05
2019.44 Dither 1	58646.50	<i>K'</i>	2	20	1.0	3850.1 ± 1.1	256.370 ± 0.012	6.23 ± 0.02
2019.44 Dither 2	58646.50	<i>K'</i>	8	20	1.0	3848.3 ± 0.5	256.367 ± 0.008	6.24 ± 0.04
cc2								
2016.72 Dither 1	57651.23	<i>K'</i>	2	10	1.0	2785 ± 7	232.51 ± 0.02	7.15 ± 0.09
2016.72 Dither 2	57651.23	<i>K'</i>	5	10	1.0	2788 ± 6	232.46 ± 0.05	7.04 ± 0.11
2019.44 Dither 1	58646.50	<i>K'</i>	2	20	1.0	2761 ± 3	232.49 ± 0.03	7.26 ± 0.10
2019.44 Dither 2	58646.50	<i>K'</i>	7	20	1.0	2763 ± 2	232.52 ± 0.03	7.44 ± 0.13

(a) Errors shown are the statistical error, corresponding to thick error bars on Figure 3.3, 3.6, and 3.7.

Systematic error of 1.4 mas applies to all separation measurements, corresponding to thin error bars.

(b) Errors shown are the statistical error. A systematic error applies to all position angle measurements which corresponds to 1.4 mas tangential angular distance at the object's separation: 0.042° for B, 0.021° for cc1, 0.029° for cc2.

(c) Errors shown are the statistical error. We adopt a conservative systematic error of 0.05 mag to account for detector systematics.

NOTE – $0.029 \text{ deg} = 1 \text{ mas}$ tangential angular distance at the projected separation of B. N_{images} is the number of images in each epoch. t_{int} is integration time per coadd. Some images were excluded from the astrometry of cc2 due to insufficient detection of the object in those images.

median error for images in an epoch given by offset crosses. We computed a weighted mean of image positions as the mean position in an epoch, given by small crosses in those figures.

The geometric distortion solution for NIRC2 removes almost all of the distortion introduced by the telescope and instrument, but it does leave residual systematic uncertainties of $\sigma_{s,pos} \sim 1$ mas in the position measurements of individual sources, or $\sigma_s \sim \sqrt{2}$ mas in the relative astrometry between two sources. For a given detector location, any further residual error associated with that location (such as from temperature variations and non-repeatable positioning of the telescope/instrument optics) appears to be negligible across a timescale of years when compared to the empirical scatter seen within an individual epoch (< 0.2 mas; Dupuy et al. 2016; Dupuy et al., in prep). It is therefore possible to achieve substantial further improvement in the precision of relative astrometric measurements if source positions and orientations can be duplicated in multiple epochs. Our observations in 2019 replicated the two position/orientation arrangements used in 2016, so we have encapsulated these systematic uncertainties in the covariance matrix for the five epochs (2014, 2016-1, 2019-1, 2016-2, 2019-2):

$$C = \begin{bmatrix} \sigma_{14}^2 + \sigma_s^2 & 0 & 0 & 0 & 0 \\ 0 & \sigma_{16-1}^2 + \sigma_s^2 & \sigma_s^2 & 0 & 0 \\ 0 & \sigma_s^2 & \sigma_{19-1}^2 + \sigma_s^2 & 0 & 0 \\ 0 & 0 & 0 & \sigma_{16-2}^2 + \sigma_s^2 & \sigma_s^2 \\ 0 & 0 & 0 & \sigma_s^2 & \sigma_{19-2}^2 + \sigma_s^2 \end{bmatrix}$$

where each diagonal term contains a contribution from the statistical variance σ_{NN}^2 (estimated from the RMS of the individual-image measurements at that epoch) as well as the systematic variance σ_s^2 , and the systematic variance also contributes to the off-diagonal terms for epochs that were taken with the same source positions/orientations and hence share a common systematic error.

In subsequent measurements of the χ^2 goodness-of-fit statistic, we then use its modified definition:

$$\chi^2 = \mathbf{r}^T \mathbf{C}^{-1} \mathbf{r}$$

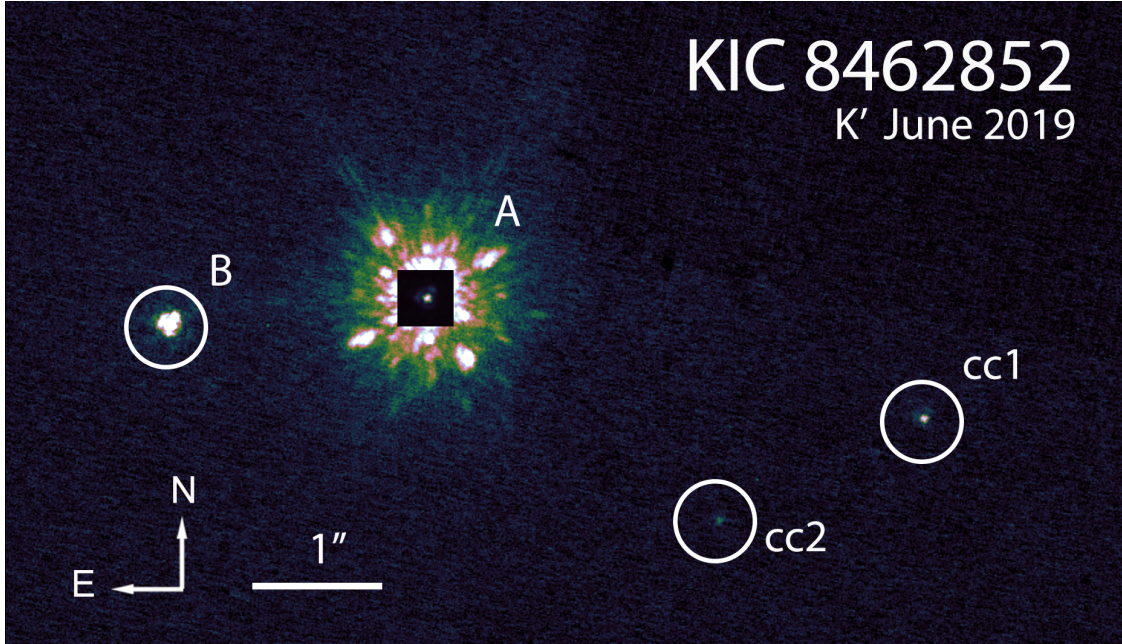


Figure 3.1: Keck/NIRC2 adaptive optics image of KIC 8462852 A, B, and candidate companions, shown in log stretch to emphasize the faint candidate companions. The primary, KIC 8462852 A, is shown inside a linear stretched box to avoid saturation. The secondary, labeled B, is located 2'' to the east. The two candidate companions are labeled cc1 for the brighter companion, 3.8'' southwest, and cc2, 2.8'' southwest.

where r is the vector of residuals for the observations about the model being tested and C^{-1} is the weight matrix corresponding to the inverse of the observational covariance matrix.

We computed a relative velocity using the `scipy` least squares fitting function `curve_fit` (Virtanen et al., 2020) by fitting a linear function to the mean positions, weighted with the weight matrix C^{-1} . We also use this formulation of the χ^2 goodness-of-fit in the orbit fitting calculations presented in Section 3.3.1. We computed the contrast in each filter as the mean and standard deviation of the flux ratio of our analytical models in each image.

Table 3.1 displays the results of our relative astrometry and photometry for the three candidate companions.

3.2.3 Stellar Parameters

In Table 3.2 we summarize relevant properties of KIC 8462852 AB. B16 found that the primary (F3V, $M = 1.43 M_{\odot}$; $T_{\text{eff}} = 6750 \pm 120$ K) has a space velocity inconsistent with any moving groups, and were unable to estimate an age.

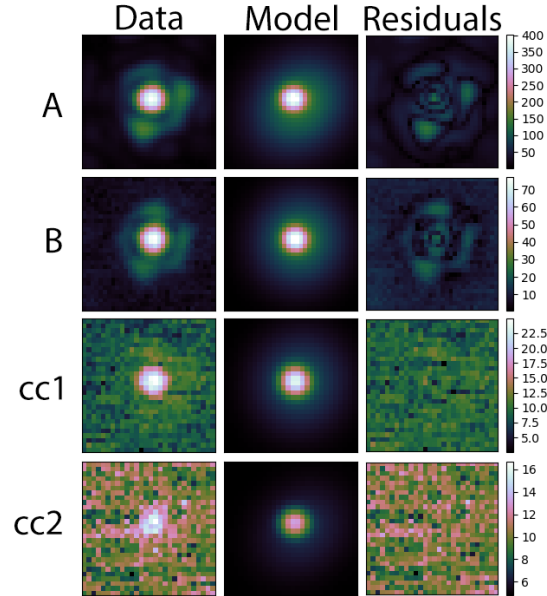


Figure 3.2: Data, model, and residual map of the primary (labeled "A"), companion (labeled "B"), and candidate companions ("cc1" and "cc2") for one image from the 2019 dataset. The model shown is built using the mean values of the parameter chains from the MCMC fit for that image, and is shown with a square root stretch to emphasize the faint residuals.

The nearby companion, KIC 8462852 B, is comoving with A (demonstrated in Section 3.3.1), so its stellar parameters are also relevant to establish. In the absence of spectroscopic followup, we adopt the spectral type of M2V estimated by B16.

To update the stellar parameters for both components we used `isoclassify` (Huber et al., 2017), with input constraints including T_{eff} for the primary from B16, the 2MASS K magnitude, Gaia DR2 parallax (corrected for the zeropoint offset in the Kepler field, Zinn et al., 2019), a solar metallicity prior with a width of 0.1 dex and the median measured K' contrast in Table 3.1 with a conservative uncertainty accounting for errors in the synthetic fluxes ($\Delta K' = 3.64 \pm 0.05$ mag). This procedure is essentially the same as in Kraus et al. (2016), but with an improved stellar classification method and a newer grid of MIST isochrones (Choi et al., 2016) supplemented with the empirical relations by Mann et al. (2015) and Mann et al. (2019) for low-mass stars, as described in Berger et al. (2020). The resulting classification yields a self-consistent classification of the primary and secondary assuming both components have the same age and metallicity. We estimate an isochronal age of ~ 1.2 Gyr, and the resulting updated stellar parameters are listed in

Table 3.2: System and Stellar Properties for KIC 8462852 AB

Property		Ref
Distance (pc)	$451.0^{+4.9}_{-4.8}$	1
ρ (mas)	1951.48 ± 0.23	Sec 3.1
ρ (AU)	880 ± 10	2, Sec 3.1
PA ($^\circ$)	96.063 ± 0.004	Sec 3.1
<i>KIC 8462852 A</i>		
Proper Motion	$\mu_\alpha = -10.422 \pm 0.040$	2
(mas yr ⁻¹)	$\mu_\delta = -10.288 \pm 0.041$	2
Luminosity (L_\odot)	4.3 ± 0.3	Sec 2.3
Mass (M_\odot)	1.36 ± 0.05	Sec 2.3
Radius (R_\odot)	1.51 ± 0.04	Sec 2.2
T_{eff} (K)	6750 ± 120	3
SpT	F3V	3
Age (Gyr)	~ 1.2	Sec 2.3
J (mag)	10.763 ± 0.021	4
H (mag)	10.551 ± 0.019	4
K (mag)	10.499 ± 0.020	4
<i>KIC 8462852 B</i>		
Mass (M_\odot)	0.44 ± 0.02	5, Sec 2.3
Radius (R_\odot)	0.45 ± 0.02	Sec 2.3
T_{eff} (K)	3720 ± 70	Sec 2.3
SpT	M2V	3

(1) [Bailer-Jones et al. \(2018\)](#) (2) [Gaia DR2 \(Gaia Collaboration et al., 2016, 2018\)](#); (3) [Boyajian et al. \(2016\)](#); (4) 2MASS ([Skrutskie et al., 2006](#)) ; (5) [Mann et al. \(2019\)](#)

Table 3.2. Note that the uncertainties do not account for systematic errors between different model grids.

3.3 Results

3.3.1 *KIC 8462852 B*

Our measured relative motion indicates that KIC 8462852 and its close, bright neighbor are a common proper motion pair. We determined a relative motion in the plane of the sky of $\Delta\mu = 0.14 \pm 0.44 \text{ mas yr}^{-1}$ ($\Delta\mu = 0.3 \pm 1.0 \text{ km s}^{-1}$) over the five year span of observations, which is consistent with a bound companion. Figure 3.3 (left) displays the motion of B relative to the primary. As discussed above, the 2016 epoch was obtained in two dither positions; we matched

observations in 2019 to the same two positions on the detector as 2016, to enable comparison. The change in position from 2016 to 2019 is consistent between images in the same dither position (i.e. 2016-1 to 2019-1 is consistent with 2016-2 to 2019-2). Our astrometry is sufficiently precise that the differences between 2016 and 2019 could be due to orbital motion. The 2014 epoch is offset from the others, most likely due to the NIRC2 realignment which occurred in 2015 (Service et al., 2016).

KIC 8462852 A and B are in *Gaia* EDR3² (Gaia Collaboration et al., 2021, 2016), which was released to the public while this paper was under review. *Gaia* EDR3 reports a total relative proper motion within $1\text{-}\sigma$ of our measured value ($0.44 \pm 0.34 \text{ mas yr}^{-1}$) and parallaxes for A and B that are consistent to within their uncertainty. We continued to use *Gaia* DR2 for some calculations such as stellar parameters due to independent validations and the Kepler field zero point.

Tests for Binarity

To test the level of consistency with co-movement, we computed the χ^2 goodness-of-fit for the specific cases of the companion being a distant background object (zero absolute proper motion) or completely co-moving (zero relative proper motion). Figure 3.3 (right) displays the common proper motion of KIC 8462852 B with KIC 8462852 A. Our measurements reject the null hypothesis that the object is a non-moving background star with zero proper motion ($\chi_{\text{non-moving}}^2 = 1060$, $\chi_{\text{co-moving}}^2 = 25.6$, for 4 degrees of freedom). We interpret the disagreement with the zero relative proper motion case as likely due to orbital motion.

We performed two additional statistical tests to assess the probability of observing a non-bound star at the position, velocity, magnitude, and parallax of the common proper motion candidate companion. First, we used a statistical approach similar to Sec. 4.5 of Correia et al. (2006) to estimate the probability of chance alignment given the surface density of similar objects in the vicinity. We queried the *Gaia* EDR3 catalog for objects within a 30° radius of KIC 8462852 A with proper motion within $1\text{-}\sigma$ of the *Gaia* proper motion of KIC 8462852 A ($\mu_\alpha = 10.4 \pm 0.6 \text{ mas yr}^{-1}$, $\mu_\delta = 10.3 \pm 0.6 \text{ mas yr}^{-1}$) and parallax within $1\text{-}\sigma$ of KIC 8462852 A ($\pm 0.025 \text{ mas}$), in order to determine the most conservative comparison. This returned 140 objects, a surface density of $\Sigma = 3.8 \times 10^{-9} \text{ arcsec}^{-2}$. The probability of observing a field object within $\theta = 2''$ of

²Source IDs: A: 2081900940499099136, B: 2081900944807842560, cc1: 2081900944800715648

KIC 8462852 A is given as:

$$P(\Sigma, \theta) = 1 - e^{-\pi\Sigma\theta^2} = 2.4 \times 10^{-8} \quad (3.1)$$

Second, we factored in the known demographics of binary companions (i.e., the frequency, mass ratio distribution, and semimajor axis distribution) by modifying the method of [Deacon et al. 2016](#), hereafter D16, Appendix A for distinguishing likely binary systems from chance alignments of field stars. D16 Eqn A2 gives the probability of a pair being a true binary pair rather than a coincident pair of field stars as:

$$P = \frac{\phi_c}{\phi_c + \phi_f} \quad (3.2)$$

where ϕ_c and ϕ_f are densities for companion and field stars respectively. While D16 considers the full range of binary population, here we are only concerned with the binary fraction that falls within the relevant parameter space, and so we modified D16 Eqn A3 to:

$$\phi_c = f_{bin} \times \frac{1}{A} \times \frac{1}{\Delta m} \times \left[\frac{e^{-\Delta\mu^2/2\sigma_\mu^2}}{2\pi\sigma_\mu^2} \right] \times \left[\frac{e^{-\Delta\pi^2/2\sigma_\pi^2}}{\sqrt{2\pi}\sigma_\pi} \right] \quad (3.3)$$

where $\Delta\mu$ is relative proper motion in RA/DEC, $\Delta\pi$ is the parallax difference, Δm is the size of the magnitude bin used for potential similar companions, A is the total area of the separation bin used, and f_{bin} is the binary companion fraction in those bins. Using the binary demographics of [Raghavan et al. 2010](#), we determined the binary fraction to be $f_{bin} = 0.01$ in a bin of $\Delta\rho = \pm 0.5$ dex of \log_{10} projected separation centered on the value for KIC 8462852 B, and $q = \pm 0.05$ in mass ratio between KIC 8462852 AB. We then estimated the corresponding apparent magnitude range ($\delta m_G = \pm 0.6$ mag) using the relations of [Pecaut and Mamajek 2013](#)³. For ϕ_f , we performed a *Gaia* EDR3 query for all objects within a radius from 50,000 AU (to exclude potential companions) to 30° within the same magnitude bin, $+/- 0.5$ mas yr⁻¹ proper motion in RA and DEC, and $+/- 0.25$ mas in parallax, returning 132 objects. We computed the field density as:

$$\phi_f = \frac{objects}{A \times \Delta m \times (\Delta\mu)^2 \times \Delta\pi} \quad (3.4)$$

³Version 2019.3.22, accessed on 2021-01-06, from http://www.pas.rochester.edu/~emamajek/EEM_dwarf_UBVIJHK_colors_Teff.txt

We determined a density ratio of

$$P = \frac{\phi_c}{\phi_c + \phi_f} = 0.999972$$

Given the extremely high density ratio for a binary companion compared to a field star, and the extremely small probability of chance alignment, we conclude that KIC 8462852 AB is a binary system.

Test for Orbital Motion

Since KIC 8462852 B is a bound companion, we assume that it follows a Keplerian orbit around the center of mass of the system. An object on a circular, face-on orbit at the current 880 AU separation and total system mass of $1.9 M_{\odot}$ would have a velocity $v_{\text{circ}} = 1.4 \text{ km s}^{-1}$, and period $P = 18600 \text{ yrs}$. Our time baseline and measurement precision is therefore marginally capable of measuring linear orbital motion, but is very unlikely to yield a measure of acceleration. Astrometric monitoring alone is unlikely to yield a fit with well-constrained posteriors on the orbit elements, though a refined measure of the linear motion might offer meaningful limits on the joint values of some elements.

To verify this conclusion, we performed a fit to our astrometry for Keplerian orbital elements using our custom implementation of the Orbits for the Impatient (OFTI) rejection sampling algorithm (Blunt et al., 2017). OFTI is well-suited to fit poorly constrained astrometric orbits with only small orbit fractions observed for which a Markov Chain Monte Carlo algorithm might not converge (Blunt et al., 2020). OFTI is described in detail in Blunt et al. 2017, and our implementation in Pearce et al. 2019. In brief, OFTI generates a random set of orbital elements from prior probability distributions, scales the semi-major axis and longitude of periastron to match observations, computes a χ^2 probability for each scaled orbit, and accepts an orbit if the probability of the orbit exceeds a randomly chosen uniform number on the interval [0,1]. We used a total system mass of $1.9 \pm 0.2 M_{\odot}$, based on the the mass estimates on Table 3.2. We ran our OFTI fitter until 100,000 orbits were accepted.

Figure 3.4 displays the posterior distributions for orbital elements, and periastron and apastron distances in our 100,000 orbit sample. The posterior distributions of orbital elements are similar

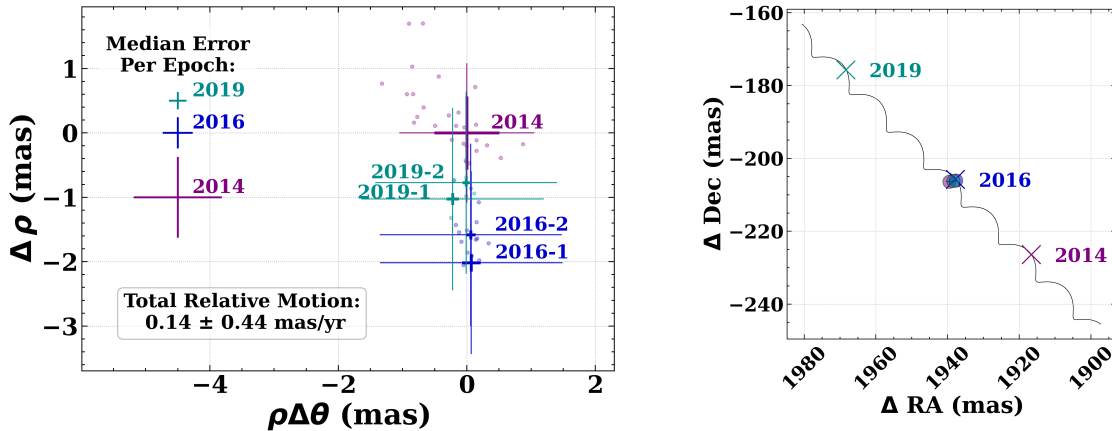


Figure 3.3: Left: Change in relative astrometry for KIC 8462852 B in separation (y-axis) and angular direction (x-axis) in individual images (circles) and mean values for each epoch (crosses). Epochs 2016 and 2019 dither positions are reported as separate observations. Thick crosses show statistical uncertainty, thin crosses show systematic uncertainty. Crosses to the left display the median error in individual image measurements. We measure a total relative velocity of $\mu = 0.14 \pm 0.44$ mas yr⁻¹, which is consistent with zero. Right: Observed position of KIC 8462852 B (circles, error bars smaller than marker size) with expected motion if it were a background star (black track, crosses indicate expected position at observation times). KIC 8462852 B displays common proper motion with KIC 8462852 A, consistent with a bound companion.

to priors and do not meaningfully constrain the orbit of KIC 8462852 B relative to A. We also note that the data did not rule out high eccentricity orbits with extreme values of apastron and periastron, however the apparent prominence of high eccentricity values is likely a reflection of the uniform eccentricity prior. We do not interpret this fit to reveal anything physically meaningful about the orbital elements due to the poor constraint.

3.3.2 KIC 8462852 cc1

Figure 3.6 (left) displays the astrometry results for KIC 8462852 cc1. We measure a relative proper motion in the plane of the sky of $\Delta\mu = 5.0 \pm 0.7$ mas yr⁻¹ ($\Delta\mu = 10.4 \pm 1.5$ km s⁻¹), which exceeds the circular velocity at that separation by 6σ ($v_{\text{circ}} \approx 1$ km s⁻¹), and is not consistent with being a bound companion. Figure 3.6 (right) shows that its relative motion is not consistent with being bound, nor with a non-moving background star. In testing for co-movement, our measurements fail to reject the null hypothesis that the object is a non-moving background star, yet neither is it consistent with being co-moving ($\chi^2_{\text{non-moving}} = 500$, $\chi^2_{\text{comoving}} = 250$).

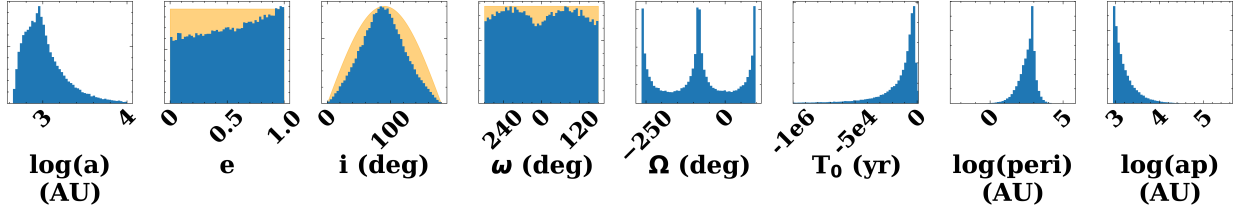


Figure 3.4: Orbital parameter posterior distributions for KIC 8462852 B. Posterior distributions on eccentricity, inclination, and argument of periastron are similar to priors shown in orange. Semi-major axis and longitude of nodes have no prior due to the scale-and-rotate process of OFTI (see Blunt et al. 2017), while T_0 , periastron, and apastron are derived from orbital parameters.

Additionally, we performed a search of all objects in *Gaia* DR2 within 0.5° of KIC 8462852 A, displayed in Figure 3.5, with our three candidate companions. While the proper motion of KIC 8462852 AB is distinct from the majority, cc1 is similar to the other objects with chance alignment. We conclude it is most likely a star with similar space velocity and a chance alignment.

3.3.3 KIC 8462852 cc2

Figure 3.7 (left) displays the astrometry results for KIC 8462852 cc2. We measure a relative proper motion in the plane of the sky of $\Delta\mu = 11.9 \pm 2.5 \text{ mas yr}^{-1}$ ($\Delta\mu = 25.2 \pm 5.2 \text{ km s}^{-1}$), which exceeds the circular velocity at that separation by $> 5\sigma$ ($v_{\text{circ}} \approx 1.2 \text{ km s}^{-1}$), and is not consistent with being a bound companion. Figure 3.7 (right) shows that its relative motion is more consistent with zero proper motion than with zero relative motion. Our measurements more strongly support that it is a background object than co-moving, but are not consistent with being completely non-moving ($\chi^2_{\text{non-moving}} = 150$, $\chi^2_{\text{comoving}} = 1670$). The motion of cc2 is consistent with the majority of nearby objects, shown in Figure 3.5. The *Gaia* DR2 objects have a mean proper motion of 4.8 mas yr^{-1} , within 1σ of cc2’s absolute proper motion of $5.1 \pm 2.4 \text{ mas yr}^{-1}$. We conclude that cc2 is an unassociated, distant object that is aligned by chance.

3.4 Discussion

Given the current 880AU projected separation of KIC 8462852 B, it is unlikely to be currently directly influencing the light curve of KIC 8462852 A. However, the binary companion may influence the long-term evolution of the system. Simulations of wide binary systems have found the

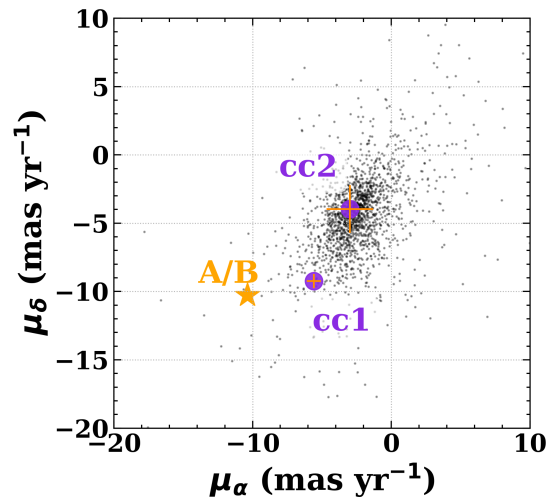


Figure 3.5: The absolute proper motions of KIC 8462852 A, B, cc1, and cc2, and objects in *Gaia* DR2 in a 0.5° cone search around the position of KIC 8462852 A. The proper motion for cc1 and cc2 are consistent with the motion of nearby stars with chance alignment.

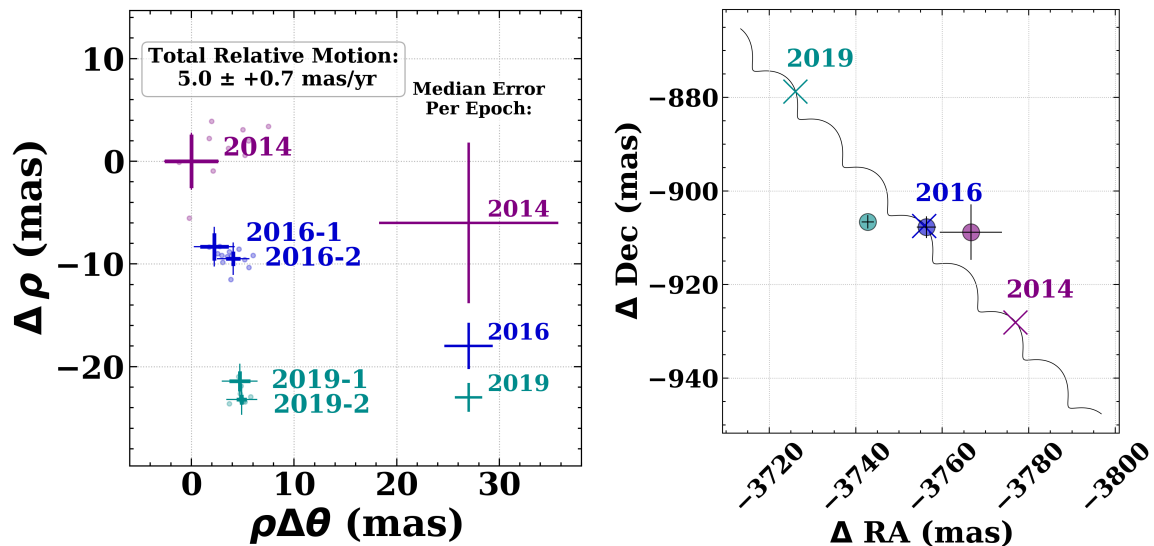


Figure 3.6: Left: Relative astrometry for KIC 8462852 cc1 in individual images (circles) and mean values in each epoch (crosses). Thick crosses show statistical uncertainty, thin crosses show systematic uncertainty. Crosses to the left display the median error in individual image measurements. We measure a total relative velocity of $\mu = 5.0 \pm 0.7 \text{ mas yr}^{-1}$. Epochs 2016 and 2019 dither positions are reported separately. Right: Observed position of KIC 8462852 cc1 (circles) with expected motion if it were a background star (black track, crosses indicate expected position at observation times). The relative motion of KIC 8462852 cc1 is not consistent with being a bound companion. It is likely a star with similar space velocity and chance alignment.

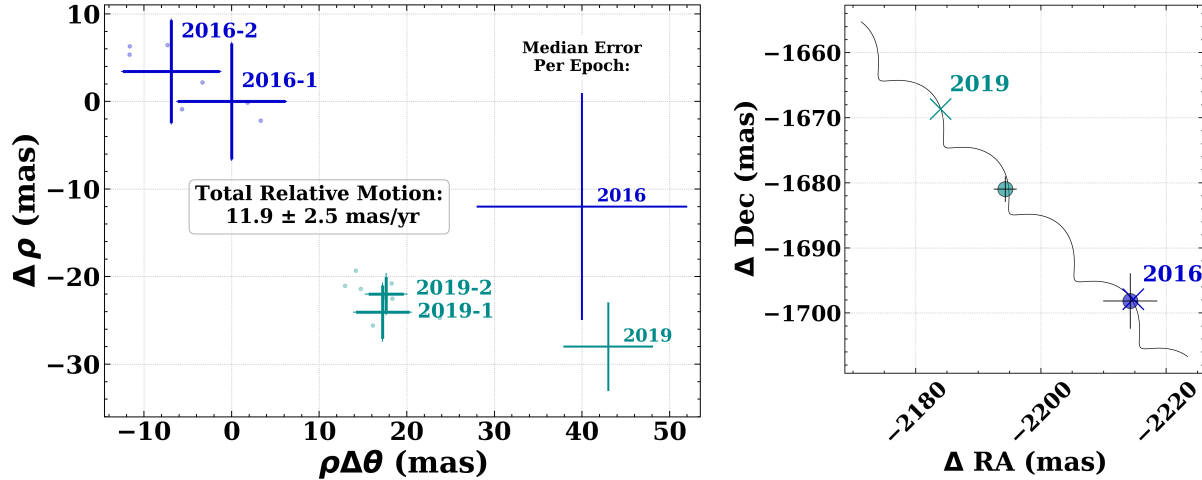


Figure 3.7: Left: Relative astrometry for KIC 8462852 cc2 in individual images (circles) and mean values in each epoch (crosses). Statistical uncertainty dominates systematic uncertainty for this object. Crosses to the left display the median error in individual image measurements. We measure a total relative velocity of $\mu = 11.9 \pm 2.5$ mas yr⁻¹. Right: Observed position of KIC 8462852 cc2 (circles) with expected motion if it were a background star (black track, crosses indicate expected position at observation times). The relative motion of KIC 8462852 cc2 is consistent with an unbound field object.

Milky Way galactic potential and stellar flybys have significant effect on these systems. [Kaib et al. \(2013\)](#) found that wide binaries pass through phases of very low pericenter distances (~ 100 AU) several times over the course of 10 Gyr due to galactic tides and passing stars, which propagate to disrupting eccentricities of planets and small bodies around one of the stars. [Correa-Otto et al. \(2017\)](#) found a similar result using an analytic model of the galactic potential. [Correa-Otto et al. \(2017\)](#) built on this numerically to find that a common configuration after 10 Gyr is high eccentricity with semi-major axis from 2000-5000 AU, regardless of the initial orbital configuration. [Bazsó and Pilat-Lohinger \(2020\)](#) found that secular resonances can arise in the habitable zone of stars in binaries even wider than 1000AU if there is also a giant planet present, and the effect of the galactic tide and stellar flybys can push the habitable zone into a high-eccentricity or chaotic state. There are many combinations of parameter space for which there are not stable orbits, and bodies are disrupted due to secular and mean motion resonances, with significant areas of chaotic orbits. If the secondary's pericenter is on the move as suggested by [Kaib et al. \(2013\)](#), disruption of objects in formerly stable orbits is possible as the location of resonances change, as has also been investigated by [Bancelin et al. \(2019\)](#) and [Zakamska and Tremaine \(2004\)](#).

The prospect of long-term orbital evolution for wide binaries suggests that KIC 8462852 B may play a role in the evolution and disruption of stable orbits of objects around the primary. Given the estimated age of this system, this binary may have already undergone at least one phase of close pericenter passage, commonly occurring around 1 Gyr (Kaib et al., 2013). Our astrometry does not prohibit high-eccentricity/low-pericenter orbits for the binary currently. A current or recent low-pericenter phase could excite the eccentricities of planets around A, and disrupt small bodies in the system. Further astrometric monitoring will continue to improve the picture of the potential influence of the binary on the system.

We have shown that the pair are not a chance alignment of unassociated stars, but we cannot yet confirm that they follow a bound Keplerian orbit. It remains possible KIC 8462852 B is a recently ejected star, which could explain the apparent chaos in the system. However testing this would require a longer astrometric time baseline and a firm measurement of whether high-eccentricity orbits are preferred or disallowed. It is also possible that the stars are separate members of the same moving group that have remained in close proximity over time. However, Figure 3.5 and our analysis in Section 3.3.1 show that there are very few objects with similar proper motions in the vicinity. In *Gaia* EDR3 the closest object with similar proper motion and parallax beyond KIC 8462852 B is two orders of magnitude further in separation, and in Section 3.3.1 we found a density of $\rho = 9 \text{ objects (mas yr}^{-1}\text{)}^{-2} \cdot \text{mas}^{-1} \cdot \text{degree}^{-2}$ with similar parameters to KIC 8462852 B. Given the 1.2 Gyr age of the system, the population that it formed in should be well dispersed, which is born out by *Gaia* astrometry. Given the small projected separation ($\rho = 880 \text{ AU}$), we conclude that this explanation is unlikely.

3.5 Conclusion

We have shown that KIC 8462852 B is a common proper motion pair, and extremely likely to be a gravitationally bound companion to KIC 846285 A using astrometry from Keck/NIRC2 imaging spanning five years. The relative velocity is consistent with zero during this period. The time baseline was not long enough to provide meaningful constraints to the pair’s orbit, however our analysis shows that they do represent a wide binary pair rather than chance alignment of field stars. We have also shown that two other objects in imaging data are not associated. Although it has not been thought to be a likely explanation for Boyajian’s Star A’s light curve, it is a potential

source of instability in the long-term evolution of the system, and could excite chaotic orbits of objects in the system. Efforts to explain KIC 8462852 A's dimming events should be informed by the existence of a wide stellar binary companion to the system.

Chapter 4

Companion Mass Limits for 17 Binary Systems Obtained with Binary Differential Imaging and MagAO/Clio

“Ants occupy the same landscape that we do. They have plenty to do, things to occupy themselves. On some level they’re very well aware of their environment. But we don’t try to communicate with them. So I don’t think they have the foggiest notion that we exist.”

Carl Sagan

Contact

This chapter is reproduced from [Pearce et al. 2022](#)

4.1 Introduction

Giant planets on wide enough orbits to be accessible by direct imaging are rare (occurrence rate $9_{-4}^{+5}\%$ for 5-13 M_{Jup} companions within 10-100 AU in the recent results from the Gemini Planet Imager Exoplanet Survey (GPIES); [Nielsen et al. 2019](#)). Brown dwarf companions appear to be even more rare, with an occurrence rate of $\sim 0.8_{-0.5}^{+0.8}\%$ for 13-80 M_{Jup} from GPIES. Yet radial velocity, transit, and microlensing surveys have found that giant planets close to their stars are common in regions promising for future direct imaging. [Bryan et al. 2019](#) found an occurrence rate of $39\% \pm 7\%$ for masses 0.5-20 M_{Jup} and separations 1-20 AU from radial velocity surveys; [Herman et al. 2019](#) found $0.7_{-0.20}^{+0.40}$ planets per solar-type star for radius 0.3-1 R_{Jup} and 2-10 yr periods from *Kepler* ([Borucki et al., 2010](#)); [Poleski et al. 2021](#) observed $1.4_{-0.6}^{+0.9}$ ice giants per microlensing star with separations $\approx 5-15$ AU from 20 years of the OGLE microlensing survey. Improving direct detection capability close to the star is of paramount importance for increasing the directly-imaged companion sample size and inferring population property statistics.

In addition to building larger telescopes and better instruments for ground- and space-based direct imaging, improving on observational and data analysis techniques can push detection limits closer and deeper. Point-spread function (PSF) subtraction via Reference Differential Imaging (RDI; commonly used with space telescopes) images the science target and a PSF reference star, but is hindered by time-varying PSFs, and requires observing two stars to reduce one. An improvement on RDI utilizes a library of PSF reference images (e.g. [Sanghi et al., 2021](#)) and a Locally Optimized Combination of Images (LOCI; [Lafrenière et al., 2007](#)) to optimally reconstruct the PSF, but is still susceptible to time variation between reference and science images. Spectral Differential Imaging (SDI; [Racine et al. 1999](#); [Marois et al. 2000](#)), in which the science target is imaged simultaneously in multiple filter bands, does not obtain photon-noise limited PSF subtraction due to the chromatic variation in speckles that doesn't scale with wavelength ([Rameau et al., 2015](#)), suffers from a difference in Strehl ratios between images in different bands, and depends on spectral features like Methane in the companion's atmosphere. With Angular Differential Imaging (ADI; [Marois et al. 2006](#)), the star serves as its own PSF reference through sky rotation; however, it is susceptible to self-subtraction of candidate companion signals and requires significant sky rota-

tion to avoid flux attenuation, especially close to the star. A way to avoid these various drawbacks is to simultaneously image a science and reference star in the same filter band.

[Kasper et al. \(2007\)](#) simultaneously imaged 22 young stars in the Tucana and β Pictoris moving groups in L' ($\sim 4\mu\text{m}$) band on NACO/VLT with adaptive optics, including two medium separation binaries (HIP 116748, $\rho = 5.8''$ and GJ 799, $\rho = 2.8''$). For these systems, both target and reference star fit on the detector simultaneously, yet were separated such that their PSFs did not overlap. They used each star in the binary to subtract the starlight from the other, termed this Binary Differential Imaging (BDI; in Figure 5 of their paper), and saw improved contrast at close separations compared to contemporaneously imaged single stars. Similarly, [Heinze et al. \(2010\)](#) applied “binary star subtraction” to binaries in their L' and M' nearby star survey with MMT AO with the Clio instrument, in which the PSF of the secondary was scaled and subtracted from the primary and vice versa. They also saw improvement in achievable contrast with binary star subtraction compared to single stars in their survey.

[Rodigas et al. \(2015\)](#) (hereafter [R15](#)) expanded on the BDI technique by combining the advantages of simultaneous imaging with advanced data analysis algorithms like Karhunen-Loève Image Processing (KLIP; [Soummer et al. 2012](#)) — an application of Principle Component Analysis (PCA) to image data — to better remove the speckle structure in the PSF. They compared the expected signal-to-noise ratio (S/N) for BDI to ADI and determined that BDI is advantageous close to the star, achieving ~ 0.5 mag better contrast within $\sim 1''$, which they estimate translates to $\sim 1M_{\text{Jup}}$ improvement in sensitivity. They also note that observing binaries near $4\mu\text{m}$ takes advantage of the large isoplanatic patch ($\sim 10''\text{--}30''$), in addition to being where young substellar companions will be bright ([Baraffe et al., 2015](#), hereafter BHAC15). They note that a limitation of BDI is the potential for companion flux around one star to be attenuated by flux from a companion around the other star, but that there is low probability of this ($\sim 2\%$ at $0.15''$, and even smaller farther out). Additionally, while coronagraphs employing a focal plane occulter cannot easily be used with BDI, pupil-plane only coronagraphs (such as apodizing phase plates, [Kenworthy et al. 2007](#); [Ottén et al. 2014](#)) that affect the PSFs of both stars could further increase sensitivity.

[R15](#) identified a target list of ~ 140 binary systems optimized for effective BDI. Targets are young ($\lesssim 200$ Myr) so that brown dwarf and planetary companions will be bright at near-infrared (NIR) wavelengths. Their binary separations are between $2''\text{--}10''$ so that their PSFs do not over-

lap and are within the isoplanatic patch at L' , and their apparent magnitudes in L' are similar to $\lesssim 2$ mag, making their PSF features have similar signal-to-noise.

In this paper, we describe the results of our MagAO/Clio NIR survey of 17 of the R15 binary star target list. In Section 4.2 we review current relevant studies of substellar companions in binaries. In Section 4.3 we describe our survey sample, with detailed descriptions of each system in Appendix A.1. In Section 4.4 we describe our BDI observations and KLIP data reduction application. In Section 4.5 we show contrast limits for each binary system, discuss limitations on our achievable contrast, and discuss our detection of a candidate companion to HIP 67506 A.

4.2 Motivation: Substellar Companions in Wide Binaries

The occurrence rate of planet and brown dwarf companions in binaries, and the influence the binary has on the formation and evolution of the planetary environment, is not well understood, and is hampered by small numbers of observed systems.

Circumstellar planets in wide binaries (S-type, in which the companions orbits one component of the binary) have been shown to be fully suppressed for close binaries (semi-major axis (sma) $\lesssim 1$ AU, Moe and Kratter 2019), an occurrence rate of $\sim 15\%$ at sma ~ 10 AU, and increasing with binary separation out to sma ~ 100 AU (Kraus et al., 2016; Moe and Kratter, 2019; Ziegler et al., 2020). Several recent observational studies have found a higher fraction of close-in S-type companions in multiple systems compared to single stars. (Knutson et al., 2014; Ngo et al., 2015; Piskorz et al., 2015). Ngo et al. (2016) found a $\sim 3\times$ inflation in occurrence rate of hot Jupiters in multiple systems over single stars, and infer that stellar companions beyond 50 AU might actually facilitate giant planet formation. Fontanive et al. (2019) found an inflated binary fraction of 80% with separations from 20-10,000 AU for stars hosting close in higher-mass planetary and brown dwarf companions ($7-60 M_{\text{Jup}}$). Cadman et al. (2022) showed that the binary companions can trigger instability and fragmentation in gravitationally unstable disks, leading to formation of these giant planet and brown dwarf companions in outer regions of the disk, which somehow move to the close-in orbits currently observed. However other studies have concluded that the frequency of planets in binaries is not statistically different from that of single stars (e.g. Bonavita and Desidera, 2007; Harris et al., 2012). Deacon et al. (2016) found no evidence that binaries with $\rho > 3000$ AU affected occurrence rate of *Kepler* planets with $P < 300$ days around FGK stars. Moe and

Kratter (2019) found that for $sma \gtrsim 100$ AU the binary does not suppress planet occurrence, and the apparent inflated occurrence is due to selection effects.

Although it is unclear if wide ($\gtrsim 100$ AU) stellar companions are consequential to the formation of planetary systems, it is likely to impact the evolution of a planetary system through gravitational scattering and migration. While the wide binary may be too wide to induce binary von Zeipel-Kozai-Lidov oscillations (von Zeipel, 1910; Kozai, 1962; Lidov, 1962) on an S-type planet directly (Ngo et al., 2016), it could still induce chaos in the system. Mean motion resonance overlap from the companion star leads to regions of chaotic diffusion and eventual planet ejection even in circular binary orbits (Holman and Wiegert, 1999; Mudryk and Wu, 2006; Kratter and Perets, 2012). Simulations by Kaib et al. (2013) and Correa-Otto and Gil-Hutton (2017) showed the influence of the galactic gravitational potential and stellar flybys perturbs the wide companion's orbit over time, causing S-type companion orbits to be disrupted, pushed into high-eccentricity orbits, and potentially scattered (see also Hamers and Tremaine 2017). The presence of an additional giant planet can further induce secular resonances (Bazsó and Pilat-Lohinger, 2020) or high-e migration (Hamers, 2017; Hamers and Tremaine, 2017) interior to the giant planet, planet-planet scattering, and push the surviving planet into high-eccentricity orbits which could be further boosted by Kozai-Lidov cycles from the stellar companion (Mustill et al., 2021). Wide-orbit stellar companion(s) can also be sufficient to explain stellar spin-planetary orbit misalignment even if the companion is orders of magnitude more distant, including inducing retrograde obliquities (Best and Petrovich, 2022).

More population members at various stages of evolution are needed to better develop the picture observationally. In addition to the surveys of Kasper et al. 2007 and Heinze et al. 2010 discussed in the introduction, several other recent surveys have looked for companions in binaries using other starlight subtraction techniques. Hagelberg et al. (2020) targeted 26 visible binary and multiple star young moving group members with SPHERE on VLT (Beuzit et al., 2008) in dual-H band filters, with a Lyot coronagraph masking the brighter star, and used ADI to subtract the starlight. The SPOTS survey (Thalmann et al., 2014; Bonavita et al., 2016; Asensio-Torres et al., 2018) searched for wide circumbinary planets in the 30-300 AU range. While neither survey detected new substellar companions, they placed upper limits on occurrence rates. Dupuy et al. (2022) found evidence for mutual alignment between S-type planet and binary orbits $\lesssim 30^\circ$ for *Kepler*

planet hosts in visual binaries. Additionally, the precise astrometry of Gaia (Gaia Collaboration et al., 2016) enabled identification of 1.3 million spatially resolved binaries (El-Badry et al., 2021), and several recent studies utilized the Gaia astrometric information to examine the orbit of the wide stellar companion to transiting planet host stars (e.g. Newton et al., 2019; Venner et al., 2021; Newton et al., 2021), search for new unresolved companions (e.g. Kervella et al., 2019; Currie et al., 2021), refine the masses of known companions (e.g. Brandt et al., 2019; Brandt et al., 2021), and observe an overabundance of alignments between planet and wide binary orbits for binaries with semi-major axis < 700 AU (Christian et al., 2022). Orbital obliquity alignment studies such as Bryan et al. 2020 and Xuan et al. 2020 are important probes of the angular momentum evolution of planetary systems and the influence of scattering and/or Kozai-Lidov mechanisms (Mustill et al., 2021), especially in the presence of a wide stellar companion (Hjorth et al., 2021). Future Gaia data releases will contain improved astrometry and acceleration information for hundreds of millions of sources¹, making new companion identification through astrometry common place, and promising to deliver numerous planets and brown dwarf companions in wide binaries

Multiple star systems should be prioritized as prime direct imaging targets for probing planetary system formation and evolution, population statistics, and planet characterization studies.

4.3 Binary Systems in our Survey

We observed 17 binary star systems between 2014 - 2017, chosen for their utility for BDI data reduction, to span a range of spectral types, and their availability between other observing programs. Table 4.2 summarizes the properties of each young binary system observed. Binary separation, distance, and the primary’s G-band magnitude were taken from Gaia EDR3 (Gaia Collaboration et al., 2021); age and spectral type were taken from literature values; group membership is from literature and/or Banyan Σ membership probabilities (Gagné et al., 2018). Our observations were conducted in MKO L' and the narrowband $3.95\mu\text{m}$ ($\Delta\lambda_{\text{eff}} = 0.08\mu\text{m}$, $\lambda_0 = 3.95\mu\text{m}$; hereafter [3.95]²) filters, so we have included the primary’s WISE W1 and W2 magnitudes for reference (Cutri et al., 2012). A subset of systems were unresolved in WISE, so the photometry includes flux from both members, and are indicated with a dagger in Table 4.2.

¹<https://www.cosmos.esa.int/web/gaia/dr3>

²Previous papers have called it the [3.9] filter, we here refer to it as [3.95] for clarity

Table 4.2: Summary of Binary Systems

HD Name	Alt Name	Separation ^{a,*} (arcsec)	Distance ^{a,**} (pc)	Age (Myr)	SpT
HD 36705	AB Dor	8.8609 ± 50	14.93 ± 0.02	100^b	K0V + M5-6 ^c
HD 37551	WX Col	4.00175 ± 1	80.45 ± 0.07	130 ± 20^d	G7V + K1V ^c
HD 47787	HIP 31821	2.15685 ± 2	47.83 ± 0.04	16.5 ± 6.5^f	K1IV + K1IV ^c
HD 76534	OU Vel	2.06874 ± 2	869 ± 14	0.27^h	B2Vn ⁱ
HD 82984	HIP 46914	2.0041 ± 30	274 ± 7	53.4 ± 15.1^f	B4IV ^f
HD 104231	HIP 58528	4.45718 ± 5	102.7 ± 0.5	21^k	F5V ^l
HD 118072	HIP 66273	2.27647 ± 7	79.5 ± 0.4	$40-50^n$	G3V ^c
HD 118991	Q Cen	5.56444 ± 6	88.3 ± 0.3	$130-140^p$	B8.5 + A2.5 ^q
HD 137727	HIP 75769	2.20358 ± 3	111.7 ± 0.3	8.2 ± 0.6^f	G9III + G6IV ^c
HD 147553	HIP 80324	6.23216 ± 7	138.2 ± 1.3	16 ± 1^k	B9.5V + A1V ^s
HD 151771	HIP 82453	6.8957 ± 3	270 ± 2	$200-300^t$	B8III + B9.5 ^u
HD 164249	HIP 88399	6.49406 ± 2	49.30 ± 0.06	25 ± 3^v	F6V + M2V ^c
HD 201247	HIP 104526	4.17040 ± 3	33.20 ± 0.04	$200-300^y$	G5V + G7V ^z
HD 222259	DS Tuc	5.36461 ± 3	44.12 ± 0.07	$45 \pm 4^\alpha$	G6V + K3V ^c
–	HIP 67506 [‡]	9.38117 ± 9	220 ± 2	210 ± 5^t	G5 ^β
–	TYC 7797-34-2 [‡]		1700 ± 100	–	–
–	TWA 13	5.06925 ± 3	59.9 ± 0.1	$10_{-7}^{+10;\gamma}$	M1Ve + M1Ve ^c
–	2MASS J01535076-1459503	2.8543 ± 10	33.85 ± 0.09	25 ± 3^v	M3 ^ε

*Uncertainties in units of 10^{-5} arcsec

**Distances and uncertainties are were computed using the method of [Bailer-Jones et al. 2018](#) and Gaia EDR3 parallaxes.

[§]Sco-Cen: Scorpius–Centaurus Association, UCL: Upper Centaurus Lupis association, Tuc-Hor: Tucana-Horologium Young Moving Group, ARG: Argus Association, Beta Pic: Beta Pictoris Moving Group, AB Dor: AB Doradus Moving Group, LCC: Lower Centaurus-Crux

[†]Binary is unresolved in WISE photometry

[‡]HIP 67506 and TYC 7797-34-2 (WDS J13500-4303 AB) were believed to be a 9'' binary at the time of the survey, but we show in this work that they are an unassociated pair.

This has no impact on the BDI reduction of both stars. See Appendix [A.1](#).

There are no age or spectral type estimates in literature for TYC 7797-34-2.

Table 4.2: Summary of Binary Systems (continued)

Name	Group Membership [§]	RUWE ^a A / B	G Mag ^a A / B	WISE W1 Mag (3.35 μ m)	WISE W2 Mag (4.6 μ m)
HD 36705	AB Dor	25.13 / 3.52	6.69 / 11.35	4.598 \pm 0.121 [†]	4.189 \pm 0.057 [†]
HD 37551	AB Dor ^e	0.96 / 0.97	9.45 / 10.35	7.284 \pm 0.027 [†]	7.385 \pm 0.019 [†]
HD 47787	Field ^j	1.11 / 1.11	8.91 / 9.01	6.348 \pm 0.042 [†]	6.457 \pm 0.042 [†]
HD 76534	Field ^j	1.53 / 0.89	8.25 / 9.42	7.271 \pm 0.029 [†]	7.066 \pm 0.020 [†]
HD 82984	Field ^j	1.09 / 0.89	5.53 / 6.26	5.346 \pm 0.064 [†]	5.202 \pm 0.030 [†]
HD 104231	LCC ^m	0.83 / 2.29	8.45 / 13.43	A: 7.198 \pm 0.028 B: 9.499 \pm 0.228	7.248 \pm 0.020 9.338 \pm 0.119
HD 118072	90% ARG ^j	1.20 / 1.20	9.02 / 9.14	6.875 \pm 0.034 [†]	6.941 \pm 0.020 [†]
HD 118991	Sco-Cen ^j	1.11 / 1.07	5.24 / 6.60	4.975 \pm 0.070 [†]	4.629 \pm 0.036 [†]
HD 137727	Field ^j	1.42 / 0.88	9.16 / 9.66	6.739 \pm 0.038 [†]	6.815 \pm 0.020 [†]
HD 147553	UCL ^j	0.93 / 0.89	7.00 / 7.46	A: 7.039 \pm 0.116 B: 7.219 \pm 0.112	7.055 \pm 0.026 7.283 \pm 0.037
HD 151771	Field ^j	1.22 / 0.80	6.19 / 8.46	A: 5.802 \pm 0.069 B: 7.412 \pm 0.302	5.696 \pm 0.033 7.536 \pm 0.157
HD 164249	Beta Pic ^{w,x}	1.09 / 1.23	6.91 / 12.31	5.882 \pm 0.057 [†]	5.841 \pm 0.021 [†]
HD 201247	Field ^j	0.96 / 0.89	7.53 / 7.71	5.211 \pm 0.0657 [†]	5.055 \pm 0.041 [†]
HD 222259	Tuc-Hor ^g	0.91 / 0.95	8.34 / 9.41	A: 7.062 \pm 0.068 B: 7.089 \pm 0.179	7.072 \pm 0.030 7.140 \pm 0.056
HIP 67506 [‡]	Field ^j	2.01	10.67	9.189 \pm 0.021	9.242 \pm 0.023
TYC 7797-34-2 [‡]	Field ^j	1.73	11.99	9.475 \pm 0.023	9.561 \pm 0.021
TWA 13	TW Hydra ^δ	1.25 / 1.27	10.89 / 10.91	A: 7.635 \pm 0.052 B: 7.408 \pm 0.087	7.545 \pm 0.030 7.470 \pm 0.030
2MASS J01535076-1459503	Beta Pic ^w	1.36 / 1.38	11.49 / 11.52	6.810 \pm 0.028 [†]	6.729 \pm 0.014 [†]

- (a) Gaia EDR3, [Gaia Collaboration et al. 2021](#), (b) [Mamajek and Hillenbrand 2008](#), (c) [Torres et al. 2006](#), (d) [Binks et al. 2020](#); [Barrado y Navascues et al. 2004](#), (e) [McCarthy and White 2012](#), (f) [Tetzlaff et al. 2011](#), (g) [Kraus et al. 2014](#), (h) [Arun et al. 2019](#), (i) [Houk 1978](#), (j) [Gagné et al. 2018](#), (k) [Pecaut et al. 2012](#), (l) [Houk and Cowley 1975](#), (m) [Hoogerwerf 2000](#), (n) [Zuckerman 2019](#), (p) [David and Hillenbrand 2015](#), (q) [Gray and Garrison 1987](#), (s) [Corbally 1984](#), (t) This work, Sec 4.3, (u) [Corbally 1984](#), (v) [Messina et al. 2016](#), (w) [Messina et al. 2017](#), (x) [Deacon and Kraus 2020](#), (y) [Zuckerman et al. 2013](#), (z) [Gray et al. 2006](#), (α) [Bell et al. 2015](#), (β) [Spencer Jones and Jackson 1939](#), (γ) [Barrado Y Navascués 2006](#), (δ) [Schneider et al. 2012](#), (ϵ) [Riaz et al. 2006](#),

We have made use of literature ages for the estimation of mass limits in Section 4.5. Age estimates we adopted were derived using a variety of methods; specifics for each binary system are noted in Table 4.2 and described in Appendix A.1. We used the most-recent and lowest-uncertainty age estimate for an individual star where available; most were derived using isochrone model fitting to photometry, lithium equivalent widths, or chromospheric and coronal activity. Where individual age estimates were not available we adopted the average age and uncertainty for the associated moving group. Two systems in our survey did not have literature ages or moving group membership (HIP 67506/TYC 7797-34-2 and HD 151771), and we estimated age using isochrone fitting (see Appendix A.1 for details). In Section 4.5 we discuss the impact the estimated age of the star has on our results.

4.4 Methods

4.4.1 Observations

Observations for this survey were carried out between 2014 to 2017 with Magellan Adaptive Optics system (MagAO) (Close et al., 2013) and Clio science camera on the 6.5 m Magellan Clay telescope at Las Campanas Observatory, Chile. All images were obtained in [3.95] or MKO L' observing bands with the narrow camera (plate scale = $15.9 \text{ mas pixel}^{-1}$, field of view = $16 \times 18''$; Morzinski et al. 2015) in full frame mode (512×1024 pixels), and with the telescope rotator off. Observation parameters varied between datasets and are documented in Table 4.3. There were two observing modes: ABBA Nod mode, in which two nod positions (A and B) with both stars on the detector, 10 frames each, were alternated in an ABBA pattern during the observations; and “Sky” mode, where science frames were observed in a single nod and the telescope was offset to get starless “sky frames”.

4.4.2 Data Reduction

Due to the difficulty of flat fielding Clio images (see Morzinski et al., 2015, Appendix B.3), we performed sky subtraction using Karhunen-Loève Image Processing (KLIP; Soummer et al. 2012), an implementation of principle component analysis (PCA) applied to image data. To sky subtract a science image from Nod A (in ABBA observing mode) with KLIP, we:

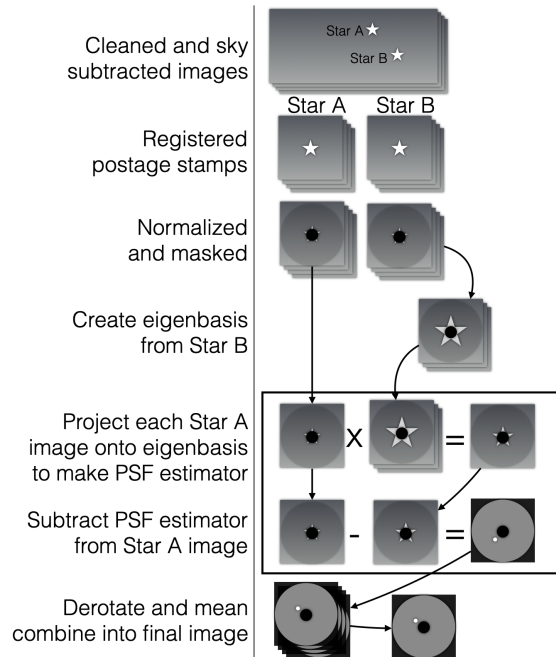


Figure 4.1: Illustration of our BDI implementation of the KLIP methodology. This process is repeated for Star B using Star A as the eigenbasis.

1. masked the stars in every Nod B image in the dataset to a radius of $8 \lambda/D$ to capture variation in the sky alone,
2. constructed a PCA eigenimage basis set from the Nod B images in the dataset, following the prescription of [Soummer et al. \(2012\)](#) Section 2.2 step 2,
3. projected the Nod A target image onto the eigenbasis constructed from Nod B up to a desired number of basis modes K_{klip} ([Soummer et al., 2012](#), Section 2.2 step 4), to create a sky estimator,
4. subtracted the sky estimator from the Nod A image.

We repeated this process for Nod B images using a basis constructed from all Nod A images in the dataset. For datasets observed in “Sky” mode, we constructed the basis set from the sky frames. All datasets were sky subtracted with $K_{\text{klip}} \leq 5$. We then corrected bad pixels using the bad pixel maps of [Morzinski et al. \(2015\)](#); we also used a high-pass filter and flagged pixels with excessive variation during the course of the dataset to identify and correct additional bad pixels. Bad pixels within star PSFs were identified by eye and corrected. Finally, images were inspected for quality by eye, and sharpest images were kept for use in starlight subtraction. None of the images in our survey fell outside the linear regime and did not require linearity correction.

4.4.3 KLIP PSF Subtraction

As with sky subtraction, we subtracted the star’s PSF using a custom implementation of KLIP PSF subtraction. Our algorithm, illustrated in Figure 4.1, proceeds in the following way:

1. Each star is cut out of each cleaned and sky-subtracted full frame image into a “postage stamp” and assembled into a cube of all images of Star A and another cube of Star B.
2. Each image in each cube is registered (PSF core centered in frame), normalized (entire frame is divided by the sum of all pixels in the frame so that the pixel values all now sum to one), and the inner core of the PSF is masked to avoid fitting the PSF core and prioritize fitting the PSF wings. We determined a radius of $1\lambda/D$ for the inner core mask was optimal for our data by inspection. We did not have any saturated stars in our datasets.
3. For the Star A cube, a PCA eigenbasis set is constructed from the Star B cube, following the prescription of [Soummer et al. \(2012\)](#) Section 2.2 as before.
4. Each image in the Star A cube is projected onto the Star B basis set up to specified number of modes K_{klip} to create a PSF estimator, then the PSF estimator is subtracted from the Star A image.
5. Each image is rotated to North up/East left, then a sigma-clipped mean image of the cube is created as the final reduced image. PSF estimation via ADI was not employed in our analysis.
6. Repeat 3-5 for the Star B cube using Star A to create eigenbasis.

Postage stamp size varied by dataset due to the binary separation (star PSFs must be able to be isolated), proximity to glints and detector defects, and proximity to the edge of the frame. One system in our initial survey, 53 Aquarii, is a 1.2” binary, which ended up being too close to effectively separate the PSFs to serve as references for KLIP and was excluded. Another system, WDS J00304-6236, is a triple system, with WDS J00304-6236 Aa,Ab separated by 0.1”, enough to cause elongation of Star A’s PSF and disqualifying it from serving as a PSF reference to WDS J00304-6236 B and was excluded.

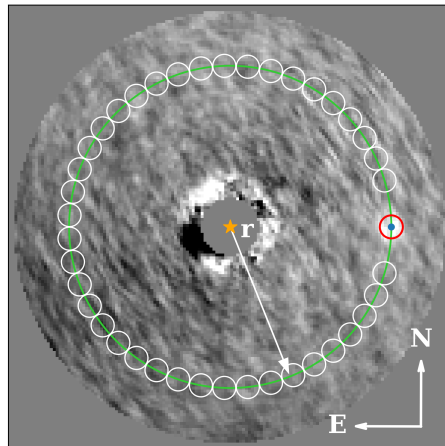


Figure 4.2: Illustration of our method for determining signal to noise ratio (S/N) based on [Mawet et al. \(2014\)](#). The image is a post-BDI reduction of HD 82984 A with a fake signal injected right at the $5\text{-}\sigma$ S/N limit at separation $r = 7\lambda/D$ and position angle 270° East of North. HD 82984 A is behind the mask and marked with an orange star. The sum of the pixels within the red aperture, with diameter $= 1\lambda/D$, is \bar{x}_1 in Eqn 4.1; the mean and standard deviation of the sum of the pixels in the white apertures are \bar{x}_2 and s_2 respectively; n_2 is the number of white apertures. This computation was repeated for all $N = 2\pi r$ apertures along the ring of radius r , and for rings of radius $r = n\lambda/D$, where n is an integer.

4.4.4 Contrast and mass limits

To quantify achievable contrast limits for each system, we performed injection-recovery of synthetic “planet” signals and determined the contrast at which injected signals can be recovered at the $5\text{-}\sigma$ level. We produced the synthetic signal by scaling the star’s image to a specified contrast, injected the synthetic signals into Star A’s postage stamp cube, then performed KLIP reduction using Star B as above, and measured the signal-to-noise ratio (S/N) of the resulting signal (repeating for Star B using Star A as basis). To measure the S/N of recovered signals, we implemented the methodology of [Mawet et al. \(2014\)](#) for small number statistics induced by close separations. To summarize briefly, we injected a synthetic planet signal of a known contrast at a specific position angle and a separation $r = n\lambda/D$, where n is an integer. Figure 4.2 illustrates the S/N calculation for a synthetic signal injected at S/N = 5 to the HD 82984 A dataset. At separation r (green circle) there are $N = 2\pi r$ resolution elements of size λ/D , the characteristic scale of speckle noise. We defined a resolution element centered at the injected signal (Figure 4.2 red aperture) and in $N-3$ resolution elements at that radius (Figure 4.2 white apertures), neglecting those immediately to

either side to avoid the wings of the injected PSF. Then, using Eqn (9) of [Mawet et al. \(2014\)](#), which is simply the Student’s two-sample t-test, we have

$$p(x, n_2) = \frac{\bar{x}_1 - \bar{x}_2}{s_2 \sqrt{1 + \frac{1}{n_2}}} \quad (4.1)$$

where $\bar{x}_1 = \Sigma(\text{pixels in red aperture})$, $\bar{x}_2 = \text{mean}[\Sigma(\text{pixels in white apertures})]$, and $s_2 = \text{stdev}[\Sigma(\text{pixels in white apertures})]$, $n_2 = N-3$, and $S/N = p$. This calculation was repeated for signals injected in all N resolution elements in the ring at radius r , and we took the mean S/N value as the S/N for that specified radius and contrast. We computed S/N for all $n \lambda/D$ radii from $r = 1.7 \lambda/D$ ($0.2''$) to the outer extent of the postage stamp (indicated in [Table 4.3](#)) and for various contrast values and interpolated the $5\text{-}\sigma$ contrast limit.

For each system we determined an apparent L' or [3.95], as appropriate to the observation, magnitude for the primary star by retrieving the WISE W1 ($\lambda_{\text{central}} = 3.35\mu\text{m}$) and W2 ($\lambda_{\text{central}} = 4.6\mu\text{m}$) and interpolating an apparent magnitude at L' or [3.95] using spectral type models from CALSPEC (HST flux standard spectra, [Bohlin et al. 2014](#)). We converted the apparent $5\text{-}\sigma$ contrast limits to absolute magnitudes using the distances in [Table 4.2](#). We determined an age for each system from literature, and used the age and contrast limit absolute magnitude as constraints to interpolate a mass from evolutionary models. For mass limits in the stellar regime, we used isochrones from the [BHAC15](#) evolutionary models; for substellar regime, we used the [Marley et al. \(2021\)](#) evolutionary models. For observations in [3.95] filter, we re-interpreted for the [3.95] filter in Clio by computing synthetic photometry for each isochrone point under the assumption of a 2.3 mm PWV atmospheric transmission model (ATRAN, [Lord, 1992](#)) and airmass of 1.0. As noted in [Section 4.3](#), we were unable to determine a literature age for two systems, HIP 67506 and HD 151771, and used BHAC15 and SYCLIST isochrones respectively to interpolate an estimated age, which we then used with BHAC15 to convert contrast limits to mass estimates in the same manner.

Table 4.3: Summary of Observations and Results by Binary System

System	Obs. Date	Obs. Mode*	N _{images}	Filter	T _{int} (s)	N _{coadds}	Obs. ΔMag	Binary Sep (") PA (deg)	Inner Sep [†] (AU)	Outer Sep	N _{KLIP} Modes	Best Contrast (Δmag)	Mass Limit (M _☉)
HD 36705	2017-02-18	ABBA	28	[3.95]	5	6	2.0	8.881±0.003" 347.57±0.05°	4	1.5" 22 AU	A 20 B 20	5.3 6.8	0.07 0.01
HD 37551	2014-11-26	Sky	167	[3.95]	5	2	0.4	4.0165±0.0006" 115.167±0.007°	17	1.5" 120 AU	A 15 B 15	7.8 7.5	0.02 0.02
HD 47787	2017-02-11	ABBA	10	[3.95]	3	20	0.1	2.178±0.003" 201.46±0.07°	10	1.6" 72 AU	A 9 B 9	6.0 5.75	0.01 0.01
HD 76534	2017-02-18	ABBA	63	[3.95]	5	6	2.1	2.0794±0.0009" 303.94±0.04°	190	1.2" 970 AU	A 10 B 10	5.0 3.0	0.39** 0.39**
HD 82984	2015-05-29	ABBA	16	[3.95]	4	5	0.7	2.018±0.006" 220.69±0.03°	60	1.2" 300 AU	A 15 B 15	6.5 6.5	0.47 0.31
HD 104231	2017-02-18	Sky	49	[3.95]	5	6	1.7	4.479±0.001" 161.45±0.01°	22	2.4" 240 AU	A 30 B 30	5.5 6.0	0.04 0.009
HD 118072	2015-05-29	Sky	10	[3.95]	3	5	0.06	2.28±0.03" 80.7±0.9°	18	1.6" 120 AU	A 7 B 15	5.0 6.3	0.06 0.02
	2017-02-19	Sky	35	[3.95]	5	6	0.06	2.290±0.002" 79.49±0.05°	18	1.6" 120 AU	A 30 B 10	4.0 4.0	0.12 0.13
HD 118991	2015-05-30	ABBA	16	[3.95]	4	5	0.8	2.29±0.03" 162.91±0.01°	20	1.2" 100 AU	A 15 B 15	5.5 5.5	0.40 0.27
HD 137727	2017-02-20	ABBA	18	[3.95]	3	10	1.0	2.2108±0.0006" 185.3±0.1°	25	1.2" 150 AU	A 17 B 17	4.5 4.5	0.09 0.04
HD 147553	2015-05-24	Sky	52	[3.95]	4	3	0.2	6.274±0.004" 152.48±0.04°	30	0.8" 110 AU	A 15 B 3	5.8 6.3	0.04 0.02
	2015-06-02	ABBA	31	[3.95]	4	10	0.2	6.259±0.002" 152.478±0.008°	30	0.8" 110 AU	A 30 B 30	5.8 5.5	0.04 0.04

Table 4.3: Summary of Observations and Results by Binary System (continued)

System	Obs. Date	Obs. Mode *	N_{images}	Filter	T_{int} (s)	N_{coadds}	Obs. ΔMag	Binary Sep (") PA (deg)	Inner Sep [†] (AU)	Outer Sep	N_{KLIP} Modes	Best Contrast (Δmag)	Mass Limit (M_{\odot})	
HD 151771	2017-09-05	ABBA	25	[3.95]	5	1	1.3	6.79 \pm 0.01"	55	1.2"	A	20	6.3	0.66
										300 AU	B	20	6.0	0.43
HD 164249	2017-09-04	ABBA	54	[3.95]	3.5	1	2.3	6.547 \pm 0.007"	10	1.2"	A	30	4.5	0.08
										75 AU	B	30	3.0	0.04
HD 201247	2015-05-24	ABBA	34	[3.95]	4	3	0.1	4.190 \pm 0.003"	6	1.2"	A	5	7.5	0.03
										37 AU	B	30	7.3	0.03
HD 222259	2017-09-02	ABBA	30	[3.95]	5	6	0.1	4.216 \pm 0.003"	6	1.6"	A	3	5.5	0.09
										50 AU	B	5	6.0	0.06
HD 222259	2015-06-03	Sky	25	[3.95]	4	10	0.4	5.388 \pm 0.002"	10	1.8"	A	24	6.5	0.01
										82 AU	B	24	6.5	0.01
HIP 67506 TYC 7797-34-2	2017-09-05	ABBA	32	[3.95]	5	1	0.4	5.391 \pm 0.005"	10	0.8"	A	10	5.0	0.04
										33 AU	B	10	5.0	0.03
TWA 13	2015-05-31	Sky	44	MKO L'	0.6	20	0.4	9.424 \pm 0.004"	50	1.43"		30	6.5	0.03
										140 AU		30	6.5	0.02
2MASS J01535076- 1459503	2015-05-23	ABBA	27	MKO L'	0.5	200	0.05	5.080 \pm 0.007"	15	1.6"	A	10	4.8	0.02
										90 AU	B	25	4.8	0.02
2MASS J01535076- 1459503	2017-09-05	ABBA	132	[3.95]	4	1	0.1	2.875 \pm 0.006"	8	1.6"	A	10	6.0	0.01
										50 AU	B	3	5.8	0.01

*Two observing modes: ABBA - two nods, A and B, 10 frames each, alternating in an ABBA pattern throughout observation;

Sky: one nod position and a set of "sky" frames without stars in the frame.

*The age of HD 76534 is < 1Myr below the age range of most isochrone models.

†All systems used inner working angle of $1.7 \lambda D^{-1} = 0.2''$

NOTE - N_{images} is the number of images used in the KLIP reduction; N_{coadds} is the number of coadded frames per image; Observed ΔMag is the contrast in magnitudes measured in our survey between components A and B;

Binary separation (sep) and position angle (PA) are the mean and standard deviation of position measurements of images in each dataset; Inner/Outer sep are the inner and outer radius of working mask for BDI reduction; N_{KLIP} Modes records the number of basis modes used in the KLIP reduction of the star.

4.5 Results

We report in Table 4.3 a summary of the deepest contrast achieved for each binary system as a function of number of KLIP modes (N_{KLIP}) and separation in arcseconds and AU. Contrast is reported in units of $\Delta\log_{10}(\text{flux})$ between injected companion signal and host star at the $5\text{-}\sigma$ level, with corresponding mass in M_{\odot} . Figure 4.3 displays the results of our pipeline for HD 37551. Figure 4.3 (top) shows the reduced images of HD 37551 A (left) and B (right), with the inner $1 \lambda/D$ and outer ring masked. Figure 4.3 (bottom) shows the $5\text{-}\sigma$ flux contrast limits (left) and mass limits (right) for A (purple) and B (red) as a function of separation in AU and arcseconds. Similar plots for all stars in our survey are included in the supplementary material and are available online.

4.5.1 Factors Affecting Contrast and Mass Limits

Variable conditions. We found that variable conditions during the observations dramatically affected achievable contrast. Similarly, bad pixels, poor pixel correction, a high background level relative to star peak also decreased achievable contrast. We found that limiting the datasets to only the very best quality images achieved deeper contrast limits compared to having more lower quality images in the basis set. For each dataset we inspected by eye and retained only the sharpest images. In Table 4.3 we report the number of images used in the final reduction for each dataset (N_{images}). The varying levels of contrast achieved from dataset to dataset is mostly a function of the image quality of that particular observation; i.e. the highest Strehl images achieved the deepest contrast limits.

Number of KLIP basis modes. We also found that the optimal number of KLIP modes to obtain the deepest contrast varied between datasets. Figure 4.4 displays an example of contrast limits as a function of KLIP modes for TWA 13 A. In this example, there is dramatic improvement in contrast for $N_{\text{KLIP}} > 7$, and the deepest contrast is achieved at $N_{\text{KLIP}} = 10$ at $0.5''$ ($4 \lambda/D$). The optimal N_{KLIP} for each system is reported in Table 4.3.

Binary contrast. The binary stars' contrast, reported as ΔMag in Table 4.3, also affected the depth of the companion search. The strength of BDI relies on achieving identical PSF signal-to-noise between reference and target star, which will vary inversely with flux ratio between the

two stars. In our survey, achieved contrast was generally poorer for systems with higher binary contrast.

Age. Finally, the assumed age for the system affects the final mass limits we derived from our measured contrast limits. As discussed in Sections 4.3 and 4.4.4, we made use of literature ages to derive mass limits corresponding to our contrast limits for each system. For limits in the substellar regime, this introduces some uncertainty that is not captured in the reported mass limits, as luminosity in the infrared depends on age for substellar objects. For some systems in our survey there were several discrepant ages in the literature; for others, there was no independent age for the system, and we assumed the average age of the associated moving group, which has a range of possible ages of members. For systems with literature age estimates, they were typically derived from model fitting, which can vary with the assumptions underlying the model. Details of the age we used for each system are described in Appendix A.1. Substellar objects cool with age, so for two hypothetical objects with the same properties but different ages, the younger one will appear brighter than the older one in observations. So if the actual age of our system were younger than the age we assumed, our contrast limits would correspond to lower mass limits, and vice versa. In most cases, the effect on limits would be minimal. For example, 2MASS J01535076-1459503 is a Beta Pictoris Moving Group member (Messina et al., 2017), and we adopted the moving group age of 25 ± 3 Myr (Messina et al., 2016). Computing corresponding mass limits for ages $2\text{-}\sigma$ younger (19 Myr) and $2\text{-}\sigma$ older (31 Myr) results in a difference of $\sim 0.05 M_{\text{Jup}}$ at the highest contrast. However in some cases there are widely discrepant ages in literature, such as for AB Dor AB, which has age estimates spanning 5-240 Myr. This results in a $\sim 15 M_{\text{Jup}}$ difference in the mass limits at the highest contrast between the youngest and oldest ages estimates. Our reported mass limits and completeness estimates assume the age given in Table 4.2 for each system, and the variation induced by differing ages is not captured in those limits.

4.5.2 Notable System Results

Here we discuss some notable results of select binary systems in our sample. The results for the remaining objects in our survey are available digitally³.

³<https://github.com/logan-pearce/Pearce2022-BDI-Public-Data-Release>

HD 37551 – The Deepest Contrast

HD 37551 achieved the deepest contrast limits in our sample ($\Delta[3.95] = 7.8$ and 7.6 magnitudes) at the deepest points for A and B respectively). This dataset also retained the highest number of high-quality images in the final BDI reduction, due to the stable seeing conditions and AO correction throughout the observation. We did not identify any candidate companion signals in the reduced images. Figure 4.3 displays the reduced images and corresponding contrast and mass limits for HD 37551.

HD 36705 – The Effect of Binary Contrast

HD 36705 is the most extreme case of the effect of binary contrast on the reduction in our sample. HD 36705 A is a nearby (15 pc) bright (Gaia G mag = 6.7) K0V type star with an M5-6 binary companion. We observed $\Delta[3.95] \approx 2$. Figure 4.5 displays a single image from the HD 36705 dataset with a ZScale stretch to emphasize faint PSF features.

The image for HD 36705 A (left) is bright with many features apparent with strong signal-to-noise. Several rings of the Airy pattern and a second set of diffraction spikes (oriented left-right) visible for A which are lost in the noise for B. Figure 4.5 (bottom) shows the reduced image for HD 36705 A (left), in which both sets of diffraction spikes are visible in the residuals, showing incomplete starlight subtraction. The resulting contrast limits are poor, especially for A, due to the residual starlight.

As there was no infrared excess observed for this system (see Appendix A.1), we interpret the apparent “fuzziness” of the residuals near the core of HD 36705 B to be due to incomplete starlight subtraction and not physical features. We do not expect either of the known stellar companions to be visible in our reduction as they both have separations $< 0.2''$.

HD 222259 – The Effect of Instrument Ghosts

The 2015 observation of HD 222259 contained an elongated PSF core shape due to residual vibrations from suboptimal tip/tilt gain setting, as well as different optical ghosts to the lower left of each star, shown in Figure 4.5 (bottom). These features show up clearly in the BDI reduction as positive and negative valued areas to the northeast and around the center masked region in both

Table 4.4: Gaia EDR3 Multiplicity Metrics for HIP 67506

Metric	Value
RUWE	2.02
astrometric_excess_noise	0.22
astrometric_excess_noise_sig	75.2
astrometric_chi2_al	2277.97
ipd_gof_harmonic_amplitude	0.0099
ipd_frac_multi_peak	0

reduced images, and degraded the achieved contrast. Neither of these features are present in the 2017 epoch observation of HD 222259.

HIP 67506 – A Candidate Companion Signal

The BDI reduction of HIP 67506 contains a promising candidate companion signal, marked with a red circle in Figure 4.7, which shows the BDI reduction of HIP 67506 and TYC 7797-34-2 (labeled A and B) in MKO L' reduced with 30 KLIP modes. The candidate signal, located at separation $\approx 1.3 \lambda/D$ ($\approx 0.2''$) and position angle $\approx 90^\circ$, is more similar to a PSF shape than any other features in reduced images in our survey, although it is distorted due to its proximity to the star core. The candidate signal rotated with the sky and did not smear azimuthally like the other features at similar separation.

Other lines of evidence. HIP 67506 has an elevated RUWE in EDR3 (RUWE = 2.02; see Appendix A.1), indicating the possible presence of a companion unresolved in Gaia that caused it to deviate from the assumed single-star model (Lindgren, 2018b). RUWE has been shown to be highly sensitive to the presence of unresolved subsystems (Stassun and Torres, 2021; Penoyre et al., 2020; Belokurov et al., 2020). Additionally, HIP 67506 has a statistically significant acceleration ($\chi^2 = 24$) in the Hipparcos-Gaia Catalog of Accelerating Stars (HGCA, Brandt 2018). Kervella et al. (2019) computed a statistically significant (S/N = 5) proper motion anomaly in the Gaia DR2 epoch which could be caused by a $\sim 230 M_{\text{Jup}}$ object at the candidate signal separation of 18 AU ($0.2''$). Similarly, the Kervella et al. (2022) PMa catalog for Gaia EDR3 astrometry measured a PMa which could be caused by a $\sim 200\text{-}300 M_{\text{Jup}}$ object at 18 AU.

While RUWE is the most complete and easy to interpret metric (Lindgren, 2018a), other metrics in Gaia can probe multiplicity. Perturbations of the source photocenter (caused by orbiting

unresolved objects) compared to the center-of-mass motion (which moves as a single star) will cause the observations to be a poor match to the fitting model, which registers as excess noise via the `astrometric_excess_noise` parameter, and whose significance is captured in the `astrometric_excess_noise_sig` parameter (>2 indicates significant excess noise). The `astrometric_chi2_all` term reports the χ^2 value of the observations to the fitting model. From the image parameter determination (IPD) phase, `ipd_gof_harmonic_amplitude` is sensitive to elongated PSF shapes relative to the scan direction (larger values indicate more elongation), and `ipd_frac_multi_peak` reports the percentage of observations which contained more than one peak in the windows⁴.

Table 4.4 shows values of these metrics for HIP 67506. The IPD parameters are small, suggesting that there are no marginally resolved sources (separation larger than the resolution limit but smaller than the confusion limit, ~ 0.1 - $1.2''$, Gaia Collaboration et al. 2021) present in the images, however the astrometric noise parameters are large and significant, affirming the presence of sub-systems. It appears possible that the subsystem(s) affecting the astrometry are closer than $0.1''$, however the candidate signal’s position of $\approx 0.2''$ is near the resolution limit so it is not ruled out as a genuine signal by these metrics.

Candidate signal properties. Treating this candidate signal as a genuine companion, we estimated the mass by injecting a negative template PSF in the same manner as Section 4.4.4. We varied the separation, position angle, and relative contrast of the negative signal to minimize the residual root-mean-square value of pixels within a diameter = $1\lambda/D$ aperture centered on the injected signal. We estimated the contrast between star and candidate companion to be $\Delta L' \approx 5 - 5.5$ magnitudes. We used the age of the system (≈ 200 Myr) and L' magnitude to interpolate a mass estimate using BHAC15 evolutionary atmosphere models, and estimated a corresponding mass of ≈ 60 – $90 M_{\text{Jup}}$, which spans the divide between high-mass brown dwarf and low-mass M-dwarf regimes. This is however smaller than the mass estimates derived from the PMA. Given the proximity to the star’s core, at separation $\approx 1.3 \lambda/D$, it is possible that some of the companion flux was subtracted in the reduction. However the smaller mass estimate places the candidate companion in an (age, luminosity, mass) regime with few other detected young high-mass brown dwarf com-

⁴See https://gea.esac.esa.int/archive/documentation/GEDR3/Gaia_archive/chap_datamodel/sec_dm_main_tables/ssc_dm_gaia_source.html for complete description of Gaia catalog contents

panions (see [Faherty et al., 2016](#), Fig 34), so if the small-mass estimate is valid this will be an interesting benchmark object. This makes HIP 67506 a good target for follow-up observations to confirm the companion, obtain spectral type, T_{eff} , and $\log(g)$ estimates, and potentially a dynamical mass measurement.

4.5.3 Completeness

We determined the survey completeness to stellar and substellar companions using a Monte Carlo approach. Over a grid that is uniform in $\log(\text{mass}) \in [-3,0] M_{\odot}$ and $\log(\text{semimajor axis}) \in [0,3]$ AU we generated 5×10^3 simulated companions for each grid point, randomly assigned orbital parameters from priors⁵, and computed the projected separation. A companion was considered detectable if it fell above the contrast curve and undetectable if below. We determined completeness as the fraction of simulated companions at each grid point that would have been detected at at least SNR=5, with 1.0 corresponding to detecting every simulated companion, and 0.0 detecting none. We computed survey completeness for each star in our survey, with contours at 10%, 50%, and 90% of simulated companions detected.

Figure 4.8 displays completeness for the entire survey, made by summing completeness maps for every star in the survey ([Lunine et al., 2008](#); [Nielsen et al., 2019](#)). Contours and colormap give number of stars for which the survey is complete for a given (sma, mass) pair. Stars in our survey cover a variety of separation regimes, and so individual completeness plots do not line up; additionally individual completeness plots never reach 100% as some simulated planets fall outside the inner resolution limit or outside detector when projected, and become undetectable. Thus the maximum value in composite completeness plot is ~ 14 stars, even though all stars have some fractional sensitivity to companions.

⁵eccentricity (e): $P(e) = 2.1 - 2.2 \times e$, $e \in [0,0.95]$, following [Nielsen et al. 2019](#); inclination (i): $\cos(i) \in \text{Unif}[-1,1]$; argument of periastron (ω): $\omega \in \text{Unif}[0,2\pi]$; mean anomaly (M): $M \in \text{Unif}[0,2\pi]$; since contrast curves are one-dimensional we did not simulate longitude of nodes

4.6 Discussion

4.6.1 BDI Performance Compared to Other Observing Modes.

R15 described several advantages to BDI over ADI or “classical” RDI: 1. PA rotation is not a consideration when planning and executing observations, 2. BDI allows reducing two stars with 1 observation ($2\times$ more efficient than ADI, $4\times$ more efficient than RDI), and 3. It targets stars often excluded from large direct imaging surveys (wide binaries). They used simulated companion injections into a single MagAO/Clio [3.95] dataset of HD 37551 to determine that BDI performed ~ 0.5 mag better than ADI at small separations ($\sim 1''$).

We did not explicitly test only-BDI vs only-ADI in our survey — some amount of rotation was included with each BDI dataset but was not the source of diversity used to reconstruct the stellar PSF. We found that the effectiveness of our reduction depends highly on the observing conditions and image/detector quality, but these are factors which would affect both ADI and BDI equally. However, ADI is not susceptible to the contrast between the two binary components, as discussed in Section 4.5. R15 selected binaries with NIR $\Delta m \lesssim 2$, but state this was not a strict requirement based on their analysis. We found that for systems in the regime $\Delta m_{\text{IR}} \sim 1-2$, $5\text{-}\sigma$ contrast limits were shallower for higher Δm_{IR} , as PSF features visible in the bright star do not have sufficient signal-to-noise in the fainter star to be fully subtracted. BDI is also susceptible to variation due to anisotropy, unlike ADI and SDI, and the separation between the stars should be designed to fall within the isoplanatic patch for the observing wavelength.

4.6.2 The Scientific Context of Our Survey

The small number of stars in our survey and their diversity of characteristics does not allow us to make meaningful contributions to the occurrence rates discussed in Section 4.2. The 35 stars in our survey to date span a range of spectral types, ages, (lack of) group membership, and binary separations, and were chosen for their utility in the BDI technique. This initial survey represents a contribution to probes of (sub)stellar companions in wide binaries; further observations of wide binary systems are needed to continue to fill in the picture of brown dwarfs and giant planets in wide stellar binaries.

4.7 Conclusion

We have presented the results of 17 binary star systems imaged in NIR with MagAO/Clio and reduced using Binary Differential Imaging and PCA techniques. Our achieved contrast was limited by image quality, observing conditions, and binary star contrast. We detected a candidate companion signal around HIP 67506 A which is near the stellar-substellar boundary, and merits follow-up to confirm companion status and characterize the companion.

Targeting young wide multiple star systems with direct imaging surveys is advantageous from both a technical and astrophysical perspective. Simultaneously imaging the science and reference star in the same filter within the same isoplanatic patch should provide superior PSF matching for starlight subtraction, particularly when combined with PCA for building a PSF model. This promises to be an even more powerful technique for space-based observations, including JWST, as the PSF is much more stable and is not subject to anisoplanatism. Brown dwarf and giant planet formation and dynamical evolution in binaries is a data-starved problem with many unanswered questions, and is an important piece of the star and planet formation picture.

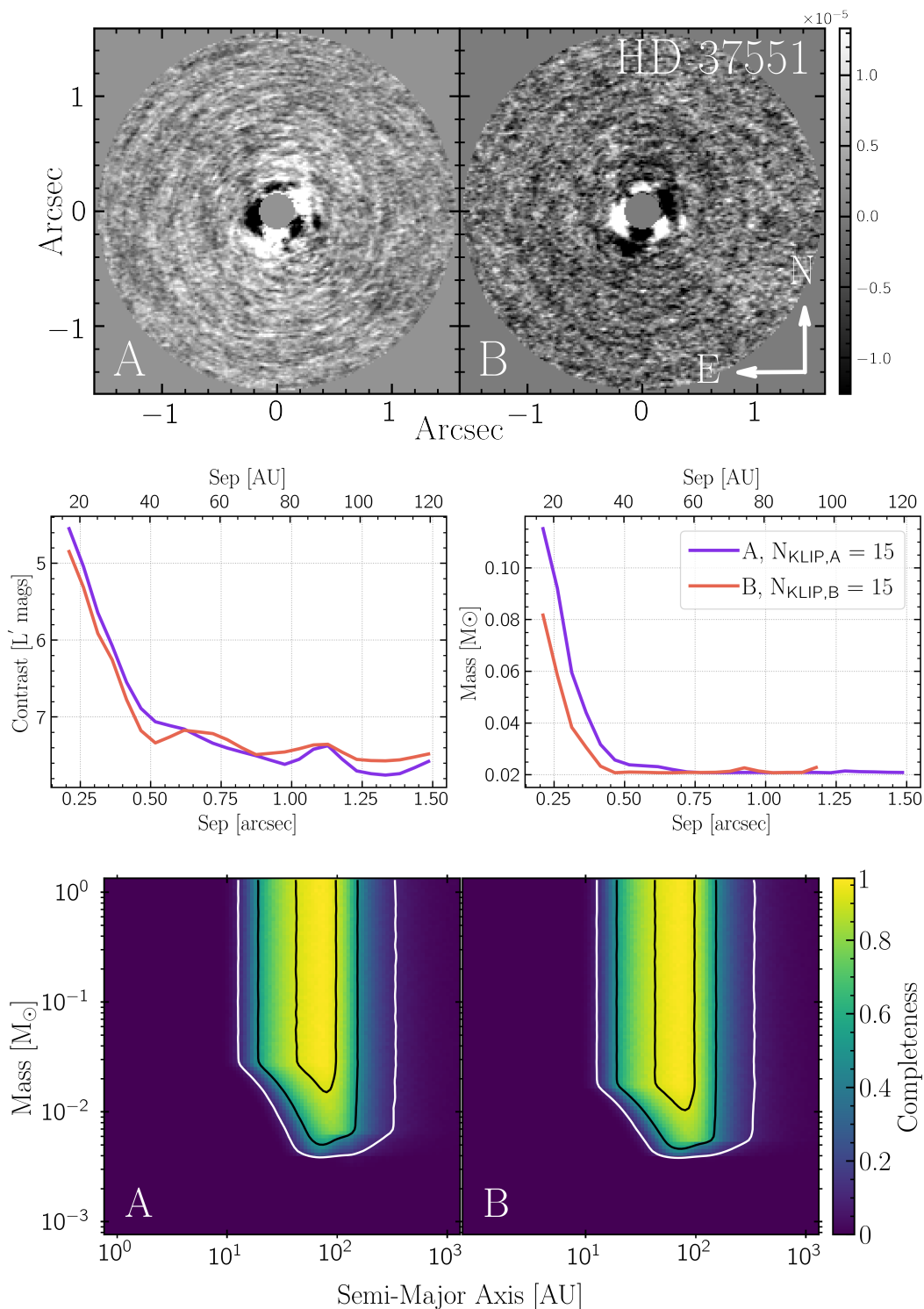


Figure 4.3: Results of BDI-KLIP reduction of HD 37551. Top: reduced image of HD 37551 A reduced with HD 37551 B as reference (left) and vice versa (right) using 15 KLIP modes. North is up and East is to the left in both images. Middle: Contrast limits (left) and mass limits (right) as a function of separation for HD 37551 A (purple) and HD 37551 B (red). These are the deepest contrast and mass limits in our survey, reaching as low as $5M_{\text{Jup}}$ in to 40 AU for both A and B. Bottom: Survey completeness maps for both stars for a grid of (semi-major axis, mass) pairs. Color map indicates fraction of simulated companions which would have been detected at each grid point. Contours indicate 10% (white), 50%, and 90% (inner-most contour) of simulated companions detected.

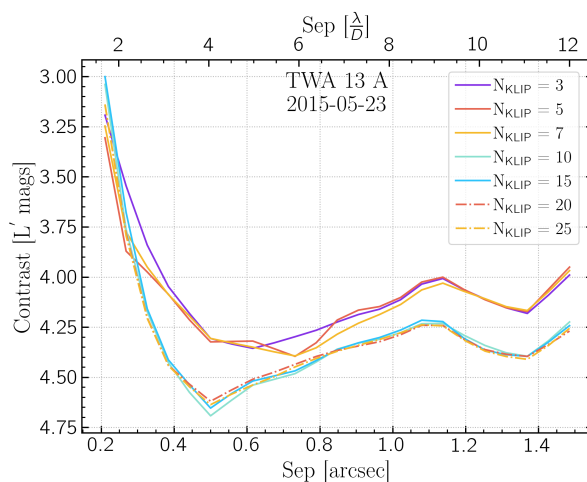


Figure 4.4: Contrast for TWA 13 A as a function of number of basis modes (N_{KLIP}). The deepest contrast is achieved at $N_{\text{KLIP}} = 10$ for this system. Optimal number of basis modes varies between datasets and is reported in Table 4.3.

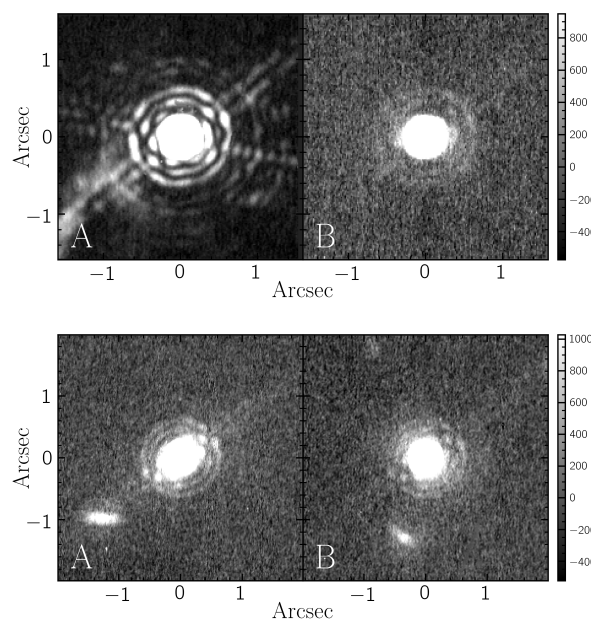


Figure 4.5: Top: A selected image of HD 36705 A (left) and HD 36705 B (right) from our 2017 dataset, shown with a ZScale stretch to emphasize the faint PSF features, with gray scale showing pixel counts. The image of the two stars appear significantly different due to their large relative contrast ($\Delta\text{mag} \approx 2$) and the brightness of HD 36705 A in the MagAO [3.95] filter, with many features visible on A lost in the noise for B. This resulted in contrast limits when used to perform BDI due to insufficient starlight subtraction. Bottom: A selected image from the 2015 epoch HD 222259 observation, shown with a ZScale stretch. The HD 222259 A PSF (left) contains a glint (bottom left corner), HD 222259 B (right) contains a different glint (bottom of frame); both PSF cores are elongated. These features show up prominently in the BDI reduction.

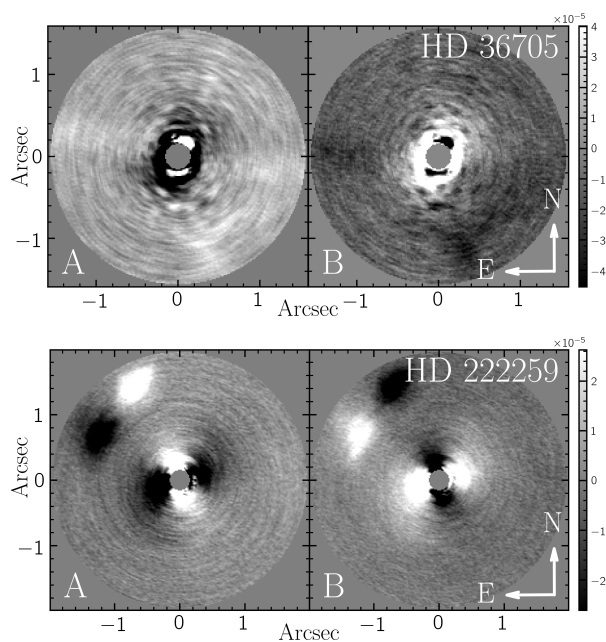


Figure 4.6: Top: BDI reduction of HD 36705 using 20 KLIP modes. North is up and East is to the left in both images. HD 36705 A is significantly brighter than HD 36705 B, and PSF features visible in A are lost to noise in B, resulting in poor starlight subtraction and contrast limits, particularly for A. Bottom: BDI reduction of HD 222259 using 24 KLIP modes. North is up and East is to the left in both images. Regions of bright and dark pixels in the upper northeast corner are due to the ghosts visible in Figure 4.5, as are bright and dark areas in the central regions.

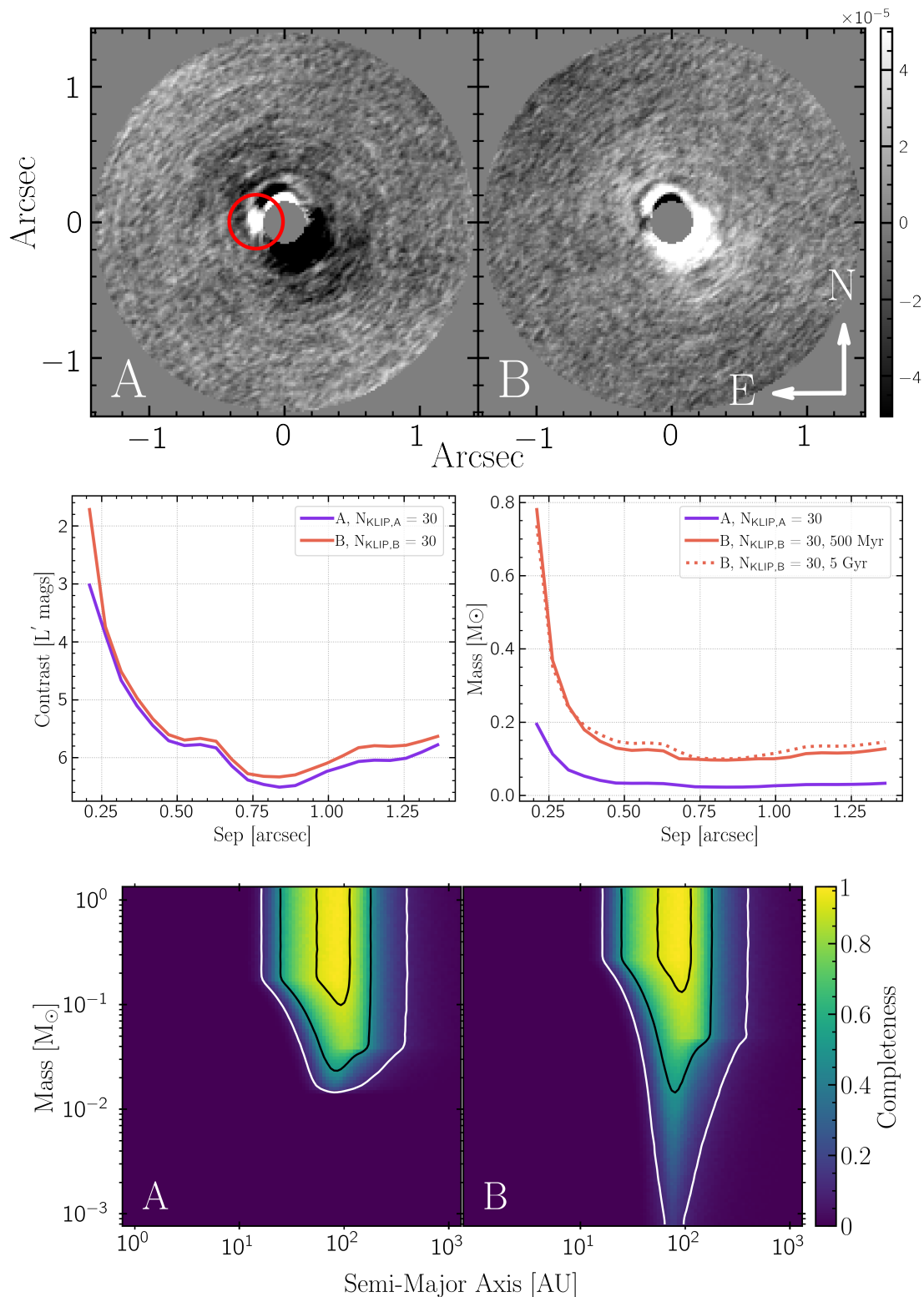


Figure 4.7: Top: BDI reduction of HIP 67506 (labeled A) and TYC 7797-34-2 (labeled B) using 30 KLIP modes. North is up and East is to the left in both images. The candidate companion signal is located $\sim 0.2''$ ($\sim 2\lambda/D$) to the east of HIP 67506 (behind mask), indicated by the red circle. The candidate signal rotated with the sky rotation, unlike the azimuthally broadened features at similar separation. Middle: contrast curves for HIP 67506 and TYC 7797-34-2. We show mass limits for TYC 7797-34-2 using a young age (500 Myr) and a field age (5 Gyr). Bottom: Completeness map for HIP 67506 and TYC 7797-34-2. Contours show 10%, 50%, and 90% completeness.

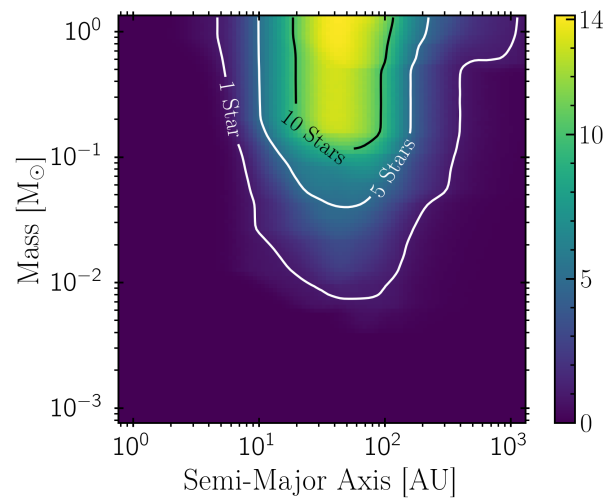


Figure 4.8: Completeness map for every star in our survey as a function of mass and semi-major axis. Colormap and contours give the number of stars for which a given (sma, mass) pair is complete.

Chapter 5

HIP 67506 C: MagAO-X Confirmation of a New Low-Mass Stellar Companion to HIP 67506 A

“The story so far: In the beginning the Universe was created. This has made a lot of people very angry and been widely regarded as a bad move.”

Douglas Adams

Hitchhiker's Guide to the Galaxy

This chapter is reproduced from [Pearce et al. 2023](#)

5.1 Introduction

High-contrast imaging searches have found very low occurrence rates for close substellar companions. For example, $9_{-4}^{+5}\%$ for 5-13 M_{Jup} , $\sim 0.8_{-0.5}^{+0.8}\%$ for 13-80 M_{Jup} companions within 10-100 AU in the recent results from the Gemini Planet Imager Exoplanet Survey (GPIES); ([Nielsen et al., 2019](#)), while the SHINE survey ([Vigan et al., 2021](#)) found frequency of systems with at least one substellar companion to be $23.0_{-9.7}^{+13.5}\%$, $5.8_{-2.8}^{+4.7}\%$, and $12.6_{-7.1}^{+12.9}\%$ for BA, FGK, and M stars. Yet radial velocity, transit, and microlensing surveys point to higher occurrence rates in regions promising for future direct imaging contrasts and separation (e.g. [Bryan et al., 2019](#); [Herman et al., 2019](#); [Poleski et al., 2021](#)). Decreasing the effective inner working angle (IWA) or resolution of observations increases the area of the accessible region proportional to $(\text{IWA})^{-2}$. Smaller IWAs extend the reach to tighter regimes of nearby stars, and to the planetary regime of more distant stars ([Mawet et al., 2012](#)). Working at small IWAs will be vital for the future of the high-contrast imaging field.

[Rodigas et al. 2015](#) demonstrated that for visual binaries of separation $\approx 2 - 10''$ and approximately equal magnitude, a starlight subtraction via a principal component analysis-based reference differential imaging (RDI) algorithm using each star of the binary as reference for the other – termed binary differential imaging (BDI) – outperforms the common angular differential imaging technique at close separations. In [Pearce et al. 2022](#) we used BDI to reduce a set of 17 visual binaries imaged in L' and $3.95\mu\text{m}$ filters with MagAO/Clio instrument on the Magellan Clay Telescope at Las Campanas Observatory from 2015-2017. In that work we reported detection of a candidate companion signal at $2\lambda/D$ separation to the star HIP 67506 A. Due to the proximity to the star's core we were unable to determine the nature of the companion, but had evidence to suggest it might be near the stellar/substellar mass boundary.

In this work we report the results of follow-up observations of HIP 67506 A with the MagAO-X instrument on the Magellan Clay telescope in April 2022 to confirm the candidate signal. We report the discovery of HIP 67506 C, a previously unknown early-M type $0.1''$ (~ 20 AU) companion to HIP 67506 A. In Section 5.2 we describe the indirect indications pointing to the existence of a hidden companion. In Section 5.3 we describe our MagAO-X follow up observations and confirmation of HIP 67506 C, and in Section 5.4 our astrometric and photometric characteriza-

tion. Additionally in Appendix A we demonstrate that the previously identified 9''-separated star HIP 67506 B is not actually physically associated.

5.2 Stellar Properties

HIP 67506 A is a field star (99.9% probability in BANYAN Σ ; [Gagné et al. 2018](#)) at 221.6 ± 1.8 pc ([Gaia Collaboration et al., 2021](#)). It was identified as type G5 ([Spencer Jones and Jackson, 1939](#)), mass $1.2 M_{\odot}$ ([Chandler et al., 2016](#)), with effective temperature $T_{\text{eff}} = 6077 \pm 150$ K and luminosity $L = 0.37 \pm 0.07 L_{\odot}$ ([McDonald et al., 2012](#)). In [Pearce et al. \(2022\)](#) we used these values to estimate an age of ≈ 200 Myr from isochrone fitting to [Baraffe et al. \(2015\)](#) isochrones. It was identified in the Hipparcos and Tycho Doubles and Multiples Catalog ([Esa, 1997](#)) as a binary system with another star (HIP 67506 B) with separation 9'', and dubbed HIP 67506 A and B.

5.2.1 Indicators of a Companion to HIP 67506 A

In the previous chapter we observed 17 visual binary systems and reduced the images using the Binary Differential Imaging (BDI) technique (see also [Rodigas et al., 2015](#)) with Magellan Adaptive Optics system (MagAO) ([Close et al., 2013](#)) and Clio science camera on the Magellan Clay Telescope at Las Campanas Observatory in MKO L' and $3.95\mu\text{m}$ filters, from 2014–2017. To summarize briefly, we simultaneously observed a science and PSF reference target by selecting binaries of nearly equal magnitude, separated enough that their PSF features do not overlap, but close enough to be within the isoplanatic patch at these wavelengths, making the target and reference PSF as close to equal in structure and signal-to-noise ratio as possible. We then reduced each star with the other as the PSF reference, using Karhunen-Loève Image Projection (KLIP; [Soumerai et al., 2012](#)) to reconstruct a model PSF from the reference star to subtract from the target star.

We observed HIP 67506 AB on 2015-05-31 as part of this survey and detected a candidate companion signal $\sim 0.2''$ East of HIP 67506 A. Figure 5.1 displays the KLIP-reduced image of HIP 67506 A from that paper, with the candidate signal marked by the red circle. The candidate signal is distorted from a typical PSF shape – due its proximity to the star's core (at $2\lambda/D$) the signal was corrupted by PSF subtraction. However the fact that it did not appear to smear azimuthally like

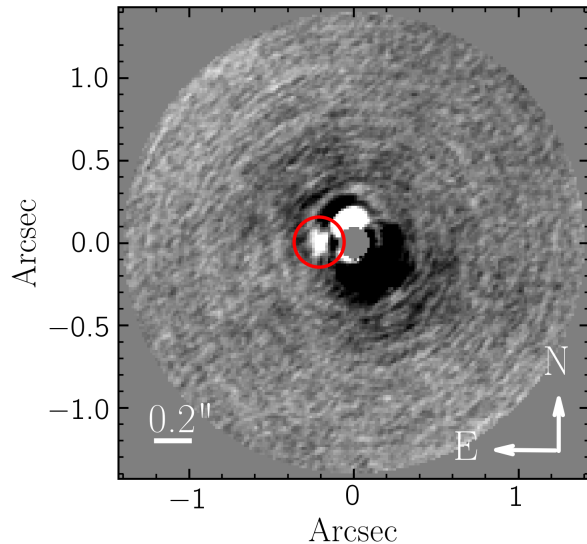


Figure 5.1: MKO L' KLIP-reduced image of HIP 67506 A from our Binary Differential Imaging survey described in [Pearce et al. \(2022\)](#). The central star is masked in the reduction, and the candidate signal is marked with a red circle $\sim 2''$ ($2.0 \lambda/D$) to the east. This was identified as a candidate signal due to the fact that it did not appear to smear azimuthally with derotation like the other residual structures at similar separation, and the other indications described in Section 5.2.1

the other residuals at that same separation points to the possibility of its being a true companion signal.

There are secondary indications of a companion to HIP 67506 A. Figure 5.2 shows a Gaia EDR3 BP minus RP vs absolute G magnitude color-magnitude diagram of Praesepe Cluster members identified in [Deacon and Kraus 2020](#) (orange), reproducing their Figure 4. Members they flagged as overluminous and with elevated astrometric noise in Gaia ERD3, indicating an unresolved companion, are marked with blue and purple triangles respectively. HIP 67506 A is marked with a red star in the main and inset axes. HIP 67506 A clearly falls on the overluminous region above the main sequence, indicating that the flux measured by Gaia is abnormally high for a single star, pointing to the presence of an unresolved stellar companion.

HIP 67506 A also has indicators of an unresolved companion in Gaia astrometry. The Gaia Renormalized Unit Weight Error (RUWE) is a signpost for unresolved companions. RUWE encapsulates all sources of error in the fit to the assumed single star astrometric model, corrected for correlation with source color and magnitude. $\text{RUWE} \approx 1$ is expected for a well-behaved so-

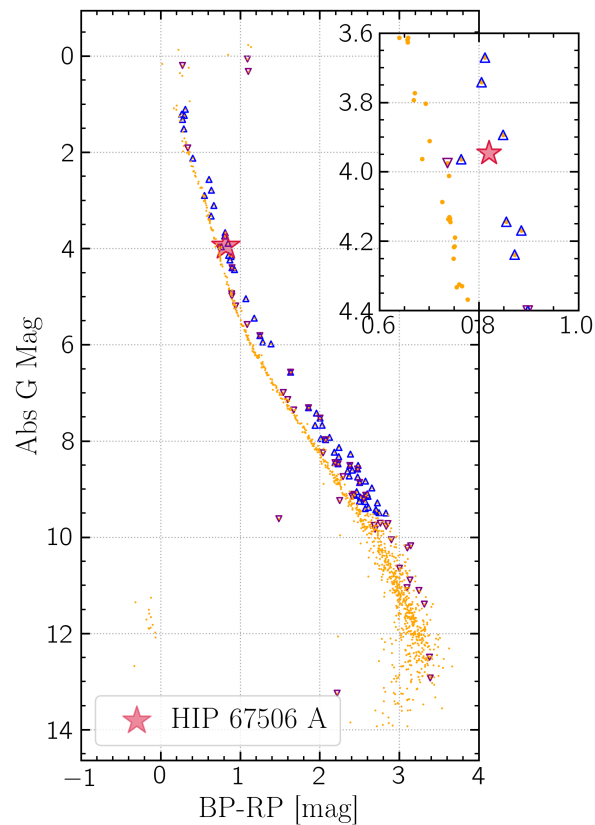


Figure 5.2: Gaia EDR3 BP minus RP vs absolute G magnitude color-magnitude diagram of Praesepe Cluster members identified in [Deacon and Kraus 2020](#) (orange). Objects they flagged as possible overluminous binaries are outlined in blue up-pointing triangles, and purple down-pointing triangles are objects they flagged with elevated astrometric noise, following their Figure 4. The position of HIP 67506 is marked with a red star in the main and inset axis, which shows a close view of the region surrounding HIP 67506 A. HIP 67506 A falls on the overluminous region above the main sequence, pointing to the presence of an unresolved stellar companion.

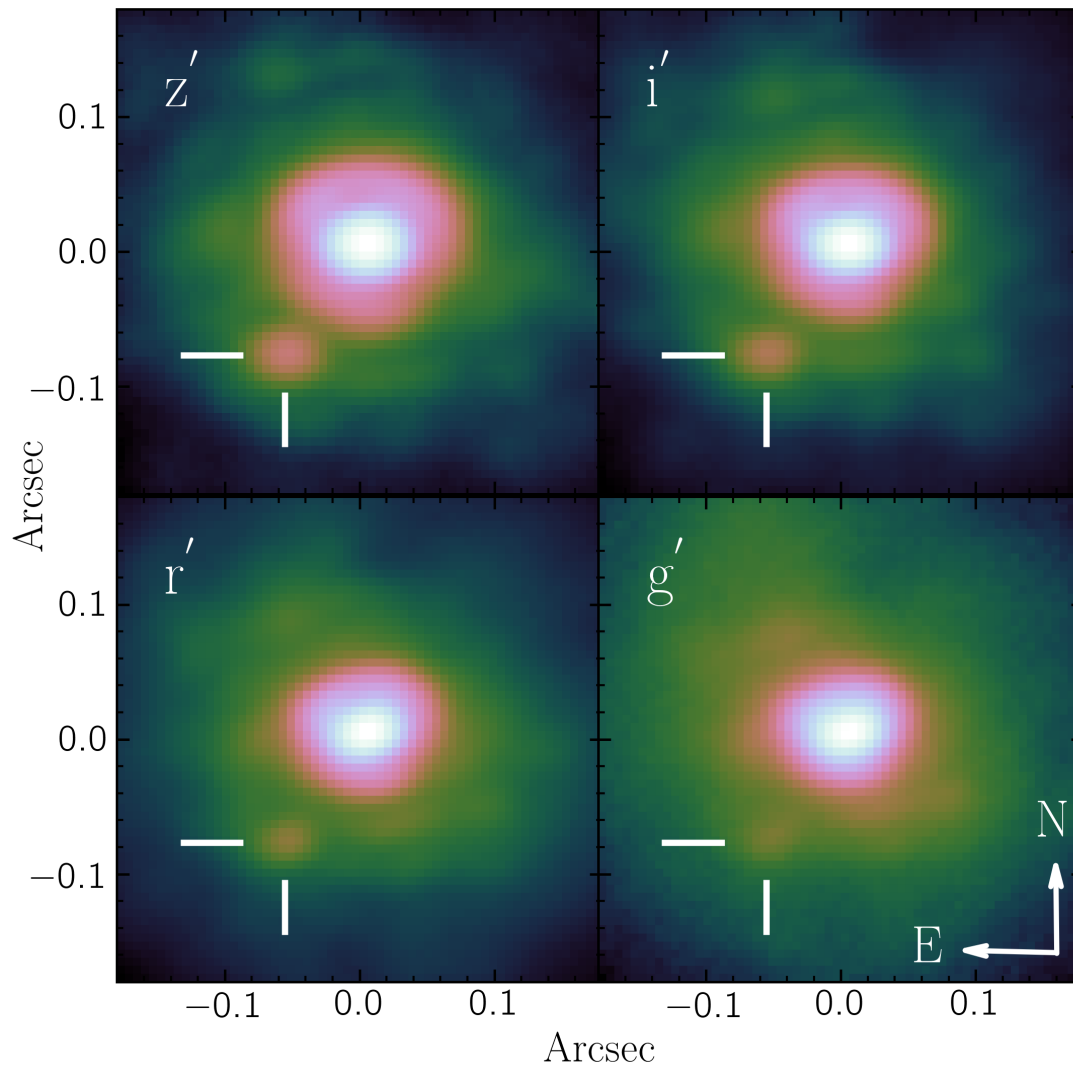


Figure 5.3: MagAO-X images of HIP 67506 A and HIP 67506 C in the four photometric filters g' , r' , i' , z' , shown with log stretch. HIP 67506 A is centered in each image, and HIP 67506 C, located 0.1" to the south east, is marked by the white pointers. North is up and East is left, and the stretch and spatial scale is same for each image.

Table 5.1: Multiplicity Metrics for HIP 67506 A

Metric	Value
Gaia	
RUWE	2.02
<code>astrometric_excess_noise</code>	0.22
<code>astrometric_excess_noise_sig</code>	75.16
<code>astrometric_chi2_al</code>	2277.97
<code>ipd_gof_harmonic_amplitude</code>	0.0099
<code>ipd_frac_multi_peak</code>	0
Hipparcos-Gaia Accelerations	
HGCA χ^2 (Brandt, 2021)	41
M_2 at 23AU from from PMa (Kervella et al., 2022)	270 M_{Jup}

lution (Lindgren, 2018b)¹. RUWE >2 indicates significant deviation from a single star model. HIP 67506 A has RUWE= 2.02 in Gaia EDR3, indicating that a companion is likely.

While RUWE is the most complete and easy to interpret metric (Lindgren, 2018b), other metrics in Gaia can probe multiplicity. Perturbations of the source photocenter (caused by orbiting unresolved objects) compared to the center-of-mass motion (which moves as a single star) will cause the observations to be a poor match to the fitting model, which registers as excess noise via the `astrometric_excess_noise` parameter, and whose significance is captured in the `astrometric_excess_noise_sig` parameter (>2 indicates significant excess noise). The `astrometric_chi2_al` term reports the χ^2 value of the observations to the fitting model, with lower values indicating better fit to observations. From the image parameter determination (IPD) phase, `ipd_gof_harmonic_amplitude` is sensitive to elongated PSF shapes relative to the scan direction (larger values indicate more elongation), and `ipd_frac_multi_peak` reports the percentage of observations which contained more than one peak in the windows².

Table 5.1 shows values of these metrics for HIP 67506 A. The IPD parameters are small and insignificant, suggesting that there are no marginally resolved sources ($\rho \sim 0.1\text{-}1.2''$, separation larger than the resolution limit but smaller than the confusion limit, Gaia Collaboration et al. 2021) present in the images, however the astrometric noise parameters are large and significant, affirming the presence of subsystems. This points to a companion near or below the resolution limit of $\approx 0.1''$.

¹<https://www.cosmos.esa.int/web/gaia/dr2-known-issues#AstrometryConsiderations>

²See https://gea.esac.esa.int/archive/documentation/GEDR3/Gaia_archive/chap_datamodel/sec_dm_main_tables/ssec_dm_gaia_source.html for complete description of Gaia catalog contents

Finally, HIP 67506 A also shows significant acceleration between the Hipparcos and Gaia astrometric measurements. The Hipparcos-Gaia Catalog of Accelerations (HGCA; [Brandt, 2021](#)) measures the change in proper motion between a star’s Hipparcos and Gaia proper motion measurements, as well as the positional difference between the missions, divided by the ~ 24 year time baseline, and quantifies the deviation from linear motion. This acceleration is called the proper motion anomaly (PMa). The HGCA shows a significant PMa for HIP 67506 A, with a $\chi^2 = 41$ for the goodness of fit of a linear proper motion to the measured astrometry. This points to unresolved subsystems causing acceleration.

Additionally, [Kervella et al. 2022](#) produced a PMa catalog for Hipparcos-Gaia EDR3 which also shows significant acceleration for HIP 67506 A (S/N = 9.31). They used the measured tangential velocity anomaly to constrain the mass of the object causing acceleration (which is degenerate with separation; [Kervella et al. 2019](#)). Using a mass of $1.3 M_{\odot}$ for HIP 67506 A, they estimate a companion of mass $180 M_{\text{Jup}}$ at 10 au causing the observed acceleration of HIP 67506 A. Extrapolating this out to the 2015 projected separation of HIP 67506 C (48 AU), the acceleration would be caused by a $\sim 400 M_{\text{Jup}}$ object. The position angle of the acceleration given in [Kervella et al. 2022](#) is $96.6 \pm 3.8^\circ$ for the 2016.0 Gaia epoch, which agrees within uncertainty with the candidate signal position angle in 2015.4, as would be expected if the candidate signal were the cause of the observed acceleration.

Combined with the candidate signal in our 2015 MagAO observation, these other lines of evidence point to a strong chance of this being a genuine companion signal which merited follow-up for confirmation and characterization.

5.3 Observations and Analysis

5.3.1 Observations

We observed HIP 67506 A on April 18th, 2022 with the extreme adaptive optics instrument MagAO-X ([Males et al., 2022](#)) on the 6.5m Magellan Clay Telescope at Las Campanas Observatory. We observed HIP 67506 A in four science filters: g' ($\lambda_0 = 0.527\mu\text{m}$, $\Delta\lambda_{\text{eff}} = 0.044\mu\text{m}$), r' ($\lambda_0 = 0.614\mu\text{m}$, $\Delta\lambda_{\text{eff}} = 0.109\mu\text{m}$), i' ($\lambda_0 = 0.762\mu\text{m}$, $\Delta\lambda_{\text{eff}} = 0.126\mu\text{m}$), and z' ($\lambda_0 = 0.908\mu\text{m}$,

Table 5.2: Stellar Properties of HIP 67506 A

Parameter	Previous Value	Ref	Our Value
Distance (pc)	102±86	1	221.6±1.8 ^a
Mass (M_{\odot})	1.2±0.1	2	1.2±0.2
Spectral Type	G5	3	F8–G2
T_{eff} (K)	6077 ± 150	4	6000±350
Luminosity (L_{\odot})	0.37 ± 0.07	4	1.91 ^{+0.28} _{-0.32}
Sloan $m_{g'}$	11.04±0.01	5	11.04±0.01
Sloan $m_{r'}$	10.66±0.01	5	10.67±0.01
Sloan $m_{i'}$	10.56±0.01	5	10.59±0.01
Sloan $m_{z'}$	10.50±0.01	5	10.55±0.01
Sloan g-r	0.38±0.02	5	0.37±0.02
Sloan r-i	0.11±0.02	5	0.09±0.02

- (1) [van Leeuwen 2007](#), (2) [Chandler et al. 2016](#),
(3) [Spencer Jones and Jackson 1939](#), (4) [McDonald et al. 2012](#),
(5) [Zacharias et al. \(2012\)](#), ^a[Gaia EDR3 Gaia Collaboration et al. \(2021\)](#)

Table 5.3: Properties of HIP 67506 C

Parameter	Value
Stellar Properties	
Spectral Type	K7–M2
T_{eff}	3600 ⁺²⁵⁰ ₋₃₅₀ K
log(L)	-1.17 ^{+0.06} _{-0.08} L_{\odot}
Sloan $m_{g'}$	16.7±0.1
Sloan $m_{r'}$	15.61±0.05
Sloan $m_{i'}$	14.45±0.04
Sloan $m_{z'}$	14.05±0.03
Sloan g-r	1.1±0.1
Sloan r-i	1.16±0.07
Astrometry	
2015-05-31	
Separation	240 ± 42 mas
Position Angle	85 ± 13 deg
2022-04-18	
Separation	100.9 ± 0.7 mas
Position Angle	145.1 ± 0.8 deg

$\Delta\lambda_{\text{eff}} = 0.130\mu\text{m}$)³. MagAO-X is equipped with two science cameras, so we carried out science observations in two filters simultaneously. The science camera EMCCDs were set to 5 MHz read-out speed with EM gain 100. Observations in r' , i' , and z' had exposure time 0.115 sec; g' had exposure time of 3 sec. We obtained dark frames of the same settings. The pixel scale is 6 mas pixel⁻¹ (Long et al. in prep), and the science and dark frames were 512×512 pixels (3"×3"). Seeing was stable at 0.4" throughout the observations.

We were unable to obtain observations of a photometric standard star. We observed HIP 67121 as a photometric standard, only to discover that it is itself a binary with separation too close to resolve but large enough to distort the shape of the PSF core. We performed all further analysis using HIP 67506 A as a photometric reference.

To reduce the raw images in each filter, we dark subtracted each science frame, registered each frame using PHOTUTILS DAOSTARFINDER (Bradley et al., 2020; Stetson, 1987) to find the peak of HIP 67506 A (uncertainty ± 0.05 pixels on peak finding) and SCIPY NDIMAGE (Virtanen et al., 2020) to center it, and rotated each frame to North up and East left (rotate CCW by telescope parallactic angle $+ 1.995 \pm 0.61$ deg, Long et al. in prep). Finally we summed the images in each filter to maximize the signal to noise ratio of the faint companion.

Figure 5.3 displays the final images in each science filter, shown with a log stretch. The companion, HIP 67506 C, is clearly visible at 0.1" to the south east, indicated by the white cross-hairs. The spacial scale and stretch are the same in each image. The companion signal was strongest in the z' filter.

5.3.2 MagAO-X Photometry

Measuring photometry. We obtained relative photometry for each filter with the following procedure. We estimated the background level by computing the median value in a wide annulus far from the star's halo (0.6"-1.2"). We used PHOTUTILS aperture photometry tools to sum all pixels in an aperture of radius $1\lambda/D$ centered on A, and subtracted the sum of pixels with the same aperture area valued at the background level, to estimate the flux from HIP 67506 A. To estimate the flux from HIP 67506 C we repeated the previous with an aperture of the same size centered at

³Filter specifications and filter curves can be found in the MagAO-X instrument handbook at <https://magao-x.org/docs/handbook/index.html>

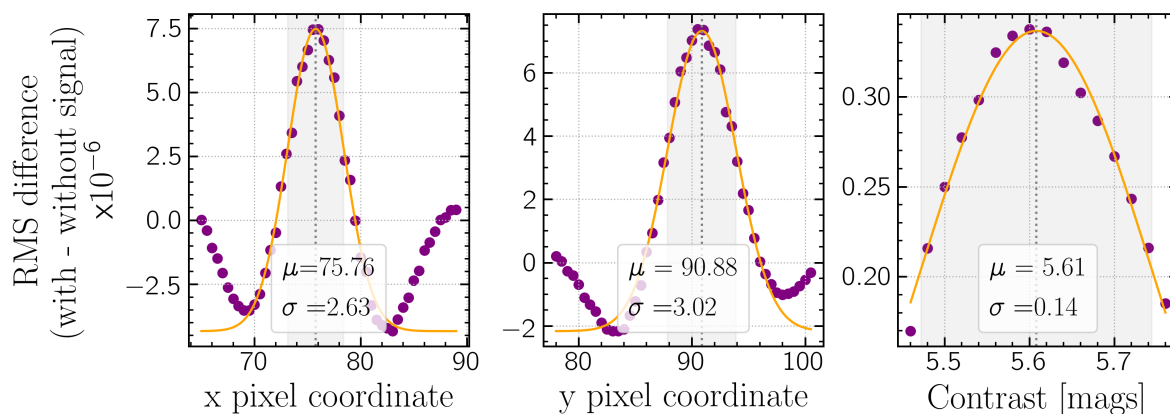


Figure 5.4: Results of our grid search of $[x, y, c]$ values for a model which minimizes HIP 67506 C residuals post-KLIP processing for the 2015 MagAO/Clio epoch. Each parameter is plotted versus the difference in RMS between KLIP-reduced image with and without the model subtracted. Each parameter was fit with a Gaussian function while keeping the others fixed at their peak value.

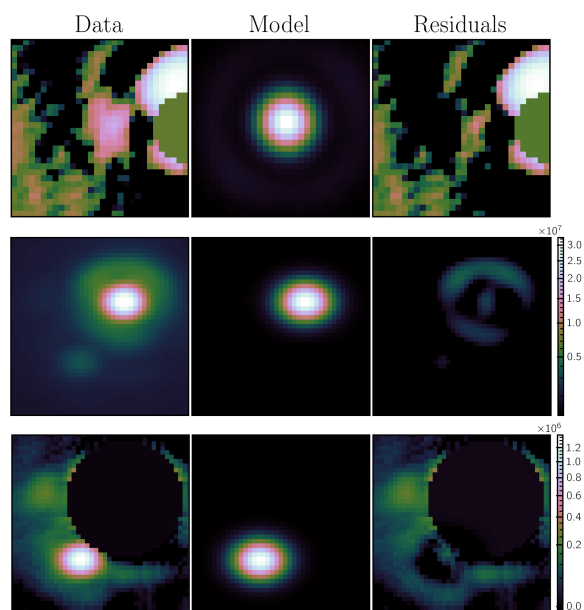


Figure 5.5: Top: Data, model, and residual of the $[x, y, c]$ that minimizes residuals in 2015 MagAO/Clio observation. Data and residual images are post-KLIP processing, and shown with a log stretch; model image shows the signal with peak values in Figure 5.4 that was subtracted from images prior to KLIP processing. Middle and bottom: Data, model, and residuals from the 2D Gaussian model in the 2022 MagAO-X z' image for HIP 67506 A (middle) and HIP 67506 C (bottom).

its location. We subtracted the mean background value from the image, computed a radial profile of the background subtracted image (excluding the region containing C), and used the flux at C's location in the radial profile to estimate the contribution from HIP 67506 A's halo at that location, and subtracted that as well. We converted the flux estimates into magnitudes and subtracted to obtain the contrast in MagAO-X filters.

Uncertainty. To estimate the uncertainty in the photometry measurements, we used the method of Mawet et al. 2014 for estimating signal to noise ratio in the regime of small number of photometric apertures, as we have at the separation of HIP 67506 C. At the separation HIP 67506 C, there are $N = 2\pi r$ resolution elements of size λ/D (the characteristic scale of speckle noise), where $r = n\lambda/D$ and n varies with the filter wavelength. We defined a ring of $N-3$ resolution elements (neglecting those at and immediately to each side of HIP 67506 C) at separation r with radius $0.5\lambda/D$, then applied Eqn (9) of Mawet et al. (2014), which is the Student's two-sample t-test:

$$p(x, n_2) = \frac{\bar{x}_1 - \bar{x}_2}{s_2 \sqrt{1 + \frac{1}{n_2}}} \quad (5.1)$$

where $\bar{x}_1 =$ HIP 67506 C flux, $\bar{x}_2 = \text{mean}[\Sigma(\text{pixels in apertures})]$, $s_2 = \text{stdev}[\Sigma(\text{pixels in apertures})]$, $n_2 = N-3$, and $S/N = p$. The denominator of that equation is the noise term. We repeated this procedure for HIP 67506 A, defining a ring of apertures beyond the halo of both stars to estimate the background noise.

Applying the standard. We used HIP 67506 A as the photometric standard star, however literature photometry for HIP 67506 A consisted of a blend of flux from HIP 67506 A and HIP 67506 C, since it was previously unresolved. To use HIP 67506 A as a standard we used our measured contrasts to separate the flux contributions from both stars. First we computed color transformations for MagAO-X filters to Sloan prime system filters using MagAO-X filter curves, public Sloan Digital Sky Survey transmission curves⁴, and a spectral type G5V model from the Pickles Atlas (Pickles, 1998)⁵. We obtained published photometry for HIP 67506 A, displayed in Table 5.2, from the UCAC4 catalog (Zacharias et al., 2012) and converted to MagAO-X filters using our color transformation. We then computed the magnitude of HIP 67506 A and HIP 67506 C in the

⁴<http://classic.sdss.org/dr3/instruments/imager/#filters>

⁵MagAO-X to SDSS color transformations for all spectral types can be found in the MagAO-X instrument handbook

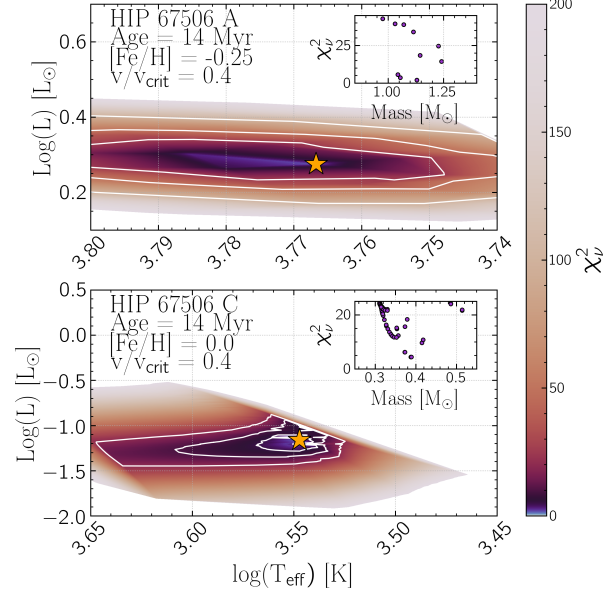


Figure 5.6: The lowest χ^2 of all MIST model fits occurred for age ~ 14 Myr when ages were constrained to be the same for both objects. This figure shows the map of the reduced χ^2 surface in $\log(T_{\text{eff}})$ and $\log(L)$ for HIP 67506 A (top) and HIP 67506 C (bottom) for age = 14 Myr and the best-fitting values of metallicity and rotation for each. The lowest reduced χ^2 value for each is marked with an orange star. Contours denote $\chi^2 = 25, 50,$ and 100 . Inset axis: χ^2 of model versus model star mass for fits of models with age = 14 Myr. The lowest χ^2 values occurred at $M_A = 1.13 M_{\odot}$ and $M_C = 0.39 M_{\odot}$.

MagAO-X system as:

$$A_{\text{Flux}} + C_{\text{Flux}} = F_{0,\text{Vega}} \times 10^{-0.4 \times \text{Total mag in MagAO-X system}} \quad (5.2)$$

$$C_{\text{Flux}} = A_{\text{Flux}} \times \text{Flux Contrast} \quad (5.3)$$

$$A_{\text{Flux}} \times (1 + 10^{-0.4 \times \text{mag Contrast}}) = F_{0,\text{Vega}} \times 10^{-0.4 \times \text{Total mag}} \quad (5.4)$$

We then converted flux of A and C into the Sloan system using color transformation, displaying in Tables 5.2 and 5.3.

5.3.3 Astrometry

Relative Astrometry Measurements

The 2015 MagAO/Clio L' epoch and 2022 MagAO-X epoch give relative astrometry spanning a 7 year baseline.

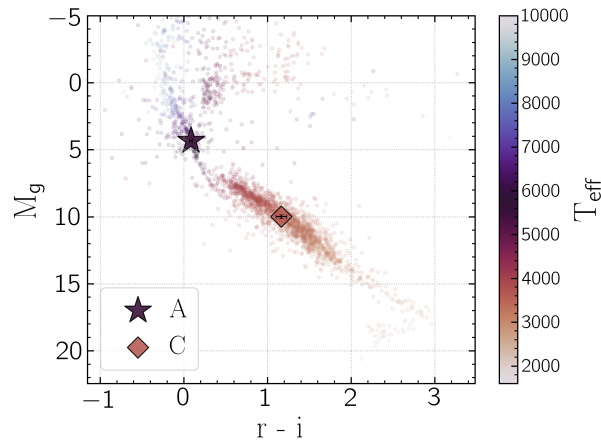


Figure 5.7: Color-magnitude diagram (CMD) of Sloan $r'-i'$ vs. Sloan g' absolute magnitude. Points are photometry from the CARMENES sample of well-characterized M- and L dwarfs (Cifuentes et al., 2020) and a selection of Hipparcos stars with SDSS photometry and T_{eff} estimates from McDonald et al. 2012. Our photometry of HIP 67506 A (star) and HIP 67506 C (diamond) and uncertainties (black errorbars) are overplotted. A and C are colored according to the T_{eff} of the best-fit MIST model shown in Figure 5.6. The best-fitting MIST models correspond to T_{eff} values consistent with nearby objects on the CMD.

The 2015 epoch. The companion signal has been corrupted by the BDI KLIP algorithm – it is no longer a recognizable PSF shape, and in Pearce et al. 2022 we estimated a smaller flux than we measure in this work. The companion signal has been subject to over-subtraction by KLIP, and is not reliable for estimating photometry and astrometry (Soummer et al., 2012; Pueyo, 2016).

To estimate the position of the companion, we performed a grid search of the parameters which influence the signal strength in post-processing, similar to Morzinski et al. (2015) Appendix E. For a grid of $[x, y]$ pixel position and contrast c , we injected a negative signal, modeled from the PSF of a median image of the HIP 67506 B 2015 dataset, into each HIP 67506 A image. We then performed KLIP reduction via the method in Pearce et al. 2022 and measured the root-mean-square (RMS) of pixels in a circle of radius $1.5\lambda/D$ (~ 11 pixels) centered at the location of the companion signal.

Figure 5.4 displays the grid search results for the x-pixel coordinate (left), y-pixel coordinate (middle), and contrast (right) versus the difference in RMS between the reduced image with and without the injected signal. We fit a Gaussian to each parameter, while keeping the other parameters fixed at their best value, and took the mean and standard deviation as the best modeled parameter.

Figure 5.5 (top) shows the unsubtracted, KLIP-reduced image of HIP 67506 C (left, same as Figure 5.1, log stretch), the best value model from Figure 5.4 (middle, linear stretch), and the residuals post-KLIP with that model subtracted from each image pre-KLIP (right, log stretch). With HIP 67506 A registered at $[x, y] = [89.5, 89.5]$ (origin is lower left), we find: $\bar{x} = 75.76 \pm 2.63$ pixels, and relative separation $\rho_x = 218 \pm 42$ mas; $\bar{y} = 90.88 \pm 3.02$ pixels, $\rho_y = -22 \pm 48$ mas; total separation and position angle is $\rho = 240 \pm 42$ mas, $\theta = 85 \pm 13$ deg.

The 2022 epoch. We measured the relative astrometry in the MagAO-X z' image following a modified version of the method described in Pearce et al. (2019) and Pearce et al. (2021). We modeled the PSF core as a simple 2-dimensional Gaussian function and varied the model parameters using the python Markov Chain Monte Carlo package EMCEE (Foreman-Mackey et al., 2013) with 100 walkers. Our model had seven parameters: x, y subpixel position (Gaussian prior with $\mu =$ center from DAOSTarFinder, $\sigma = \text{FWHM}/2.35$, $\text{FWHM} = 1\lambda/D$ at $z' = 0.03''$), amplitude (Gaussian prior with $\mu =$ peak from DAOSTarFinder, $\sigma =$ Poisson noise), background level (Gaussian prior with $\mu =$ mean background level, $\sigma =$ background noise), Gaussian width in the x and y direction (Gaussian prior with $\mu = \text{FWHM}/2.35$, $\sigma = 0.01$), and rotation relative to x axis (Uniform prior on $[0, \pi/2]$). The chains converged quickly and we found that 5000 steps was sufficient for chains to converge (Gelman-Rubin statistic < 1.2 for all parameters), with a burn-in of 1000 steps.

We computed the model fit for the location of HIP 67506 A and HIP 67506 C in the 2022 z' image, where HIP 67506 C's signal was strongest. The data, model, and residuals for the two measurements are shown in Figure 5.5 (middle and bottom). We used the MagAO-X astrometric solution (Long et al., in prep)⁶ to compute $[\rho \text{ (mas)}, \theta \text{ (deg)}]$ for each $[\Delta x, \Delta y]$ (pixels) between A and C in the MCMC chains, then took the mean and standard deviation as the $[\rho, \theta]$ for the 2022 epoch. Detector distortion is negligible at $0.1''$ (Long et al. in prep). We find $\rho = 100.9 \pm 0.7$ mas, $\theta = 145.1 \pm 0.8$ deg.

⁶Available in the MagAO-X instrument handbook, <https://magao-x.org/docs/handbook/>

5.4 Results

5.4.1 Photometry

We compared our magnitudes in the Sloan filter system with synthetic photometry from two stellar evolution grids, the Mesa Isochrones and Stellar Tracks (MIST, [Dotter, 2016](#); [Choi et al., 2016](#); [Paxton et al., 2011, 2013, 2015](#)), and stellar tracks and isochrones with the Padova and Trieste Stellar Evolution Code (PARSEC, [Bressan et al., 2012](#)).

We used our absolute g' , r' , i' , and z' SDSS magnitudes for HIP 67506 A and HIP 67506 C as well as $g'-r'$ and $r'-i'$ colors for evaluating which models in each grid best describe our observations. For each isochrone set we minimized the χ^2 of the synthetic photometry to our data as

$$\chi^2 = \sum \left(\frac{M_{x,\text{obs}} - M_{x,\text{model}}}{M_{x,\text{uncert}}} \right)^2 \quad (5.5)$$

where M_x is the absolute magnitude in a given filter or Δ magnitude in a color. We imposed the constraint that the age must be the same for HIP 67506 A and HIP 67506 C, and computed the final goodness of fit as $\chi^2 = \chi_A^2 + \chi_C^2$.

We obtained the MIST⁷ isochrone synthetic photometry in the SDSS ugriz system with rotation rate $v/v_{\text{crit}} = 0.0$ and 0.4 , $[\text{Fe}/\text{H}] = [-4.00, -2.00]$ in 0.50 dex steps and $[\text{Fe}/\text{H}] = [-2.00, +0.50]$ in 0.25 dex steps, and $\log(\text{Age}) = [5.0, 10.3]$ in 0.05 dex steps.

For MIST isochrone χ^2 minimization, we determine $T_{\text{eff}} = 6000 \pm 350$ K and $\log(L) = 0.28_{-0.08}^{+0.06} L_{\odot}$ for HIP 67506 A, $T_{\text{eff}} = 3600_{-350}^{+250}$ K and $\log(L) = -1.17_{-0.08}^{+0.06} L_{\odot}$ for HIP 67506 C.

Figure 5.6 shows the reduced χ^2 surface for $\log(T_{\text{eff}})$ and $\log(L)$ for the overall lowest χ^2 MIST isochrone ($\chi^2 = 36.7$), with age = 14 Myr, rotation $v/v_{\text{crit}} = 0.4$, and $[\text{Fe}/\text{H}] = 0.25$ for A and $[\text{Fe}/\text{H}] = 0.0$ for C. Values of $\log(T_{\text{eff}})$ are not well constrained for A, spanning from $\log(T_{\text{eff}}) \sim 3.76$ – 3.78 (5700–6000K). The insets in Figure 5.6 display reduced χ^2 as a function of mass at 14 Myr, with the best fitting values occurring at $M_A = 1.1 M_{\odot}$, $M_C = 0.4 M_{\odot}$. A second local minimum ($\chi^2 = 39.2$) occurred at age = 5.6 Gyr, $M_A = 1.1 M_{\odot}$, and $M_C = 0.65 M_{\odot}$. (A plot of χ_{min}^2 as a function of age is included in the supplementary material.)

⁷Accessed from https://waps.cfa.harvard.edu/MIST/model_grids.html

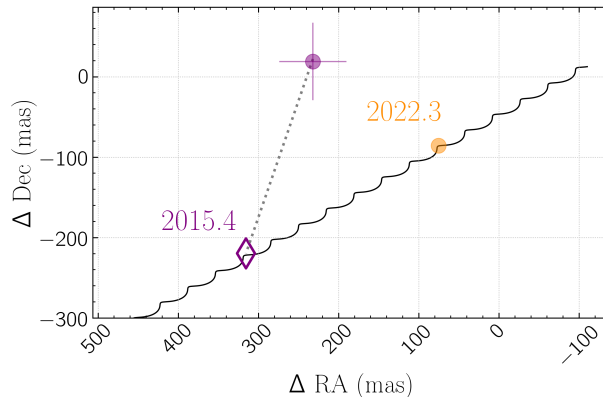


Figure 5.8: Relative astrometry of HIP 67506 C relative to A for the MagAO 2015 epoch (purple) and the MagAO-X 2022 epoch (orange). The abscissa and ordinate axes display position of HIP 67506 C relative to A in mas in right ascension (RA) and declination (Dec). The motion of a non-moving background object at the position of HIP 67506 C is given by the black track; the predicted position in 2015, given then 2022 position, is an open diamond. The observed position and uncertainty in each epoch is shown as filled circles (uncertainties are smaller than the marker for the 2022 epoch). The observed motion of the HIP 67506 C is not consistent with a background object, and is likely due to orbital motion.

We used PARSEC version 1.2S⁸ with the YBC bolometric correction library (Chen et al., 2019) and revised Vega SED from Bohlin et al. (2020), and retrieved isochrone tables from $\log(\text{age}) = [6.0, 10.13]$ dex in intervals of 0.1 dex and metallicities $[M/H] = [-4.0, 0.5]$ dex in intervals of 0.5 dex, with synthetic photometry in the SDSS ugriz system. For PARSEC isochrone χ^2 minimization, we determine $T_{\text{eff}} = 6000 \pm 350$ K and $\log(L) = 0.29^{+0.06}_{-0.08} L_{\odot}$ for HIP 67506 A, $T_{\text{eff}} = 3600^{+250}_{-350}$ K and $\log(L) = -1.18^{+0.06}_{-0.08} L_{\odot}$ for HIP 67506 C. Our photometry was insufficient to place meaningful constraints on the age of either star.

Figure 5.7 shows a color-magnitude diagram of SDSS r-i color vs. SDSS g absolute magnitude. HIP 67506 A (purple star) and HIP 67506 C (orange diamond) are plotted with our photometry and colored according to our isochrone-derived T_{eff} estimates. Also plotted are reference stars from the CARMENES sample of well-characterized M- and L dwarfs (Cifuentes et al., 2020) and a selection of Hipparcos stars with SDSS photometry and T_{eff} estimates from McDonald et al. 2012. Our colors and temperature estimates are consistent with the reference stars. We estimate the spectral type of HIP 67506 A and HIP 67506 C to be $\text{SpT}_A \approx \text{F8V-G2V}$ and $\text{SpT}_C \approx \text{K7V-M2V}$.

⁸Accessed from <http://stev.oapd.inaf.it/cgi-bin/cmd>

5.4.2 Astrometry

Figure 5.8 displays a common proper motion plot of HIP 67506 C relative to HIP 67506 A. We show the observed separation of HIP 67506 C in right ascension and declination for the 2015 and 2022 epochs (filled circles and error bars), the expected track if HIP 67506 C were a non-moving background object (zero proper motion; black track), and the predicted position of HIP 67506 C at the 2015 observation if it were a background object (open diamond). The observed position of HIP 67506 C does not follow the expected motion for a distant background object. We infer that the relative motion of HIP 67506 C is more consistent with a bound object than an unassociated object. This is supported by the large proper motion anomaly of HIP 67506 A.

Using the two position angles of Table 5.3, we determined that the position angle of HIP 67506 C at the Gaia epoch of 2016.0 was $90 \pm 12^\circ$, which agrees with the proper motion anomaly vector PA at the Gaia epoch of $96.6 \pm 4.1^\circ$ (Kervella et al., 2022).

Our astrometry was insufficient to meaningfully constrain the orbit or dynamical mass, due to there being only two astrometric points and large error bars on the 2015 epoch.

5.5 Conclusion

We have shown that HIP 67506 A has a previously unknown 0.1'' companion, originally detected in 2015 with MagAO/Clio and BDI in L' . The shape was distorted from a typical PSF due to post-processing, and might have been easily dismissed with the other residuals at that radius. However several secondary indications hinted that the dubious candidate companion signal for HIP 67506 A in Pearce et al. (2022) was a strong candidate and merited follow-up observations: the poor Gaia astrometric signal, the significant PMa with the right acceleration vector angle, and the overluminosity of the Gaia photometry. Our analysis in Pearce et al. 2022 pointed to a possible high mass brown dwarf. We followed up in 2022 with MagAO-X and the companion was immediately and easily detected and determined to be a low mass star. The low S/N signal of HIP 67506 C at such a small IWA was bolstered by secondary indicators, which turned out to be powerful predictors of the genuine companion. We estimate HIP 67506 A and HIP 67506 C to be type F8–G2 and K7–M2 respectively. Further astrometric and photometric measurements are required to constrain properties and orbital elements.

Chapter 6

The ExAO Pup Search I: Five New (Candidate) Sirius-Like WD+MS Star Systems

“Any faith that admires truth, that strives to know
God, must be brave enough to accommodate the
universe.”

Carl Sagan

Contact

6.1 Introduction

6.1.1 White Dwarf Pollution and Wide Stellar Companions.

In the Milky Way $\sim 95\%$ of stars will become white dwarfs (Althaus et al., 2010). White dwarfs (WDs) are excellent laboratories for study of exoplanetary material compositions as their extreme gravity causes elements to quickly stratify, with heavier elements sinking to the core, typically retaining only hydrogen and/or helium in their photospheres (Schatzman, 1958; Koester, 2009; Althaus et al., 2010; Koester, 2013). Around 30–50% of WDs show metal lines in their photospheric spectra (Zuckerman et al., 2003; Koester, 2009; Zuckerman et al., 2010; Wilson et al., 2019). The source of this “pollution” has been well established to be from tidally disrupted planetary material rather than other sources such as the interstellar medium (Jura, 2008; Zuckerman et al., 2010). Pollution has shown evidence of asteroid-like material, material from differentiated (core/crust) bodies, icy bodies, and material chemically similar to the inner solar system (Zuckerman et al., 2007; Gänsicke et al., 2012; Farihi et al., 2013). The debris-disk hosting WD 1145+017 was found to also host at least one minor planet in the process of disintegrating (Vanderburg et al., 2015).

Yet the reservoir of pollution material has been difficult to observe. Over 40 WDs are known to host dusty debris disks (Farihi, 2016), some of which also contain gas (Gänsicke et al., 2006, 2008; Farihi et al., 2012; Melis et al., 2012; Wilson et al., 2014; Manser et al., 2016), and which formed after the main sequence and giant branch phases (Veras et al., 2018). Every known WD debris disk orbits a polluted white dwarf, however confusingly only a small fraction of polluted WDs are known to host debris disks; Wilson et al. (2019) measured a pollution fraction of $45 \pm 4\%$ but only $1.5^{+1.5}_{-0.5}\%$ of WDs had measurable IR excess.

Given the short sinking times of most WDs, we expect pollution levels $\lesssim 0.1\%$ (Veras et al., 2016), but given that we see pollution fractions of 30–50%, accretion must be ongoing or very recent. Tidal disruption with subsequent deposition onto the surface of the white dwarf first requires perturbation of a body’s orbit into a high-eccentricity orbit with a pericenter within the tidal disruption radius of the star – the Roche radius, typically $\sim 1 R_{\odot}$ (~ 0.01 AU, Fulton et al. 2014) – where it is subsequently broken down into smaller pieces which eventually grind down into dust and eventually deposit on the surface (Brouwers et al., 2022). Mechanisms for perturbing material onto star-grazing orbits, however, are not well tested observationally. Post-main sequence

mass loss can drive orbital evolution and instability for planets which survive engulfment (Debes and Sigurdsson, 2002). The presence of a giant planet during mass loss pushes planetesimals into mean-motion resonances (Bonsor et al., 2011; Debes et al., 2012; Frewen and Hansen, 2014; Antoniadou and Veras, 2016), secular resonances (Smallwood et al., 2018; O'Connor et al., 2022), or planet-planet scattering (Payne et al., 2016).

However such single-star mechanisms for driving pollution (post-MS mass loss, giant planet influences) predict a steep drop-off of mass accretion rate with white dwarf cooling time, which is not supported by observations, and fails to account for pollution seen at Gyr cooling ages (e.g. Koester and Wilken, 2006; Koester et al., 2014; Wyatt et al., 2014). Approximately three-quarters of WDs with a binary companion are wide enough for the WD progenitor to evolve independently from the companion and avoid a common envelope stage (Willems and Kolb, 2004), and the orbit expands even wider as the progenitor evolves off the main sequence and loses mass. A wide binary stellar companion presents one possible mechanism for driving WD accretion independent of cooling age. The companion may be perturbed into highly eccentric orbits by stellar flybys, supernovae, and the influence of the Galactic gravitational tide (Heisler and Tremaine, 1986; Brassier, 2001; Fouchard et al., 2006; Veras and Evans, 2013; Veras et al., 2014; Kaib et al., 2013; Correa-Otto et al., 2017; Hamers, 2018; Bazsó and Pilat-Lohinger, 2020), perturbing material onto star-grazing orbits on close periastron passages (Bonsor and Veras, 2015). Companion-induced von Zeipel-Kozai-Lidov (vZ-K-L) (von Zeipel, 1910; Kozai, 1962; Lidov, 1962) oscillations can push bodies into high eccentricity and star-grazing orbits (Hamers and Portegies Zwart, 2016; Mustill et al., 2022). Secular resonances can arise even in binaries wider than 1000 AU if a giant planet is present around the primary (Bazsó and Pilat-Lohinger, 2020; Petrovich and Muñoz, 2017; Mustill and Villaver, 2012). The presence of a main sequence companion may also facilitate 2nd and even 3rd generation planet formation around the WD (Perets, 2011).

If the companion is influencing pollution, then we should expect a higher fraction of polluted WDs in binaries than for a random sample of WDs. Zuckerman (2014) examined 38 WDs with common proper motion companions from literature and found no measurable difference in fraction of polluted vs not polluted WDs in WD+MS wide binary systems (WDMS), although this study was hampered by small sample size. Additionally they excluded any systems with semi-major axis < 120 AU, and their closest separation system was $3.7''$. Wilson et al. (2019) also examined the

frequency of pollution in single vs binary WDs using UV metal lines for pollution and IR excess for disks. Their sample from literature included 196 single and 38 WDs in binaries, of which 22 were resolved in *Gaia* or *Spitzer* IRAC images, and was limited to WDs with cooling age 9–300 Myr. They found that for 15 WDs in wide binaries, none exhibited measurable IR excess in *Spitzer*, and that for 40 known polluted WDs with IR excess, none had wide companions in *Gaia*, and concluded that companions can't be involved in material delivery to the WD. However this study is limited to the IR excess detection limits of *Spitzer* and the companion resolution limit of *Gaia*. [Noor et al. \(2024\)](#) used *Gaia* DR3 to draw a large sample of polluted WDs from literature and searched for common proper motion companions, and compared it to the occurrence of companions for random selection of WDs in *Gaia* DR3 from 9 Myr – 8 Gyr. They used the simplifying assumptions that projected separation = semi-major axis, and $\Delta PM = \Delta v_{orb}$, and so don't consider the effects of a non-circular, non-face-on orbit (a likely condition given the probability of wide companions being perturbed, e.g. [Kaib et al. 2013](#)). Additionally they made use of the *Gaia* RUWE parameter < 1.4 ([Lindgren et al., 2021](#)) as indication of lack of any other companions in the system, a reasonable assumption but not a definitive indication of lack of additional companions, especially companions wider than $\sim 0.5''$. This study provided a large sample size spanning a wide age range, however was limited to only objects resolved in *Gaia*, with its magnitude limit of 20 mags and its resolution limit of $0.5\text{--}1''$ ([Lindgren et al., 2021](#)). They also concluded that a wide companion has no influence on pollution. To date no studies have looked at the orbital parameters of polluted and non-polluted WDMS systems.

While the roll of wide companion plays in pollution is starting to look negligible, there is still room in the parameter space meriting continued exploration. The majority of known WDMS systems are WD companions to M-dwarf stars. WD companions are easier to find around M dwarfs where the WD-M dwarf contrasts are very low and the WD dominates the blue end of the system SED. For earlier type stars (AFGK spectral types), the WD companion signal can be drowned out by the brighter, bluer (compared to M stars) MS star signal. WD companions to such so-called “Sirius-like Systems” (SLS; [Holberg et al. 2013](#), hereafter H13) are rare compared to evolutionary predictions (50-60% of F–B stars are binaries yet only $32 \pm 8\%$ are observed, [Holberg 2009](#); [Ferrario 2012](#)), indicating many WD companions are likely being missed in the glare of their brighter hosts, particularly if they are close enough to be unresolvable in imaging. The surveys

described above targeting SLS were typically limited to separations $\gtrsim 1''$ (see Section 6.4.1). Surveys targeting more massive AGK type stars at closer separations will continue to fill in the WDMS population parameter space.

6.1.2 *The ExAO Pup Search: Extreme AO and WD Pollution*

The new generation of ground-based, extreme adaptive optics (ExAO) high contrast imaging instrumentation is well suited to push this to closer separations and probe SLS systems. ExAO instruments are designed to work at high contrasts (10^{-6} and greater) and close angular resolutions (\mathcal{O} 10's – 100's of mas) for direct detection of exoplanets. Close WD companions will have much lower contrasts (\mathcal{O} 10^{-3} – 10^{-4}), enabling relatively simple detection.

We are leveraging the power of the new ExAO instrument MagAO-X (Males et al., 2022) towards these problems with a survey called TheExAO Pup Search: The extreme AO non-interacting white dwarf-main sequence binary system survey¹. The Pup Search has three main objectives:

1. Detect new non-interacting WDMS binary systems with ExAO instruments MagAO-X (and eventually SCExAO) and observe new systems for pollution with high-resolution spectroscopy in the near UV with HST and/or Keck/HIRES.
2. Determine pollution rates for WDMS systems compared to single WDs, and as a function of cooling age and compare to estimates such as Veras et al. (2018)
3. Monitor orbits of new and previously known resolved WDMS system to determine prevalence of high-eccentricity orbits of MS companions for polluted WDs and compare to estimated orbital parameters for the binary to be influencing pollution, such as those in Stephan et al. 2017 and Veras et al. 2017 Fig 3.

We observed an initial set of Pup Search targets in 2022 and 2024, and detected 5 new WDMS star system candidates, 2 new stellar binaries, and one candidate companion of undetermined nature. In this work we report the design of the Pup Search and present the initial detection and photometry of new WD candidate companions. In Section 6.2 we describe the Pup Search target

¹The name is a reference to the first known wide White Dwarf- Main Sequence system, Sirius AB discovered in 1844 by Friedrich Bessel when he observed changes in the proper motion of Sirius (Bessel, 1844), first observed by Alvin Graham Clark (Flammarion, 1877), and confirmed as the second ever known WD via its spectrum obtained by Walter Adams (Adams, 1915). Since Sirius A is the “Dog Star”, Sirius B was nicknamed “The Pup”

selection, recent observations, and data reduction. In Section 6.3 we report new confirmed and candidate signal detections, non-detections, and contrast curves. In Section 4 we discuss implications of these new detections in the wider WDMS picture and the future of the Pup Search.

6.2 Observations

6.2.1 Target Selection

Our Pup Search targets are drawn from the catalog produced by the White Dwarf Binary Pathways Survey (Parsons et al., 2016) in Ren et al. 2020 (hereafter R20). The White Dwarf Binary Pathways Survey is interested in post-common envelope WDMS systems (PCEB). They measured radial velocities of 275 WD+AFGK candidates identified from TGAS (Tycho-Gaia Astrometric Solution, Michalik et al. 2015), Gaia DR2 (Gaia Collaboration et al., 2016, 2018), and GALEX (Bianchi et al., 2017) UV excess, 151 of which have ≥ 2 RV observations, and selected 23 candidate systems most likely to be close PCEBs based on RV variation. Thus they produced a well-vetted catalog of 128 candidate WD+AFGK systems with wider separations potentially accessible to ExAO. From those 128 we selected 84 which were not identified as spectroscopic binaries in Simbad (Wenger et al., 2000) and for which the MS star is bright enough for ExAO (*Gaia* G magnitude < 11).

Figure 6.1 (bottom) shows a *Gaia* color-magnitude diagram of our 84 target MS star candidate WD companion hosts. All of our targets fall within the AFGK region of the CMD, and approximately 60% fall in the giant branch region, estimated as the region outlined in blue in Figure 6.1. To prioritize targets we use the star’s *Gaia* renormalized unit weight error (RUWE, Lindgren 2018b) as a guide for multiplicity. RUWE encapsulates in a single number all deviation from *Gaia*’s assumed singly star model, and $\text{RUWE} \gtrsim 1.2$ could indicate multiplicity within the range of *Gaia*’s sensitivity (Belokurov et al., 2020; Andrew et al., 2022; El-Badry, 2024).

6.2.2 Imaging Data

We observed 5 Pup Search targets in 2022 and 14 in 2024 with the ExAO instrument MagAO-X (Males et al., 2022) on the 6.5m Magellan Clay Telescope at Las Campanas Observatory in Chile. MagAO-X is equipped with four broadband science filters: g' ($\lambda_0 = 0.527\mu\text{m}$, $\Delta\lambda_{\text{eff}} = 0.044\mu\text{m}$), r'

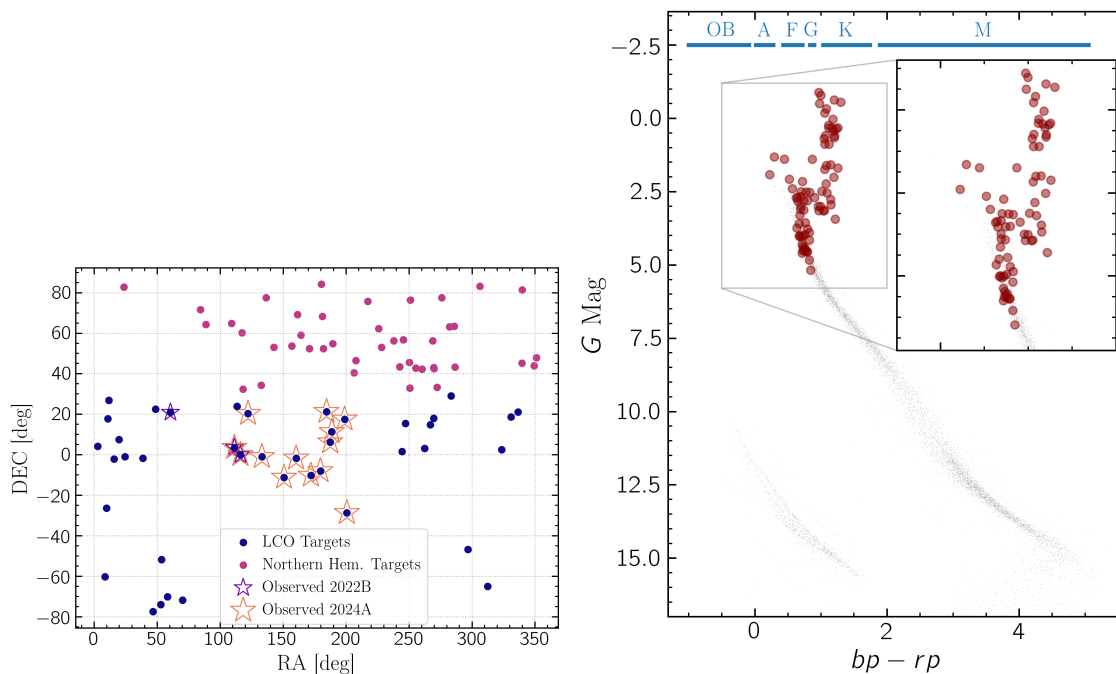


Figure 6.1: Left: Pup Search targets in RA/Dec. Targets accessible to MagAO-X from Las Campanas Observatory are plotted in blue, targets accessible to northern hemisphere instruments are in magenta. Targets outlined by the purple star were observed in fall 2022, and the yellow star in spring 2024. Right: Pup Search targets color magnitude diagram in *Gaia* absolute G magnitude vs *Gaia* $bp - rp$ color. The red points mark the 84 wide candidate WDMS systems identified in Sec 6.2.1. The grey points are the 10,000 nearest high-quality solutions ($ruwe < 1.1$) in *Gaia* DR3, with approximate spectral type ranges marked in blue (adapted from the spectral type-color relations in Pecaut and Mamajek 2013). The inset axis shows a zoomed view of the region of interest. The blue region marks the approximate location of the giant branch. All of our target MS stars fall within the AFGK region, and $\sim 60\%$ are in the giant star region.

($\lambda_0 = 0.614\mu\text{m}$, $\Delta\lambda_{\text{eff}} = 0.109\mu\text{m}$), i' ($\lambda_0 = 0.762\mu\text{m}$, $\Delta\lambda_{\text{eff}} = 0.126\mu\text{m}$), and z' ($\lambda_0 = 0.908\mu\text{m}$, $\Delta\lambda_{\text{eff}} = 0.130\mu\text{m}$)² and two science cameras, so we carried out science observations in two filters simultaneously. The pixel scale is $5.9 \text{ mas pixel}^{-1}$ (Long et al. submitted), and the science and dark frames were 1024×1024 pixels ($6'' \times 6''$).

The science camera EMCCDs were set to 5 MHz readout speed with EM gain 100. Observations in r' , i' , and z' had exposure time 0.115 sec; g' had exposure time of 3 sec. We obtained dark frames of the same settings. Seeing was stable at $0.4''$ throughout the observations.

December 2022

Conditions in 2022 were variable and we were only able to obtain usable images for 3 of the 2022 targets (TYC 4831-473-1, TYC 169-1942-1, and TYC 1262-1500-1). All targets were observed in i' and r' simultaneously with the science camera EMCCDs set to 5 MHz readout speed with EM gain chosen based on conditions to maximize potential companion signal without saturating host star, and is tabulated in Table 6.1.

March–May 2024

We observed 13 Pup Search targets in March of 2024 and one in May 2024. All observations were obtained without a coronagraph in z'/i' simultaneously and r'/g' simultaneously. All observations were made using the science camera EMCCDs set to 5 MHz readout speed with EM gain chosen based on conditions to maximize potential companion signal without saturating host star, and is tabulated in Table 6.1. Seeing was variable across observations and ranged from $\sim 0.4\text{--}0.9''$ and conditions were excellent for most observations.

6.2.3 Data Reduction

We made use of multiple different reduction methods for removing the stellar point-spread function (PSF) depending on the observation. Which method was applied to each system is tabulated in Table 6.1. Here we describe how each method was accomplished.

²And an $\text{H}\alpha$ narrow and continuum filter and a CH_4 narrow and continuum filter, which are not relevant to this survey. Filter specifications and filter curves can be found in the MagAO-X instrument handbook at <https://magao-x.org/docs/handbook/index.html>

Radial Profile Subtraction (“rad sub”): For some systems, the fainter companion was bright enough and well-separated enough to be readily visible on-sky before any PSF subtraction. For these observations, we frame-selected to 700-800 of the best images, dark subtracted, registered, derotated, and summed the images. We estimated the background as the median of an annulus around the central star outside the companion and deformable mirror speckles using `photutils`, (Bradley et al., 2023) and subtracted the background, and finally subtracted the host star’s radial profile to remove stellar halo at the location of the companion. We estimated the location of host and companion in the reduced image by fitting an `Astropy` 2D Gaussian function (Astropy Collaboration et al., 2022) to the PSF core, and computed the relative photometry using a `photutils` aperture with radius $1\lambda/D$ centered on host and companion.

Karhunen-Loève Image Processing + Angular Differential Imaging (KLIP ADI): Systems for which a companion was not readily visible in imaging, and for which we had adequate sky rotation, were reduced using the principal component analysis (PCA) based Karhunen-Loève Image Processing (KLIP; Soummer et al. 2012) method with angular differential imaging (ADI) using the python package `pyklip` (Wang et al., 2015). Briefly, ADI observations involve allowing the field to rotate during observations, such that astrophysical sources rotate through the image while optical artifacts (speckles, diffraction spikes, deformable mirror speckles) remain fixed. For each image in a dataset, KLIP produces an eigenimage basis set from the other images, then projects the target image onto the first N eigenimages of the basis set, where N is an integer, to create a PSF estimator; assuming adequate sky rotation companion signals should not be in the PSF estimator. The PSF estimator is then subtracted from each image, the image is rotated to north-up-east-left, and the resulting image cube is combined to produce the final image. For each KLIP reduced dataset we selected ~ 700 frames that span the observing time but allow rotation between frames to mitigate self-subtraction.

Classical Angular Differential Imaging (Classical ADI): We also made use of classical ADI (Marois et al., 2006) to search for candidate signals, particularly at large separations where KLIP is computationally inefficient. We performed classical ADI by selecting the best frames spanning the observation time, producing a PSF estimator from the median of those frames, subtracting the PSF estimator from each frame, then rotating and combining the frames into a single image. We also applied an unsharp mask to bring out and candidate signals.

Reference Differential Imaging (RDI): For some targets we were unable to attain much sky rotation during the observation due to varying observing constraints. We reduced these datasets using reference differential imaging (RDI). With RDI a reference PSF is produced by observing another star nearby in time and space to the target star, or by using an established reference star image database for the instrument. We did not plan RDI observations, and so didn't obtain observations of a reference target; since MagAO-X is a new instrument no pre-existing reference star dataset exists. Thus our RDI reduction is sub-optimal. Nevertheless, for each relevant star we had another Pup Search target observed that same night in similar seeing conditions (although not nearby in space) which we could make use of for an RDI reduction. For these datasets we made a PSF estimator as the median image of the reference star dataset, then for each image in the target star dataset we scaled the estimator to match the image, subtracted the estimator from the image, rotated and combined the dataset, applying an unsharp mask to the final image.

6.3 Results

We detected 8 new candidate companions, identified in Table 6.1 by their Pup Search name. Seven are identified as candidate companions since they only have one epoch of imaging. However for the companion to TYC 4831-473-1 we have two epochs and were able to establish companion status through common proper motion analysis (see Sec 6.3.1). Companion properties are given in Table 6.2 and in the text that follows.

6.3.1 Detections

Companion Photometry

Radial profile reduced datasets: For each wide companion reduced via radial profile subtraction, we used the host star as the photometric reference star to obtain absolute photometry for the companion. Candidate signal photometry is shown on a color-magnitude diagram in Figure 6.2 and Figure 6.7.

KLIP reduced datasets: For candidate signals discovered in KLIP-reduced datasets, we estimated the photometry using negative signal injection. Into each image in the dataset we injected a negative PSF estimator (a scaled and inverted median PSF from the dataset) at a known separa-

Table 6.1: Observations and Data Reduction

TYC	Obs Date (YYYY-mm-dd)	Camsci1 Filter: EM Gain, Exp Time	Camsci2 ^b Gain, Exp Time	Field Rotation (deg)	Red. Type ^a Detected	Comp.	Alt Name ^c
4831-473-1	2022-12-14	i' : 5, 0.5s	r' : 5, 0.5s	i'/r' : 5.6	Rad Sub	Yes	PupS-1B
169-1942-1	2022-12-14	i' : 5, 1s	r' : 5, 1s	i'/r' : 17.7	KLIP/cADI	No	–
1262-1500-1	2022-12-14	i' : 100, 1s	r' : 100, 1s	i'/r' : 10.0	KLIP/cADI	No	–
4831-473-1	2024-03-22	z' : 50, 0.23s	i' : 50, 0.23s	z'/i' : 1.2	Rad Sub	Yes	PupS-1B
4913-1224-1	2024-03-21	r' : 50, 0.23s	g' : 100, 0.23s	r'/g' : 3.3	Rad Sub	Yes	PupS-cc2
1385-562-1	2024-03-22	z' : 20, 0.23s	i' : 1, 0.23s	z'/i' : 0.3	Rad Sub	Yes	PupS-cc3
4865-655-1	2024-03-22	r' : 10, 0.23s	g' : 100, 0.23s	r'/g' : 0.5	Rad Sub	Yes	PupS-cc4
1451-111-1	2024-03-22	z' : 100, 0.23s	i' : 50, 0.23s	z'/i' : 1.7	Rad Sub	Yes	PupS-cc5
288-976-1	2024-03-27	r' : 100, 0.23s	g' : 1000, 0.23s	r'/g' : 2.5	Rad Sub	Yes	PupS-cc6
5518-135-1	2024-03-23	z' : 10, 0.23s	i' : 100, 0.23s	z'/i' : 6.4	Rad Sub	Yes	PupS-cc7
169-1942-1	2024-03-26	r' : 50, 0.23s	g' : 100, 0.23s	r'/g' : 6.8	Rad Sub	Yes	PupS-cc8
5480-589-1	2024-03-21	z' : 100, 0.23s	i' : 50, 0.23s	z'/i' : 1.9	Rad Sub	Yes	PupS-cc9
5512-916-1	2024-03-22	r' : 100, 0.23s	g' : 1000, 0.23s	r'/g' : 2.6	Rad Sub	Yes	PupS-cc10
6712-1511-1	2024-03-22	z' : 50, 0.23s	i' : 10, 0.23s	z'/i' : 0.6	Rad Sub	Yes	PupS-cc11
877-681-1	2024-03-23	r' : 50, 0.23s	g' : 700, 0.23s	r'/g' : 0.1	KLIP ADI	Yes	PupS-cc12
1447-1616-1	2024-03-28	z' : 10, 0.23s	i' : 5, 0.23s	z'/i' : 15.4	KLIP ADI	Yes	PupS-cc13
368-1591-1	2024-05-18	r' : 10, 0.23s	g' : 200, 0.23s	r'/g' : 1.0	KLIP ADI	Yes	PupS-cc14
5480-589-1	2024-03-21	z' : 20, 0.23s	i' : 1, 0.23s	z'/i' : 27.3	KLIP/cADI	No	–
5512-916-1	2024-03-22	r' : 5, 0.23s	g' : 50, 0.23s	r'/g' : 4.5	KLIP/cADI	No	–
6712-1511-1	2024-03-22	z' : 10, 0.23s	i' : 5, 0.23s	z'/i' : 33.1	RDI with TYC 5512-916-1	No	–
877-681-1	2024-03-23	r' : 100, 0.23s	g' : 100, 0.23s	r'/g' : 16.3	RDI with TYC 5518-135-1	No	–
1447-1616-1	2024-03-28	z' : 100, 2.0s	i' : 1, 0.23s	z'/i' : 7.1	KLIP/cADI	No	–
368-1591-1	2024-05-18	r' : 5, 0.23s	g' : 100, 0.23s	r'/g' : 2.6	KLIP/cADI	No	–
1447-1616-1	2024-03-28	z' : 100, 2.0s	i' : 100, 2.0s	z'/i' : 17.1	KLIP/cADI	No	–
368-1591-1	2024-05-18	r' : 1000, 2.0s	g' : 1000, 2.0s	r'/g' : 2.3	KLIP/cADI	No	–
368-1591-1	2024-05-18	z' : 1, 0.23s	i' : 1, 0.23s	z'/i' : 18.3	KLIP/cADI	No	–

(a) Reduction Type. 'Rad Sub': host PSF removed via radial profile subtraction; 'cADI': Classical ADI, host PSF removed via median image;

'KLIP ADI': host PSF removed via Karhunen-Loève image processing (Soummer et al., 2012)

(b) Camsci1: science camera # 1, we observed in z' and r' ; Camsci2: science camera #2, we observed in i' and g' . All observations used EMCCD cameras

(c) Pup Search internal designation. Confirmed companions are given a 'B' designation, candidate companions are given a 'cc' designation.

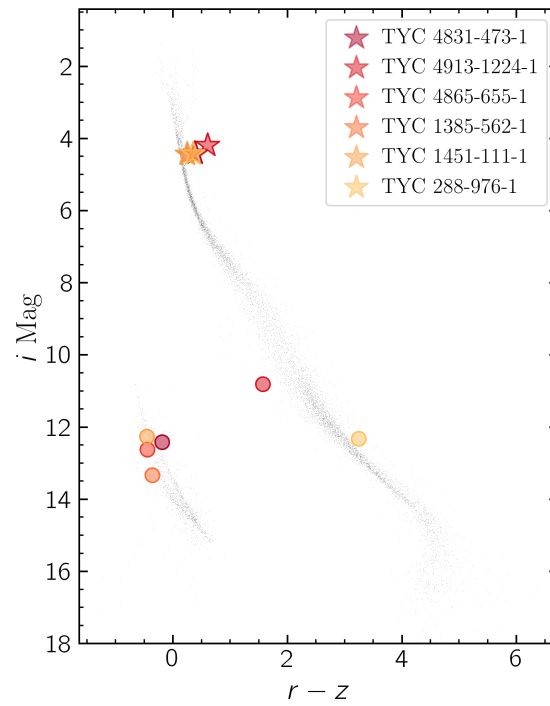


Figure 6.2: Color-magnitude diagram of the confirmed and candidate companions from Table 6.2 shown in SDSS $r' - z'$ color and SDSS i' absolute magnitude. Colored markers give measured photometry in MagAO-X filters converted to SDSS filters using color conversion table; host stars are marked with stars, companions are marked by circles. Grey dots are the same *Gaia* sample from Figure 6.1 converted to SDSS colors using *GaiaXPY* (Ruz-Mieres and zuzannakr, 2023) to generate synthetic photometry from *Gaia* DR3 spectra.

tion, position angle (PA), and contrast, reduced the dataset using the same KLIP configuration, then measured the root-mean-squared (RMS) variance at the candidate signal location. We repeated this for an array of separations, PAs, and contrasts and determined the injected signal which minimized the RMS in the reduced image.

For companions in the white dwarf regime of the CMD in Figure 6.2, we fit synthetic photometry to our measured contrast from Bergeron et al. (1995, hereafter B95) cooling models (updated in Holberg and Bergeron 2006) for hydrogen-dominated white dwarfs³. The synthetic photometry absolute magnitudes is provided for multiple photometric systems in (T_{eff} , $\log(g)$) bins, with T_{eff} from 1500–5500 K with 250 K spacing, 6000–17,000 K with 500 K spacing, 20,000–90,000 K with 5000 K spacing, and 100,000–150,000 K with 10,000 K spacing, and $\log(g)$ from 7.0–9.0 in bins of 0.5. For each WD candidate companion we used the following procedure:

1. We generated a “bootstrapped” array of 1000 simulated observations drawn from our companion fluxes and uncertainty in each filter z' , i' , r' (we excluded g' due to poor photometry in that filter), converted to AB magnitudes, then applied color correction to convert from MagAO-X filters to SDSS filters to obtain 1000 SDSS apparent magnitudes and uncertainties from our observations
2. For each WD (T_{eff} , $\log g$) pair in the synthetic photometry models we generated a random array of 20 parallaxes from a normal distribution described by the *Gaia* parallax measurements for the primary and computed absolute magnitude in each filter for each of the 1000 bootstrapped observations, such that each model (T_{eff} , $\log g$) pair has 20,000 simulated observations to compare
3. We computed goodness-of-fit using a χ^2 metric:

$$\chi^2 = \sum_f \left(\frac{M_{d,f} - M_{m,f}}{\sigma_f} \right)^2 \quad (6.1)$$

where f are the filters z' , i' , r' ; $M_{d,f}$ is the simulated observation absolute magnitude in each filter; $M_{m,f}$ is the B95 simulated photometry absolute magnitude; and σ_f is the uncertainty in

³Accessed from <https://www.astro.umontreal.ca/~bergeron/CoolingModels/> on July 30th 2024

each filter, taken from the signal-to-noise ratio (S/N) in each filter as $\sigma_f = \frac{F_{d,f}}{S/N_f}$ and converted to magnitudes.

4. we computed a total $\chi^2_{\text{tot}} = \sum_f \chi_f^2$ for each simulated observation for that model
5. The final χ^2 for each each model (T_{eff} , logg) pair is the mean and standard deviation of the χ^2_{tot} of the simulated observations

By computing model fits to bootstrapped simulated observations spanning our uncertainties and *Gaia* parallax, we incorporated the uncertainties in our observations and parallax and obtained uncertainties on the χ^2 value for each fit. This procedure assumes the companion is bound to the primary, which we have only established for PupS-1B to date (Section 3.1.3).

For companions in the main sequence regime, we fit `Phoenix` stellar spectra (Allard et al., 2012) to our photometry using `pysynphot` (STScI Development Team, 2013) and the following procedure:

1. we generated a “bootstrapped” array of 10,000 simulated observations drawn from our photometry and uncertainty in each filter z' , i' , r' (we excluded g' due to poor photometry in that filter)
2. we selected a filter and generated synthetic photometry for the model in that filter
3. for each set of simulated observations, we computed a scale factor to scale the model to the simulated photometry
4. we computed new synthetic photometry from the model for each filter and computed goodness-of-fit using a χ^2 metric:

$$\chi^2 = \sum_f \left(\frac{F_{d,f} - F_{m,f}}{\sigma_f} \right)^2 \quad (6.2)$$

where f are the filters z' , i' , r' ; $F_{d,f}$ is the simulated observation flux in each filter; $F_{m,f}$ is the scaled model flux in each filter; and σ_f is the uncertainty in each filter, taken from the signal-to-noise ratio (S/N) in each filter as $\sigma_f = \frac{F_{d,f}}{S/N_f}$.

5. we computed a total χ^2 and mean and standard deviation in the same manner as above.

In scaling this way we fit the shape of the model to our photometry and do not include uncertainties in distance and radius (which is entirely unknown).

Companion Astrometry

Rad sub reduced datasets: To estimate companion separation and position angle, we performed a bootstrap simulation:

1. We selected a random subset of N images, where $N < N_{\text{total images}}$
2. We reduced the subset of N images following the radial profile reduction described in Sec 6.2.1
3. We fit a 2D Gaussian model to the host star and companion signal and computed relative separation in mas and position angle east of north
4. We repeated this procedure N_{tot} times and took the final separation and position angle as the mean and standard deviation from the N_{tot} trials

We used $N = 500$ and $N_{\text{tot}} = 100$ for each of the candidate and confirmed companions.

KLIP reduced datasets: For the signals discovered in KLIP reductions, we took the separation and PA of the negative injected signal described above.

PupS-1B

A candidate companion was detected to the north west of TYC 4831-473-1 in Dec 2022 and again in Mar 2024. Fig 6.3 shows a i' image from 2022 and a z' image of the system from the 2024 observation, with the companion marked by a red circle ~ 900 mas to the northwest. TYC 4831-473-1 is estimated to have a spectral type of $\sim G2V$ based on *Gaia* DR3 colors and Pecaut and Mamajek (2013) reference colors. Its *Gaia* DR3 RUWE is 1.14. The companion's photometry falls in the WD sequence, as shown in Figure 6.2.

Our photometry rules out helium-dominated (DB) spectral types. Figure 6.4 (top) shows the χ^2 surface for the B95 fits to our photometry with values interpolated between model grid points. There is a relationship between T_{eff} and $\log(g)$ – higher T_{eff} models fit better at higher $\log(g)$ and vice versa. The orange star marks the best fitting model grid point at $T_{\text{eff}} = 11,000$ K, $\log(g) = 8.0$,

with orange solid and dotted contours showing regions within 1σ and 2σ respectively of that best fitting model. 6.4 (bottom) shows our observed absolute magnitude and uncertainty per filter (teal) with synthetic photometry for all models within 2σ of the lowest χ^2 (best fitting model). The best fitting model has $T_{\text{eff}} = 11,000$ K, $\log(g) = 8.0$, but in our final reported results we include all models with χ^2 within 1σ of that model's χ^2 , and determine that PupS-1B has $T_{\text{eff}} = 9,000 - 17,000$ K and $\log(g) = 7.5 - 8.5$.

PupS-1B Common proper motion

With two epochs of relative astrometry spanning ~ 1.2 years, we were able to confirm companion status. Figure 6.5 shows the common proper motion of the companion relative to the host star. The black track shows the expected path of the companion relative to TYC 4831-473-1 if it were a non-moving background object; the circles mark the observed offset from the host star in the two epochs. Relative to the 2022 epoch, if the companion were a non-moving background object we would expect to observe it at the location of the red diamond in the 2024 epoch; instead we observe it at the location of the red circle. Our observed motion is not consistent with a background object, so we conclude that PupS-1B is not a background object and posit that the observed motion is due to orbital motion. Future observations are needed to begin to constrain the orbit.

PupS-cc2

PupS-cc2 is a candidate companion signal ~ 500 mas (20 au) to the south-west of G9IV (Torres et al., 2006), subgiant (Jofré et al., 2015) star TYC 4913-1224-1 (aka 33 Sex). It falls below the main sequence as shown in Figure 6.2, suggesting it is bluer than a main sequence star. PupS-cc2 then is likely an M-dwarf + WD unresolved binary. It does not fit the properties of a cool subdwarf (Gizis, 1997), as 33 Sex is estimated to be 5 Gyr old giant star (Tsantaki et al., 2013; Jofré et al., 2015; Delgado Mena et al., 2019; Gaia Collaboration et al., 2023) with solar metallicity (Jofré et al., 2015) classified as a high-alpha metal rich Galactic disc star (Costa Silva et al., 2020), which is not consistent with the old age and subsolar metallicity comprising the subdwarf population (typically Pop II halo stars, Lépine et al. 2007). Thus we conclude it is likely an unresolved WD companion responsible for the abnormally blue color.

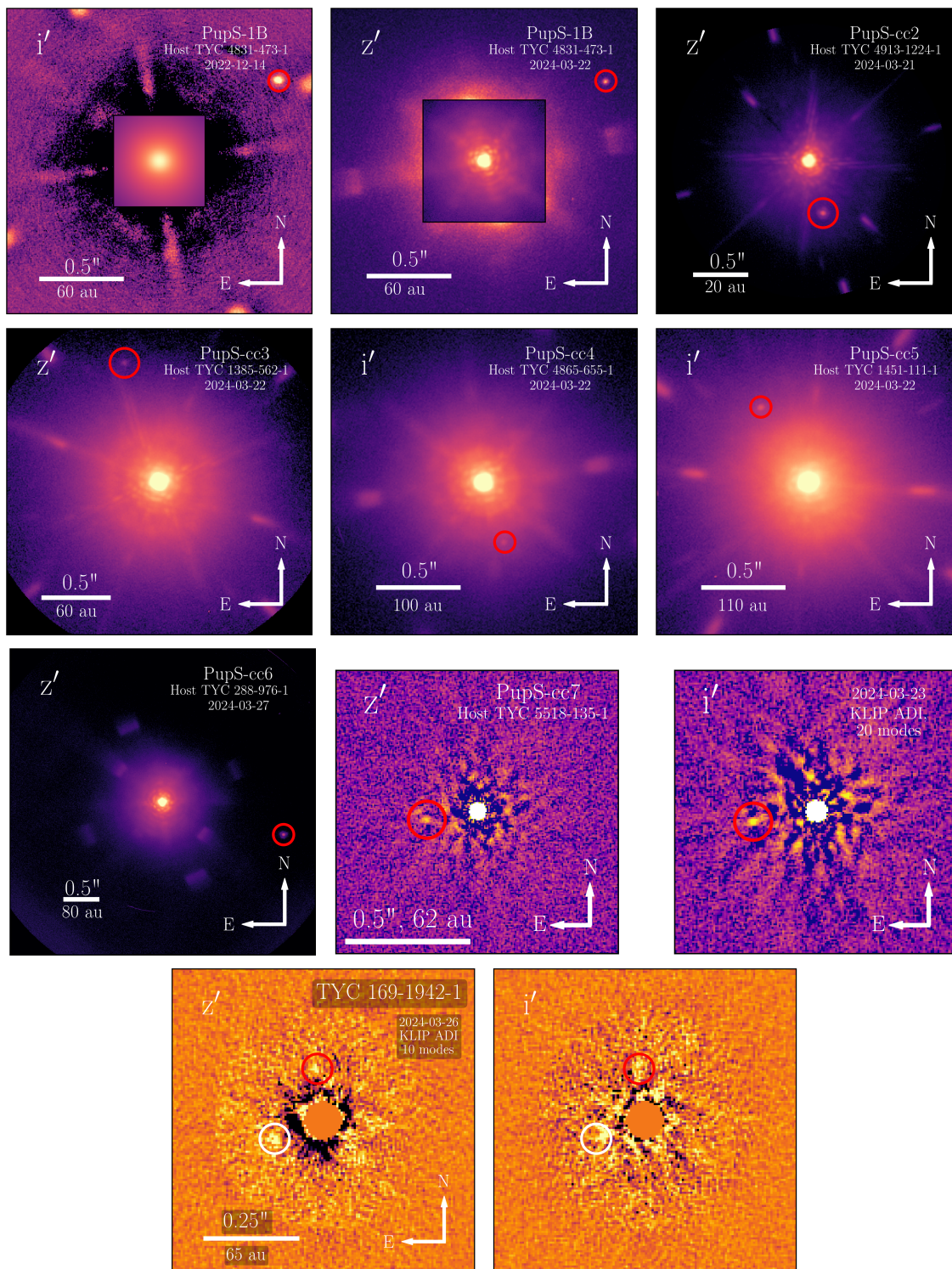


Figure 6.3: MagAO-X images of the confirmed and candidate companion signals in this work, including the 2022 and 2024 detections of PupS-1B. All images are North up/ East left; the filter, host star, and observation date are as indicated. Scale bars show 0.5'' and corresponding physical scales. The companion is marked by a red circle.

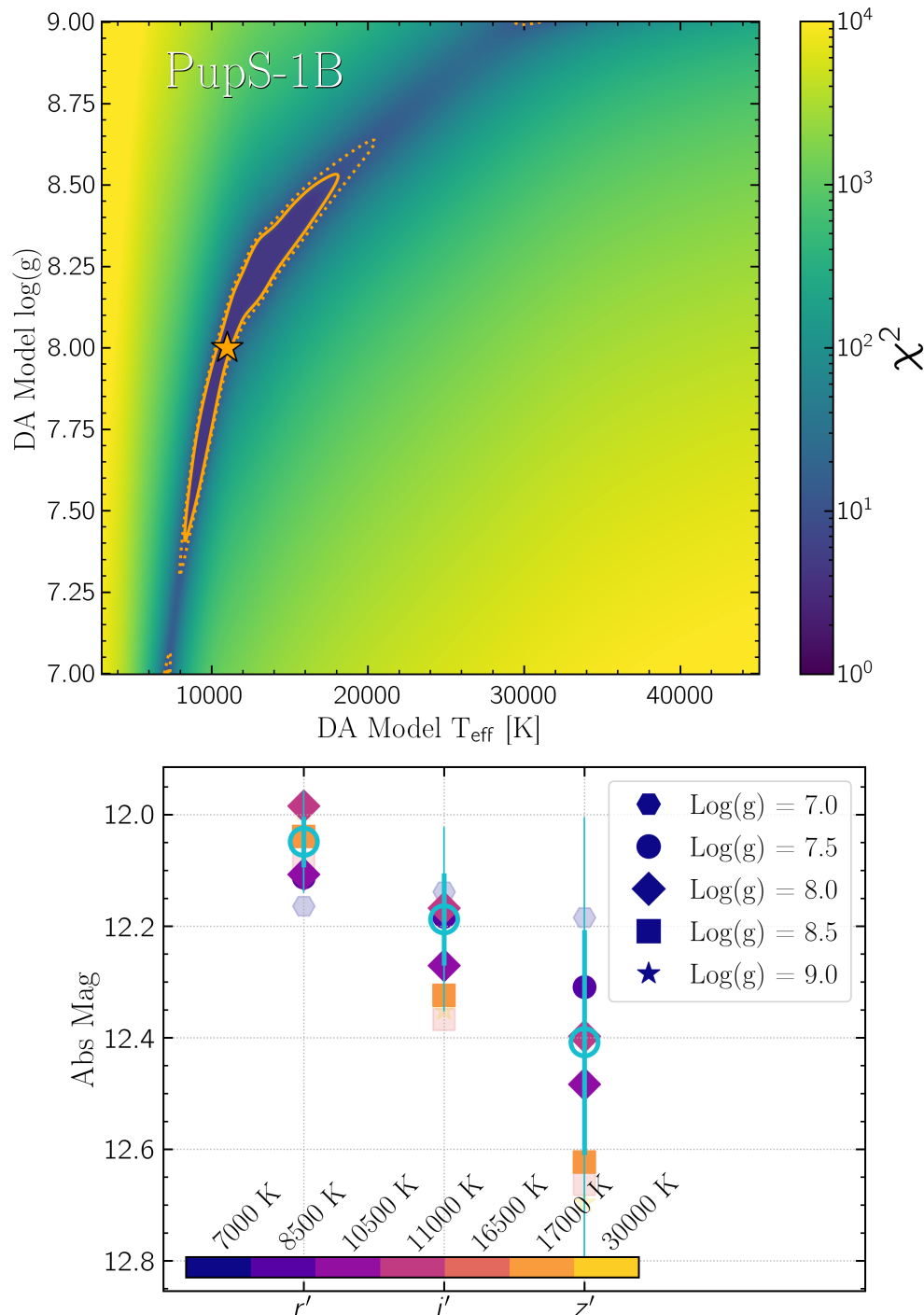


Figure 6.4: Model fit results for PupS-1B to [Bergeron et al. \(1995\)](#) synthetic photometry. Top: χ^2 map with model effective temperature on the X-axis and $\log(g)$ on the Y-axis with value interpolated between grid points. There is a degeneracy between T_{eff} and $\log(g)$. The best fitting model is marked with an orange star, with the orange solid and dotted contours showing 1- and 2 σ surfaces from that minimum χ^2 value. Bottom: the absolute magnitude in the three filters for all models within 1 σ of the best fitting model (mean $\chi^2 < \min[\chi^2] + \sigma_{\min[\chi^2]}$, solid markers) and 2 σ (mean $\chi^2 < \min[\chi^2] + 2\sigma_{\min[\chi^2]}$, transparent markers) compared to our observations (teal open circles) and uncertainties (teal bars; thick bars are 1 σ and thin bars are 2 σ uncertainties) at the mean *Gaia* DR3 parallax for the primary. The colors show the T_{eff} of the model and the marker shape shows the $\log(g)$. The best fitting model is $T_{\text{eff}} = 11,000\text{K}$, $\log(g) = 8.0$ ($\chi^2 = 4.5 \pm 4.4$), followed by $T_{\text{eff}} = 10,500\text{K}$, $\log(g) = 8.0$ ($\chi^2 = 5.2 \pm 4.2$), $T_{\text{eff}} = 8500\text{K}$, $\log(g) = 7.5$ ($\chi^2 = 5.6 \pm 4.6$), $T_{\text{eff}} = 17,000\text{K}$, $\log(g) = 8.5$ ($\chi^2 = 7.2 \pm 4.8$), $T_{\text{eff}} = 16,500\text{K}$, $\log(g) = 8.5$ ($\chi^2 = 9.6 \pm 5.8$), and $T_{\text{eff}} = 30,000\text{K}$, $\log(g) = 9.0$ ($\chi^2 = 11.4 \pm 6.2$).

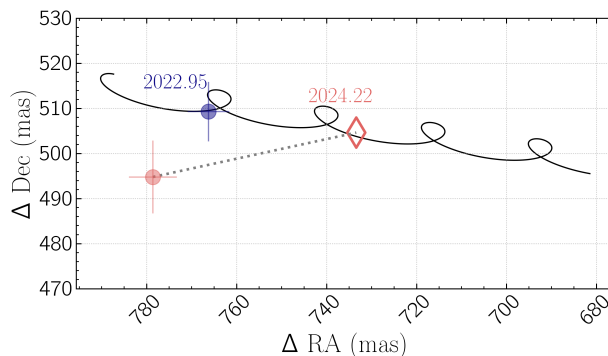


Figure 6.5: Common proper motion plot for PupS-1B. The offset from TYC 4831-473-1 in RA and Dec are given on the x- and y-axis respectively, with our observed position in 2022 and 2024 are given by the blue and red circles. If PupS-1B were an unmoving background star, it would follow the black track relative to TYC 4831-473-1, given by the host star’s proper motion and parallax; we would have observed PupS-1B at the location of the red diamond in 2024. Our observed location is highly discrepant with this predicted location and moving in the opposite direction in RA. We conclude that PupS-1B is not a background star, and posit that the apparent motion of PupS-1B is due to orbital motion. More observations are required to begin to pin down orbital parameters.

Astrometric time series is needed to establish relative motion between 33 Sex and PupS-cc2; as 33 Sex is a high-proper motion star it shouldn’t take too long to establish common proper motion. As 33 Sex is well characterized, astrometric time series should be able to constrain companion mass.

Phoenix models did not fit our photometry well, with the lowest χ^2 value being ~ 18 . Our photometry was bluer than the Phoenix models, with the r' being consistently brighter than the models as can be seen in Figure C.4, and is consistent with its being a subdwarf. We estimate this star to be approximately a mid-M dwarf, but further careful photometry and spectroscopy is needed to determine its spectral type. While it is not a new SLS system, it merits further followup as an interesting object.

Figure 6.6 (top) shows the proper motion anomaly (PMA) curve for 33 Sex (generated using the catalog and methodology of Kervella et al. 2022), indicating the mass sensitivity as a function of separation for the observed acceleration of the star between the *Hipparcos* and *Gaia* astrometric measurements; the orange vertical line marks the separation of cc2, and the horizontal line marks the approximate mass of a mid-M dwarf star. Its position well above the sensitivity curve

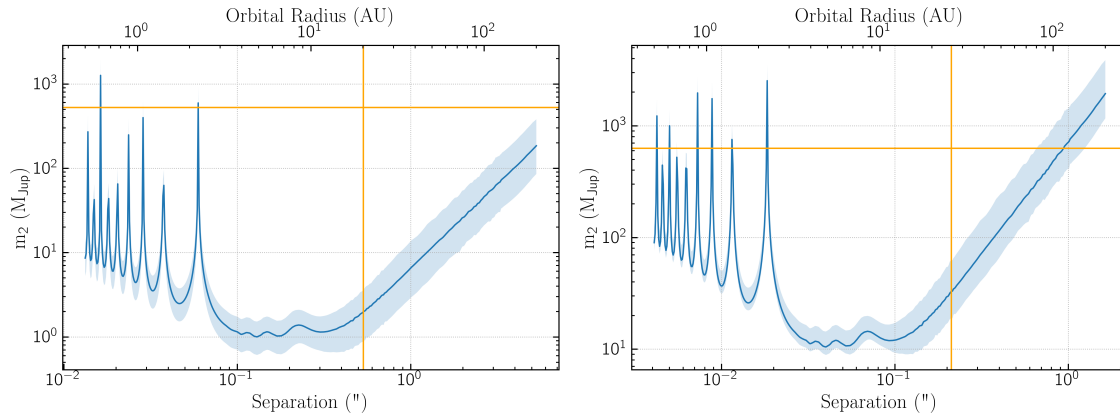


Figure 6.6: Proper motion anomaly (PMA) plot for 33 Sex (host of PupS-cc2; top) and TYC 5518-135-1 (host of PupS-cc7; bottom) using the methodology of [Kervella et al. \(2022\)](#). This plot describes the (minimum) mass of an object as a function of separation that would produce the observed proper motion anomaly between the *Hipparcos* and *Gaia* observations. Left: The orange vertical line marks the separation of cc2 from 33 Sex, and the horizontal orange line marks the approximate mass of a mid-M dwarf. This suggests the cc2 is either not in a face-on orbit (as assumed by the sensitivity function), or another object is contributing to the observed PMA and cc2 is not responsible for the observed acceleration. Right: The orange vertical line marks the separation of cc7 from host, and the horizontal vertical line marks the approximate mass of a white dwarf. cc7’s position above the sensitivity curve indicates it is either on an inclined or eccentric orbit, there is another object in the system and cc7 is not responsible for the observed acceleration.

indicates that either cc2 is on a highly-inclined and/or highly eccentric orbit, or there is another unresolved object bound to 33 Sex contributing to the PMA and cc2 is actually a chance alignment and not bound. Followup is warranted for this system to observe the orbit and search for closer-in companions.

PupS-cc3

PupS-cc3 is a candidate companion signal ~ 950 mas (110 au) to the north east of TYC 1385-562-1 in the white dwarf region of Figure 6.2. TYC 1385-562-1 is estimated to have a spectral type of $\sim G0$ based on *Gaia* DR3 colors and [Pecaut and Mamajek \(2013\)](#) reference colors; its *Gaia* DR3 RUWE is 0.83.

Our photometry rules out helium-dominated (DB) spectral types. As with PupS-1B, the χ^2 surface and best fitting models are shown in Figure C.5. The best fitting model occurred at $T_{\text{eff}} = 10,000$ K and $\log(g) = 8.5$, but models from $T_{\text{eff}} = 6000 - 18,000$ K and $\log(g)$ from 7.0 – 9.0 have χ^2 values within 1σ of that best fit, so we report these values.

PupS-cc4

PupS-cc4 is a candidate companion signal ~ 400 mas (80 au) south west of TYC 4865-655-1, an estimated F8 star with $\text{RUWE} = 0.83$. Our photometry rules out helium-dominated (DB) spectral types. Hydrogen-dominated (DA) [B95](#) synthetic photometry is best fit by models shown in [Figure C.6](#), with the best fitting model occurring at $T_{\text{eff}} = 30,000$ K, $\log(g) = 9.0$, and models from (12,000, 8.25) – (18,000, 8.5) within 1σ . We conclude it has $T_{\text{eff}} = 12,000 - 30,000$ K, $\log(g) = 8.25 - 9.0$.

PupS-cc5

PupS-cc5 is a candidate companion signal ~ 550 mas (120 au) north east of TYC 1451-111-1, an estimated F8 star with $\text{RUWE} = 1.14$. Our photometry rules out helium-dominated (DB) spectral types. The χ^2 surface and best fitting models are shown in [Figure C.7](#). The best fitting model occurred at $(T_{\text{eff}}, \log g) = (12,000 \text{ K}, 8.0)$, with models from (10,000 K, 7.4) to (22,000 K, 8.6) and an additional island of probability at (35,000 K, 9.0) within 1σ . Thus we determine this companion has $T_{\text{eff}} = 10,000 - 35,000$ K and $\log(g) = 7.4 - 9.0$.

PupS-cc6

PupS-cc6 is a candidate companion signal $\sim 2''$ (120 au) southwest of TYC 288-976-1 (HD 108738), a G0 star with $\text{RUWE} = 1.58$. It falls in the late-M dwarf section of the CMD in [Figure 6.2](#). [Figure C.8](#) shows the results of our `Phoenix` model fits. Our photometry does not constrain metallicity or $\log(g)$ and constrains $T_{\text{eff}} < 3500$ K, so we estimate it is a mid- to late M dwarf ($\lesssim M2$).

Since cc6 is approximately a mid-M dwarf, it is not the source of the GALEX excess. There is no PMa for this system as it was not observed in *Hipparcos*. The elevated RUWE suggests another companion closer than the one we detected which could be the source of the UV excess. Followup on this system is warranted to look for close-in white dwarfs, as it was not observed long enough for ADI in this dataset.

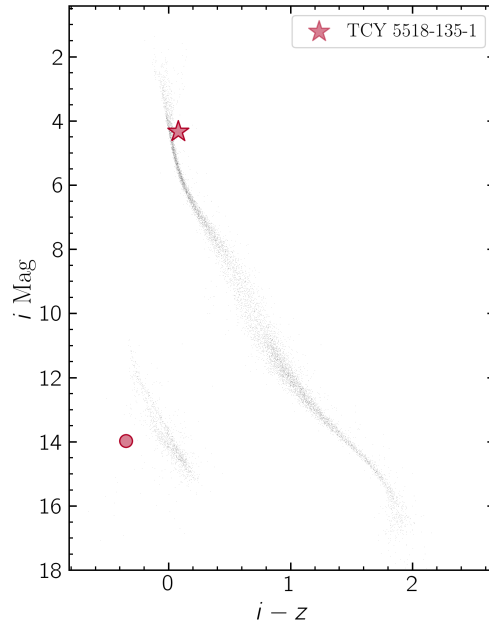


Figure 6.7: Color-magnitude diagram of the candidate companion signal to TYC 5518-135-1, PupS-cc7. Since we do not have r' photometry we show it here in SDSS $i' - z'$ color vs SDSS i' absolute magnitude. cc7 clearly falls in the WD regime, however the exact position in the WD sequence is not well constrained with only i' and z' colors.

PupS-cc7

PupS-cc7 is a candidate signal ~ 210 mas (26 au) to the southeast of TYC 5518-135-1 (HD 104018), a G6-8 subgiant star with $\text{RUWE} = 1.14$. We performed a KLIP ADI reduction with 5, 10, and 20 modes in z and i band. The candidate signal was observed in KLIP reduced images z' and i' , shown in Figure 6.3, which did not scale with wavelength, as the other artifacts did, and which displayed the self-subtraction lobes on either side that is typical of an ADI-reduced genuine astrophysical signal. In order to estimate the candidate signal's properties we performed a negative signal injection described in Section 6.3.1 and estimated the separation, pa , and contrast in z' and i' . The signal's nature is not well constrained with only z' and i' , but we show its position in a z'/i' color-magnitude diagram in Figure 6.7; it clearly falls in the WD sequence, although better photometry is needed to establish its parameters. From our fits to B95 we determined that it is a relatively cool DA WD with T_{eff} constrained to the range 5000 – 11,000 K and $\log(g) = 7.5\text{--}9.0$. Further photometry in bluer bands is necessary to refine the detection and companion properties.

We computed contrast curves for this dataset to determine limits for additional companion signals, shown in Figure C.2 with a completeness map shown in Figure C.3 (See section 3.2.1 and 3.3 for descriptions). Our observations rule out additional hydrogen-dominated WD companions beyond from ~ 20 –1000 au.

TYC 5518-153-1 was observed with *Hipparcos* and thus has a PMa measurement, shown in Figure 6.6 (bottom). The orange vertical line marks the separation of cc7, and the horizontal vertical line marks the approximate mass of a white dwarf. Its location above the sensitivity curve indicates cc7 is either not in a face-on orbit, another object is present in the system and cc7 is a chance alignment.

PupS-cc8

PupS-cc8 is a candidate signal ~ 140 mas to the north of TYC 169-1942-1. We were unable to determine a spectral type for this star. It is firmly in the giant region of Figure 6.1 (bottom) so we cannot use Pecaut and Mamajek 2013 tables, and there is no literature spectral type available. Determination of spectral type for this star is beyond the scope of this work. It is at 415 pc and has an RUWE = 2.06.

We performed a KLIP ADI reduction with 5, 10, and 20 modes in z and i band; we did not obtain sufficient rotation for ADI in r . Figure 6.3 shows z and i images reduced with 10 KLIP modes. The candidate signal is marked with a red circle; it is a marginal detection, but did not scale with wavelength and remained present with all KLIP modes. Another spurious signal which does scale with wavelength is marked with a white circle; this is ruled out as a candidate signal. We were unable to characterize the candidate signal using negative signal inject as with cc7 due to the low S/N. Follow-up is necessary with more field rotation and filters to confirm the signal and characterize it.

We computed contrast curves for this dataset to determine limits for additional companion signals, shown in Figure C.2 with a completeness map shown in Figure C.3 (See section 3.2.1 and 3.3 for descriptions). Our observations rule out additional hydrogen-dominated WD companions beyond from ~ 100 –1000 au.

TYC 169-1942-1 has a complete orbital solution in the *Gaia* DR3 Non-Single Star (NSS) catalog. We computed the predicted location in March 2024 for the two-body solution by converting

the Thiele-Innes elements in the *Gaia* archive to Campbell elements using [Halbwachs et al. \(2023\)](#) (Appendix A). The NSS solution predicted the 16 M_{Jup} companion would be at $\rho = 0.43$ mas ($\rho = 0.3$ au) and $\text{pa} = 216^\circ$, which does not correspond to our candidate signal in Section 6.3.1 and is far too close for us to resolve in imaging.

6.3.2 Non-Detections

Contrast Curves

For each star without a detected companion, we computed contrast limits for our observation following the method of [Mawet et al. \(2014\)](#) as described in Section 4.4 of [Pearce et al. \(2022\)](#). To summarize briefly, we performed an injection-recovery analysis by injecting a synthetic signal (made from the psf reference used in reduction) at a given separation ($r = n\lambda/D$ where n is an integer) and position angle at a known contrast into each image in a dataset, then reducing the dataset as before. We then measured the counts within an aperture of size $1\lambda/D$ centered on the injected signal, and the standard deviation of counts within N apertures in a ring of radius r , where $N = 2\pi r$, and computed the signal-to-noise ratio (S/N) following Eqn (9) of [Mawet et al. \(2014\)](#). We repeated this for all N apertures, then took the mean as the S/N for each r at an array of contrasts, then interpolated to find the 1-, 2-, 3-, and 5σ contrast limits. Images and contrast curves for each non-detection are shown in Figures C.1 and C.2.

TYC 1262-1500-1

TYC 1262-1500-1 an early F star at 452 pc with $\text{RUWE} = 1.37$. We reduced the data using both classical and KLIP ADI with 10 deg of field rotation and did not detect any candidate signals. Our observations rule out DA WDs hotter than 20,000 K from ~ 300 –1000 au. The elevated RUWE hints at a large-luminosity-ratio companion at closer radii. Our imaging was not very deep for this system and can be improved with longer ADI observations.

TYC 5480-589-1

TYC 5480-589-1 is a K0III giant star at 630 pc with $\text{RUWE} = 1.42$. We reduced the data using both KLIP and classical ADI and did not detect any candidate companion signals. White

Table 6.2: Companion Detections

Property	PupS-1B		PupS-cc2		PupS-cc3		PupS-cc4	
	MS Star Host Properties							
TYC	4831-473-1	4913-1224-1	1385-562-1	4865-655-1				
AKA		33 Sex, HD 92588						
RA [HMS]	07:44:37.68	10:41:24.04	08:08:40.16	08:52:39.91				
DEC [DMS]	-00:02:13.81	-00:06:58.09	01:21:08.17	-00:04:03.16				
SpT _a	G2V*	G9IV ¹	G0V*	F8V*				
Gaia DR3 ID	3085864943402832000	3805647792295621376	669892921105281024	3073915309292882816				
RUWE	1.14	1.11	0.82	0.83				
Distance _b [pc]	120.8 ^{+0.4} _{-0.2}	37.66±0.04	118.2±0.3	202.7±0.6				
Companion Properties								
	2022	2024						
Sep (mas)	908.5±1.5	910.8±1.3	534.9±0.1	396.1±1.8				
Sep (au)	110.2±0.3	110.4±0.3	20.2±0.2	80.8±0.5				
PA (deg)	304.1±0.3	302.9±0.6	289.0±0.4	199.6±0.5				
SpT	-	DA	sdM4-sdM5	DA				
T _{eff} [K]	-	9000 - 17000	3100 ⁺⁴⁰⁰ ₋₅₀₀	12000 - 30000				
log(g)	-	7.5 - 8.5		8.25 - 9.0				
r' contrast	1.30 [0.06] × 10 ⁻³	1.36 [0.06] × 10 ⁻³	2.5 [0.2] × 10 ⁻³	1.5 [0.1] × 10 ⁻³				
r' S/N	23.0	23.8	11.4	14.1				
r' N _{images}	1162	642	710	733				
i' contrast	8.5 [0.4] × 10 ⁻⁴	9.9 [0.7] × 10 ⁻⁴	3.5 [0.2] × 10 ⁻³	8.4 [0.5] × 10 ⁻⁴				
i' S/N	21.7	13.1	22.0	15.8				
i' N _{images}	1381	705	825	738				
z' contrast	-	8 [6] × 10 ⁻⁴	6.02 [0.09] × 10 ⁻³	8 [2] × 10 ⁻⁴				
z' S/N	-	5.4	38.4	3.5				
z' N _{images}	-	706	878	734				

(a) As reported in Simbad. Where not available, spectral type is estimated from Pecaut and Mamajek 2013

and Gaia DR3 colors and marked with an asterisk. Spectral Type references: ¹Torres et al. 2006, ²Cannon and Pickering 1993

(b) From Bailler-Jones et al. 2021 catalog

(c) Units Ergs s⁻¹ cm⁻² Å⁻¹; uncertainties in brackets

Table 6.2: Companion Detections Cont.

Property	PupS-cc5	PupS-cc6	PupS-cc7	PupS-cc8
MS Star Host Properties				
TYC	1451-111-1	288-976-1	5518-135-1	169-1942-1
AKA		HD 108738	HD 104018	
RA [HMS]	13:15:14.65	12:29:33.69	11:58:41.34	07:25:19.39
DEC [DMS]	01:09:55.54	00:24:57.70	-08:00:28.91	03:31:03.21
SpT ^a	F8V*	G0 ²	G6/8IV ³	–
Gaia DR3 ID	3937175633819731968	3708538031977678976	3594365947141542272	3136564420989284096
RUWE	1.14	1.58	1.14	2.06
Distance ^b [pc]	222.9 ^{+0.9} _{-1.0}	158±0.8	122.3±0.5	414±7
Companion Properties				
Sep (mas)	553.7±0.7	1996.0±1.2	230±9	140±10
Sep (au)	123.7±0.6	318±1	29±2	60±5
PA (deg)	31.6±0.1	254.9±0.1	98.3±0.3	7±3
SpT	DA	<M2	DA	–
T _{eff} [K]	10000 – 35000	<3500	5000 – 11000	–
log(g)	7.4 – 9.0	–	7.5 – 9.0	–
r' contrast ^c	1.7 [0.2] × 10 ⁻³	1.6 [0.6] × 10 ⁻⁴	–	–
r' S/N	9.4	2.6	–	–
r' N _{images}	1101	845	–	–
i' contrast ^c	1.17 [0.05] × 10 ⁻³	1.09 [0.06] × 10 ⁻³	2.2 [0.4] × 10 ⁻⁴	–
i' S/N	22.9	18.1	5.2	1.8
i' N _{images}	831	557	869	713
z' contrast ^c	9 [2] × 10 ⁻⁴	2.32 [0.08] × 10 ⁻³	1.5 [0.2] × 10 ⁻⁴	–
z' S/N	3.1	28.5	5.4	1.0
z' N _{images}	844	561	708	731

(a) As reported in Simbad. Where not available, spectral type is estimated from Pecaut and Mamajek 2013

and Gaia DR3 colors and marked with an asterisk. Spectral Type references: ¹Torres et al. 2006, ²Cannon and Pickering 1993

(b) From Bailler-Jones et al. 2021 catalog

(c) Units Ergs s⁻¹ cm⁻² Å⁻¹; uncertainties in brackets

Table 6.3: Non-Detections

TYC	RA/DEC HMS/DMS	SpT ^a	Gaia DR3 ID	RUWE	Distance ^b pc
1262-1500-1	04:02:13.84 01:23:37.33	Early F*	52921148211018368	1.37	452±7
5480-589-1	10:02:54.89 -00:44:54.20	K0III ¹	3766625330057013248	1.42	632 ⁺¹² ₋₁₃
5512-916-1	11:28:11.65 -00:40:57.41	K0*	3589837093105395712	3.03	415 ⁺¹¹ ₋₁₀
6712-1511-1	13:22:33.44 -01:54:40.54	F9*	6183075365029951488	1.09	174.1 ^{+0.5} _{-0.6}
877-681-1	12:34:37.79 00:45:12.22	G5 ²	3904521719021034880	1.00	260±2
1447-1616-1	12:18:00.46 01:24:59.29	Early F*	3953075946345237632	1.03	392±2
368-1591-1	16:17:43.20 00:06:05.32	K0III ¹	4408906185595207424	1.51	220.7 ^{+1.7} _{-1.8}

(a) As reported in Simbad. Where not available, spectral type is estimated from [Pecaut and Mamajek 2013](#)

and *Gaia* DR3 colors and marked with an asterisk. Spectral Type references: ¹[Torres et al. 2006](#), ²[Cannon and Pickering 1993](#)

(b) From [Bailer-Jones et al. 2021](#) catalog

(c) Units Ergs s⁻¹ cm⁻² Å⁻¹; uncertainties in brackets

circles in Figure C.1 mark speckles that scale with wavelength and are not candidate signals. Our observations rule out DA WD companions hotter than 6000 K from ~ 60 –1000 au. The high RUWE value hints to a large-luminosity-ratio companion being closer to the star than we were able to obtain with our observations. Longer time-baseline ADI observations could push our sensitivity at closer radii, however given the distance of this star, the typical resolution limit of $2\lambda/D$ would only push in a little bit closer to ~ 30 au.

TYC 5512-916-1

TYC 5512-916-1 is a $\sim K0$ star at 415 pc with $\text{RUWE} = 3.03$. We reduced the data using both KLIP and classical ADI and did not detect any candidate companion signals. Our observations rule out all modeled DA WD companions from ~ 30 –1000 au. This star has one of the highest RUWE values in our sample, suggesting that the large-luminosity-ratio companion is close to the host star. Longer time-baseline ADI may improve contrast limits in close, but our observations are already near a typical resolution limit so we are not likely to be able to get much closer.

TYC 6712-1511-1

TYC 6712-1511-1 is a $\sim F9$ star at 174 pc with $\text{RUWE} = 1.09$. We were unable to attain sufficient field rotation for ADI for this system. We reduced these data using classical reference differential imaging (RDI) using TYC 5512-916-1 images as stellar psf reference, which was obtained earlier the same night under the same conditions. For each filter, we created a PSF reference as the median TYC 5512-916-1 image in the same filter and reduced the TYC 6712-1511-1 images from there in the same manner as classical ADI. Obviously this was not optimal, as reflected in our contrast limits in Figure C.2, and should be revisited with longer baseline ADI. We did not detect any candidate companion signals. Nevertheless our observations rule out DA WDs hotter than 20,000 K from ~ 30 –1000 au. Our observations were not meaningfully able to rule out much of the white dwarf parameter space as the noise floor for these observations is $\sim 3 \times 10^{-4}$, which is near some of our WD detections.

TYC 887-681-1

TYC 887-681-1 is a G5 star at 260 pc and $\text{RUWE} = 1.00$. Seeing was variable during our observations and were limited in high-quality images suitable for reduction, consequently we did not achieve much sky rotation. We reduced these images using TYC 5518-135-1, observed on the same night, as a reference for RDI. Our contrast curves in Figure C.2 achieve higher contrast than for TYC 6712-1511-1, but not as high as our ADI-reduced datasets. Our observations rule out WDs hotter than ~ 8000 K from ~ 30 – 1000 au.

TYC 1447-1616-1

TYC 1447-1616-1 is a \sim F8 (Kharchenko, 2001) star at 400 pc with $\text{RUWE} = 1.03$. We were able to get 17° of rotation during our observations and did not find any candidate signals in our KLIP ADI reduced images. Our observations rule out WDs hotter than $\sim 15,000$ K from ~ 100 – 1000 au

TYC 368-1591-1

TYC 368-1591-1 is a K0III (Houk and Swift, 1999) star at 220 pc with $\text{RUWE} = 1.51$. Observing conditions were not ideal (seeing ~ 1.2 , which affected the AO correction), so future imaging could get to deeper contrasts. Our observations rule out WD's hotter than 6000 K from ~ 60 – 1000 au. It has a complete orbital solution in *Gaia* which predicts a $4.7 M_{\text{Jup}}$ planet at 0.9 mas (0.2 au), much too close for us to resolve in imaging. It was also observed in *Hipparcos* and has an observed acceleration between *Hipparcos* and *Gaia* astrometry. Our imaging rules out objects that could be causing the observed acceleration at \sim M3.5V or earlier beyond 160 mas, shown in Figure 6.8.

6.3.3 Survey Completeness

To estimate our sensitivity to white dwarf companions, we computed the survey completeness for each ADI and RDI-reduced system and total completeness for the entire survey. To estimate completeness we simulated 100 white dwarf companions over a grid uniform in $\log(\text{semi-major axis}) \in [0, 3]$ and the DA white dwarf model temperatures in the K10 models ($T_{\text{eff}} = 5000$ – $20,000$ K spaced by 250 K, $20,000$ – $30,000$ K spaced by 1000K, $30,000$ – $40,000$ K spaced by 2000 K, and $40,000$ – $80,000$ K spaced by 10,000 K). For each MS star we computed an array of MS-WD con-

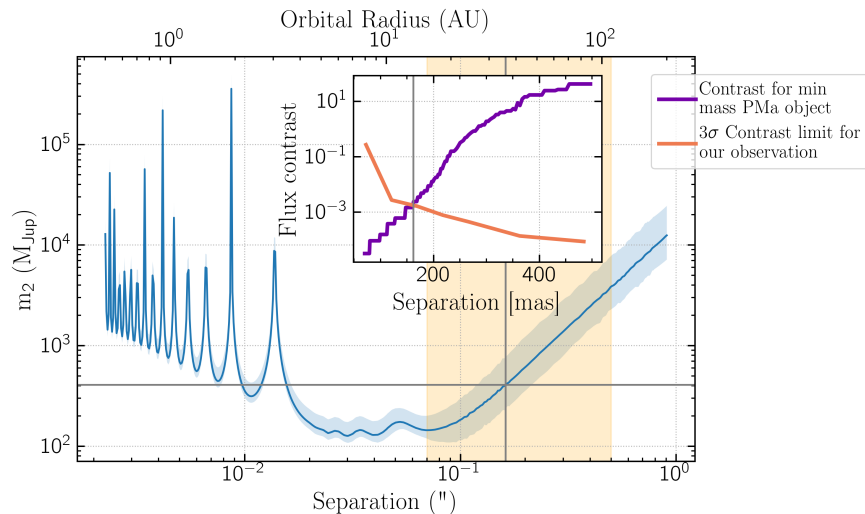


Figure 6.8: Proper motion anomaly plot for TYC 368-1591-1. See text of Figure 6.6 for explanation. The orange region marks where our imaging is sensitive. The inset axes shows the flux contrast corresponding to those minimum masses (purple) and our imaging 3σ contrast limit (red). The grey vertical lines mark where they cross, the grey horizontal line marks the minimum mass at that limit. Our contrast curves rule out at 3σ companions within the orange region outside of the grey line, which is objects $>0.35 M_{\odot}$ ($\sim 3.5 M_{\text{Jup}}$) at >160 mas.

trast from the K10. We generated 5×10^3 simulated companions for each (sma, contrast) grid point, randomly assigned orbital parameters from priors⁴ then computed projected separation. A companion was considered detectable if it fell above the $2 - \sigma$ contrast curve and undetectable if below the curve, inside the inner limit of the curve, or outside the detector. The completeness is the fraction of simulated companions at each grid point that would have been detectable at at least $S/N = 2$; 1.0 corresponds to every companion being detected, 0.0 corresponds to no companions being detected at that point. Figure C.3 shows the completeness for each observed system sensitive to close-in companions (ADI or RDI reduced systems), made by summing individual completeness maps; the colormap and contours show the completeness fraction. Figure 6.9 shows the combined completeness map for the entire survey. We are nearly complete to WD companions hotter than 20,000 K between 100–1000 au in our imaged systems, and have some fractional completeness down to ~ 50 au. These limits can be improved by longer ADI field rotation times and the use of an coronagraph.

⁴eccentricity (e): $P(e) = 2.1 - 2.2 \times e$, $e \in [0, 0.95]$, following Nielsen et al. 2019; inclination (i): $\cos(i) \in \text{Unif}[-1, 1]$; argument of periastron (ω): $\omega \in \text{Unif}[0, 2\pi]$; mean anomaly (M): $M \in \text{Unif}[0, 2\pi]$; since contrast curves are one-dimensional we did not simulate longitude of nodes

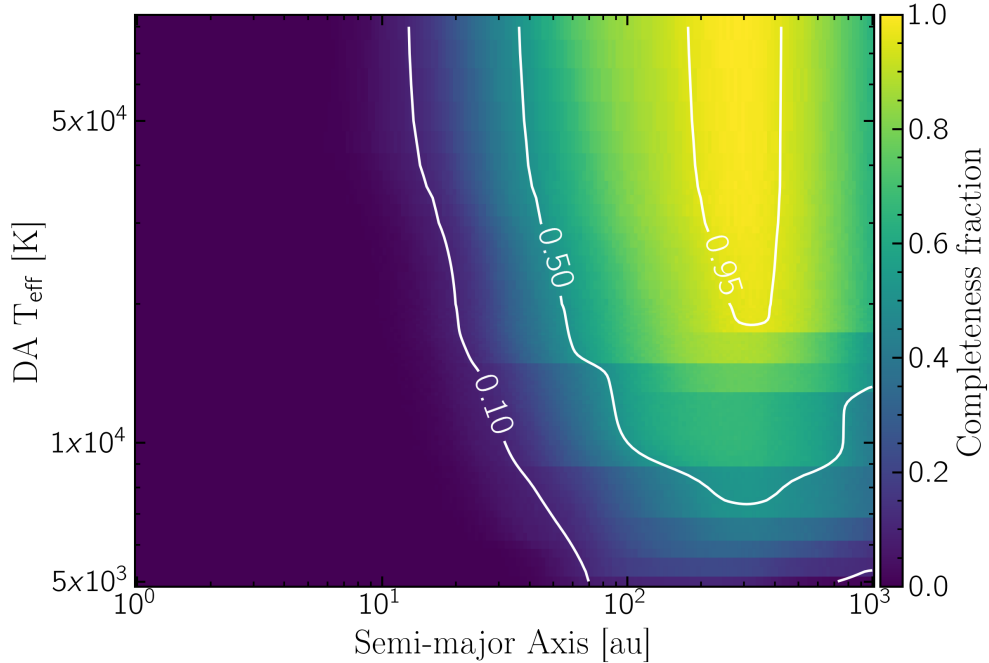


Figure 6.9: Map of completeness to hydrogen-dominated white dwarf companions in our survey.

6.4 Discussion

6.4.1 Our Survey Compared to Previous Surveys

In the preliminary Pup Search observations we detected four candidate and one confirmed new Sirius-Like Systems, along with 1 subdwarf companion, 1 MS companion, and one candidate signal of undetermined character. Figure 6.10 shows our new SLS with separation in arcseconds and au compared to other WDMS surveys: Zuckerman (2014) (red), H13 (blue), and Noor et al. (2024) (magenta), which all looked at non-interacting WDMS as discussed in Section 6.1, as well as Yamaguchi et al. (2024), which examined the orbits of PCBE and/or mass transfer WDMS with spectroscopic orbital solutions in *Gaia* DR3 in a period regime predicted to be empty. The approximate detection region for MagAO-X is marked with dashed grey lines and indicate the regime we are sensitive to (from $2\lambda/D$ at $0.8\mu\text{m}$ to $3''$) Approximately 30% of H13 and 6% of Noor et al. (2024) objects fall within that regime.

We have overlaid contours adapting Figure 10 (right) from Willems and Kolb (2004, hereafter W04) to this parameter space. That figure gives a distribution of orbital periods for all types of WDMS systems at the start of the WD phase. The distribution is bimodal – as the progenitor

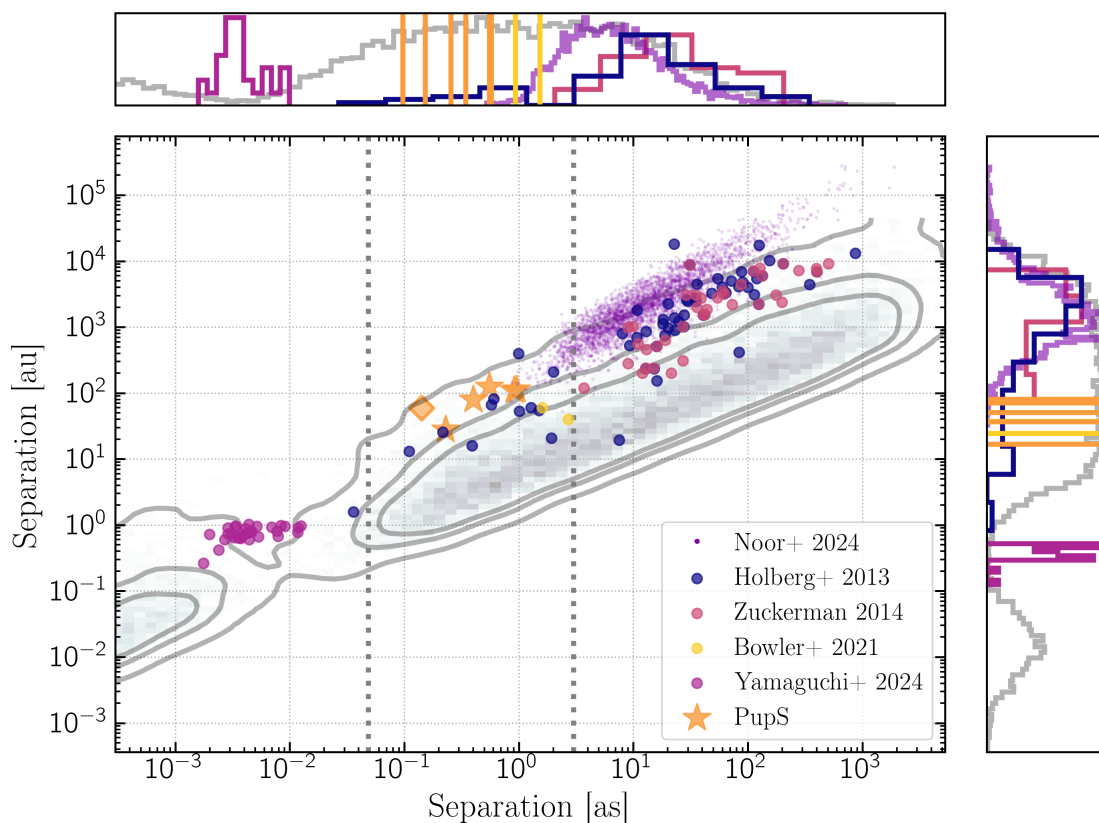


Figure 6.10: Pup Search confirmed and candidate companions in this work plotted (orange stars and diamond) against known SLS from [Zuckerman 2014](#) (red), [Holberg et al. 2013](#) (and references there-in; blue), WDMS systems in *Gaia* DR3 from [Noor et al. 2024](#) (purple), wide post-common envelope binaries in *Gaia* from [Yamaguchi et al. 2024](#) (magenta), and two SLS detected via astrometric acceleration and AO imaging in [Bowler et al. 2021](#) (yellow), plotted with separation in arcseconds on the x-axis and physical separation in au on the y-axis. The orange diamond marks the location of PupS-cc8, which is not confirmed to be a white dwarf companion. We illustrate the approximate limits of MagAO-X search space between 48 mas ($2 \lambda/D$ in i') and $3''$ (half the detector FOV) by grey dashed lines. The contours give an adaptation of [Willems and Kolb 2004](#) Figure 10 (right) to our parameter space. See text for details.

evolves from the GB into the WD phase, the orbit either contracts into a common-envelope phase (W04 channels 1–6) or expands as the progenitor loses mass (W04 channel 7, non-interacting systems). To create the contours we drew a Monte Carlo sample of orbital periods from the distribution in W04 Fig. 10 (right), drew WD and MS masses from the distributions in W04 Fig. 10 (left, center respectively) and drew distances from a uniform distribution spanning distances in the H13 sample. We drew orbital inclination from a uniform $\cos i$ distribution and then computed projected separation in au and arcseconds. Our WD detections in this work are plotted in orange.

In Figure 6.11 we reproduce Figure 1 from El-Badry (2024) showing the regime of sensitivity of various *Gaia* multiplicity metrics (for a pair of solar mass stars); we have added the purple box indicating where our new candidate companions fall on this plot. They all fall beyond regions probed by RUWE, and some fall in the spatially resolved section, yet none of them have been spatially resolved in *Gaia*. Most have RUWE values smaller than the typical multiplicity indicator of $\text{RUWE} \gtrsim 1.4$. In addition to tight companions like cc7 and cc8, our survey probes companions too faint to be resolved yet too wide to affect multiplicity metrics, a regime *Gaia* is not currently sensitive to.

Our survey is poised to fill more objects within a sparsely populated regime near the inner edge of the non-interacting WDMS regime generally inaccessible to other methods. Detection and orbital characterization of this population will constrain occurrence rates and simulations of the effect of the companion on planetesimals around the WD. For example, if a large fraction of SLS in the 10–100 au regime prove to be on highly-eccentric orbits with larger semi-major axes, we could infer that objects in this group may be undergoing eccentricity evolution into a high-e state as predicted by Stegmann et al. (2024). Simulations of planetesimal perturbation in these states are warranted (e.g. Stephan et al., 2017). If all are on nearly-circular orbits, then perturbation by external perturbers with subsequent eccentricity evolution is less likely (Stegmann et al., 2024) and pollution is less likely to be influenced by the companion. Previous surveys of more widely separated pairs (those in Figure 6.10) concluded no evidence for companion influence in pollution; this survey provides a different SLS population for which to test this mechanism.

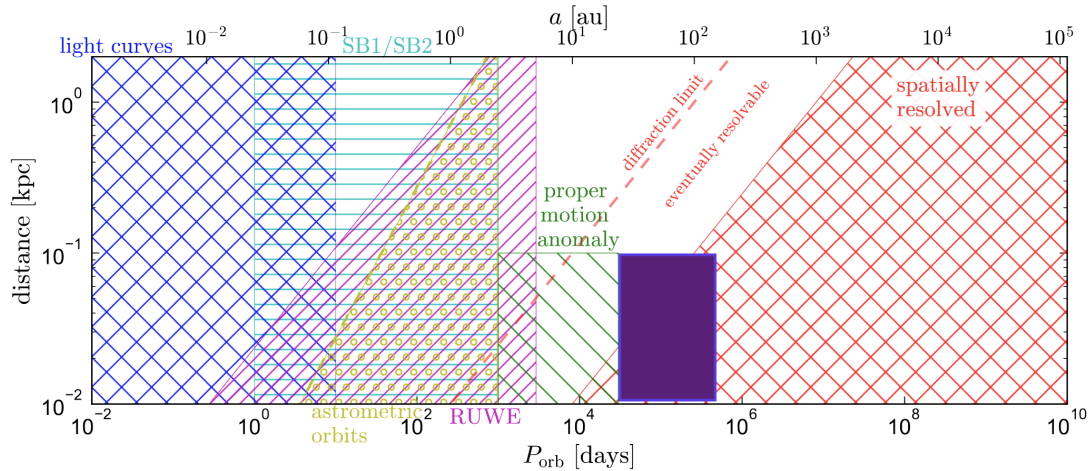


Figure 6.11: Reproduction of Figure 1 from El-Badry (2024) showing the sensitivity regimes of various multiplicity metrics for a two-solar mass binary. We have added the purple rectangle to indicate the regime of the new candidate companions in our survey. They fall outside the regime for which RUWE and PMA are most sensitive, and are too faint to be resolved in *Gaia*, illustrating that these metrics are useful but incomplete for assessing WD multiplicity.

6.4.2 Towards Probes of Companion Influence on Pollution Through Orbit Studies

While the previous studies discussed above have looked at the influence of binarity on WD pollution from a statistical perspective, none to date have examined the orbits of polluted vs non-polluted non-interacting Sirius-Like-Systems observationally. Wide (100’s – 1000’s au) stellar binary orbits evolve on Gyr timescales due to the influence of the Galactic gravitational potential and stellar flybys into (depending on initial conditions) oscillating high and low eccentricity states (Kaib et al., 2013; Bonsor and Veras, 2015; Correa-Otto and Gil-Hutton, 2017; Stephan et al., 2017) with close periastron passages (Heisler and Tremaine, 1986; Collins and Sari, 2008; Modak and Hamilton, 2023) even reaching eccentricities as high as 0.99 (Stegmann et al., 2024). Binaries with semi-major axis from 1000 – 10,000 au are most susceptible to high-e oscillations without disruption on timescales less than a Hubble time (Stegmann et al., 2024). WDMS systems are especially vulnerable as the WD progenitor loses mass and the orbit expands, and planetesimals can be scattered onto star-grazing orbits, especially if a planet is present (Bonsor et al., 2011; Debes et al., 2012). During high-e periastron passages, planetesimals will be perturbed if the binary passes interior to ~ 500 au (Bonsor and Veras, 2015). Approximately 20% of wide binaries are estimated to have orbital parameters in this range to drive WD pollution (Bonsor and Veras, 2015). The binary pollution mechanism may still play a role in pollution for individual systems.

Orbital studies of polluted and non-polluted SLS systems are warranted. Many separations in this and previous SLS surveys are in the range of susceptibility to eccentricity perturbation without disruption; a high- e binary pollution mechanism may still be at play for this population, detectable via an observable trend in eccentricity for polluted SLS systems compared to non-polluted.

A long term goal of the Pup Search is to obtain time series astrometry of new and known polluted and non-polluted SLS systems resolvable to direct imaging. This will require a long-term effort since short-orbit-arc fitting ($\lesssim 50\%$ of the orbital period) artificially inflates the prevalence of high-eccentricity orbits in the posterior, which is the main parameter of interest for this science case (Ferrer-Chávez et al., 2021). Long astrometric time baseline and precision radial velocities of both components will be important. Additionally future *Gaia* data releases containing time series astrometric data, more sources with spectra and radial velocities, and even some SLS in the 100-1000 au separation range with determined orbits will contribute to these studies (while methods currently exist to use *Gaia* data for wide binary orbit fitting [e.g. Pearce et al. 2020], these data are too loosely constraining and will exhibit biased eccentricity results). Proper motion anomaly can also help constrain SLS orbits where available. Zhang et al. (2023) determined dynamical masses and orbital parameters of six confirmed and one candidate SLS using PMA, however the majority of our target list does not have a *Hipparcos* – *Gaia* proper motion measurement, so careful observation and analysis will be required to constrain orbital parameters.

6.4.3 Revisiting the Missing White Dwarf Problem

Holberg et al. (2016) predicted that as many as 100 white dwarfs were “missing” from the 25 pc local volume. Since the sea-change provided by *Gaia*, the local population of single WDs with $G < 20$ mag and WDs in multiples in a 100 pc volume is essentially complete (Gentile Fusillo et al., 2021; Rebassa-Mansergas et al., 2021; Jiménez-Esteban et al., 2023), with $> 97\%$ completeness inside 40 pc (O’Brien et al., 2024). Jiménez-Esteban et al. (2023) determined that white dwarfs resolved in *Gaia* are 100% complete for $G_{BP} - G_{RP} < 0$ mag, $>90\%$ for $G_{BP} - G_{RP} < 0.86$ mag, and decreasing to $\sim 70\%$ at the reddest end. WDs are missing from *Gaia* due to 1) confusion with the Galactic plane ($\sim 1\%$), 2) double degenerate systems counted as single WDs ($\sim 1 - 3\%$), and 3) Unresolved WD+AFGK systems ($< 8\%$, Holberg et al. 2013). In actuality all but four⁵ of

⁵HD 27786/56 Per Ab, HD 149499/HD 149499 B, HD 202109/ ζ Cyg B, BD -7 5906/HD 217411 B

the [Holberg et al. \(2013\)](#) systems closer than 100 pc are resolved in *Gaia*, so the actual missing percentage in the [Jiménez-Esteban et al. \(2023\)](#) catalog is much lower. All of the [Zuckerman \(2014\)](#) systems are resolved in *Gaia* and so are contained in the [Jiménez-Esteban et al. \(2023\)](#) population. [Rebassa-Mansergas et al. \(2021\)](#) used *Gaia* colors to identify sources falling between the WD and main sequences to identify unresolved WD+MS systems. This method identifies mainly WD companions to M and K stars where the WD dominates the SED; they estimate from population synthesis that their sample represents 9% of the underlying WD+MS population, with the other 91% being located within the main sequence as the MS star dominates the SED. [Nayak et al. \(2024\)](#) identified 93 WD+MS candidates within 100 pc using *Gaia* DR3 and *GALEX* GR6/7 UV measurements, 80 of which are newly identified. They were identified using SED fitting and so remain unresolved.

[Katz et al. \(2014\)](#) Figure 1 displays a histogram of number of WDs within 20 pc in bins of absolute V magnitude for single WDs, WD+MS systems from [Holberg et al. \(2008\)](#), and the number predicted from theory. The single WD population matches well the prediction, but the WD+MS population falls below the prediction, implying WD companions are being missed. With the new *Gaia* data we can revisit that plot.

Figure 6.12 shows the number of WDs in the 100 pc volume as a function of absolute V mag. The dashed blue line shows the number of WDs in bins of absolute V magnitude predicted by theory. We used [Katz et al. \(2014\)](#) Eqns 1 and 2 to produce that line:

$$N \approx \dot{n}_{\text{WD}} [t_{\text{cool}}(M_{V,2}) - t_{\text{cool}}(M_{V,1})] \quad (6.3)$$

$$\log_{10}(t_{\text{cool}}/\text{yr}) = -0.04M_V^2 + 1.46M_V - 3.22 \quad (6.4)$$

where \dot{n}_{WD} is the WD formation rate with $\dot{n}_{\text{WD}} = 0.7 \times 10^{-12} \text{ pc}^{-3} \text{ yr}^{-1}$, $t_{\text{cool}}(M_V)$ is the cooling age for a WD with absolute V mag M_V . The purple line is the 100 pc *Gaia* sample from [Jiménez-Esteban et al. 2023](#), the magenta line is the 100 pc WD+MS sample from [Rebassa-Mansergas et al. 2021](#), corrected to 100% completeness of the underlying WD+MS population, the orange line is the new WD+MS from [Nayak et al. 2024](#), and the black line is the sum. The sum follows the prediction closely except at the faintest end where WD detection is challenging for the coolest and faintest WDs.

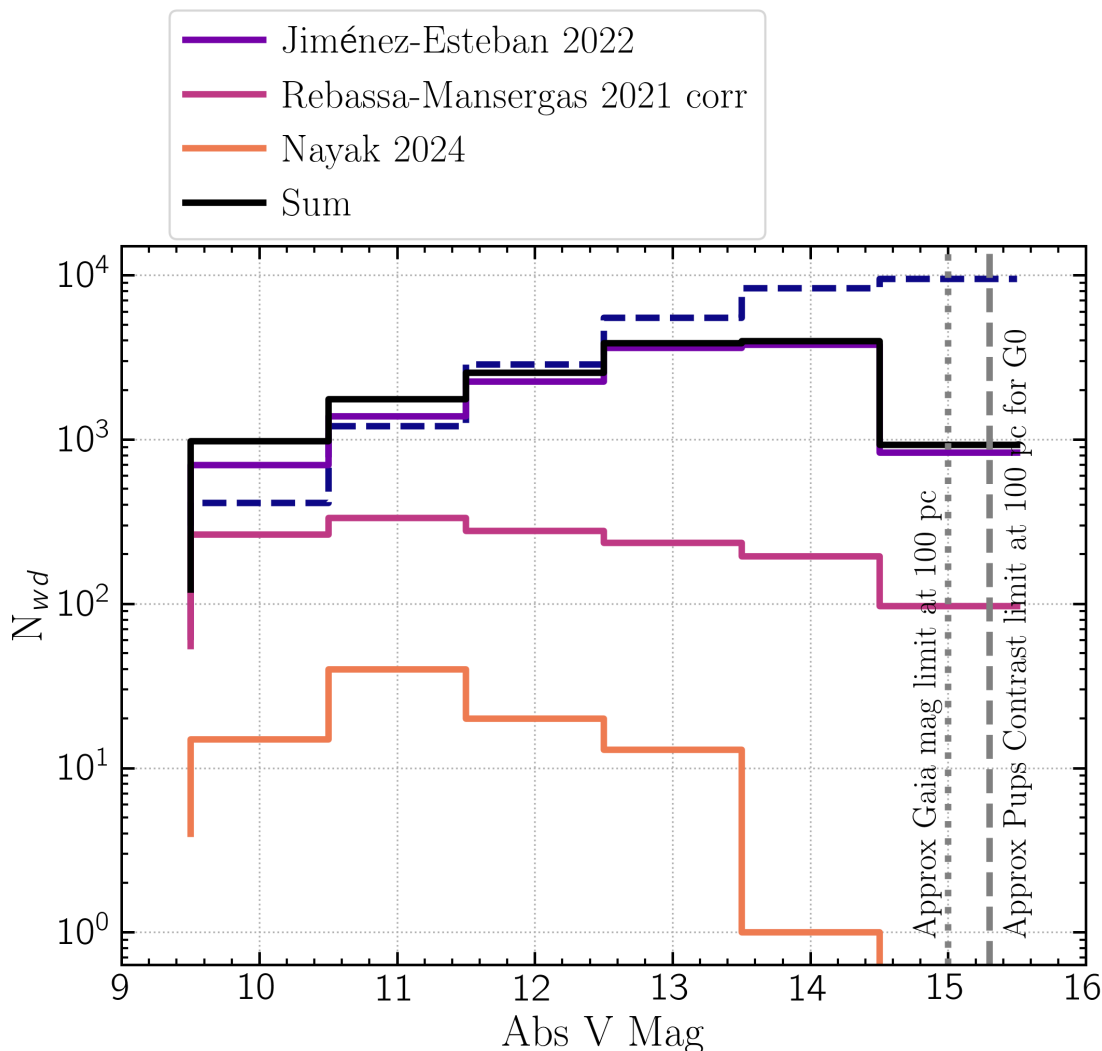


Figure 6.12: Number of WDs expected and observed within 100 pc local volume. The dashed blue line is the number of WDs predicted by theory (see text for details), the purple line is the 100 pc *Gaia* sample from Jiménez-Esteban et al. 2023, the magenta line is the 100 pc WD+MS sample from Rebassa-Mansergas et al. 2021, corrected for their 80% completeness of their sample and the 9% completeness of their sample from the underlying WD+MS population, the orange line is the new WD+MS from Nayak et al. 2024, and the black line is the sum. We did not include WD+MS surveys for which the objects are resolved in *Gaia*, since they would be captured in the Jiménez-Esteban et al. (2023) catalog. The dotted grey line shows the approximate detection limit for *Gaia* for a WD at 100 pc, assuming a detection limit of $G = 20$ mag; the dashed grey line shows the approximate detection limit for the Pup Search for a WD companion to a G0 star at 100 pc, assuming a noise floor of 5×10^{-5} , the best case in our initial survey results.

Only five of the current batch of Pup Search targets are within ~ 100 pc, so our discovery survey is not poised to make much of a dent in that particular parameter space; our 84 initial targets extend to almost 700 pc. Assuming a detection limit contrast of 5×10^{-5} to a G0 star and the same detection rate as in this paper (7/14, including the subdwarf Pups-cc2), we estimate this set of targets will return 38 ± 5 new SLS. As part of this work we will continue to compile SLS discoveries, which our results will add to, in our efforts to examine the population as a whole.

6.5 Conclusion

We have introduced the ExAO Pup Search, a survey using the tools of extreme AO instrumentation to probe the influence of non-interacting wide stellar companions to white dwarf stars. We have conducted the first Pup Search observations of 14 target stars and have detected one new confirmed Sirius-Like System, PupS-1B, a DA white dwarf ~ 100 au (900 mas) from the Sun-like star TYC 4831-473-1. We detected four additional candidate SLS: confirmed white dwarf objects close to AFGK stars which we will be following up with additional observations to confirm they are bound companions. We detected one subdwarf candidate companion ~ 500 mas from the G9IV star 33 Sex, and one main sequence companion to HD 108738, and one low-S/N candidate signal ~ 140 mas from TYC 169-1942-1. Several of our targets without detections had low contrast limits due to observational challenges and merit followup with more field rotation for adequate ADI reduction. Our target list is drawn from a high-quality sample of stars with UV excess and radial velocity trends, so non-detections are likely due to the companion being too close to the star to resolve rather than there not being a companion at all.

The goal of the Pup Search is to contribute to the discussion of the influence of wide companions in driving white dwarf pollution by probing regimes inaccessible to previous surveys, and to probe orbital parameters of polluted and non-polluted systems. Future work will continue to use the tools of ExAO, precision radial velocity, and high resolution spectroscopy towards this goal.

Chapter 7

Ongoing Project: Reflected Light Exoplanet Observations with MagAO-X and GMagAO-X

“Do you ever wonder if – well, if there are people living on the third planet?”

“The third planet is incapable of supporting life,” stated the husband patiently. “Our scientists have said there’s far too much oxygen in their atmosphere.”

Ray Bradbury

The Martian Chronicles (1950)

7.1 Introduction

7.1.1 Observing Exoplanets in Reflected Light

In Chapter 1 I showed that direct imaging (DI) planet surveys to date, which detected young giant planets through their thermal emission in Near- to Mid-IR, have had exceedingly low survey yields, and that this detection method is limited to young giant planets on wide orbits from their stars. Yet other detection methods have found numerous smaller planets closer to their stars than DI surveys have achieved to date, necessitating different observing strategies to probe older and more diverse planetary systems. Some researchers are moving to longer wavelengths to detect colder planets in thermal emission. The MagAO-X instrument (Males et al., 2022) is designed to push technology in visible wavelengths to detecting planets in the light they reflect from their host star.

This is still however technologically very challenging. In Chapter 1 I showed that the contrasts involved in reflected light imaging are extremely high ($\mathcal{O}10^{-6}$ – 10^{-10}) and that reflected light planets are brighter at closer separations, requiring controlling speckles and digging dark holes at $\sim 2\lambda/D$, neither of which has been done before.

Figure 7.1 shows ~ 400 of the nearest known exoplanets detected via radial velocity with projected separation in λ/D for a 6.5m telescope at 800 nm on the x-axis, and Lambertian contrast ratio for a uniform reflecting sphere (no atmospheric features) on the y-axis. Contrast was computed as:

$$C(\alpha, \lambda) = A_g(\lambda) \left(\frac{R_p}{r} \right)^2 \left[\frac{\sin \alpha + (\pi - \alpha) \cos \alpha}{\pi} \right] \quad (7.1)$$

where $C(\alpha, \lambda)$ is planet-star contrast at wavelength λ as a function of viewing phase α , $A_g(\lambda)$ is geometric albedo (which we set to constant 0.3 for this illustration), R_p is planet radius, r is planet-star separation in the orbit plane (“true” separation). And viewing phase α as a function of orbital elements is given by:

$$\alpha = \cos^{-1} [\sin(i) \sin(\theta + \omega_p)] \quad (7.2)$$

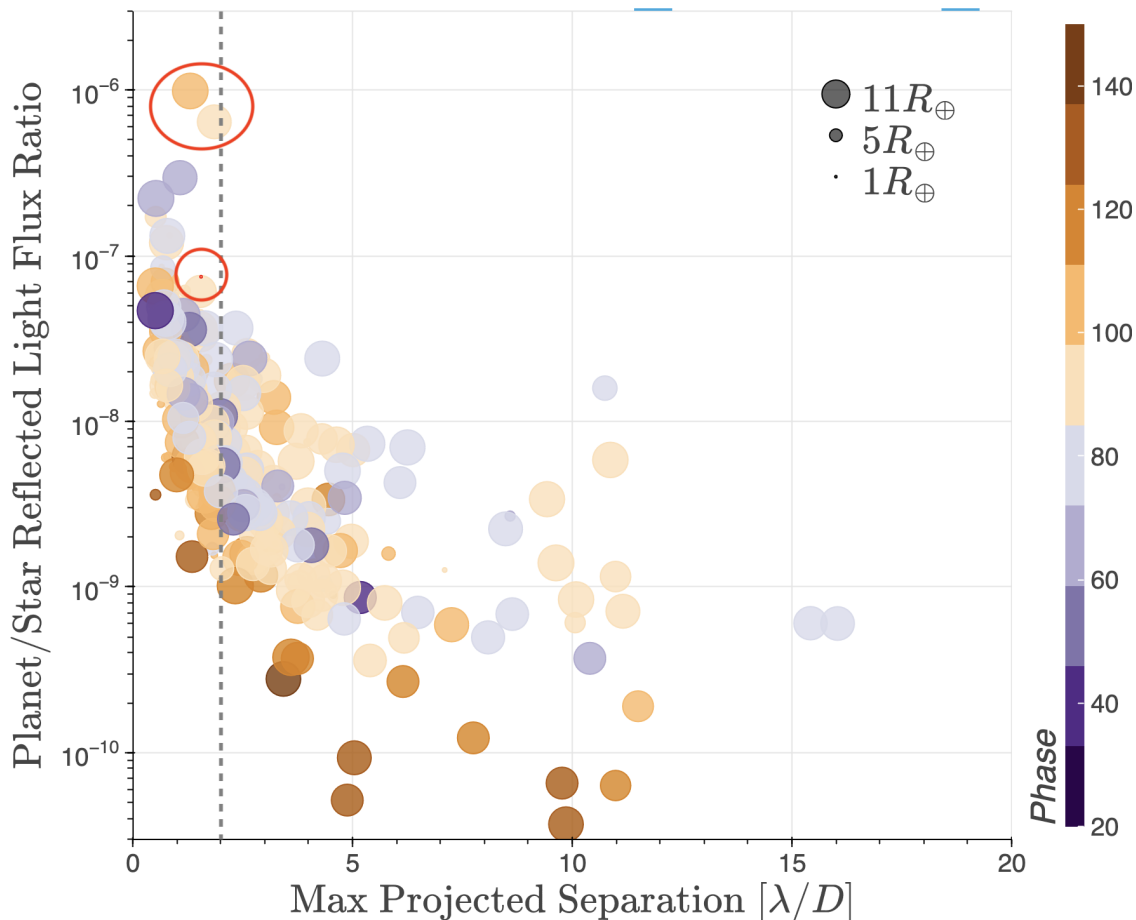


Figure 7.1: 100s of the nearest known radial velocity detected exoplanets in separation (in λ/D for a 6.5 m mirror at 800 nm) vs Lambertian contrast. The dashed grey line marks a typical resolution limit of $2\lambda/D$. Proxima Centauri b and GJ 876 b/c are marked with red circles. An interactive version of this plot with details for each planet is available here: <http://www.loganpearcescience.com/reflected-light-calculations.html>

where ω_p is argument of periastron, i is inclination, with $i = 90^\circ$ being edge on and $i = 0^\circ$ and $i = 180^\circ$ being face on, θ is the true anomaly with

$$\theta = 2 \tan^{-1} \left[\sqrt{\frac{1+e}{1-e}} \tan(E/2) \right] \quad (7.3)$$

where, e is the eccentricity, E is the eccentricity anomaly, and

$$M = E - e \sin E \quad (7.4)$$

and

$$M = 2\pi \frac{\Delta t}{P} \quad (7.5)$$

where M is the mean anomaly, Δt is the time since periastron passage], P is the orbital period, (Sobolev, 1975; Cahoy et al., 2010, 2017). For planets without a known orbital inclination we used $i = 60^\circ$ (the average inclination for a uniform half-sphere); for planets without a known mass we used $M \sin(i)$ (the minimum mass, determined from radial velocity measurements). For planets without a known radius we used an empirical Mass/Radius relation, shown in Figure 7.2.

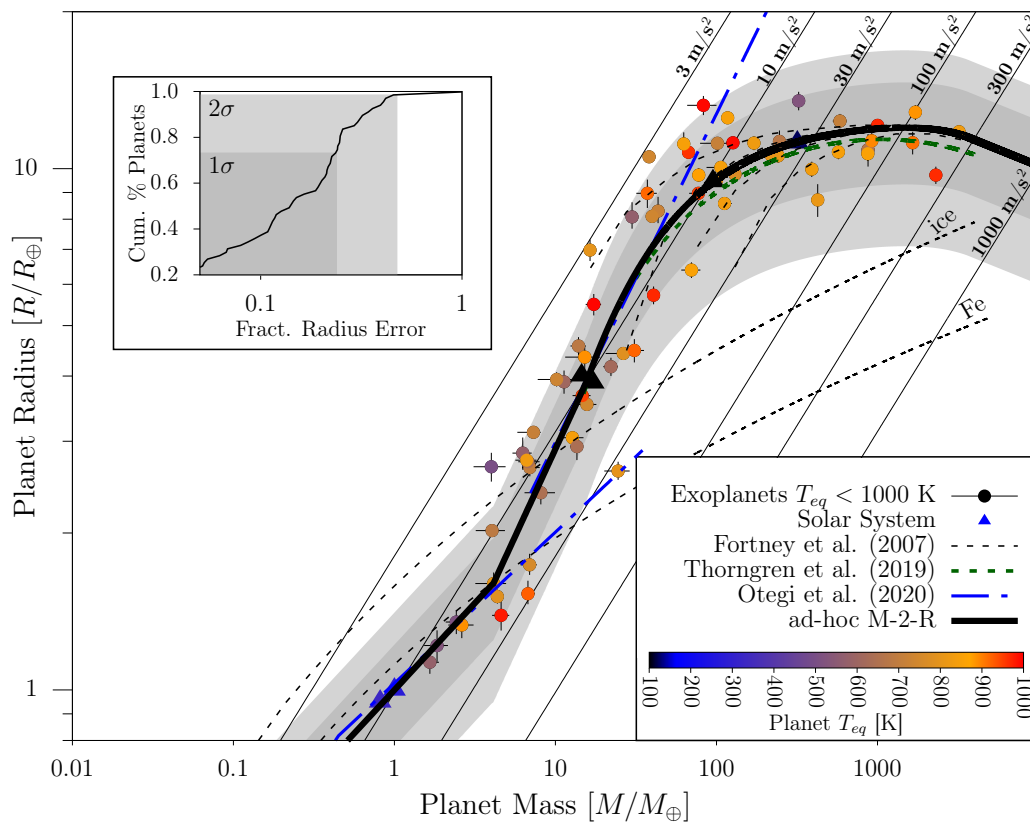


Figure 7.2: Empirical mass-radius relation for planets derived from references given and compiled at <https://jaredmales.github.io/mxlib-doc/>

From Figure 7.1 we see that for a 6.5 m telescope in visible wavelengths, most of the planets are contrast 10^{-6} – 10^{-10} , and are closer than a typical diffraction-limited resolution of $2\lambda/D$. The two brightest planets in Figure 7.1 (marked with a red circle) are GJ 876 b and c; the nearest known and likely terrestrial planet, Proxima Centauri b is also marked with a red circle at $1.7\lambda/D$ and contrast 7.5×10^{-8} .

The Extreme Wavefront Control Lab at the University of Arizona is developing the extreme AO coronagraphic instrument for Giant Magellan Telescope (GMT) called GMagAO-X, expected to be ready by first light. Compared to the 6.5 m mirror of the Magellan Clay Telescope, the GMT will have a 24.5 m primary, increasing the collecting area by a factor of ~ 14 . In addition to having a larger photon collecting bucket, this drops the diffraction-limited resolution limit at 800 nm from 25 mas to 7 mas, allowing the resolution of companions at much closer separations than capable by current telescopes. When we look at Figure 7.1 for GMagAO-X, now Proxima Centauri b and the GJ 876 planets fall at a much easier $\sim 5 \lambda/D$. GMagAO-X will be able to image tens to hundreds of exoplanets in reflected light.

7.1.2 *Breaking the Phase-Radius Degeneracy*

As discussed briefly in Chapter 1, the planet's viewing phase is a major obstacle in reflected light imaging. Planets are brightest at full phase, yet that occurs only for nearly-edge-on orbits at superior conjunction, when the planet is directly behind the star and totally inaccessible to imaging. For closer to face-on orbits the phase is nearly constant at quadrature. Additionally, there is a phase-radius degeneracy – small planets at full phase can have the same contrast as large planets at high phase, as illustrated in Figure 7.3. To understand our observations we need to know phase either or radius to break this degeneracy. The planets in Figure 7.1 are all detected via radial velocity, which gives an estimate of the minimum mass of the planet, but not the radius. Some have full mass and radius estimates, enabling breaking the degeneracy. Without a radius estimate, we can use the mass-radius relation in Figure 7.2 to estimate radius. If we have well-constrained orbital elements we can predict the phase at any point in the orbit using the equations in the previous section.

7.1.3 *Preparing for Reflected Light Observations*

The planets in Figure 7.1 represent the target list for upcoming MagAO-X and GMagAO-X reflected light surveys. To maximize survey yield, information content, atmospheric characterization, and to prioritize targets and observation timing, careful modeling and simulation work must be carried out prior to trying to perform these challenging observations.

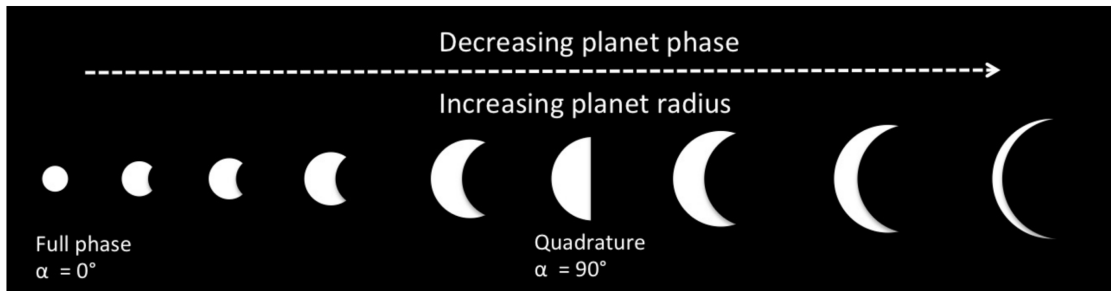


Figure 7.3: Nayak et al. (2017) Figure 1 illustrating the phase-radius degeneracy for reflected light planets. Small radius planets at full phase will appear at the same brightness as large radius planets at larger phase angles, necessitating additional information (estimates of planet radius or phase) to distinguish these cases for a flux measurement.

7.2 Methods

7.2.1 Modeling Reflected Light Observations

To prepare for reflected light observations with MagAO-X and GMagAO-X, I am conducting extensive open-source modeling work called the REFLECTX Model Suite (<https://reflectx.readthedocs.io/>). REFLECTX is built on the exoplanet atmosphere radiative transfer code PICASO (Batalha et al., 2019) and cloud code VIRGA (<https://natashabatalha.github.io/virga/>).

PICASO is a python-based open-source planetary intensity code for atmospheric scattering built on codes developed in McKay et al. (1989), Marley et al. (1999), and Cahoy et al. (2010). Figure 7.4 illustrates PICASO's approach to solving the radiative transfer equation through a 1-D plane-parallel approximation:

$$I(\tau_i, \mu) = I(\tau_{i+1}, \mu)e^{\delta\tau_i/\mu} - \frac{1}{\mu} \int_0^{\delta\tau_i} S(\tau', \mu)e^{\tau'/\mu} d\tau' \quad (7.6)$$

(Eqn 2.98 of Goody and Yung, 1989) where $I(\tau_i, \mu)$ is the azimuthally average intensity exiting the top of the atmospheric layer i , at angle μ relative to layer normal and with opacity τ in the layer. $I(\tau_{i+1}, \mu)e^{\delta\tau_i/\mu}$ is the intensity from layer $i + 1$ incident on the bottom of layer i (layer values decrease from planet surface to top of atmosphere) which is attenuated by the opacity in layer i described by the term $e^{\delta\tau_i/\mu}$. $S(\tau', \mu)$ is the source function. PICASO treats the source function via two components: single scattered radiation and multiple scattered radiation. Reproducing Eqn 2 of Batalha et al. (2019) for the source function:

$$S(\tau', \mu) = \underbrace{\frac{\omega}{4\pi} F_0 P_{\text{single}}(\mu, -\mu_0) e^{-\tau'/\mu_s}}_{\text{Single scattering component}} + \underbrace{\frac{\omega}{2} \int_{-1}^1 I(\tau', \mu') P_{\text{multi}}(\mu, \mu') d\mu'}_{\text{Multiple scattering component}} \quad (7.7)$$

where the first term describes single scattered (orange, Figure 7.4) with phase function $P_{\text{single}}(\mu, -\mu_0)$ and the second term describe multiple scattered radiation integrated over all angles with phase function $P_{\text{multi}}(\mu, \mu')$; ω is the single scattering albedo, and F_0 is the incident stellar radiation.

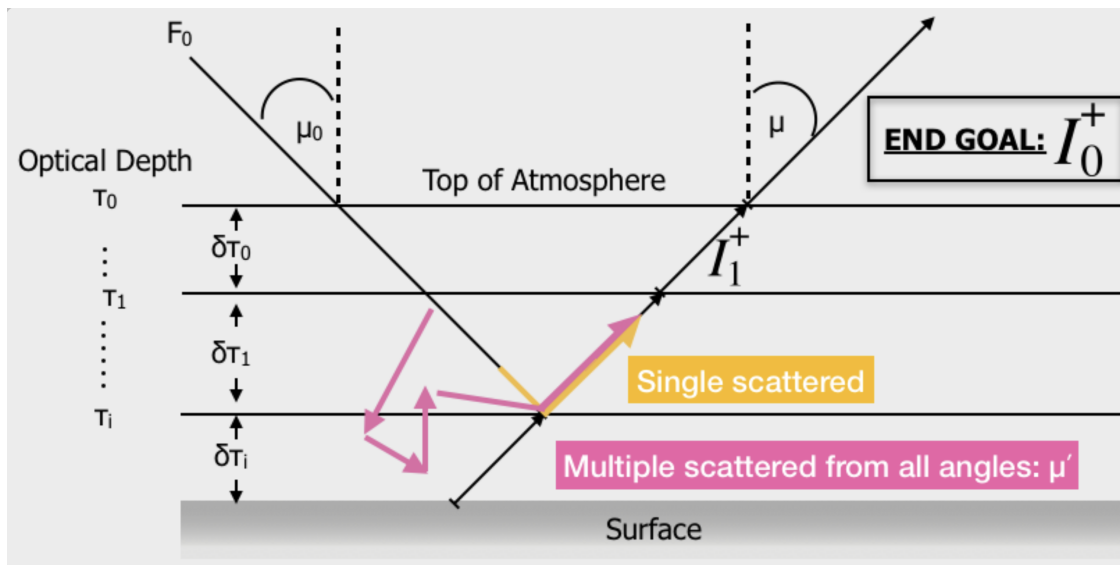


Figure 7.4: Figure 3 of Batalha et al. (2019) illustrating how PICASO solves 1D radiative transfer for exoplanet atmospheres. The observer sees emitted radiation I_0^+ as a function of angle relative to surface normal (μ). The stellar radiation F_0 is incident at angle μ_0 at the top atmosphere layer T_0 . The atmosphere is modeled as a series of plane-parallel layers T_i . Incident radiation is attenuated by optical depth in the layer δT_i .

Single scattering component P_{single} : For the single scattering component, PICASO starts with a basis in the Henyey-Greenstein phase function:

$$P_{\text{OTHG}} = \frac{1 - g^2}{(1 + g^2 - 2g \cos \Theta)^{3/2}} \quad (7.8)$$

where OTHG refers to the One-Term Henyey-Greenstein phase function, Θ is the angle between the incident and scattered directions, with $\alpha = \pi - \Theta$, and g is the asymmetry parameter which describes the fraction of photons scattered in the forward vs backward direction. Asymmetry parameter $0 < g \leq 1$ is predominantly forward scattered (photons continue in their original direction), $-1 \leq g < 0$ is predominantly back scattered (photons reverse direction), and $g = 0$ is

isotropically scattered. However this formulation fails to capture the back scattering peak observed in solar system planets, so PICASO builds on this with the Two-Term Henyey-Greenstein phase function:

$$P_{\text{TTHG}} = fP_{\text{OTHG}}(g_f) + (1 - f)P_{\text{OTHG}}(g_b) \quad (7.9)$$

that captures both forward (g_f) and backward (g_b) scattering and the fraction of forward/backward scattering f (a user-tunable parameter). Finally, PICASO also captures the contribution of Rayleigh scattering in the single scattering phase function through:

$$P_{\text{TTHG.ray}} = \frac{\tau_{\text{cld}}}{\tau_{\text{scat}}} P_{\text{TTHG}} + \frac{\tau_{\text{ray}}}{\tau_{\text{scat}}} P_{\text{ray}} \quad (7.10)$$

where $P_{\text{ray}} = \frac{3}{4}(1 + \cos^2 \Theta)$, τ_{cld} is cloud opacity, τ_{ray} is Rayleigh scattering contribution, and τ_{scat} is total scattering.

Multiple scattering component P_{multi} : For the multiple scattering component, PICASO implements the methodology of [Toon et al. \(1989\)](#) (1989). The source function must be integrated over all angles μ , so the phase function is approximated as a series of Legendre polynomials. Reproducing [Batalha et al. \(2019\)](#) Eqn 9:

$$P_{\text{multi}}(\cos \Theta) \approx \sum_{l=0}^{N-1} \beta_l P_l(\cos \Theta) \quad (7.11)$$

where $P_l(\cos \Theta)$ are the Legendre polynomials and β_l are moments of the phase function: $\beta_l = (2l + 1)g_l$. Simplifying: $P_{\text{multi}}(\cos \Theta) = 1 + 3\bar{g}\mu\mu'$, where \bar{g} is the cloud asymmetry factor and $\cos \Theta = \mu\mu'$ under the assumption of azimuthal independence. The second-order Legendre dependence on $\cos^2 \Theta$ captures Rayleigh scattering ([Snook, 1999](#)) and so the 2-term option is default in PICASO. PICASO also makes use of the δ -Eddington approximation ([Joseph et al., 1976](#)) and Raman scattering shifts to improve on the accuracy, but I will not go into depth with those here. Further improvement in accuracy was recently demonstrated using a four-term spherical harmonic solution in [Rooney et al. \(2023\)](#), which achieved enhancement of accuracy without increase in

computational time, and found that it better captured the back scattering peak of multiple scattered photons than did previous PICASO methodology.¹

All of this means that the solution of the radiative transfer equation, i.e., the intensity of radiation emitted from the top of the atmosphere, is controlled in PICASO by the single scattering albedo ω , the asymmetry parameter g , and cloud and Rayleigh opacities τ . The value of these parameters are determined in different ways for gas giant and terrestrial planets and will be discussed in the following sections.

While the phase functions described above don't fully capture the full scattering physics expected in planetary atmospheres, they have been used to reproduce Solar System spectra at an accuracy sufficient for our purposes with these models (e.g., Jupiter and Saturn, [Dyudina et al. 2016](#); [Lupu et al. 2016](#); Earth, [Feng et al. 2018](#)). [Feng et al. \(2018\)](#) specifically designed a cloud model (using the same underlying framework designed above based on [Cahoy et al. 2010](#)) to sufficiently recreate a realistic Earth-like spectrum at sufficient accuracy for parameter retrieval studies at different spectral resolutions, while being minimally parametric. Ultimately, [Lupu et al. \(2016\)](#) showed that the retrieval of properties from scattered-light observations are insensitive to the details of particular phase functions and can't constrain phase function parameters, so we expect this model framework to be accurate to a sufficient level for our purposes (e.g., scattered light retrievals, determining minimum S/N and instrument resolving powers).

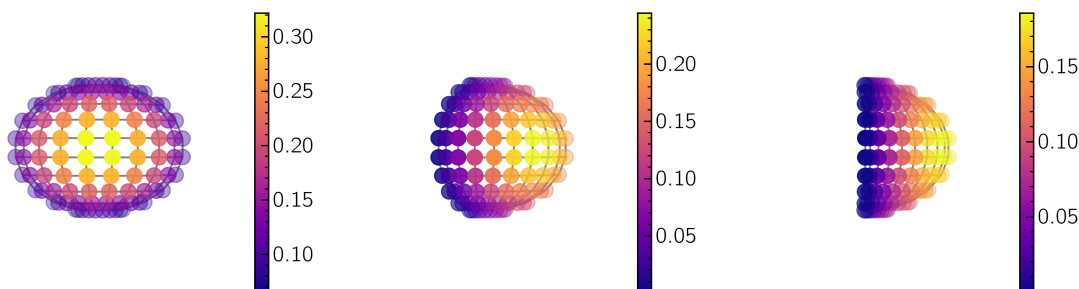


Figure 7.5: Points at which PICASO computes intensities for different phase angles – full phase, 60° , and 90° . Each example uses 10 vertical Chebyshev angles and 10 horizontal Gauss angles, following the formality of [Horak and Little \(1965\)](#). The number of angles for each is user-specified, with more angles requiring longer computation times. PICASO automatically takes advantage of symmetry where possible to speed up calculation times.

¹For a detailed derivation of all of the above, plus illustrations of how the different formulations impact the results, see https://natashabatalha.github.io/picaso_dev

Incorporating viewing phase: An advantage in PICASO is the ability to compute intensity over several facets across the surface of a planetary disk independently, and so account for phase angle dependence. Figure 7.5 shows the points at which intensities are calculated for a PICASO reflected light spectrum for $\alpha = 0^\circ$, 60° , and 90° , with calculation points determined using the method of Horak and Little (1965). For each case we have used 10 Chebyshev angles (vertical) and 10 Gauss angles (horizontal); the colormap corresponds to the intensity of reflected radiation.

Clouds: PICASO interfaces with the cloud modeling code VIRGA². VIRGA incorporates particle and gas physics to generate models for how clouds contribute to a reflected light spectrum. VIRGA uses molecular condensation curves coupled with a pressure-temperature profile to determine which species condense and at what altitude.

Cloud properties are parameterized mainly through two parameters:

- f_{sed} is the sedimentation efficiency which controls the vertical extent of clouds (Ackerman and Marley, 2001; Gao et al., 2018)
- K_{zz} is the eddy diffusion coefficient and controls the strength of vertical mixing (Mukherjee et al., 2022)

The cloud sedimentation model of Ackerman and Marley (2001) Eqn 4 states:

$$-K_{zz} \frac{\delta q_t}{\delta z} - f_{\text{sed}} \omega_* q_c = 0 \quad (7.12)$$

where q_c is the molar mixing ratio of condensed material, q_t is the total molar mixing ratio (condensed and vapor phases), ω_* is the convective velocity scale, and z is the altitude. This equation means that the upward mixing of condensates and vapor is balanced by downward sedimentation of particles. Smaller values of f_{sed} ($f_{\text{sed}} < 1$) gives lower sedimentation efficiency and so thicker, more vertically extended clouds with small particles; $f_{\text{sed}} > 1$ gives larger particles and thinner compressed clouds. Higher K_{zz} gives stronger vertical mixing producing more vertically extended clouds. So for our cloud models, the cloud properties are set mainly by the model pressure-temperature (PT) profile (which controls what condenses and where), f_{sed} , and K_{zz} . Additional tunable cloud parameters are the gas mean molecular weight (mmw) and the mass mixing ratio (mmr) which can adjusted for specific condensates.

²<https://natashabatalha.github.io/virga/index.html>

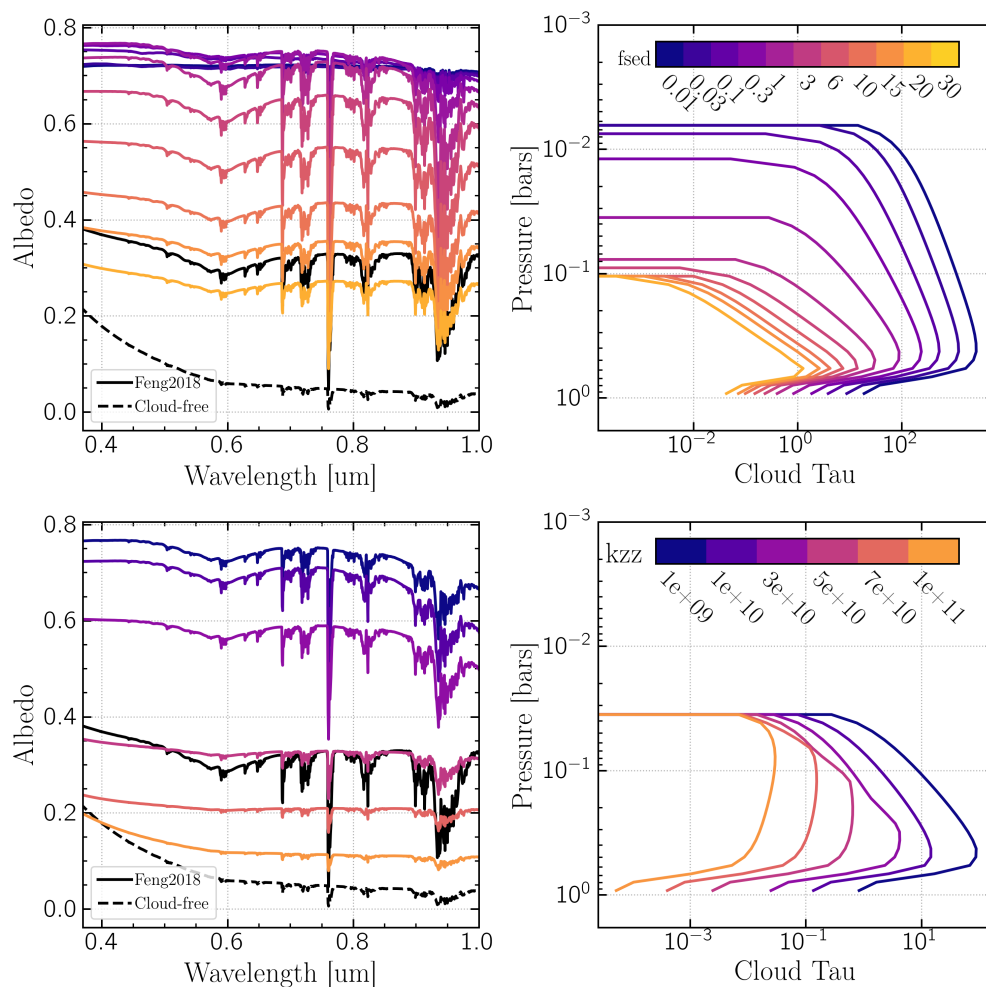


Figure 7.6: The effect of varying f_{sed} (top) and K_{zz} (bottom) on Earth-like atmosphere spectrum with water clouds. For each of the two pairs of plots, the named parameter is varied and the remaining parameters are kept constant. The left-hand plots show the resulting albedo spectrum compared to an Earth-like model in Feng et al. (2018) (black) and a cloud-free model (black dashed); the right-hand plots show the cloud vertical extent (y-axis) and optical depth (x-axis).

Figure 7.6 shows the effect of varying cloud parameters on cloud extent and albedo spectrum for an Earth-like atmosphere with water clouds. Low values of f_{sed} (upper plots) produce high-altitude thick clouds with a highly-reflective albedo, while high values produce thin less-reflective clouds. Low strength of vertical mixing K_{zz} (lower plots) produces thicker more opaque and more reflective clouds.

Putting it together into a model suite: In the REFLECTX model suite we use different methodologies for modeling terrestrial and gas giant planets in PICASO, which will be discussed in detail

below using our Proxima Centauri b models as a prototypical terrestrial planet and GJ 876 b/c as prototypical gas giant planets.

7.2.2 Modeling Gas Giant Planets: GJ 876 b/c

GJ 876 b and c are the two large bright planets near $2\lambda/D$ in Figure 7.1, making them ideal first targets for reflected light imaging. They are in a 4 planet system with planets d and e interior to c, with c, b, and e and in a 1:2:4 Laplace mean motion resonance chain (Rivera et al., 2010). Their large masses, well-characterized orbits (Correia et al., 2010; Trifonov et al., 2018) and 3-planet resonant chain, and proximity to Earth have made them a boon for dynamical studies (e.g. Batygin et al., 2015; Nelson et al., 2016) and tests of formation and evolution (e.g. Batygin et al., 2015, and numerous references therein). The system is dynamically stable for at least 100 Myr despite the large eccentricity for planet c (Correia et al., 2010; Trifonov et al., 2018). Inclination for b and c have somewhat differing solutions, we adopt the value of $i = 59^\circ$ of Rivera et al. (2010) and Trifonov et al. (2018) for both.

For gas giant planets, PICASO takes in star and planet properties and iteratively solves for the pressure-temperature (PT) profile, which describes how the temperature varies with pressure, an analog for altitude above the surface. In addition to the star and planet properties listed in Table 7.1, the PICASO climate calculation also takes a guess of the planet's T_{eff} (set by star-planet separation), a C/O ratio, an initial guess of the radiative/convective boundary layer, and an initial guess at the PT profile. For a detailed description and diagram of the PICASO climate solver see Mukherjee et al. (2023) Figure 1. For the REFLECTX gas giant models, we used the default PICASO suggestions for initial PT profile guess, which is based on the analytic approximation of Guillot (2010). For effective temperature, we approximate as the planet's equilibrium temperature, where $T_{\text{eq}} = T_{\text{eff},\odot} \sqrt{R_\odot/\rho} [f'(1 - A_b)]^{1/4}$ where ρ is star-planet separation, f' is a function describing heat distribution which approximates to 1/4, A_b is the Bond albedo which we approximate to 0.3. For the atmosphere setup we use the recommended configuration which is 91 atmospheric layers with bottom layer at 100 bars and top layer at 1×10^{-6} bars. We set one convection zone from layer 85–83, with $r_{st} = 0.5$, which sets the contribution of stellar radiation to net flux (see Mukherjee et al., 2023, Eqn 20). The C/O ratio is the final input parameter, which affects molecular mixing ratios. C/O is the most significant parameter controlling concentrations of C and O bearing species,

Table 7.1: GJ 876 Star and Planet Parameters

Parameter	Value	Ref
GJ 876		
T _{eff}	3300 K	1
Radius	0.37 R _☉	1
SpT	M2.5V	2
Log(Lum)	-1.194±0.007 L _☉	3
Log(g)	4.9 cm s ⁻²	1
Metallicity	0.21 dex	1
Distance	4.6709±0.0008 pc	6
GJ 876 b		
sma	0.2177 ^{+0.0018} _{-0.0019} au	1
period	61.03474 ^{+0.00080} _{-0.00084} d	1
ecc	0.0020 ^{+0.0019} _{-0.0014}	1
incl	59°	4
M _p	2.2756±0.0045 M _{Jup}	5
T _{eq}	190 K	This Work
GJ 876 c		
sma	0.1363 ^{+0.0011} _{-0.0012} au	1
period	30.22902 ^{+0.00052} _{-0.00055} d	1
ecc	0.25591±0.00093	5
incl	59°*	5
M _p	0.7142±0.0039 M _{Jup}	5

(1) [Rosenthal et al. 2021](#), (2) [Turnbull 2015](#),
(3) [von Braun et al. 2014](#), (4) [Trifonov et al. 2018](#),
(5) [Rivera et al. 2010](#), (6) [Bailer-Jones et al. 2018](#)
*[Rosenthal et al. \(2021\)](#) enforce coplanarity with
GJ 876 b to derive parameters for GJ 876 c

especially for temperatures $\gtrsim 1200$ K (Madhusudhan, 2012). With these input the model then iteratively computes chemistry, opacities, upwelling and downwelling, adjusting number, location, and extent of convective zones until radiative/convective equilibrium is achieved, producing a final PT profile and chemical makeup.

Once the chemistry and PT profile has been computed, we then produce cloudy and cloud-free albedo and contrast spectra. We produced cloud models for $K_{zz} = [1 \times 10^9, 1 \times 10^{11}]$, $f_{\text{sed}} = [0.03, 0.3, 1, 3, 6]$, and C/O ratio = $[0.5, 1.0, 1.5]$, .

GJ 876 b

GJ 876 b is on a nearly-circular orbit. We computed models for constant star-planet separation and 25 phase angles spanning the range of angles allowed by the orbital inclination, shown in Figure 7.7 as black x's. $1\lambda/D$ and $2\lambda/D$ for MagAO-X and GMagAO-X are marked with grey solid and dashed lines. GJ 876 b is within $2\lambda/D$ for MagAO-X for its entire orbit, making it a challenging observation; however it is entirely outside $2\lambda/D$ for GMagAO-X. The optimal time to observe it will be at quadrature, which corresponds to maximum orbital plane-of-sky elongation.

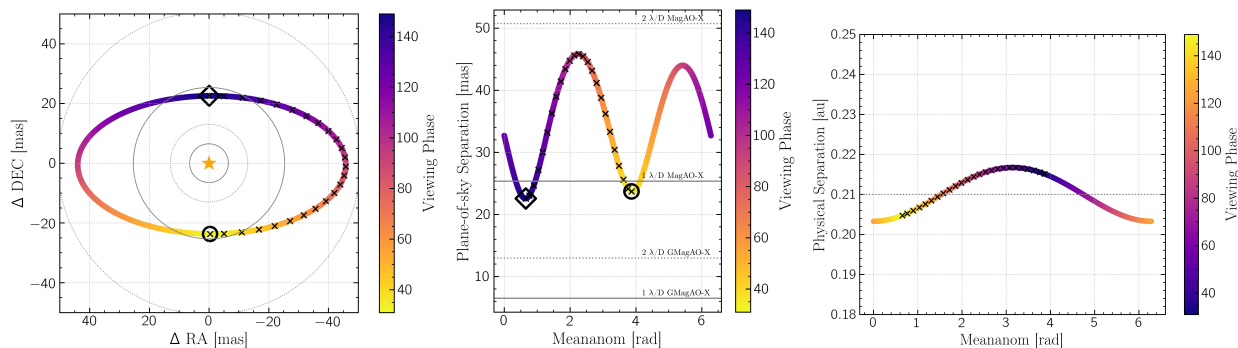


Figure 7.7: Phase angle sampling as a function of orbit for GJ 876 b modeling. We produced models for all points marked with a black x. Black circle marks inferior conjunction (brightest phase) and black diamond marks superior conjunction (faintest phase). The solid grey lines mark $1\lambda/D$ for MagAO-X ($D = 6.5$ m, $\lambda = 800$ nm) and GMagAO-X ($D = 24.5$ m, $\lambda = 800$ nm); the dashed grey lines mark $1\lambda/D$ for MagAO-X and GMagAO-X. The colormap shows the viewing phase at each point in the orbit. Left: the orbit projected on the plane of the sky (longitude of nodes arbitrarily set to 90° as it is unconstrained); Middle: the separation in the plane of the sky as a function of the orbital phase (parameterized by mean anomaly, where meananom = 0π is periastron and the orbit proceeds through meananom = 2π); Right: separation in the orbital plane, which sets the equilibrium temperature for the models and controls the chemistry. GJ 876 b remains within $2\lambda/D$ for MagAO-X throughout its orbit, but is entirely outside $2\lambda/D$ for GMagAO-X, even at its brightest phase. The orbital separation changes by less than 0.02 au throughout the orbit, so the model PT profile and chemistry do not change as a function of separation.

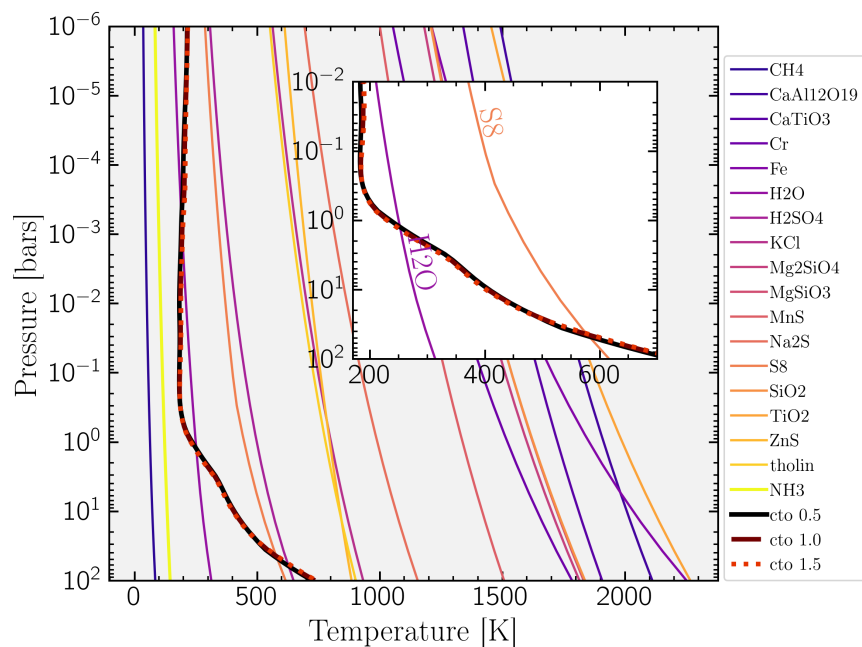


Figure 7.8: Pressure-temperature profile for GJ 876 b models plotted with condensation curves for chemical species. The thick lines give PT profile for the three C/O ratios modeled; the PT profile is not meaningfully affected by C/O ratio or orbital phase. The inset shows the region where the PT profile crosses with S_8 (sulfur hazes) and water curves showing where in the atmosphere those species condense into clouds.

Figure 7.7, right, shows the orbital separation over the course of the orbit; the planet-star separation never varies more than 0.02 au due to the nearly-circular orbit. Thus the model PT profile and chemistry do not change significantly during the orbit. Figure 7.8 shows the PICASO-computed PT profile for three values of C/O ratio (which is less critical here due to lower temperatures), plotted with condensation curves for molecular species in VIRGA. The inset shows the region where the PT profile crosses the sulfur hazes (S_8) and water curves, indicating where those species will condense. We produced cloud-free and cloudy (via parameters given above) albedo and contrast spectra for the 25 phases shown in Figure 7.7.

GJ 876 c

GJ 876 c is closer and more eccentric ($e = 0.26$) than GJ 876 b. We produced models for 25 phases spanning the range allowed by inclination, however due to the high eccentricity the planet-star separation varies significantly over the course of an orbit, enough to affect the model and resulting spectra. Figure 7.9 shows the visible phase sampling for our models as a function of the orbit. We have chosen to sample phases along the longer half of the projected orbit. As seen in

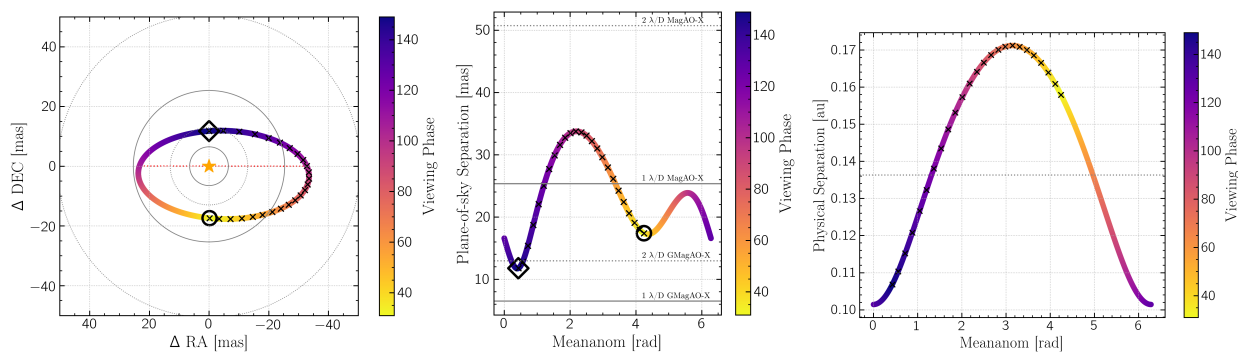


Figure 7.9: Phase angle sampling as a function of orbit for GJ 876 c modeling. See Figure 7.7 for explanation. The orbital separation changes significantly throughout the orbit, so the model PT profile and chemistry will change as a function of separation. Left: the red dashed line marks the line of nodes, with phase >90 being towards the observer and phase <90 being away from the observer

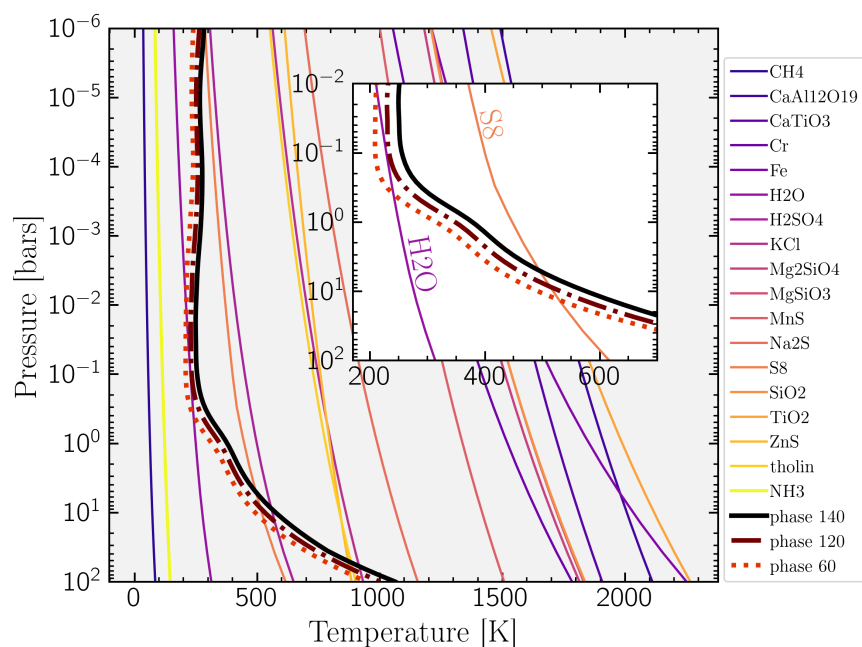


Figure 7.10: Pressure-temperature profile for GJ 876 c models plotted with condensation curves for chemical species. See Figure 7.8 caption for explanation.

Figure 7.9 (right), the planet-star separation varies by ~ 0.07 au over the course of our modeling, which will impact the planet chemistry (see Section 7.3).

Figure 7.10 shows the computed PT profile for GJ 876 c. The thick lines show the PT profile at three different phases. While all three cross the sulfur haze line, the larger phase angles do not cross the water curve, meaning water will not condense at that portion of the orbit. I will expand on this in Section 7.3.

Table 7.2: Proxima Centauri Star and Planet Parameters

Parameter	Value	Ref
Proxima Centauri		
T_{eff}	3000 K	2
Radius	$0.14 R_{\odot}$	1
SpT	M5.5V	1
Log(Lum)	$-2.8^{+0.1}_{-0.2} L_{\odot}$	1
Log(g)	5.2 cm s^{-2}	1
Metallicity	0.21 dex	3
Distance	$1.30119^{+0.00034}_{-0.00035} \text{ pc}$	
Proxima Centauri b		
sma	$0.04856 \pm 0.00030 \text{ au}$	1
period	$11.1868^{+0.0029}_{-0.0031} \text{ d}$	1
ecc	$0.020^{+0.04}_{-0.04}$	1
$M_p \sin i$	$1.07 \pm 0.06 M_{\oplus}$	1
T_{eq}	2344^{+6}_{-14}	2

(1) [Faria et al. 2022](#), (2) [Anglada-Escudé et al. 2016](#),
(3) [Schlaufman and Laughlin 2010](#)

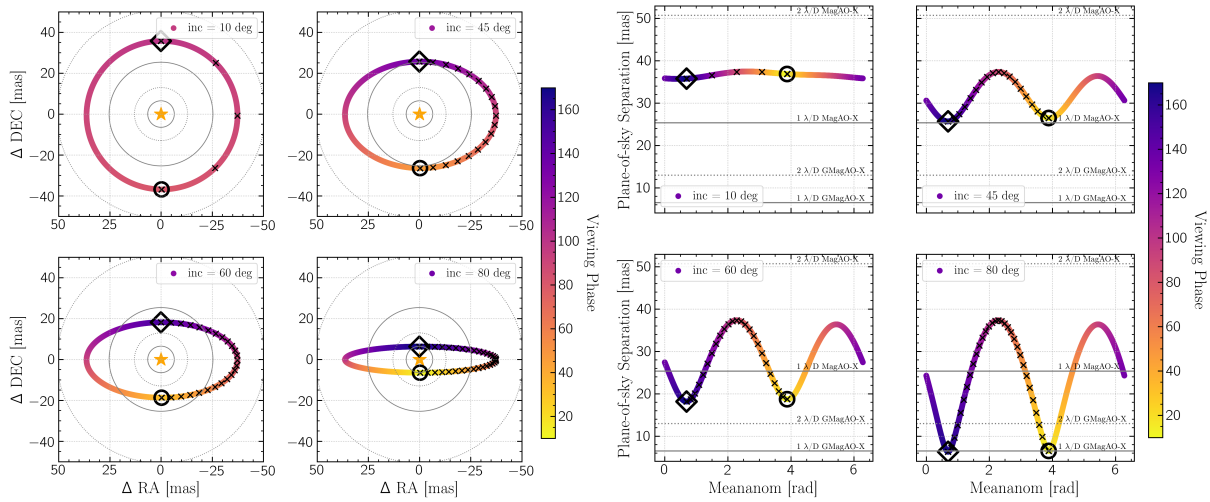
7.2.3 Modeling Terrestrial Planets: Proxima Centauri b

Proxima Centauri b is the nearest exoplanet, is likely terrestrial, and happens to fall in the habitable zone of its M-dwarf host, making it a top priority target for Earth-like planet characterization and biosignature searches. It has only been detected via radial velocity, so the inclination is unconstrained and the only mass estimate is the minimum mass. Its proximity to Earth means its the best candidate for directly imaging a habitable zone planet. Table 7.2 lists star and planet parameters used in our models.

Since inclination is unknown, the true mass of the planet is also unknown. We produced models for seven inclinations, which sets the planet mass and the potential viewing phases. Table 7.3 lists the inclinations we modeled and the corresponding planet mass (where $M_p = M_p \sin i / \sin i$) and planet radius. To estimate radius we used the empirical mass-radius relation in Figure 7.2. Figure 7.11 (left) shows the orbit in the plane of the sky for four inclinations, with phase sampling points marked with black 'x's and MagAO-X and GMagAO-X IWAs marked as before. More face-on orbits will have less phase variation along their orbits than more edge-on. Figure 7.11 (right) shows the star-planet separation in the plane of the sky for the same inclinations.

Table 7.3: Inclination, Mass, and Radius for Prox Cen b used in our models

Incl [deg]	Mass [M_{\oplus}]	Radius [R_{\oplus}]
10	6.2	2.1
20	3.1	1.5
30	2.1	1.3
45	1.5	1.15
60	1.2	1.07
70	1.1	1.04
80	1.0	1.0

**Figure 7.11:** Left: Projected orbit for four inclination values with phase sampling marked as before. Right: same orbits in plane-of-sky separation as a function of orbital phase.

Airless models. To produce models of Proxima Centauri b with no atmosphere we used the wavelength-dependent albedos as a function of surface type for airless rocky planets from [Hu et al. \(2012\)](#) (excluding surfaces unlikely to exist at these temperatures). Figure 7.12 shows the relevant surface-type contrast curves for a planet with inclination = 60° and viewed at quadrature (phase = 90°), with broadband filters g' , r' , i' , z' , J , and H shown below.

Earth-like atmosphere. Unlike for gas giant planets, PICASO does not iteratively solve the PT profile for terrestrial planets, so we approach terrestrial models differently. We provided an analytical PT profile of [Guillot \(2010\)](#) (as reported in [Batalha et al. 2018](#) Sec 2.2):

$$T^4(z) = 0.75 \times T_{\text{eq}}^4(p(z) + 2/3) \quad (7.13)$$

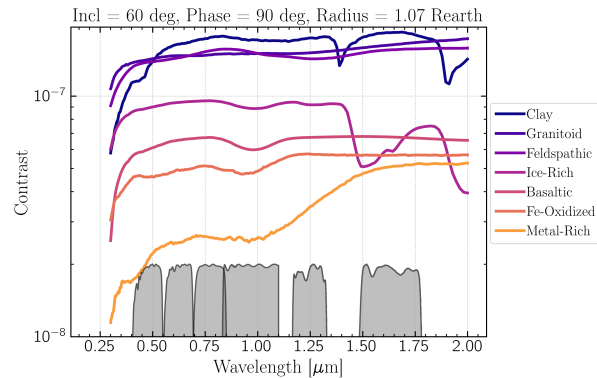


Figure 7.12: Contrast as a function of wavelength for various surface materials for the airless Prox Cen b models, with filter profiles shown below.

which determines where clouds will form where the PT profile intersects with the condensation curve. We used PICASO and VIRGA to reproduce the Earth-like model spectrum of [Feng et al. \(2018\)](#) Figure 5. We used the same atmospheric composition with composition fraction for $N_2 = 0.79$, $O_2 = 0.21$, $O_3 = 7 \times 10^{-7}$, $H_2O = 3 \times 10^{-3}$, $CO_2 = 300 \times 10^{-9}$, $CH_4 = 686 \times 10^{-9}$. We find that $T_{eq} = 237$, $f_{sed} = 8$, and the above star/planet parameters most closely reproduces the albedo spectrum of [Feng et al. \(2018\)](#) (see Figure 7.6).

Starting from this configuration, we produced Earth-like atmosphere models for varying inclinations, phases, and cloud parameters.

7.2.4 Predicting S/N

Computing Signal Intensity From Models

Following the method of [Males et al. \(2021\)](#), we need to determine the signal arriving at the detector in units of photons $s^{-1} \lambda/D^{-1}$. PICASO and other models return the flux from the surface of the object, the planet in this case. So we need to scale the flux to that arriving at the observer:

$$F = I\Omega \quad (7.14)$$

where F = flux at Earth, I = model intensity, and

$$\Omega = \frac{R_p^2}{D^2} \quad (7.15)$$

where R_p = planet radius and D = distance, both in the same unit. Next convert $\text{ergs cm}^{-1} \text{s}^{-1} \text{cm}^{-2}$ to photons s^{-1} . Energy per photon per wavelength is:

$$E [\text{ergs}] = \frac{hc}{\lambda[\text{cm}]} \quad (7.16)$$

and number of photons per wavelength:

$$n_\gamma \left[\frac{\gamma}{\text{cm s cm}^2} \right] = \frac{F_\lambda(\lambda) \left[\frac{\text{ergs}}{\text{cm s cm}^2} \right]}{E [\text{ergs}]} \quad (7.17)$$

Then the total flux in the filter is the sum over all wavelengths of the flux times the filter transmission curve:

$$\text{Total flux } [\gamma \text{ s}^{-1} \text{cm}^{-2}] = \sum (F_\lambda(\lambda) [\gamma \text{ cm}^{-1} \text{s}^{-1} \text{cm}^{-2}] \times R(\lambda) \times \delta\lambda [\text{cm}]) \quad (7.18)$$

where $R(\lambda)$ is the filter transmission curve as a function of wavelength, and $\delta\lambda$ is the interval the spectrum is sampled in. Finally now multiply by the telescope collecting area:

$$\text{Total flux } [\gamma \text{ s}^{-1}] = \text{Total flux } [\gamma \text{ s}^{-1} \text{cm}^{-2}] \times \pi r^2 \quad (7.19)$$

where r is the radius of the primary mirror. This gives total filter flux in photons per second.

Noise in the Atmospheric Speckle Limited Regime

To estimate the noise of an observation we use the method of [Males et al. \(2021\)](#). The intensity of a planet with contrast C to the host star is:

$$I_p(t) = C \times I_* \quad (7.20)$$

where I is the planet and star intensity in units of photons $\text{s}^{-1} (\lambda/D)^{-1}$, where λ/D is the fundamental spatial scale for diffraction limited imaging. Noise is primarily dominated by Poisson noise from the star's halo and speckles from different noise sources, namely atmospheric speckles with lifetimes $\sim 10\text{--}50$ ms and “quasi-static” speckles caused by the instrument with lifetimes of

minutes to hours. The noise in a single resolution element located at the planet's separation and position angle from the star (\vec{r}_p) can be written as:

$$\sigma^2 = \underbrace{I_{s,*}\Delta t}_{\text{Star Poisson noise}} \left[\underbrace{I_c + I_{as} + I_{qs}}_{\text{Star halo at planet location}} + \underbrace{I_{s,*}[\tau_{as}(I_{as}^2 + 2[I_c I_{as} + I_{as} I_{qs}])] + \tau_{qs}(I_{qs}^2 + 2I_c I_{qs})}_{\text{Atm speckles}} \right] + \underbrace{I_{p,*}\Delta t}_{\text{Planet Poisson noise}} + \underbrace{I_{sky}\Delta t N_{pix}(\lambda)}_{\text{Sky background poisson noise}} + \underbrace{\left(RN \frac{\Delta t}{t_{exp}}\right)^2}_{\text{Read noise}} + \underbrace{I_{dc}\Delta t N_{pix}(\lambda)}_{\text{dark current}} \quad (7.21)$$

where:

- $I_{s,*}/I_{p,*}$ is the peak intensity in an aperture of size λ/D centered on the Airy core without a coronagraph in photons/sec/ (λ/D) , incorporating telescope and instrument throughput, with $I_* = I \times T \times \pi/4 \times \text{Strehl Ratio}$, where I is the star/planet's intensity in a given filter, T is the telescope and instrument throughput, and $\pi/4$ is the amount of starlight contained in the Airy core in an aperture of size λ/D ,
- I_c is the fractional contribution of intensity from residual diffraction from coronagraph,
- I_{as} is the contribution from atmospheric speckles,
- I_{qs} is contribution from speckles caused by instrument imperfections ("quasi-static" speckles),
- τ_{as} is the average lifetime of atmospheric speckles (ms),
- τ_{qs} is the average lifetime of quasi-static speckles (minutes–hours),
- I_{sky} is the average sky background count rate,
- RN is the read noise,
- I_{dc} is the dark current count rate,
- Δt is the observation time,
- t_{exp} is the exposure time of a single frame.
- N_{pix} is the number of pixels within the area of a circle of a $1 \lambda/D$ radius,

- with $A_{\lambda/D}[\text{mas}] = \pi r^2$, $r = 0.5\lambda/D$, $\lambda/D[\text{mas}] = 0.2063 \frac{\lambda[\mu\text{m}]}{D[\text{m}]} \times 10^{-3}$ and A_{pix} = pixel side length $[\text{mas}^2]$, then $N_{pix} = A_{\lambda/D}[\text{mas}]/A_{pix}[\text{mas}]$.

This is [Males et al. \(2021\)](#) Eqn 7 plus the typical noise terms. We assume that we have a perfectly functioning coronagraph and instrument such that I_{qs} and I_c terms are negligible compared to the atmospheric speckle terms, thus we are in the speckle-noise limited regime. Additionally, for the purposes of these calculations I will assume that the sky, read noise, and dark current are all negligible compared to the speckles. So this equation reduces to:

$$\sigma^2 = I_* \Delta t [I_{as} + I_{s,*} \tau_{as} I_{as}^2] + I_{p,*} \Delta t \quad (7.22)$$

and companion S/N becomes:

$$S/N \approx \frac{I_{p,*} \Delta t}{\sqrt{I_{s,*} \Delta t [I_{as} + I_{s,*} \tau_{as} I_{as}^2] + I_{p,*} \Delta t}} \quad (7.23)$$

and the time to a desired S/N is:

$$\Delta t = \left(\frac{S/N}{I_p} \right)^2 [I_{s,*} (I_{as} + I_{s,*} \tau_{as} I_{as}^2) + I_{p,*}] \quad (7.24)$$

[Males et al. \(2021\)](#) gives model maps for I_{as} as a function of guide star magnitude and wavefront control (WFC; either simple integrator (SI) or linear predictive control (LP, [Males and Guyon 2018](#))). Figure 7.13 shows the radial profile for an LP controller as a function of separation in λ/D and guide star magnitude (colors). [Males et al. \(2021\)](#) Figure 10 gives the average atmospheric speckle lifetime τ_{as} as a function of several parameters. For an LP WFC on a 24.5 m (GMT sized) mirror on a 5th magnitude star $\tau_{as} \sim 0.02$ s; for an 8th magnitude star its ~ 0.03 s. For SP WFC it's significantly longer, ~ 0.07 s for a 24.5 m mirror on a 5th magnitude star.

Armed with these parameters and Eqn 7.24 we can estimate the time to a desired S/N for a given `ReflectX` model at a known contrast and guide star magnitude. Figure 7.14 shows an example of the S/N vs exposure time for `REFLECTX` models of gas giant planets GJ 876 b and c in the filters listed for a GMT-sized primary mirror. We see that in the atmospheric speckle limited regime `GMagAO-X` will easily reach $S/N = 5$ for both planets in most filters in less than an hour

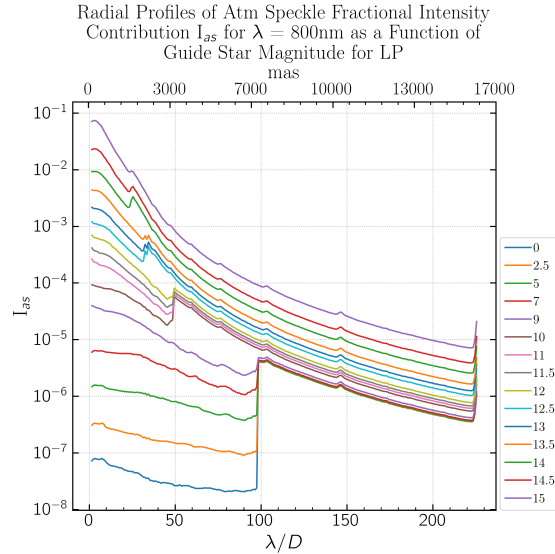


Figure 7.13: The fractional contribution of atmospheric speckles (I_{as}) for a linear predictive wavefront controller at 800 nm as a function of separation and guide star magnitude (colors), azimuthally averaged from the maps of [Males et al. \(2021\)](#).

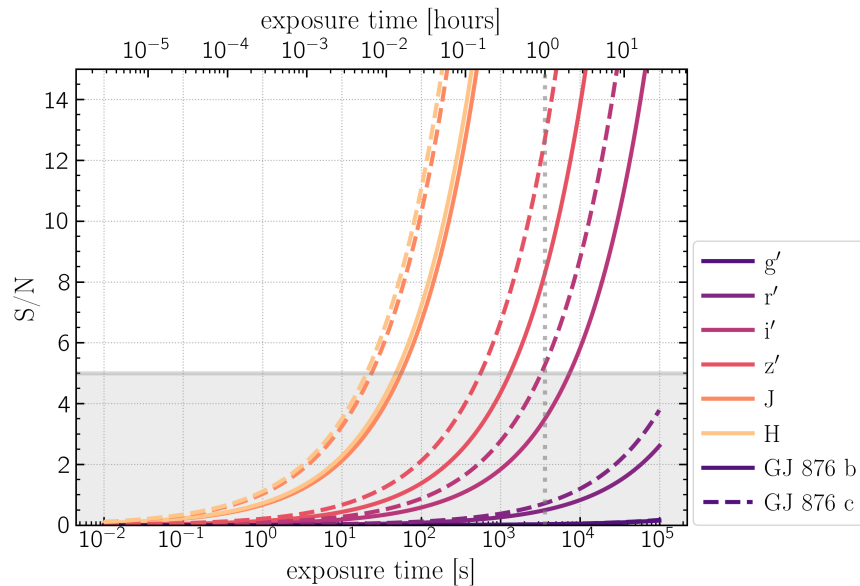


Figure 7.14: S/N as a function of exposure time for the GJ 876 b/c REFLECTX models in the filters listed for a 24.5 m primary, computed using Eqn 7.23. The models used here are at quadrature with $f_{sed} = 0.03$ and $K_{zz} = 1 \times 10^9$ (the brightest cloud configuration, see Figure 7.15). We estimated the throughput as 0.1, $\tau_{as} = 0.02$ ([Males et al., 2021](#), Fig 10), I_{as} and Strehl ratio from the tables from [Males et al. \(2021\)](#). The grey shaded region marks $S/N = 5$, a typical detection threshold. The mid-M host star is brightest in longer wavelengths, giving shorter exposure times to detection on those filters.

of exposure time. This estimate assumed contribution of scattered light and quasi-static speckles in negligible, with other parameters given in the caption.

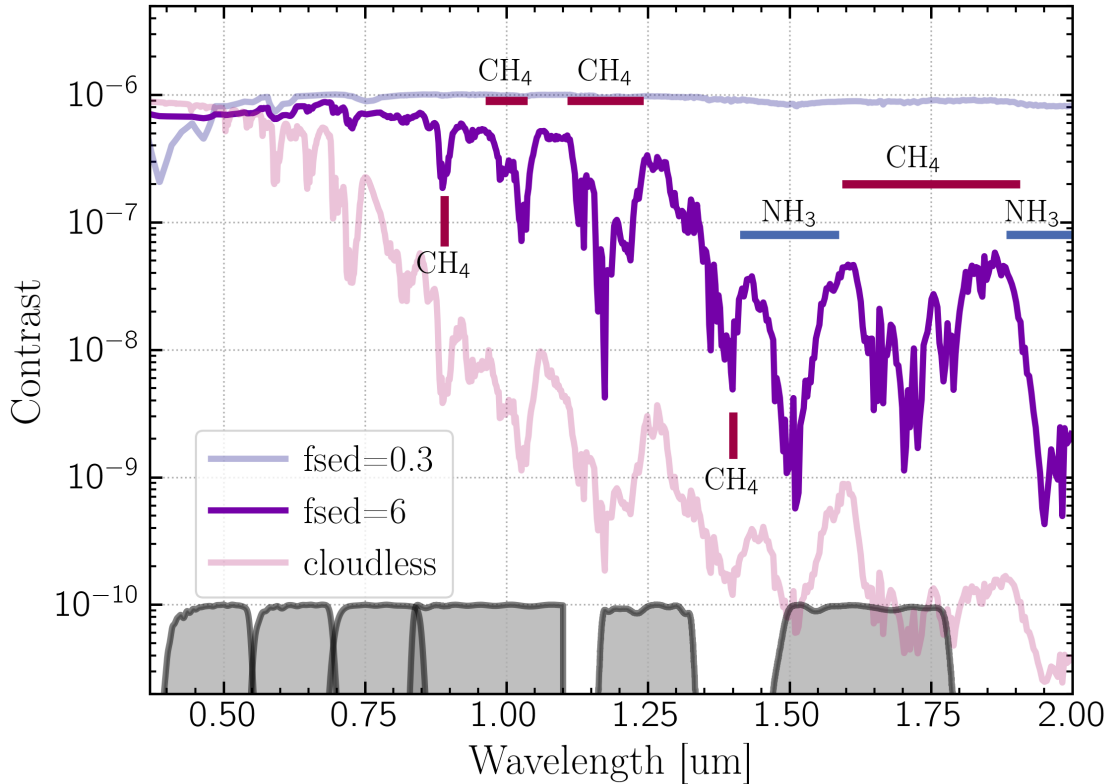


Figure 7.15: Planet-star contrast spectrum from models of GJ 876 b at quadrature with $C/O = 1.0$ for three cloud configurations, $f_{\text{sed}} = 0.3$, $K_{zz} 1 \times 10^{-9}$ (light blue), $f_{\text{sed}} = 6$, $K_{zz} 1 \times 10^{-9}$ (dark purple), and cloud-free (light pink). Molecular absorption lines are marked for the $f_{\text{sed}} = 6$ case. Filter curves used in this analysis are shown in grey below. The atmosphere is H_2 and He dominant, with water, methane, and ammonia the next most prevalent molecules. As cloud opacity decreases molecular absorption lines appear, as well as an upward slope to the blue end from Rayleigh scattering.

7.3 Results

7.3.1 GJ 876 b

Select model contrast spectra at quadrature for three cloud configurations are shown in Figure 7.15. The filter passbands are shown at the bottom in grey. The clouds are composed of water clouds and sulfur hazes, with cloud properties controlled by K_{zz} (vertical mixing) and f_{sed} (sedimentation efficiency). With thick, puffy, reflective clouds the spectrum is bright across wavelengths with no absorption features. As the cloud opacity decreases (with increasing f_{sed}/K_{zz}) molecular absorption features from CH_4 and NH_3 appear, as well as a slope caused by Rayleigh scattering which falls off towards the longer wavelengths.

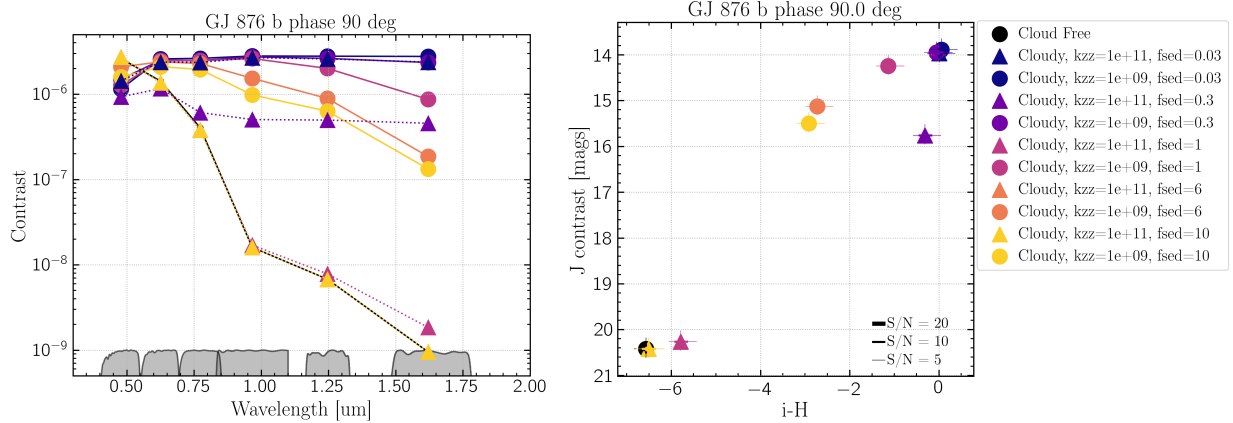


Figure 7.16: Broadband colors for GJ 876 b quadrature models for cloud free (black), cloudy with $K_{zz} = 1 \times 10^9$ (circles, solid line) and varying f_{sed} (colors), and cloudy with $K_{zz} = 1 \times 10^{11}$ (triangles, dashed line) and varying f_{sed} . Left: Planet-star flux contrast as a function of wavelength, with broadband filter profiles for g, r, i, z, J, H, K filters shown below in grey. Right: broadband $i - H$ vs J contrast colors. Cloud properties are broadly distinguishable in color-magnitude space.

Figure 7.16 (left) shows the planet/star contrast for all quadrature models at the central wavelength of each filter, where this trend is clear. We see that for high values of $K_{zz} +$ large f_{sed} the clouds aren't appreciably different from the cloud-free case. The K_{zz} value has significant impact on the contrast for higher values of f_{sed} , while for $f_{sed} = 0.03$ it makes little difference. For the smallest f_{sed} the contrast is nearly constant, while for thinner clouds (higher f_{sed}) the model is much fainter at redder wavelengths. This is also seen in the color-magnitude diagram in Figure 7.16 (right) where the puffy clouds are several magnitudes brighter and bluer than thin clouds and vigorous vertical mixing. Figure 7.17 shows contrast as a function of phase, and Figure 7.18 shows how the models move in color-magnitude space as a function of phase. Different cloud properties cause different changes in color as a function of phase.

Reflected light broadband photometry in visible and Near IR has constraining power for gas giant cloud properties. However at these temperatures varying C/O does not have a large enough effect on chemistry to be distinguished above uncertainty in broadband photometry alone.

7.3.2 GJ 876 c

GJ 876 c exhibits different behavior than b due to its eccentric orbit. Figure 7.19 shows the z' band phase curve and models in color-magnitude space as a function of phase. In particular the $f_{sed} = 1$ with strong vertical mixing and $f_{sed} = 6$ with weak vertical mixing brighten at

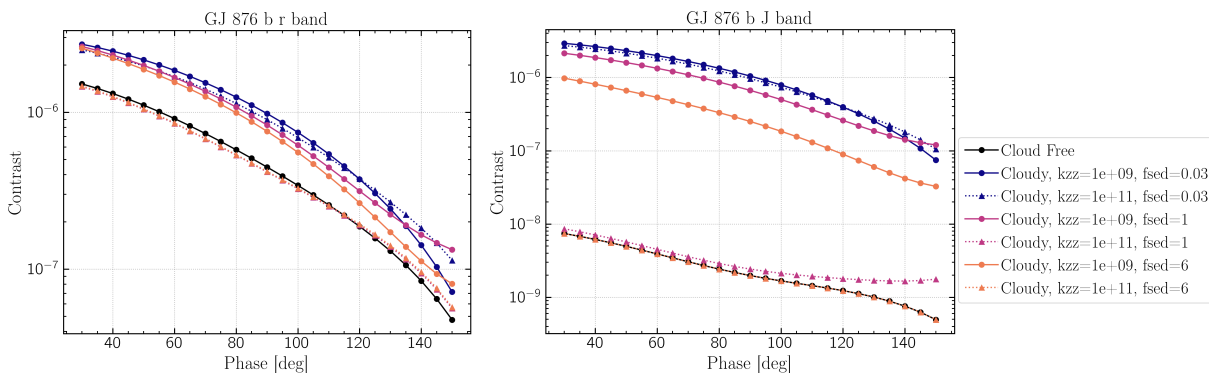


Figure 7.17: Phase curves for selected cloud models for r and J band.

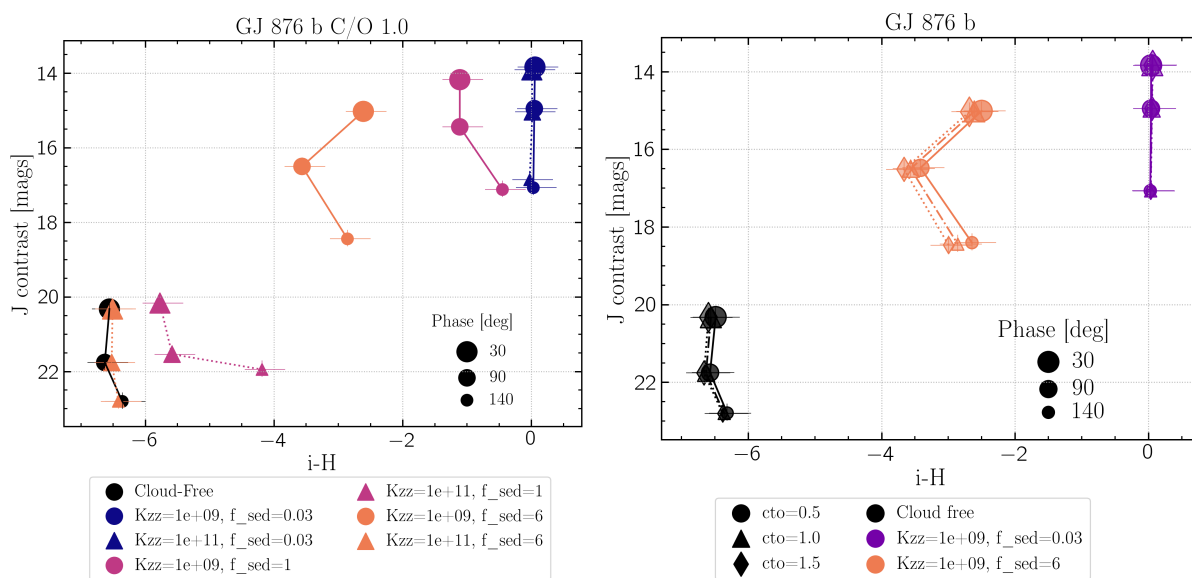


Figure 7.18: Left: Models in color-magnitude space as a function of phase; error bars are for $S/N = 5$. The cloudy spectra behave differently as a function of phase. Right: Selected cloud models in color-magnitude space as a function of phase for three C/O ratio values. Broadband photometry is not sufficient for distinguishing C/O ratio above uncertainty.

higher phase angles, with the later exhibiting a sharp turn from dimming to brightening trend at phase $\sim 115^\circ$

As shown in Figure 7.9 and 7.10, at higher phase angles GJ 876 c is at a point in its orbit closer to the star due to its higher eccentricity, which means at these points it is hot enough that the PT profile does not cross the water condensation curve under the assumptions of this model. Figure 7.20 (top, right) shows the orbital separation in the orbit plane, while (top, left) gives separation as a function of orbit phase, with viewing phase given by the colormap. Regions shaded purple are too hot for water clouds to condense in these models, which correspond to phases $\gtrsim 115^\circ$. Figure 7.20

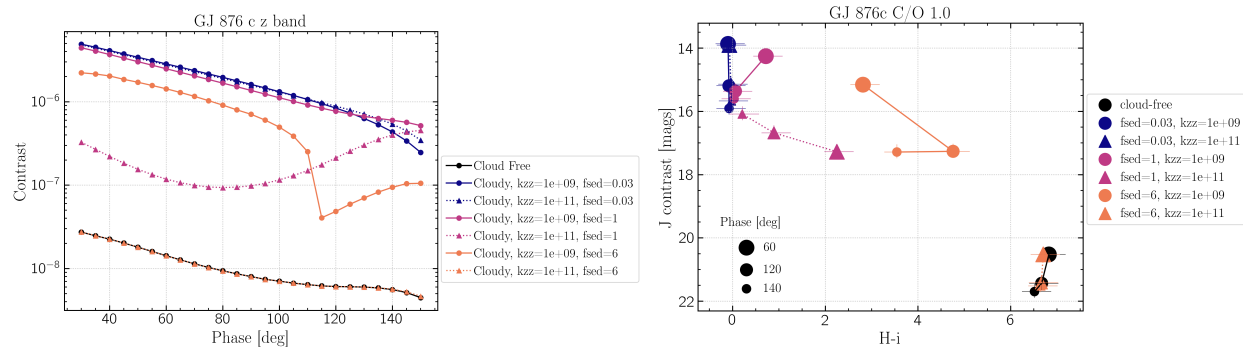


Figure 7.19

(bottom, left) shows the reflected spectrum for weak vertical mixing and thin clouds for models at four phases – 40, 110, 120, and 140°; (bottom, right) shows the cloud optical depth τ as a function of altitude (pressure). For phases $< 115^\circ$, water clouds condense between 0–0.1 bars, while phases $> 115^\circ$ don't have the water cloud feature (the lower cloud bank is sulfur hazes). This translates to brighter spectra at longer wavelengths due to the bright water clouds. The contrast trends down as phase increases, but when water clouds go away the contrast increases again as phase goes from 120 to 140°, especially at longer wavelengths. This can be seen in Figure 7.21 which shows the same spectra as Figure 7.20, focusing on z -band wavelength range highlighted in Figure 7.19.

7.3.3 *Proxima Centauri b*

Figure 7.22 shows the airless and Earth-like models in color-magnitude space. The airless and Earth-like models are well separated from each other, and for the most part from the different cases within each group, by several magnitudes, just as with the gas giant models.

Figure 7.23 (top) shows a REFLECTX Proxima Centauri b Earth-like atmosphere cloudless albedo spectrum with inclination = 60° and viewed at quadrature with atmospheric molecular features labeled. Figure 7.23 (bottom) shows the albedo spectrum for the same model with 100% water cloud coverage and 50% cloud coverage, the flux contrast spectrum (F_p/F_s), the PHOENIX stellar spectrum (F_s), and the planet flux spectrum ($=F_p/F_s \times F_s$). The presence of clouds makes the spectrum much brighter but washes out most of the molecular features. Some water features might be detectable at $> 1\mu\text{m}$.

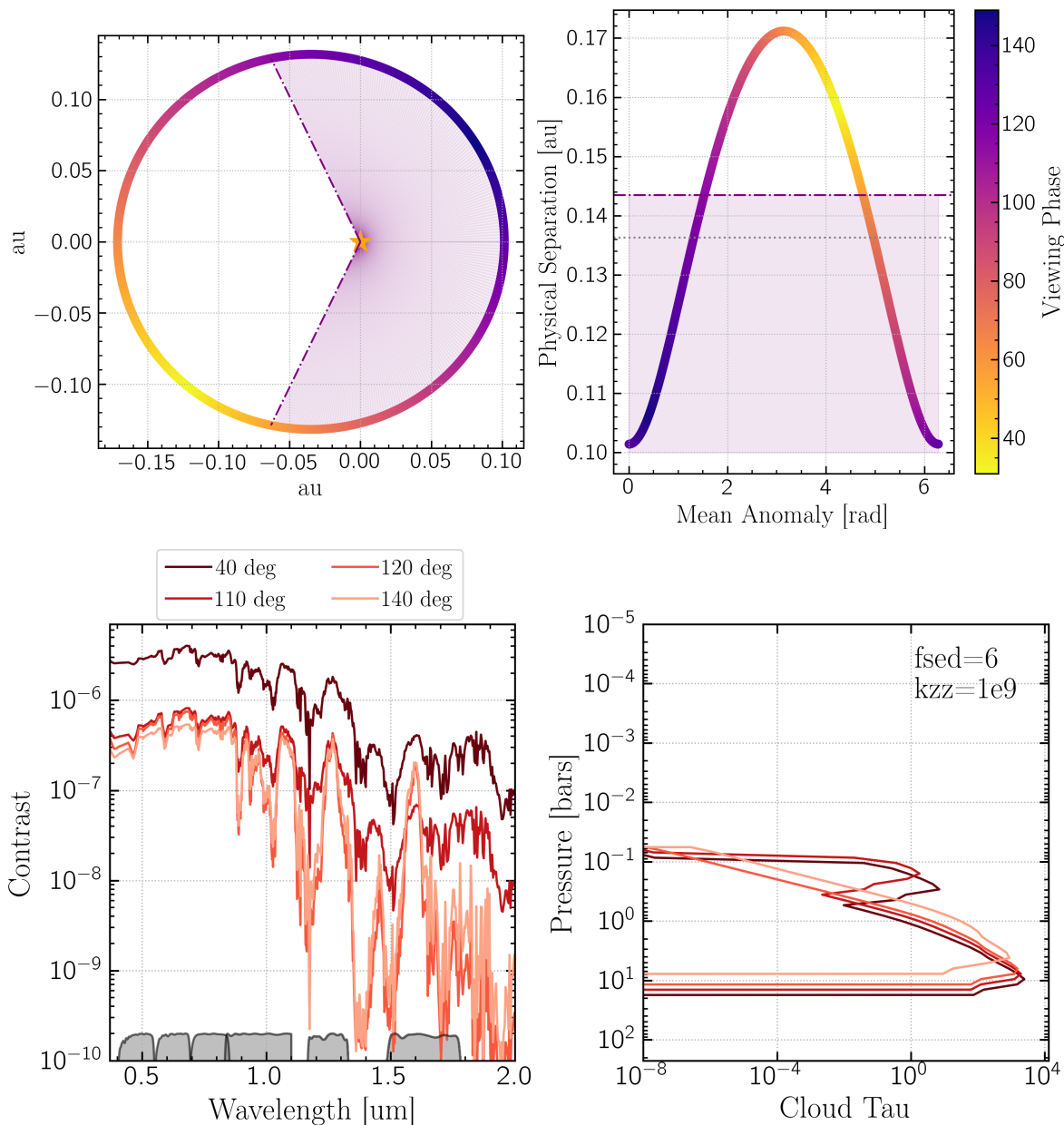


Figure 7.20: Left: Phase curves for GJ 876 c models for cloudy and cloud-free models in z' band. Some cloud configurations exhibit brightening trend at higher phase angles. Right: Models in J vs $H - i$ color space where some cloud configurations exhibit surprising behavior with phase due to the (lack of) condensation of water clouds.

7.4 Future Work

Proxima Centauri b models. We plan to produce Venus-like CO_2 dominated atmospheric models and Titan-like CH_4 and haze dominated models as well for this planet. For the airless models, we intend to expand the surface reflectivity analysis to rocky components (like silicates, carbonates,

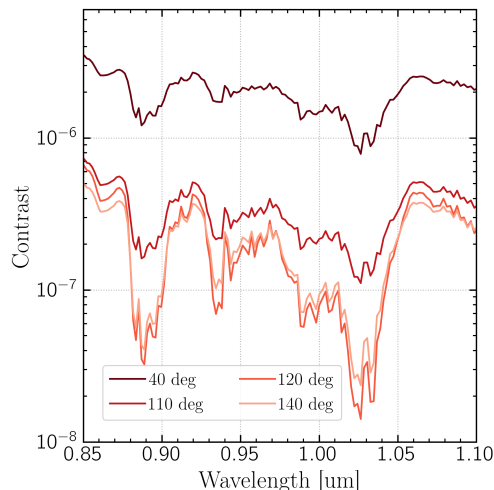


Figure 7.21: Top: GJ 876 c physical separation as a function of orbital phase and viewing phase. Orbit points within the purple regions are too hot for water clouds to condense under the assumptions of this model. Bottom left: Reflectance spectrum for four phases. Right: cloud opacity as a function of altitude (parameterized by pressure). For the smaller phase angles water clouds form between 0–0.1 bars which are absent at higher phase angles.

and basalts), and how different mixtures of components affect reflectivity in the optical; as well as trying to reproduce spectra of airless Solar System bodies such as the Moon with our model framework.

Following construction of those model sets, we will expand the model grid to generic star/-planet properties to enable modeling of any terrestrial planet. We will also be producing models of specific terrestrial planets in Figure 7.1.

Gas Giant planets. We will be expanding the gas giant models developed while modeling GJ 876 to provide models spanning star and planet properties, as well as specific gas giant planets in Figure 7.1.

Future analysis. So far we have only evaluated the models in broadband photometry. High-resolution spectroscopy is necessary to observe specific atmospheric features and quantify abundances. There is a trade-off between high-resolution for resolving features and feature shapes, and the drop in throughput (in an already photon-starved regime) and increase in detector space that comes with high-resolutions. An important analysis will be how to maximize science yield and minimize the resolution needed for optimal science return, which will inform instrument design and trade studies.

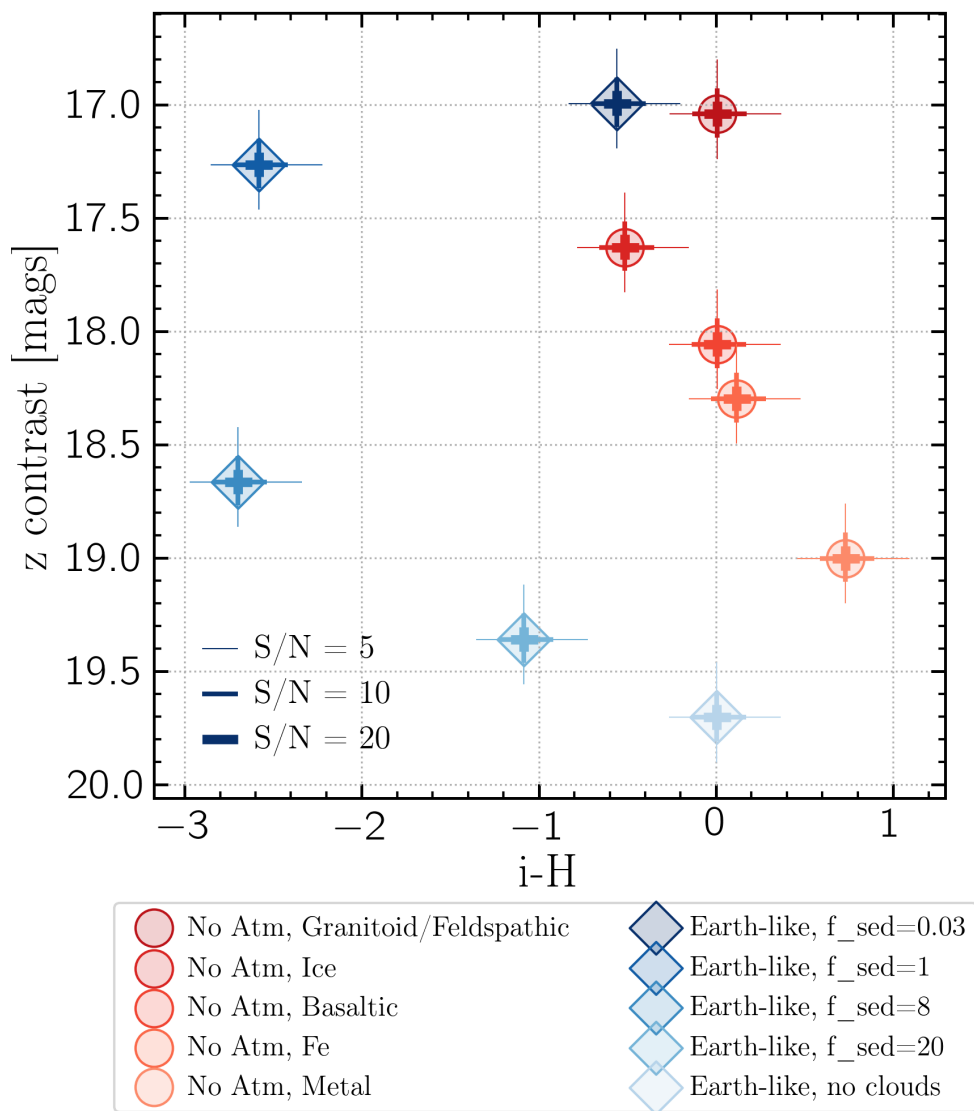


Figure 7.22: Color-magnitude diagram for airless (red) and Earth-like atmosphere models. The airless and Earth-like models are well separated from each other, and for the most part from the different cases within each group, by several magnitudes, just as with the gas giant models.

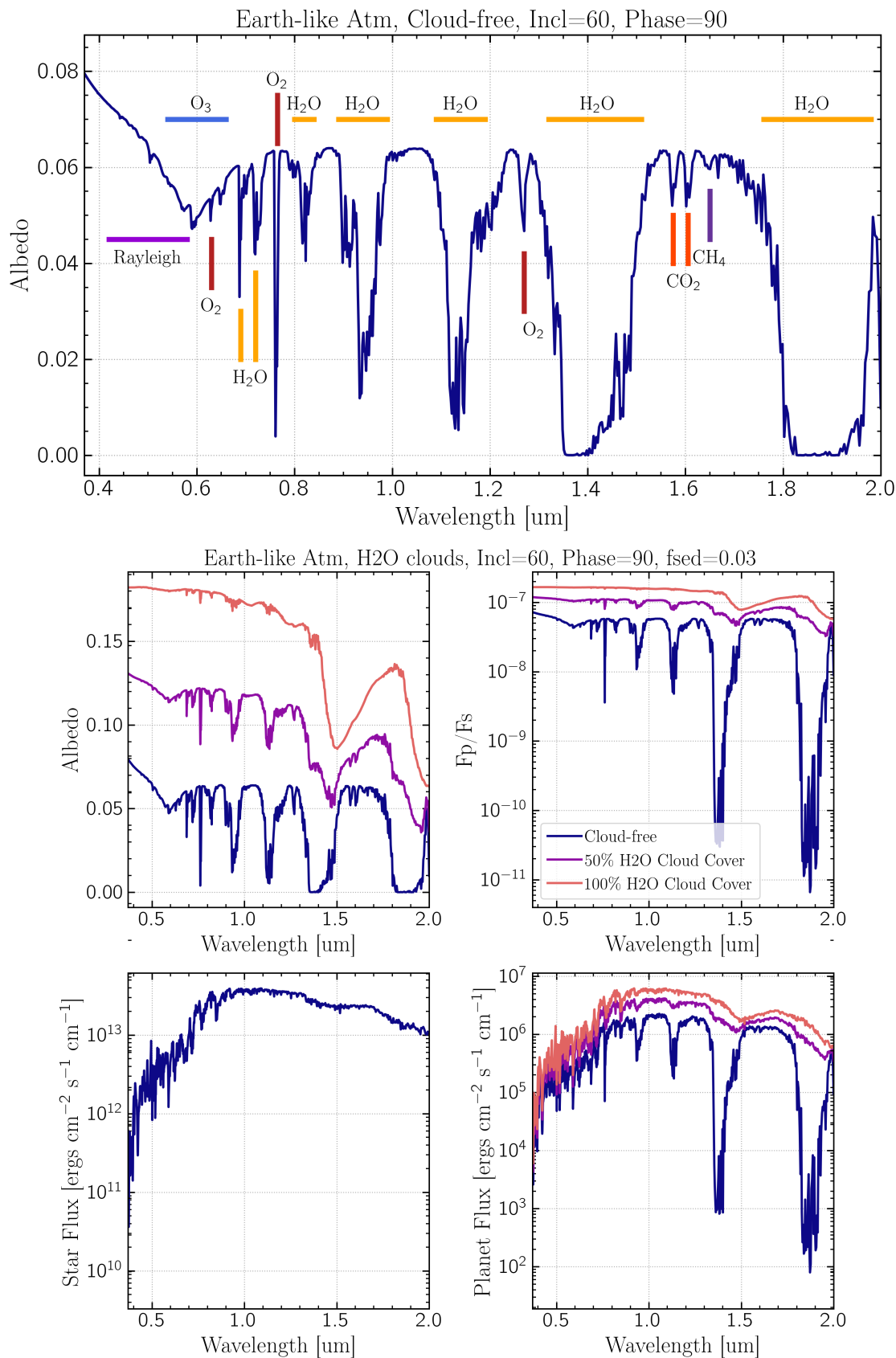


Figure 7.23: Top: Earth-like Proxima Centauri b cloudless albedo spectrum for inclination = 60° and phase = 90°, with molecular absorption features labeled. Bottom: Earth-like atmosphere albedo model under the same configurations with 100% and 50% cloud cover; the flux contrast (F_p/F_s), the stellar spectrum model, and the planet flux spectrum. More cloud cover leads to brighter planets but fewer spectral features for constraining composition.

Understanding the effect of orbital motion will be essential prior to conducting these surveys. With closer separations orbital motion will be significant enough that the planet signal will move during the course of an observation. For example, Proxima Centauri b has an orbital period of 11 days; if 10's of hours of observation are needed for adequate signal the planet will move significantly during that times. Additionally, separation for the planet from the star will vary, and there will be some nights it's not visible during the orbital period. Orbital motion is also beneficial for separating a potentially Earth-like atmosphere from the Earth's atmosphere, which we will be observing through. If there is sufficiently high signal and resolution we can distinguish Prox Cen b's atmospheric lines from lines in the Earth's atmosphere via red/blue shifting. We are planning an orbit study to inform observing strategy along the lines of [Males et al. \(2013\)](#). Additionally, [Salvador et al. \(2024\)](#) recently found that knowledge of the planet orbit accurately constrains planet radius from reflected light observations.

Comparison of our model predictions to JWST transit spectroscopy will provide an additional axis of information. For example, transit spectra only probe the atmosphere on the terminator while reflected light probes the entire planet disk. And understanding how reflected light spectra molecule detection compares to or improves on transit spectra line detection (or lack of) is important for developing a cohesive picture of transiting planet atmospheres.

Finally, we intend to develop a tool for users to interface with the REFLECTX model suite for the exoplanet community to produce and explore models for reflected light imaging with ELTs.

7.5 Conclusion

Direct imaging is the future of exoplanet science, but requires advancements in technology to detect older, closer, and smaller planets than current DI capabilities allow. MagAO-X is a development platform for these technologies, and plans to begin trying to detect planets in light they reflect from their star in the next few years. Careful modeling work is necessary to inform observing strategies, predict survey yields, inform instrument design, and forward model spectra for understanding results. We are developing the REFLECTX model suite to provide reflected light models spanning star and planet properties, models of specific nearby planets with known characteristics, and a tool for the community to interface with the models. This work is on-going and

will comprise a significant portion of my post-doctoral research fellowship beginning in September 2024. Publication of the first model results is expected in mid-2024.

Chapter 8

Conclusion

“Someone once told me that time was a predator that stalked us all our lives. I rather believe that time is a companion who goes with us on the journey and reminds us to cherish every moment, because it will never come again. What we leave behind is not as important as how we’ve lived. After all Number One, we’re only mortal.”

Capt Jean-Luc Picard
Star Trek: Generations (1994)

The work in this thesis has focused on the direct imaging of exoplanets through a variety of avenues of exploration, all focused towards the goal of directly detecting and characterizing exoplanets. Achieving this goal requires ongoing and active development of optical, wavefront control, and speckle suppression technology, observational strategies for maximally subtracting residual starlight while retaining faint companion signals, methods for determining the mostly likely stars to host detectable planets for novel detections, and predictions of known exoplanet orbits and potential reflectance spectra for detection and characterizations in reflected light. This work has contributed to most of these, while pointing towards what is still left to do.

In Chapter 4 I analyzed a dataset from 2015–2017 observed with the MagAO instrument using the binary differential imaging observing strategy, which could outperform angular differential imaging at close separations for equal-magnitude binaries separated from 2–10". I detected one candidate signal at $2\lambda/D$ separation from HIP 67506 A, a separation that is very difficult to detect companions due to starlight subtraction residuals, but a regime necessary for future reflected light imaging of nearby known planets that are close to their stars. The candidate signal was dubious, but secondary indications pointed to its being astrophysical – it displayed a curved sky path over time pointing to the presence of a massive companion, and it was over-luminous, brighter than it would be if it were a single star. We followed up on this signal with MagAO-X in 2022 and discovered it is a mid-M dwarf stellar companion. While brighter than potential brown dwarf or planet signals at $2\lambda/D$, this work showed that things can be detected at those separations and that secondary indications are vital tools for vetting candidate signals.

The majority of stars are in multiple systems; single stars like our own represent only about one quarter of stars. In Chapter 3 I described a system that got me interested in how stellar multiplicity affects planetary systems. The Boyajian's Star system is still not well explained by astrophysical phenomena, but it is possible that its wide stellar companion may contribute in some as-yet unknown way.

ExAO instruments like MagAO-X can be used to explore this question as well. In Chapter 6 I described my survey (The Pup Search) designed to use ExAO tools for detecting new WD companions to AFGK stars (a science case that ExAO has never been used for to my knowledge), probing pollution of WDs in binaries at closer separations than previous surveys, and ultimately examining the orbits of polluted/non-polluted WD+MS systems. This is a long term project and

one I will be pursuing in my post-doctoral work. In Chapter 6 I presented the first observations for the Pup Search in which we observed 14 Pup Search main sequence star targets with MagAO-X and detected 8 candidate signals, at least 5 of which are white dwarfs (one is unknown, one is a subdwarf, and one is an M dwarf). With an initial list of 84 targets, we anticipate detecting ~ 38 new Sirius-Like Systems through this survey.

The next steps for this project are to continue to observe Pup Search targets, revisit companion detections to establish common proper motion, observe new companions for pollution, and obtain long time-baseline RV and astrometric observations for orbit studies. Additionally, I intend to build on prior simulations exploring the effects of stellar companions on planetesimals in the planetary regime under the companion's influence at the separations we are sensitive to and under orbital evolution.

Directly detecting a planet in the light it reflects from its host star is the next essential step in exoplanet characterization, and is the main science goal for the MagAO-X instrument. In Chapter 7 I described work only just begun to model the potential atmospheres of nearby known exoplanets to predict their reflectance spectra in optical wavelengths. Chapter 7 presents the work to date, including the gas giants GJ 876 b and c, and airless and Earth-like models of Proxima Centauri b. Much remains to be done with those models, particularly producing more models of different possible atmospheres (or lack of), including a Titan-like methane dominant atmosphere, a Venus-like carbon dioxide dominant atmosphere, and potential worlds not in our solar system such as a water world. For gas giants, models of Neptune-like, Saturn-like, Jupiter-like, and Super-Jupiter masses and metallicities will span possible giant planet characteristics. I am planning a generic grid of gas giant and terrestrial planet models to allow users to explore the effects of planet parameters on reflectance spectrum and provide forward models for retrievals.

The ultimate goal of the model suite is to enable exploration of open questions as the field prepares to make the first reflected light exoplanet detections. An open question in preparing for this science, that this work seeks to address, is the spectral resolution and signal-to-noise ratios needed to robustly detect atmospheric molecules, constrain cloud properties, and constrain planetary properties such as gravity. Additionally, what are the optimal wavelength bands for 1) detection, and 2) characterization of reflected light planets, and are they the same? What S/N is needed to detect biosignatures and can potential biosignature gasses be distinguished from an abiotic production

case? What can we learn from current and ongoing JWST transmission spectra that are complementary or different from what we can learn from future reflected light spectra? How can we plan for ground-based observations of planets with short periods, like Prox Cen b's 11-day period, with the day-night cycle and observable orbital motion during the hours-long observations? This work is not the only avenue for exploring these questions, but will be a valuable tool for the MagAO-X team and the larger community preparing for these detections. Answering these questions will comprise the majority of my post-doctoral work.

A driving question through the history of humanity is if our small planet represents the only instance of life in the universe. We now know that each star on average hosts more than one planet, a revolutionary discovery only made through the last 30 years of human history. We stand on the precipice of unprecedented tools and technology to try to answer this question, and I am hopeful that in my lifetime we will witness the first unambiguous biosignature detection on another world. Because if we are the only one, in the face of billions of planets around billions of stars contained within each of billions of galaxies, then it sure is an awful waste of space.

Appendix A

Appendix to Chapter 4

A.1 Binary System Details

Here we present details of each binary system in our survey. In the following discussion, we have made use of the Gaia EDR3 Renormalized Unit Weight Error (RUWE) metric as a signpost for the (non-)existence of unresolved companions. RUWE encapsulates all sources of error in the fit to the assumed single star astrometric model, corrected for correlation with source color and magnitude. RUWE ≈ 1 is expected for a well-behaved solution (Lindgren, 2018b)¹. RUWE has been shown to be sensitive to companions on separations from $\sim 0.2''$ - $1.2''$ (Kervella et al., 2022), periods of months $\lesssim P \lesssim 10$ years, and mass and luminosity ratios < 1 , for which photocenter motion is perturbed from motion of a single star model (Penoyre et al., 2021). RUWE 1–1.4 has been shown to be very strongly correlated with photocenter perturbation from an unresolved companion (Stassun and Torres, 2021; Belokurov et al., 2020); RUWE 1.4–2 indicates deviation from a single star model but the astrometry may still be reliable (Maíz Apellániz et al., 2021); RUWE > 2 indicates significant deviation from a single star model. Elevated RUWE in young sources ($\tau \lesssim 10$ Myr) may also be attributed to the presence of a disk (Fitton et al., 2022).

Additionally, we have made use of the Hipparcos–Gaia Catalog of Accelerations (Brandt, 2021) as a signpost for unresolved companions on wider orbits for which RUWE is less sensitive. Significant difference between the long-baseline proper motion vector and the instantaneous PM vectors in Hipparcos and Gaia observation epochs (proper motion anomaly, PMa) can indicate the presence of an unresolved companion causing acceleration. We made use of the Kervella et al. 2019 (for DR2) and Kervella et al. 2022 (for EDR3) PMa catalogs to indicate the (non-)existence of significant PMa; $S/N > 3$ is considered significant in Kervella et al. 2019. We note that PMa sensitivity depends on mass, distance, and orbital period, and use it as an indicator only and not a tool for prediction of companion properties.

HD 36705 — HD 36705 (AB Dor) is a nearby (15 pc), K0V+M5-6 (Torres et al., 2006), 9'' T-Tauri type binary in the AB Doradus moving group with masses $0.865 \pm 0.034 M_{\odot}$ (Close et al., 2005) and $0.37 M_{\odot}$ (Sebastian et al., 2021) respectively. AB Dor A is an ultra-fast rotator that is chromospherically active (Lalitha et al., 2013). AB Dor B (RST 137B, HBC 434) was first detected by Vilhu and Linsky (1987) in X-ray emission. Close et al. (2005) placed the age of AB

¹<https://www.cosmos.esa.int/web/gaia/dr2-known-issues#AstrometryConsiderations>

Dor A at 50_{-20}^{+50} Myr due to lithium (Mewe et al., 1996), X-ray activity, and rotation rate, younger than the average age of 149_{-19}^{+51} for the AB Dor moving group (Bell et al., 2015). A wide variety of ages have been estimated for AB Dor spanning 5 Myr to 240 Myr (75-150 Myr– Luhman et al. 2005; 100 Myr– Mamajek and Hillenbrand 2008, 70 Myr– Chauvin et al. 2010, 240 Myr– Vican 2012, 10 Myr– Gáspár et al. 2013, 150 Myr– Richey-Yowell et al. 2019, 5.6 Myr– Binks et al. 2020). We adopted the average age of 100 Myr for our analysis.

Both stars have their own subsystems. Close et al. (2005) detected a significantly redder companion to AB Dor A, which they named AB Dor C, at $0.156 \pm 0.010''$ and position angle $127 \pm 1^\circ$, with a dynamical mass of $0.090 \pm 0.008 M_\odot$ (Azulay et al., 2017). Climent et al. (2019) inferred the presence of a companion to AB Dor C in VLTI/AMBER J,H,K band, with 38 ± 1 mas separation and masses of 0.072 ± 0.013 and $0.013 \pm 0.01 M_\odot$ for AB Dor Ca, Cb respectively. Close et al. (2005) also detected a $0.070''$ companion to AB Dor B (AB Dor Ba, Bb) at position angle $238.6 \pm 0.38^\circ$. AB Dor A and B are resolved in Gaia EDR3, both with large RUWE values (A: RUWE = 25.13; B: RUWE = 3.52), nevertheless uncertainties of astrometric quantities are small, the parallaxes are consistent with Hipparcos (van Leeuwen, 2007), and separation/PA is consistent with the Washington Double Star catalog (WDS; Mason et al., 2001). No significant IR excess was detected by McDonald et al. (2012) (average excess infrared (EIR) = 1.108 for 4.2-25 μm , where EIR = 1 indicates no excess).

HD 37551 — HD 37551 (WX Col) is a young, 4'' binary at a distance of 80 pc. HD 37551 A and B have a mass of $0.93 M_\odot$ and $0.80 M_\odot$ respectively (Anders et al., 2019), and spectral type G7V and K1V (Torres et al., 2006). Both stars have RUWE values ~ 1 (A: RUWE = 0.97; B: RUWE = 0.96), indicating that unresolved companions are unlikely (Lindegren et al., 2018).

Rodigas et al. (2015) used this system as a test case in their BDI paper. They noted that it had previously been identified as an AB Dor member (Torres et al., 2006; Elliott et al., 2014), and that low-mass AB Dor members have Li-depletion boundary ages indistinguishable from that of the Pleiades, i.e., 130 ± 20 Myr (Barrado y Navascues et al., 2004), and adopted this age for the system. Binks et al. (2020) retained it as an AB Dor member, and BANYAN Σ (Gagné et al., 2018) gives 86.7% AB Dor membership probability. However Binks et al. (2020) determined ages of $18.3_{-4.1}^{+3.6}$ and $11.6_{-5.1}^{+4.1}$ via SED fitting for A and B respectively. We adopted an age of

130 ± 20 Myr for our analysis. The younger age of [Binks et al. \(2020\)](#) would result in mass limits $\sim 15M_{\text{Jup}}$ smaller.

HD 47787 — HD 47787 is a young (16.5 ± 6.5 Myr derived from evolutionary models, [Tetzlaff et al. 2011](#)) 2'' binary of roughly equal brightness at 48 pc. It is not a member of a known young moving group (99.9% field in Σ in [Banyan](#)). A second possible companion is seen at 12.2'' ([Dommanget and Nys, 2000](#); [Fabricius et al., 2002](#)) however the Gaia EDR3 parallax is significantly different from HD 47787 A, suggesting they may not be associated. A and B are both spectral type K1IV ([Torres et al., 2006](#)), and have mass $0.85 M_{\odot}$ and $0.89 M_{\odot}$ respectively ([Anders et al., 2019](#)). Both have $\text{RUWE} = 1.1$, suggesting any unresolved companions are unlikely to be resolvable in imaging if present.

HD 76534 — HD 76534 (OU Vel) is a very young Herbig Be star with spectral type B2Vn ([Houk, 1978](#)) in a 2'' binary at 869 pc with associated nebulosity. The age is 0.27 ± 0.01 Myr, derived from MESA Isochrones and Stellar Tracks ([Choi et al., 2016](#)) and Gaia DR2 colors, in [Arun et al. 2019](#). [Finkenzeller and Mundt \(1984\)](#) observed a double peaked $\text{H}\alpha$ emission line with an unshifted absorption line; [Berrilli et al. \(1992\)](#) confirmed dust structures around this and other Herbig Ae/Be stars with optical and Mid- to Far IR luminosities. HD 76534 A has a mass of $6.31 \pm 0.05 M_{\odot}$ ([Arun et al., 2019](#)), HD 76534 B has a mass of $\sim 2 M_{\odot}$ ([Anders et al., 2019](#)). HD 76534 A has an elevated RUWE ($\text{RUWE} = 1.53$), suggesting a possible unresolved companion, however RUWE can also be elevated for highly variable stars ([Belokurov et al., 2020](#)). HD 76534 B has $\text{RUWE} = 0.88$, making a companion unlikely.

HD 82984 — HD 82984 is a 2'' pre-main sequence field star binary at a distance of 274 pc, and an age of 53.4 ± 15.1 Myr (derived from evolutionary models, [Tetzlaff et al. 2011](#)). Both stars are nearly equal magnitude, with mass $6.3 \pm 0.1 M_{\odot}$ ([Tetzlaff et al., 2011](#)) and spectral type B4-5III ([Houk, 1978](#); [Tetzlaff et al., 2011](#)). HD 82984 AB has $\text{RUWE} = 1.04$ and 1.25 respectively. [Kervella et al. \(2019\)](#) identified a statistically significant PMA in both Hipparcos ($\text{S/N} = 9.24$) and Gaia DR2 ($\text{S/N} = 10.04$) astrometry for HD 82984 A, indicating the possible presence of a companion. They computed that a normalized mass of $m'_2 = 513.26 M_{\text{Jup}} \text{AU}^{-1/2}$ would cause the observed acceleration. Extending to the binary separation, this becomes

$$m'_2 = 513.26 M_{\text{Jup}} \text{AU}^{-1/2} = \frac{m_2}{\sqrt{550 \text{AU}}}; m_2 = 11 M_{\odot} \quad (\text{A.1})$$

so the influence of the secondary might contribute to the observed PMa. PMa reported for Gaia EDR3 (Kervella et al., 2022) is consistent with this estimate.

HD 104231 — HD 104231 is a 4.5'' binary at 100 pc in Lower Centaurs Crux (Hoogerwerf, 2000) with an age of 21 Myr (derived from isochrone model fitting, Pecaut et al., 2012). HD 104231 A has spectral type F5V (Houk and Cowley, 1975) and mass $1.33 M_{\odot}$; HD 104231 B has mass $0.30 M_{\odot}$ (Hagelberg et al., 2020). HD 104231 AB have RUWE = 0.82 and 2.29, suggesting a possible unresolved companion around B, although there is no significant PMa in Kervella et al. (2019). Mittal et al. (2015) observed statistically significant infrared excess luminosity for HD 104231 A in *Spitzer* $10\mu\text{m}$ (S/N = 6.85) and $20\mu\text{m}$ (S/N = 12.82) bands, corresponding to silicate emission line features. Tobal (2000) reported astrometry for a companion at 7.7'' observed in 1997, labeled HD 104231 B in the Washington Double Star catalog (WDS), however no further observations of this companion are reported, nor is there a corresponding source in Gaia EDR3. We conclude this is spurious and adopt the 4.5'' companion (labeled HD 104231 C in WDS) to be HD 104231 B.

HD 118072 — HD 118072 (V347 Hya) is a G-type 2.3'' binary at 80 pc in the Argus Association (89.2% Banyan Σ probability). We adopted the mean age of 40-50 Myr for the Argus Association (Zuckerman, 2019). HD 118072 A has a spectral type G3V (Torres et al., 2000) and mass $1.11 M_{\odot}$ (Chandler et al., 2016). Both have RUWE close to one (A: RUWE = 1.027, B: RUWE = 0.962) and no significant PMa.

HD 118991 — HD 118991 (Q Cen) is a SpT B8.5 + A2.5 (Gray and Garrison, 1987), 5.6'' binary at 88 pc in the Scorpius-Centaurus Association (76.7% Lower Centaurus-Crux, 21.5% Upper Centaurus-Lupus, 1.8% Field Banyan Σ probabilities), with an age of 130-140 Myr (derived from isochrone fitting of Strömgren photometry, David and Hillenbrand, 2015). HD 118991 A has a mass of $3.6\text{-}3.7 M_{\odot}$ (David and Hillenbrand, 2015). Both have RUWE close to one (A: RUWE = 1.108, B: RUWE = 1.065) and no significant PMa.

HD 137727 — HD 137727 contains a pair of G-type stars (G9III+G6IV, Torres et al. 2000) in a 2.2'' binary at 112 pc, with an age of 8 Myr (Tetzlaff et al., 2011). HD 137727 A has a mass of $0.88 M_{\odot}$ (Chandler et al., 2016). HD 137727 A has RUWE = 1.416, but Kervella et al. (2019) did not detect a significant PMa. HD 137727 B has RUWE = 0.88 and no significant PMa.

HD 147553 — HD 147553 is a 6'' B9.5V + A1V (Corbally, 1984) binary in Upper Centaurus-Lupus (Banyan Σ : 90.7% probability UCL, 9.0% USco) at a distance of 138 pc. We adopted the median age of UCL 16 ± 1 Myr derived from isochrone fitting (Pecaut et al., 2012). HD 147553 A has a mass of $2.7 M_{\odot}$ (Hernández et al., 2005). Both have RUWE close to one (A: RUWE = 0.927, B: RUWE = 1.017) and no significant PMa.

HD 151771 — HD 151771 contains a pair of late B-type (B8III + B9.5, Corbally 1984) field stars with separation 7'' at 270 pc. Kervella et al. (2019) found a slightly significant (S/N = 3.79) proper motion anomaly on the Gaia DR2 epoch only for HD 151771 A, which at the current separation of the binary (~ 1890 AU) would result from an object of mass $3.5 M_{\odot}$, and so is likely explained by the influence of the secondary star. HD 151771 A and B have RUWE = 1.22 and 0.797 respectively in Gaia EDR3.

We could not find an age in the literature for either star. We used SYCLIST isochrones for B-type stars computed in Georgy et al. 2013, which used the Geneva stellar evolution code (Ekström et al., 2012) to compute grids from 1.7 to $15 M_{\odot}$ for three metallicities ($Z = 0.014$ (solar), $Z = 0.006$, and $Z = 0.002$) and a range of rotation rates (Ω) from zero to critical velocity (Ω_{crit}). We used the stellar luminosity estimate of McDonald et al. 2012 ($L = 311.76 L_{\odot}$) and the 2MASS J-K color ($J-K = 0.08$) to interpolate age from the Georgy et al. 2013 isochrones. We estimated ages for all three metallicities and for three rotation rate values ($\Omega/\Omega_{\text{crit}} = 0.0, 0.5, 0.9$), which returned age estimates spanning 200-300 Myr. We performed our analysis for all nine estimated ages.

HD 164249 — HD 164249 is a 6'' binary at 50 pc in the β Pic moving group (Messina et al., 2017). We adopted the average age of the β Pictoris moving group of 25 ± 3 Myr, derived from lithium depletion boundary modeling (Messina et al., 2016). HD 164249 AB have masses 1.29 and $0.54 M_{\odot}$ (Zúñiga-Fernández et al., 2021) and SpT F6V + M2V (Torres et al., 2006) respectively. HD 164249 AB have RUWE = 1.09 and 1.22. HD 164249 A does not have a significant PMa value.

HD 201247 — HD 201247 is a pair of G-type stars (G5V + G7V; Gray et al. 2006) at 33 pc with separation 4'' and age of 200-300 Myr (derived from chromospheric and coronal X-ray activity and Li EW, Zuckerman et al., 2013). HD 201247 A has mass $0.94 M_{\odot}$ and HD 201247 B has mass $0.89 M_{\odot}$ (Osborn et al., 2020). Both have RUWE close to one (A: RUWE = 1.064, B: RUWE = 1.002) and no significant PMa (S/N < 3).

HD 222259 — HD 222259 (DS Tuc) is a 5'' binary of SpT G6V + K3V (Torres et al., 2000) at 44 pc in the Tucana-Horologium Moving Group. We adopted the average age of 45 Myr derived from isochrone fitting of moving group members (Bell et al., 2015). DS Tuc A and B have masses 1.01 ± 0.06 and $0.84 \pm 0.06 M_{\odot}$ (Newton et al., 2019). Both have RUWE close to one (A: RUWE = 0.95, B: RUWE = 0.91) and no significant PMa ($S/N < 3$). Newton et al. (2019) detected a transiting planet around DS Tuc A with the *Transiting Exoplanet Survey Satellite* (TESS; Ricker et al., 2015) with an 8 day period whose orbit is likely aligned with the binary orbit. They did not find additional companions using the Gemini Planet Imager (GPI, Macintosh et al. 2014) integral field spectroscopy in *H*-band or in the TESS photometry.

HIP 67506 and TYC 7797-34-2 — HIP 67506 is a field star (99.9% probability in Σ in the Banyan catalog). It was identified as a wide binary in the Hipparcos and Tycho Doubles and Multiples Catalog (ESA, 1997) with another star (TYC 7797-34-2) with separation 9'', and dubbed HIP 67506 A and B. HIP 67506 has a distance 89.5 ± 30 pc according to the Hipparcos catalog (van Leeuwen, 2007). HIP 67506 is identified as type G5 (Spencer Jones and Jackson, 1939) and mass $1.2 M_{\odot}$ (Chandler et al., 2016). Both stars have Gaia ERD3 RUWE > 1.4 (A: RUWE = 2.02; B: RUWE = 1.73).

There is no age in the literature for these stars. To estimate the age of HIP 67506, we used the luminosity and effective temperature estimates of McDonald et al. (2012) for the primary ($T_{\text{eff}} = 6077 \pm 150$ K; $L = 0.37 \pm 0.07 L_{\odot}$) to interpolate an age of ≈ 200 Myr using BHAC15 isochrones. There is no literature age nor stellar parameter estimates for TYC 7797-34-2, so we performed our analysis assuming a range of ages from 200 Myr to 10 Gyr.

Status as gravitationally bound binary. Gaia EDR3 shows two sources corresponding to the expected separation and position angle given by Hipparcos, yet differing parallax solutions (A: source id = 6109011780753115776, $\pi = 4.51$ mas; B: source id = 6109011742094383744, $\pi = 0.55$ mas). The dramatically different Gaia parallaxes for A and B question if the two stars are actually a gravitationally bound pair versus a chance alignment of unassociated stars at different distances.

We conducted a common proper motion analysis using Washington Double Star Catalog astrometry of the pair (WDS J13500-4303A and B) and determined the previously-identified HIP 67506 B (TYC 7797-34-2) is in fact an unassociated star that is much further distant. This analysis will be presented in a forthcoming follow up paper on this system, Pearce et al. (in prep). This has no

impact on the utility of the pair for BDI, however it does impact the contrast and mass limits we are able to achieve for the much further distant star.

TWA 13 — TWA 13 is a pair of M1Ve (Torres et al., 2006) T-Tauri stars (Samus' et al., 2003) at 60 pc and 5'' separation in the TW Hydra Association (Schneider et al., 2012). We adopted the mean age of TW Hydra (10_{-7}^{+10} Myr, from isochrone fitting, lithium equivalent width, and H α emission in Barrado Y Navascués 2006. Both have mass of 0.57 M $_{\odot}$ (Herczeg and Hillenbrand, 2014). TWA 13 A has RUWE = 1.085 while TWA 13 B has a slightly elevated RUWE = 1.266.

2MASS J01535076-1459503 — 2MASS J01535076-1459503 is a 3'' young (25 ± 3 Myr, Messina et al. 2016) binary in the β Pictoris Moving Group (Messina et al., 2017) at 33 pc. We adopted the mean age of β Pictoris Moving Group (25 ± 3 Myr, Messina et al. 2016). 2MASS J01535076-1459503 A has a mass of 0.34 M $_{\odot}$ (Osborn et al., 2020) and SpT M3 (Riaz et al., 2006). 2MASS J01535076-1459503 A has a slightly elevated RUWE while 2MASS J01535076-1459503 B has an RUWE close to one (A: RUWE = 1.220, B: RUWE = 1.089).

Appendix B

Appendix to Chapter 5

B.1 HIP 67506 B is not a wide binary companion to HIP 67506 A

The Gaia solutions for HIP 67506 A and HIP 67506 B show differing parallax solutions (A: source id = 6109011780753115776, $\pi = 4.51$ mas; B: source id = 6109011742094383744, $\pi = 0.55$ mas), indicating that HIP 67506 B is an order of magnitude more distant than HIP 67506 A. This raises the question if the two stars are actually a gravitationally bound pair versus a chance alignment of unassociated stars at different distances. We queried the Gaia catalog for all objects within a 1° radius of HIP 67506 A and used a simple Monte Carlo simulation to determine that, given the density of objects in the local region, the probability of a chance alignment of two stars within a $9''$ radius is $38.9 \pm 1.6\%$. The probability of chance alignment of two stars within $9''$ and 2 magnitudes is $4.5 \pm 0.7\%$. So it is plausible that they are a chance alignment.

The Washington Double Star Catalog (WDS; [Mason et al., 2001](#)) astrometry for this system (WDS J13500-4303 A and B) is shown in Table B.1. Figure B.1 displays the motion of HIP 67506 B relative to HIP 67506 A as observed in WDS (circles), the predicted position of HIP 67506 B if it were an unmoving background star and HIP 67506 A moved with the proper motion given by Gaia DR3 (black track and diamonds), and the Gaia DR3 proper motion and parallax track for HIP 67506 B (blue track). The WDS astrometry is consistent with the Gaia proper motion and parallax and not a gravitationally bound pair with common proper motion, indicating that the small parallax in Gaia DR3 for HIP 67506 B is correct and the two are unassociated.

Assuming a mass of $1.2 M_\odot$ for both stars (since HIP 67506 B appears to have a similar brightness as A), the escape velocity at the current separation is $1.306 \pm 0.005 \text{ km s}^{-1}$. Taking the case of a face-on orbit (radial velocity = 0 km s^{-1} , the smallest possible value for the relative velocity vector), the observed linear motion shown in Figure B.1 gives a velocity of $24 \pm 2 \text{ km s}^{-1}$, roughly $14\text{-}\sigma$ larger than the escape velocity. [Clarke \(2020\)](#) and [Belokurov et al. \(2020\)](#) showed that unresolved hierarchical triples and high RUWE astrometric solutions can produce relative velocities exceeding escape velocity and an apparent deviation from Newtonian gravity in the case of bound systems, so we are unable to entirely rule out their being a gravitationally bound system. But the remarkable agreement of WDS astrometry with the Gaia proper motion solutions strongly favors the Gaia parallaxes and proper motions being accurate.

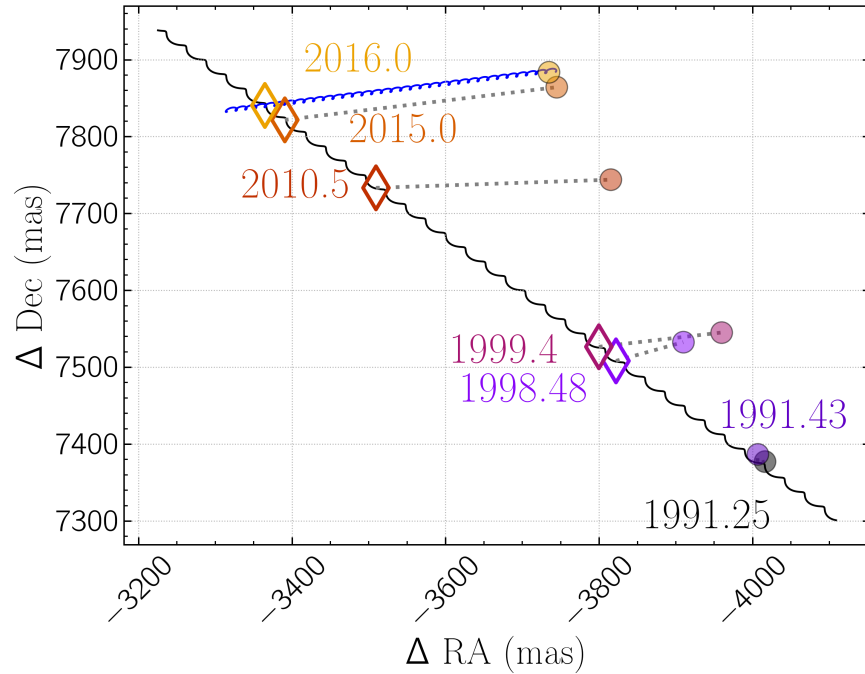


Figure B.1: Relative astrometry of HIP 67506 A and HIP 67506 B (WDS J13500-4303 A and B). The abscissa and ordinate axes display position of HIP 67506 B relative to HIP 67506 A in mas in right ascension (RA) and declination (Dec). The motion of a non-moving background object at the position of HIP 67506 B is shown by the black track for the Gaia DR3 proper motion and parallax given for HIP 67506 B, with the predicted position at WDS observation epochs marked by colored diamonds. The blue track shows the track over the same time span given by the Gaia DR3 proper motion and parallax of HIP 67506 B. The observed WDS positions shown in Table B.1 are marked by filled circles with corresponding epoch colors. The observed motion of HIP 67506 B relative to HIP 67506 A is consistent with the Gaia DR3 proper motion and not with a common proper motion pair. We conclude that the order-of-magnitude higher distance for HIP 67506 B than HIP 67506 A given by Gaia DR3 is correct.

We conclude that the two sources are not a gravitationally bound system, and that the star HIP 67506 B is not in fact a companion to HIP 67506 A, but a much further distant background star.

Table B.1: WDS catalog entry for HIP 67506 A and HIP 67506 B (WDS J13500-4303 A and B)

Date	Position Angle (deg)	PA Error (deg)	Sep (arcsec)	Sep Error (arcsec)	Ref
1991.25	323.3	-	9.190	-	Esa 1997
1991.43	323.4	-	9.19	-	Fabricius et al. 2002
1998.482	324.6	0.1	9.230	0.001	Hartkopf et al. 2013
1999.40	324.3	-	9.28	-	Cutri et al. 2003
2010.5	326.0	0.9	9.33	0.15	Cutri et al. 2012
2015.0	326.899	-	9.377	-	Knapp and Nanson 2018
2016.0	327.0363	0.0002	9.38593	3e-05	Gaia Collaboration et al. 2021

Appendix C

Appendix to Chapter 6

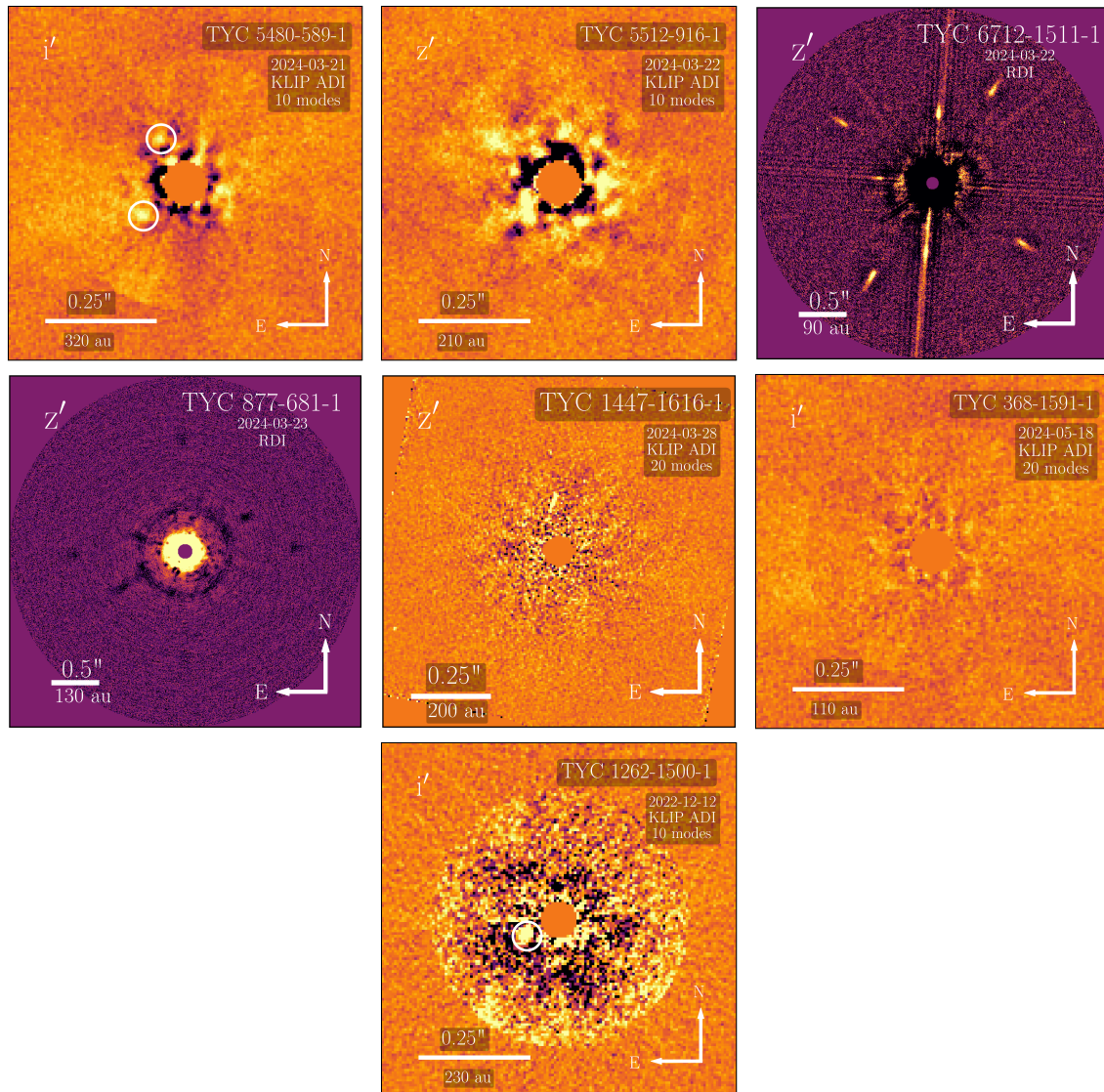


Figure C.1: Reduced images for the systems without companion detection. Each system was reduced using the method indicated. White circles in TYC 5480-589-1 and TYC 1262-1500-1 mark speckles that aren't candidate signals. See the text for details for each system.

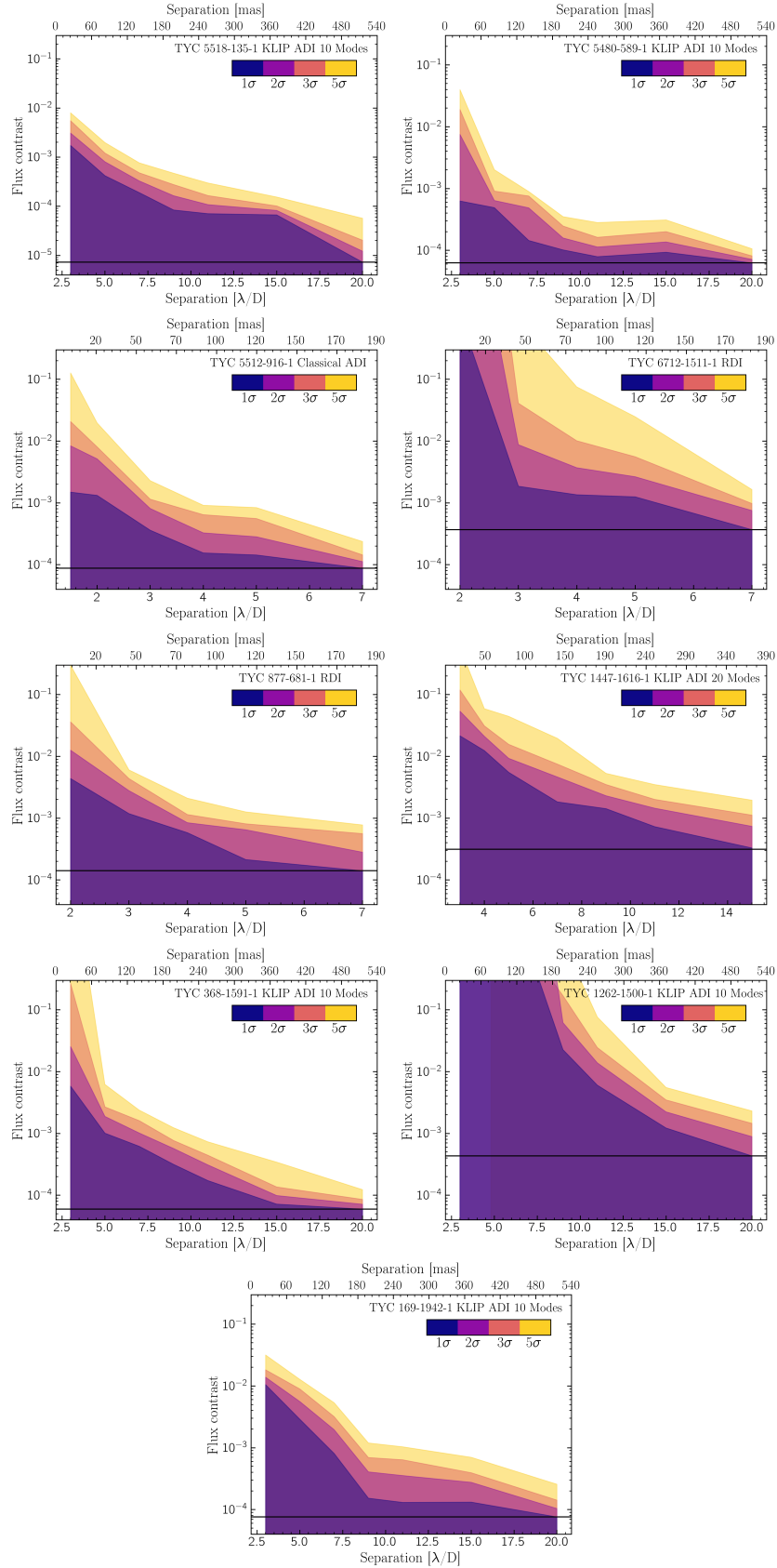


Figure C.2: Contrast curves for non-detections. The colored regions mark the 1-, 2-, 3-, and 5- σ limits as a function of separation for each system and reduction method given. Separation is given in both λ/D units (bottom) and milliarcseconds (top); contrasts are given in flux contrast units. The black line gives the 1- σ noise floor for each observation. The classical ADI reduction got lower limits for TYC 5512-916-1 than KLIP ADI. Contrast curves were computed using the method described in Section 6.3.2

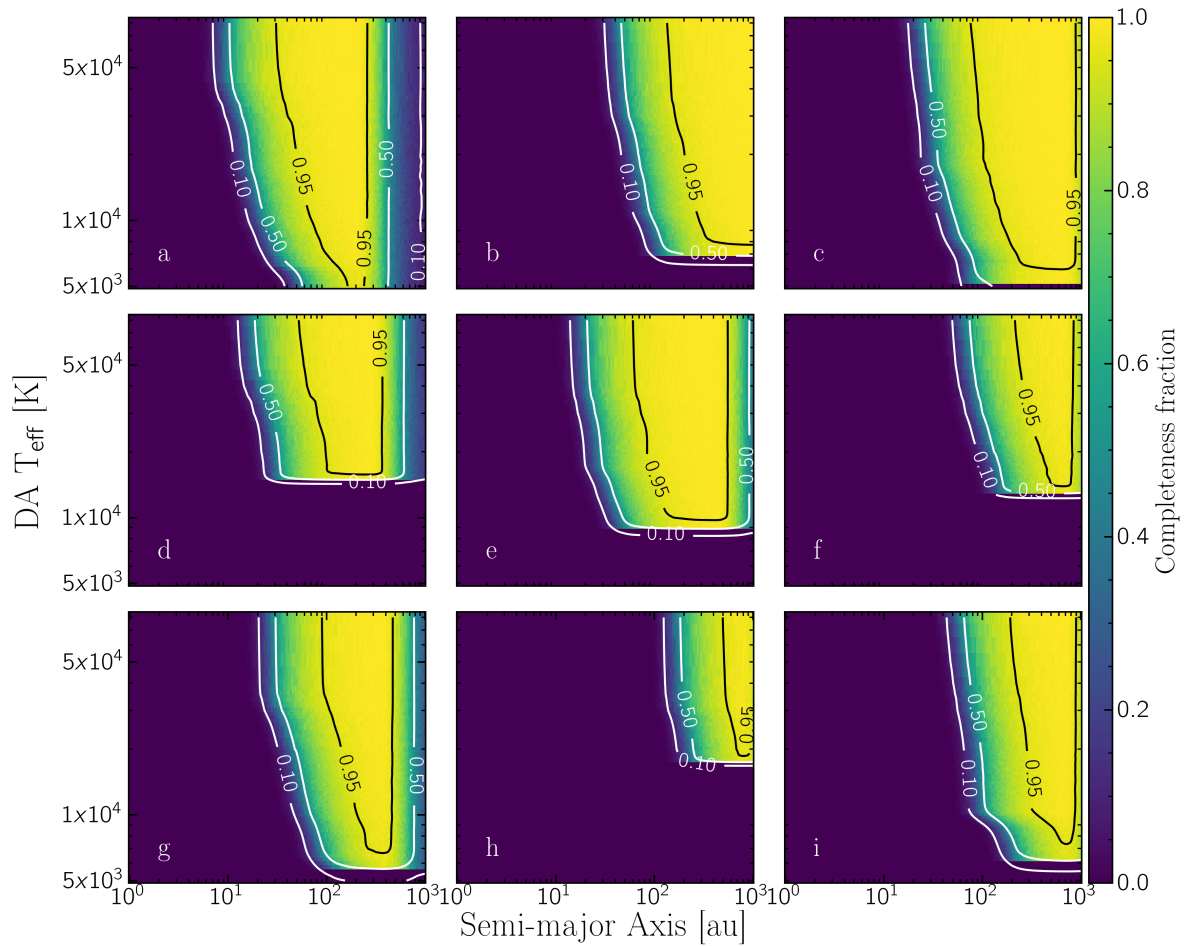


Figure C.3: Completeness maps for non-detections. See text for details. a: TYC 5518-135-1, b: TYC 5480-589-1, c: TYC 5512-916-1, d: TYC 6712-1511-1, e: TYC 877-681-1, f: TYC 1447-1616-1, g: TYC 368-1591-1, h: TYC 1262-1500-1, i: TYC 169-1942-1

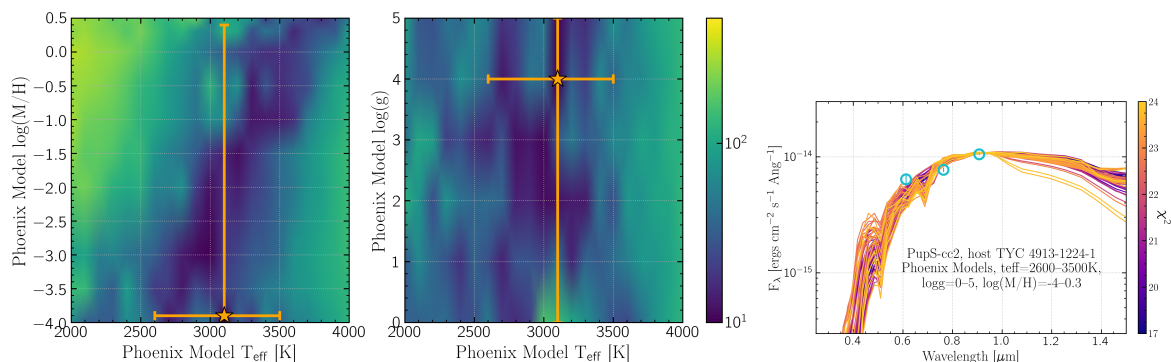


Figure C.4: Fit results for PupS-cc2 to Phoenix models. Top left: χ^2 surface for models in the (T_{eff} , M/H) space with $\log(g)$ fixed at 4.0. The location of the lowest χ^2 is marked by the orange star, and the error bars show models within the uncertainty on that χ^2 value. Top right: χ^2 surface for models in the (T_{eff} , $\log(g)$) space with M/H fixed at -4.0. Both $\log(g)$ and M/H are not constrained by our photometry. Bottom left: Models within 1σ of the lowest χ^2 model, with our photometry and uncertainty overplotted in teal. Bottom right: Violin plots for each model showing the distribution of χ^2 values for the model from our bootstrap simulation with $M/H = -3.5$, $\log(g) = 0$.

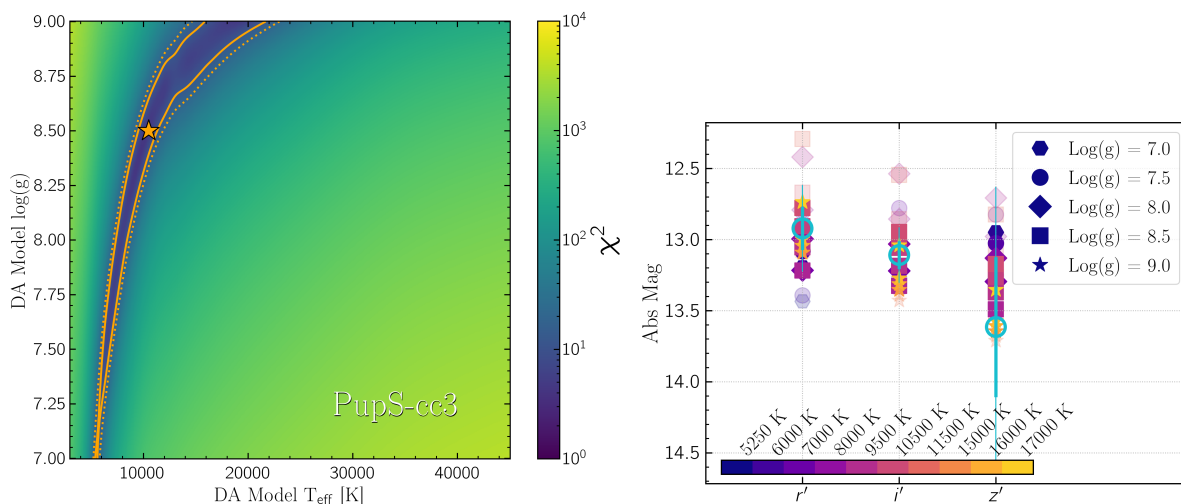


Figure C.5: Model fit results for PupS-cc3. See caption of Figure 6.4 for plot explanation.

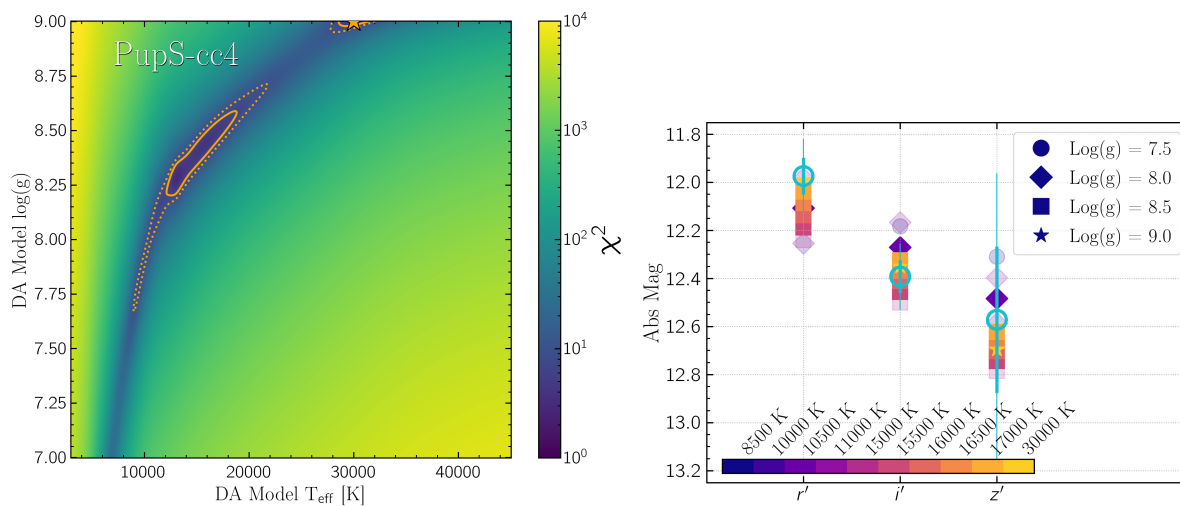


Figure C.6: Model fit results for PupS-cc4. See caption of Figure 6.4 for plot explanation.

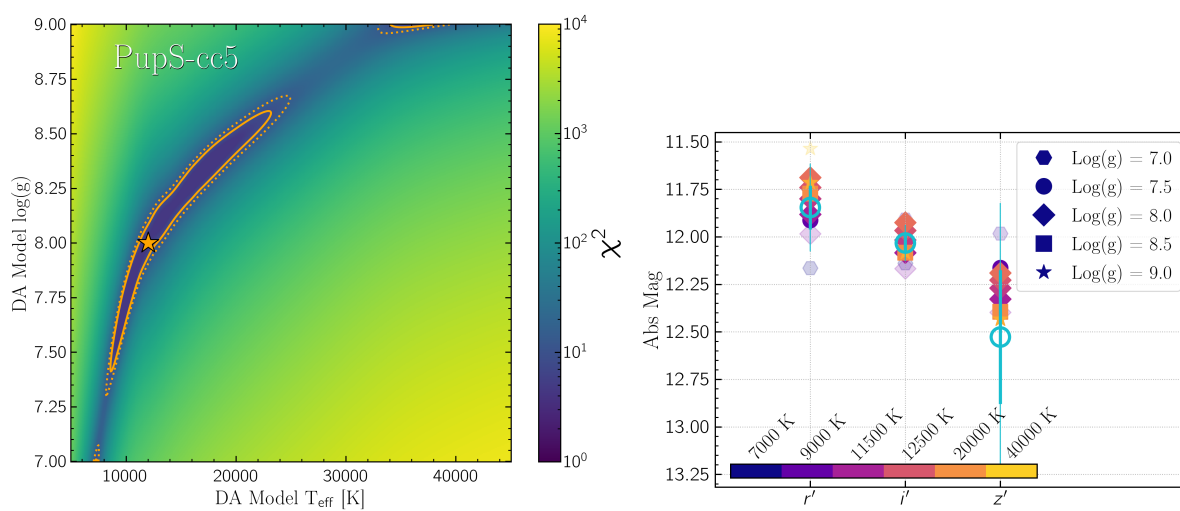


Figure C.7: Model fit results for PupS-cc5. See caption of Figure 6.4 for plot explanation.

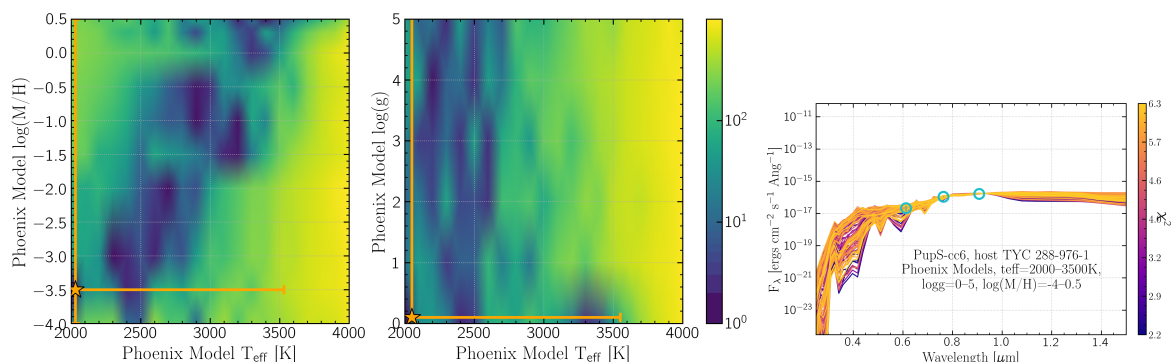


Figure C.8: Fit results for PupS-cc6 to Phoenix models. Top left: χ^2 surface for models in the (T_{eff} , M/H) space with $\log(g)$ fixed at 0.0. The location of the lowest χ^2 is marked by the orange star, and the error bars show models within the uncertainty on that χ^2 value. Top right: χ^2 surface for models in the (T_{eff} , $\log(g)$) space with M/H fixed at -3.5. Both $\log(g)$ and M/H are not constrained by our photometry. Bottom: Models within 1σ of the lowest χ^2 model, with our photometry and uncertainty overplotted in teal.

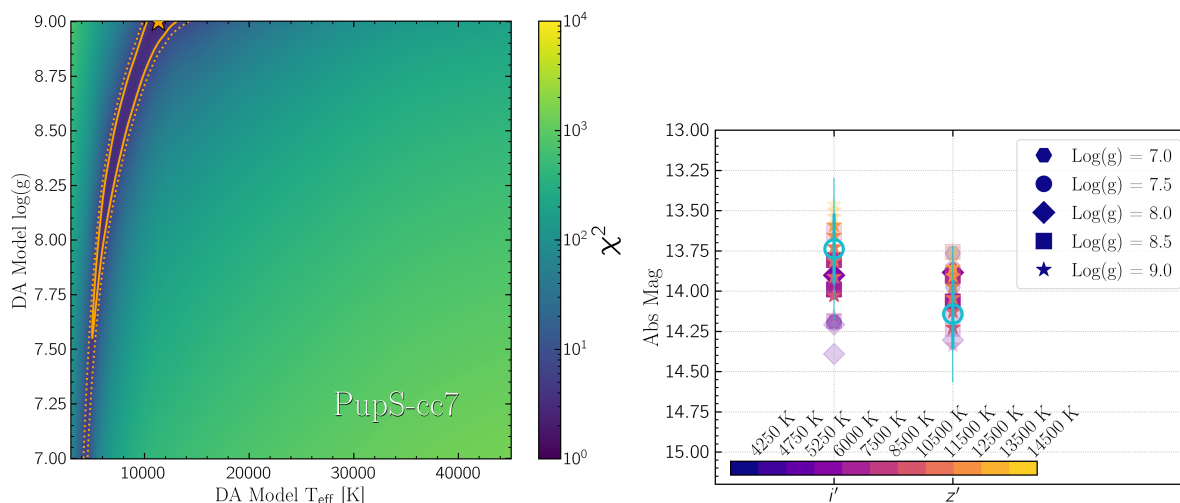


Figure C.9: Model fit results for PupS-cc7. See caption of Figure 6.4 for plot explanation.

References

- A. S. Ackerman and M. S. Marley. Precipitating Condensation Clouds in Substellar Atmospheres. *The Astrophysical Journal*, 556:872–884, Aug. 2001. ISSN 0004-637X. doi: [10.1086/321540](https://doi.org/10.1086/321540). URL <https://ui.adsabs.harvard.edu/abs/2001ApJ...556..872A>. ADS Bibcode: 2001ApJ...556..872A.
- W. S. Adams. The Spectrum of the Companion of Sirius. *PASP*, 27(161):236, Dec. 1915. doi: [10.1086/122440](https://doi.org/10.1086/122440).
- F. Allard, D. Homeier, and B. Freytag. Models of very-low-mass stars, brown dwarfs and exoplanets. *Philosophical Transactions of the Royal Society of London Series A*, 370(1968):2765–2777, June 2012. ISSN 0080-4614. doi: [10.1098/rsta.2011.0269](https://doi.org/10.1098/rsta.2011.0269). URL <http://adsabs.harvard.edu/abs/2012RSPTA.370.2765A>.
- L. G. Althaus, A. H. Córscico, J. Isern, and E. García-Berro. Evolutionary and pulsational properties of white dwarf stars. *A&Ar*, 18(4):471–566, Oct. 2010. doi: [10.1007/s00159-010-0033-1](https://doi.org/10.1007/s00159-010-0033-1).
- F. Anders, A. Khalatyan, C. Chiappini, A. B. Queiroz, B. X. Santiago, C. Jordi, L. Girardi, A. G. A. Brown, G. Matijević, G. Monari, T. Cantat-Gaudin, M. Weiler, S. Khan, A. Miglio, I. Carrillo, M. Romero-Gómez, I. Minchev, R. S. de Jong, T. Antoja, P. Ramos, M. Steinmetz, and H. Enke. Photo-astrometric distances, extinctions, and astrophysical parameters for Gaia DR2 stars brighter than $G = 18$. *A&A*, 628:A94, Aug. 2019. doi: [10.1051/0004-6361/201935765](https://doi.org/10.1051/0004-6361/201935765).
- S. Andrew, Z. Penoyre, V. Belokurov, N. W. Evans, and S. Oh. Binary parameters from astrometric and spectroscopic errors - candidate hierarchical triples and massive dark companions in Gaia DR3. *MNRAS*, 516(3):3661–3684, Nov. 2022. doi: [10.1093/mnras/stac2532](https://doi.org/10.1093/mnras/stac2532).
- G. Anglada-Escudé, P. J. Amado, J. Barnes, Z. M. Berdiñas, R. P. Butler, G. A. L. Coleman, I. de La Cueva, S. Dreizler, M. Endl, B. Giesers, S. V. Jeffers, J. S. Jenkins, H. R. A. Jones,

- M. Kiraga, M. Kürster, M. J. López-González, C. J. Marvin, N. Morales, J. Morin, R. P. Nelson, J. L. Ortiz, A. Ofir, S.-J. Paardekooper, A. Reiners, E. Rodríguez, C. Rodríguez-López, L. F. Sarmiento, J. P. Strachan, Y. Tsapras, M. Tuomi, and M. Zechmeister. A terrestrial planet candidate in a temperate orbit around Proxima Centauri. *Nature*, 536(7617):437–440, Aug. 2016. doi: [10.1038/nature19106](https://doi.org/10.1038/nature19106).
- K. I. Antoniadou and D. Veras. Linking long-term planetary N-body simulations with periodic orbits: application to white dwarf pollution. *MNRAS*, 463(4):4108–4120, Dec. 2016. doi: [10.1093/mnras/stw2264](https://doi.org/10.1093/mnras/stw2264).
- R. Arun, B. Mathew, P. Manoj, K. Ujjwal, S. S. Kartha, G. Viswanath, M. Narang, and K. T. Paul. On the Mass Accretion Rate and Infrared Excess in Herbig Ae/Be Stars. *AJ*, 157(4):159, Apr. 2019. doi: [10.3847/1538-3881/ab0ca1](https://doi.org/10.3847/1538-3881/ab0ca1).
- R. Asensio-Torres, M. Janson, M. Bonavita, S. Desidera, C. Thalmann, M. Kuzuhara, T. Henning, F. Marzari, M. R. Meyer, P. Calissendorff, and T. Uyama. SPOTS: The Search for Planets Orbiting Two Stars. III. Complete sample and statistical analysis. *A&A*, 619:A43, Oct. 2018. doi: [10.1051/0004-6361/201833349](https://doi.org/10.1051/0004-6361/201833349).
- Astropy Collaboration, A. M. Price-Whelan, P. L. Lim, N. Earl, N. Starkman, L. Bradley, D. L. Shupe, A. A. Patil, L. Corrales, C. E. Brasseur, M. N’othe, A. Donath, E. Tollerud, B. M. Morris, A. Ginsburg, E. Vaher, B. A. Weaver, J. Tocknell, W. Jamieson, M. H. van Kerkwijk, T. P. Robitaille, B. Merry, M. Bachetti, H. M. G’unther, T. L. Aldcroft, J. A. Alvarado-Montes, A. M. Archibald, A. B’odi, S. Bapat, G. Barentsen, J. Baz’an, M. Biswas, M. Boquien, D. J. Burke, D. Cara, M. Cara, K. E. Conroy, S. Conseil, M. W. Craig, R. M. Cross, K. L. Cruz, F. D’Eugenio, N. Dencheva, H. A. R. Devillepoix, J. P. Dietrich, A. D. Eigenbrot, T. Erben, L. Ferreira, D. Foreman-Mackey, R. Fox, N. Freij, S. Garg, R. Geda, L. Glattly, Y. Gondhalekar, K. D. Gordon, D. Grant, P. Greenfield, A. M. Groener, S. Guest, S. Gurovich, R. Handberg, A. Hart, Z. Hatfield-Dodds, D. Homeier, G. Hosseinzadeh, T. Jenness, C. K. Jones, P. Joseph, J. B. Kalmbach, E. Karamehmetoglu, M. Kaluszy’nski, M. S. P. Kelley, N. Kern, W. E. Kerzendorf, E. W. Koch, S. Kulumani, A. Lee, C. Ly, Z. Ma, C. MacBride, J. M. Maljaars, D. Muna, N. A. Murphy, H. Norman, R. O’Steen, K. A. Oman, C. Pacifici, S. Pascual, J. Pascual-Granado, R. R. Patil,

- G. I. Perren, T. E. Pickering, T. Rastogi, B. R. Roulston, D. F. Ryan, E. S. Rykoff, J. Sabater, P. Sakurikar, J. Salgado, A. Sanghi, N. Saunders, V. Savchenko, L. Schwardt, M. Seifert-Eckert, A. Y. Shih, A. S. Jain, G. Shukla, J. Sick, C. Simpson, S. Singanamalla, L. P. Singer, J. Singhal, M. Sinha, B. M. SipHocz, L. R. Spitler, D. Stansby, O. Streicher, J. Sumak, J. D. Swinbank, D. S. Taranu, N. Tewary, G. R. Tremblay, M. d. Val-Borro, S. J. Van Kooten, Z. Vasovi'c, S. Verma, J. V. de Miranda Cardoso, P. K. G. Williams, T. J. Wilson, B. Winkel, W. M. Wood-Vasey, R. Xue, P. Yoachim, C. Zhang, A. Zonca, and Astropy Project Contributors. The Astropy Project: Sustaining and Growing a Community-oriented Open-source Project and the Latest Major Release (v5.0) of the Core Package. *ApJ*, 935(2):167, Aug. 2022. doi: [10.3847/1538-4357/ac7c74](https://doi.org/10.3847/1538-4357/ac7c74).
- R. Azulay, J. C. Guirado, J. M. Marcaide, I. Martí-Vidal, E. Ros, E. Tognelli, D. L. Jauncey, J. F. Lestrade, and J. E. Reynolds. The AB Doradus system revisited: The dynamical mass of AB Dor A/C. *A&A*, 607:A10, Oct. 2017. doi: [10.1051/0004-6361/201730641](https://doi.org/10.1051/0004-6361/201730641).
- C. A. L. Bailer-Jones, J. Rybizki, M. Fouesneau, G. Mantelet, and R. Andrae. Estimating Distance from Parallaxes. IV. Distances to 1.33 Billion Stars in Gaia Data Release 2. *The Astronomical Journal*, 156:58, Aug. 2018. ISSN 0004-6256. doi: [10.3847/1538-3881/aacb21](https://doi.org/10.3847/1538-3881/aacb21). URL <http://adsabs.harvard.edu/abs/2018AJ....156...58B>.
- C. A. L. Bailer-Jones, J. Rybizki, M. Fouesneau, M. Demleitner, and R. Andrae. VizieR Online Data Catalog: Distances to 1.47 billion stars in Gaia EDR3 (Bailer-Jones+, 2021). art. I/352, Feb. 2021.
- W. O. Balmer, L. Pueyo, T. Stolker, H. Reggiani, A. L. Maire, S. Lacour, P. Mollière, M. Nowak, D. Sing, N. Pourré, S. Blunt, J. J. Wang, E. Rickman, J. Kammerer, T. Henning, K. Ward-Duong, R. Abuter, A. Amorim, R. Asensio-Torres, M. Benisty, J. P. Berger, H. Beust, A. Boccaletti, A. Bohn, M. Bonnefoy, H. Bonnet, G. Bourdarot, W. Brandner, F. Cantalloube, P. Caselli, B. Charnay, G. Chauvin, A. Chavez, E. Choquet, V. Christiaens, Y. Clénet, V. Coudé Du Foresto, A. Cridland, R. Dembet, J. Dexter, A. Drescher, G. Duvert, A. Eckart, F. Eisenhauer, F. Gao, P. Garcia, R. Garcia Lopez, E. Gendron, R. Genzel, S. Gillessen, J. H. Girard, X. Haubois, G. Heißel, S. Hinkley, S. Hippler, M. Horrobin, M. Houllé, Z. Hubert, L. Jocu, M. Keppler,

- P. Kervella, L. Kreidberg, A. M. Lagrange, V. Lapeyrère, J. B. Le Bouquin, P. Léna, D. Lutz, J. D. Monnier, D. Mouillet, E. Nasedkin, T. Ott, G. P. P. L. Otten, C. Paladini, T. Paumard, K. Perraut, G. Perrin, O. Pfuhl, J. Rameau, L. Rodet, G. Rousset, Z. Rustamkulov, J. Shang-guan, T. Shimizu, J. Stadler, O. Straub, C. Straubmeier, E. Sturm, L. J. Tacconi, E. F. van Dishoeck, A. Vigan, F. Vincent, S. D. von Fellenberg, F. Widmann, E. Wieprecht, E. Wiezorrek, T. Winterhalder, J. Woillez, S. Yazici, A. Young, and Gravity Collaboration. VLT/GRAVITY Observations and Characterization of the Brown Dwarf Companion HD 72946 B. *ApJ*, 956(2): 99, Oct. 2023. doi: [10.3847/1538-4357/acf761](https://doi.org/10.3847/1538-4357/acf761).
- D. Bancelin, T. Nordlander, E. Pilat-Lohinger, and B. Loibnegger. Dynamics of passing-stars-perturbed binary star systems. *Monthly Notices of the Royal Astronomical Society*, 486(4): 4773–4780, July 2019. doi: [10.1093/mnras/stz1173](https://doi.org/10.1093/mnras/stz1173). URL <http://adsabs.harvard.edu/abs/2019MNRAS.486.4773B>.
- I. Baraffe, D. Homeier, F. Allard, and G. Chabrier. New evolutionary models for pre-main sequence and main sequence low-mass stars down to the hydrogen-burning limit. *A&A*, 577:A42, May 2015. doi: [10.1051/0004-6361/201425481](https://doi.org/10.1051/0004-6361/201425481).
- D. Barrado y Navascues, J. R. John R. Stauffer, and R. Jayawardhana. Spectroscopy of very low mass stars and brown dwarfs in IC 2391: Lithium depletion and $h\alpha$ emission. *ApJ*, 614(1): 386–397, oct 2004. doi: [10.1086/423485](https://doi.org/10.1086/423485). URL <https://doi.org/10.1086/423485>.
- D. Barrado Y Navascués. On the age of the TW Hydrae association and 2M1207334-393254. *Astronomy and Astrophysics*, 459:511–518, Nov. 2006. ISSN 0004-6361. doi: [10.1051/0004-6361:20065717](https://doi.org/10.1051/0004-6361:20065717). URL <http://adsabs.harvard.edu/abs/2006A%26A...459..511B>.
- N. E. Batalha, N. K. Lewis, M. R. Line, J. Valenti, and K. Stevenson. Strategies for Constraining the Atmospheres of Temperate Terrestrial Planets with JWST. *The Astrophysical Journal*, 856: L34, Apr. 2018. ISSN 0004-637X. doi: [10.3847/2041-8213/aab896](https://doi.org/10.3847/2041-8213/aab896). URL <https://ui.adsabs.harvard.edu/abs/2018ApJ...856L..34B>. ADS Bibcode: 2018ApJ...856L..34B.
- N. E. Batalha, M. S. Marley, N. K. Lewis, and J. J. Fortney. Exoplanet Reflected-light Spectroscopy with PICASO. *The Astrophysical Journal*, 878:70, June 2019. ISSN 0004-637X. doi:

- 10.3847/1538-4357/ab1b51. URL <http://adsabs.harvard.edu/abs/2019ApJ...878...70B>. ADS Bibcode: 2019ApJ...878...70B.
- K. Batygin, K. M. Deck, and M. J. Holman. Dynamical Evolution of Multi-resonant Systems: The Case of GJ876. *AJ*, 149(5):167, May 2015. doi: [10.1088/0004-6256/149/5/167](https://doi.org/10.1088/0004-6256/149/5/167).
- A. Bzszó and E. Pilat-Lohinger. Fear the Shadows of the Giants: On Secular Perturbations in Circumstellar Habitable Zones of Double Stars. *AJ*, 160(1):2, June 2020. ISSN 1538-3881. doi: [10.3847/1538-3881/ab9104](https://doi.org/10.3847/1538-3881/ab9104). URL <https://doi.org/10.3847/1538-3881/ab9104>. Publisher: American Astronomical Society.
- C. P. M. Bell, E. E. Mamajek, and T. Naylor. A self-consistent, absolute isochronal age scale for young moving groups in the solar neighbourhood. *Monthly Notices of the Royal Astronomical Society*, 454:593–614, Nov. 2015. ISSN 0035-8711. doi: [10.1093/mnras/stv1981](https://doi.org/10.1093/mnras/stv1981). URL <http://adsabs.harvard.edu/abs/2015MNRAS.454..593B>.
- V. Belokurov, Z. Penoyre, S. Oh, G. Iorio, S. Hodgkin, N. W. Evans, A. Everall, S. E. Koposov, C. A. Tout, R. Izzard, C. J. Clarke, and A. G. A. Brown. Unresolved stellar companions with Gaia DR2 astrometry. *Monthly Notices of the Royal Astronomical Society*, 496(2):1922–1940, June 2020. ISSN 0035-8711. doi: [10.1093/mnras/staa1522](https://doi.org/10.1093/mnras/staa1522). URL <http://adsabs.harvard.edu/abs/2020MNRAS.496.1922B>.
- T. A. Berger, D. Huber, J. L. van Saders, E. Gaidos, J. Tayar, and A. L. Kraus. The Gaia-Kepler Stellar Properties Catalog. I. Homogeneous Fundamental Properties for 186,301 Kepler Stars. *AJ*, 159(6):280, June 2020. doi: [10.3847/1538-3881/159/6/280](https://doi.org/10.3847/1538-3881/159/6/280).
- P. Bergeron, F. Wesemael, and A. Beauchamp. Photometric Calibration of Hydrogen- and Helium-Rich White Dwarf Models. *Publications of the Astronomical Society of the Pacific*, 107:1047, Nov. 1995. doi: [10.1086/133661](https://doi.org/10.1086/133661).
- F. Berrilli, G. Corciulo, G. Ingrassio, D. Lorenzetti, B. Nisini, and F. Strafella. Infrared Emission from Dust Structures Surrounding Herbig Ae/Be Stars. *ApJ*, 398:254, Oct. 1992. doi: [10.1086/171853](https://doi.org/10.1086/171853).

- F. W. Bessel. On the variations of the proper motions of Procyon and Sirius. *MNRAS*, 6:136–141, Dec. 1844. doi: [10.1093/mnras/6.11.136](https://doi.org/10.1093/mnras/6.11.136).
- S. Best and C. Petrovich. The Chaotic History of the Retrograde Multi-planet System in K2-290A Driven by Distant Stars. *ApJL*, 925(1):L5, Jan. 2022. doi: [10.3847/2041-8213/ac49e9](https://doi.org/10.3847/2041-8213/ac49e9).
- J.-L. Beuzit, M. Feldt, K. Dohlen, D. Mouillet, P. Puget, F. Wildi, L. Abe, J. Antichi, A. Baruffolo, P. Baudoz, A. Boccaletti, M. Carbillet, J. Charton, R. Claudi, M. Downing, C. Fabron, P. Feautrier, E. Fedrigo, T. Fusco, J.-L. Gach, R. Gratton, T. Henning, N. Hubin, F. Joos, M. Kasper, M. Langlois, R. Lenzen, C. Moutou, A. Pavlov, C. Petit, J. Pragt, P. Rabou, F. Rigal, R. Roelfsema, G. Rousset, M. Saisse, H.-M. Schmid, E. Stadler, C. Thalmann, M. Turatto, S. Udry, F. Vakili, and R. Waters. SPHERE: a 'Planet Finder' instrument for the VLT. In I. S. McLean and M. M. Casali, editors, *Ground-based and Airborne Instrumentation for Astronomy II*, volume 7014 of *Society of Photo-Optical Instrumentation Engineers (SPIE) Conference Series*, page 701418, July 2008. doi: [10.1117/12.790120](https://doi.org/10.1117/12.790120).
- L. Bianchi, B. Shiao, and D. Thilker. Revised Catalog of GALEX Ultraviolet Sources. I. The All-Sky Survey: GUVcat_AIS. *ApJs*, 230(2):24, June 2017. doi: [10.3847/1538-4365/aa7053](https://doi.org/10.3847/1538-4365/aa7053).
- A. S. Binks, R. D. Jeffries, and N. J. Wright. A kinematically hot population of young stars in the solar neighbourhood. *MNRAS*, 494(2):2429–2439, May 2020. doi: [10.1093/mnras/staa909](https://doi.org/10.1093/mnras/staa909).
- S. Blunt, E. L. Nielsen, R. J. De Rosa, Q. M. Konopacky, D. Ryan, J. J. Wang, L. Pueyo, J. Rameau, C. Marois, F. Marchis, B. Macintosh, J. R. Graham, G. Duchêne, and A. C. Schneider. Orbits for the Impatient: A Bayesian Rejection-sampling Method for Quickly Fitting the Orbits of Long-period Exoplanets. *The Astronomical Journal*, 153:229, May 2017. ISSN 0004-6256. doi: [10.3847/1538-3881/aa6930](https://doi.org/10.3847/1538-3881/aa6930). URL <http://adsabs.harvard.edu/abs/2017AJ....153..229B>.
- S. Blunt, J. J. Wang, I. Angelo, H. Ngo, D. Cody, R. J. De Rosa, J. R. Graham, L. Hirsch, V. Nagpal, E. L. Nielsen, L. Pearce, M. Rice, and R. Tejada. orbitize!: A Comprehensive Orbit-fitting Software Package for the High-contrast Imaging Community. *The Astronomical Journal*, 159:89, Mar. 2020. ISSN 0004-6256. doi: [10.3847/1538-3881/ab6663](https://doi.org/10.3847/1538-3881/ab6663). URL <http://adsabs.harvard.edu/abs/2020AJ....159...89B>.

- E. H. L. Bodman and A. Quillen. KIC 8462852: Transit of a Large Comet Family. *The Astrophysical Journal Letters*, 819:L34, Mar. 2016. ISSN 0004-637X. doi: [10.3847/2041-8205/819/2/L34](https://doi.org/10.3847/2041-8205/819/2/L34). URL <http://adsabs.harvard.edu/abs/2016ApJ...819L..34B>.
- R. C. Bohlin, K. D. Gordon, and P. E. Tremblay. Techniques and Review of Absolute Flux Calibration from the Ultraviolet to the Mid-Infrared. *PASP*, 126(942):711, Aug. 2014. doi: [10.1086/677655](https://doi.org/10.1086/677655).
- R. C. Bohlin, I. Hubeny, and T. Rauch. New Grids of Pure-hydrogen White Dwarf NLTE Model Atmospheres and the HST/STIS Flux Calibration. *AJ*, 160(1):21, July 2020. doi: [10.3847/1538-3881/ab94b4](https://doi.org/10.3847/1538-3881/ab94b4).
- M. Bonavita and S. Desidera. The frequency of planets in multiple systems. *A&A*, 468(2):721–729, June 2007. doi: [10.1051/0004-6361:20066671](https://doi.org/10.1051/0004-6361:20066671).
- M. Bonavita, S. Desidera, C. Thalmann, M. Janson, A. Vigan, G. Chauvin, and J. Lannier. SPOTS: The Search for Planets Orbiting Two Stars. II. First constraints on the frequency of sub-stellar companions on wide circumbinary orbits. *A&A*, 593:A38, Sept. 2016. doi: [10.1051/0004-6361/201628231](https://doi.org/10.1051/0004-6361/201628231).
- A. Bonsor and D. Veras. A wide binary trigger for white dwarf pollution. *Mon. Not. R. Astron. Soc.*, 454:53–63, Nov. 2015. ISSN 0035-8711. doi: [10.1093/mnras/stv1913](https://doi.org/10.1093/mnras/stv1913).
- A. Bonsor, A. J. Mustill, and M. C. Wyatt. Dynamical effects of stellar mass-loss on a Kuiper-like belt. *Mon. Not. R. Astron. Soc.*, 414(2):930–939, June 2011. ISSN 0035-8711. doi: [10.1111/j.1365-2966.2011.18524.x](https://doi.org/10.1111/j.1365-2966.2011.18524.x).
- W. J. Borucki, D. Koch, G. Basri, N. Batalha, T. Brown, D. Caldwell, J. Caldwell, J. Christensen-Dalsgaard, W. D. Cochran, E. DeVore, E. W. Dunham, A. K. Dupree, T. N. Gautier, J. C. Geary, R. Gilliland, A. Gould, S. B. Howell, J. M. Jenkins, Y. Kondo, D. W. Latham, G. W. Marcy, S. Meibom, H. Kjeldsen, J. J. Lissauer, D. G. Monet, D. Morrison, D. Sasselov, J. Tarter, A. Boss, D. Brownlee, T. Owen, D. Buzasi, D. Charbonneau, L. Doyle, J. Fortney, E. B. Ford, M. J. Holman, S. Seager, J. H. Steffen, W. F. Welsh, J. Rowe, H. Anderson, L. Buchhave, D. Ciardi, L. Walkowicz, W. Sherry, E. Horch, H. Isaacson, M. E. Everett, D. Fischer, G. Torres,

- J. A. Johnson, M. Endl, P. MacQueen, S. T. Bryson, J. Dotson, M. Haas, J. Kolodziejczak, J. Van Cleve, H. Chandrasekaran, J. D. Twicken, E. V. Quintana, B. D. Clarke, C. Allen, J. Li, H. Wu, P. Tenenbaum, E. Verner, F. Bruhweiler, J. Barnes, and A. Prsa. Kepler Planet-Detection Mission: Introduction and First Results. *Science*, 327(5968):977, Feb. 2010. doi: [10.1126/science.1185402](https://doi.org/10.1126/science.1185402).
- M. Bottom, J. K. Wallace, R. D. Bartos, J. C. Shelton, and E. Serabyn. Speckle suppression and companion detection using coherent differential imaging. *MNRAS*, 464(3):2937–2951, Jan. 2017. doi: [10.1093/mnras/stw2544](https://doi.org/10.1093/mnras/stw2544).
- B. P. Bowler. Imaging Extrasolar Giant Planets. *Publications of the Astronomical Society of the Pacific*, 128(10):102001, Oct. 2016. ISSN 0004-6280. doi: [10.1088/1538-3873/128/968/102001](https://doi.org/10.1088/1538-3873/128/968/102001). URL <http://adsabs.harvard.edu/abs/2016PASP..128j2001B>.
- B. P. Bowler and E. L. Nielsen. Occurrence Rates from Direct Imaging Surveys. In H. J. Deeg and J. A. Belmonte, editors, *Handbook of Exoplanets*, page 155. Springer International Publishing AG, 2018. doi: [10.1007/978-3-319-55333-7_155](https://doi.org/10.1007/978-3-319-55333-7_155).
- B. P. Bowler, W. D. Cochran, M. Endl, K. Franson, T. D. Brandt, T. J. Dupuy, P. J. MacQueen, K. M. Kratter, D. Mawet, and G. Ruane. The McDonald Accelerating Stars Survey (MASS): White Dwarf Companions Accelerating the Sun-like Stars 12 Psc and HD 159062. *AJ*, 161(3): 106, Mar. 2021. doi: [10.3847/1538-3881/abd243](https://doi.org/10.3847/1538-3881/abd243).
- T. S. Boyajian, D. M. LaCourse, S. A. Rappaport, D. Fabrycky, D. A. Fischer, D. Gandolfi, G. M. Kennedy, H. Korhonen, M. C. Liu, A. Moor, K. Olah, K. Vida, M. C. Wyatt, W. M. J. Best, J. Brewer, F. Ciesla, B. Csák, H. J. Deeg, T. J. Dupuy, G. Handler, K. Heng, S. B. Howell, S. T. Ishikawa, J. Kovács, T. Kozakis, L. Kriskovics, J. Lehtinen, C. Lintott, S. Lynn, D. Nespral, S. Nikbakhsh, K. Schawinski, J. R. Schmitt, A. M. Smith, G. Szabo, R. Szabo, J. Viuhö, J. Wang, A. Weiksnar, M. Bosch, J. L. Connors, S. Goodman, G. Green, A. J. Hoekstra, T. Jebson, K. J. Jek, M. R. Omohundro, H. M. Schwengeler, and A. Szewczyk. Planet Hunters IX. KIC 8462852 - where's the flux? *Monthly Notices of the Royal Astronomical Society*, 457:3988–4004, Apr. 2016. ISSN 0035-8711. doi: [10.1093/mnras/stw218](https://doi.org/10.1093/mnras/stw218). URL <http://adsabs.harvard.edu/abs/2016MNRAS.457.3988B>.

T. S. Boyajian, R. Alonso, A. Ammerman, D. Armstrong, A. Asensio Ramos, K. Barkaoui, T. G. Beatty, Z. Benkhaldoun, P. Benni, R. O. Bentley, A. Berdyugin, S. Berdyugina, S. Bergeron, A. Bieryla, M. G. Blain, A. Capetillo Blanco, E. H. L. Bodman, A. Boucher, M. Bradley, S. M. Brincat, T. G. Brink, J. Briol, D. J. A. Brown, J. Budaj, A. Burdanov, B. Cale, M. Aznar Carbo, R. Castillo García, W. J. Clark, G. C. Clayton, J. L. Clem, P. H. Coker, E. M. Cook, C. M. Copperwheat, J. L. Curtis, R. M. Cutri, B. Cseh, C. H. Cynamon, A. J. Daniels, J. R. A. Davenport, H. J. Deeg, R. De Lorenzo, T. de Jaeger, J.-B. Desrosiers, J. Dolan, D. J. Dowhos, F. Dubois, R. Durkee, S. Dvorak, L. Easley, N. Edwards, T. G. Ellis, E. Erdelyi, S. Ertel, R. G. Farfán, J. Farihi, A. V. Filippenko, E. Foxell, D. Gandolfi, F. Garcia, F. Giddens, M. Gillon, J.-L. González-Carballo, C. González-Fernández, J. I. González Hernández, K. A. Graham, K. A. Greene, J. Gregorio, N. Hallakoun, O. Hanyecz, G. R. Harp, G. W. Henry, E. Herrero, C. F. Hildbold, D. Hinz, G. Holgado, B. Ignácz, I. Ilyin, V. D. Ivanov, E. Jehin, H. E. Jermak, S. Johnston, S. Kafka, C. Kalup, E. Kardasis, S. Kaspi, G. M. Kennedy, F. Kiefer, C. L. Kielty, D. Kessler, H. Kiiskinen, T. L. Killestein, R. A. King, V. Kollar, H. Korhonen, C. Kotnik, R. Könyves-Tóth, L. Kriskovics, N. Krumm, V. Krushinsky, E. Kundra, F.-R. Lachapelle, D. Lacombe, P. Lake, K. Lam, G. P. Lamb, D. Lane, M. W. Lau, P. Lewin, C. Lintott, C. Lisse, L. Logg, N. Longeard, M. Lopez Villanueva, E. Whit Ludington, A. Mainzer, L. Malo, C. Maloney, A. Mann, A. Mantero, M. Marengo, J. Marchant, M. J. Martínez González, J. R. Masiero, J. C. Mauerhan, J. McCormac, A. McNeely, H. Y. A. Meng, M. Miller, L. A. Molnar, J. C. Morales, B. M. Morris, M. W. Muterspaugh, D. Nespral, C. R. Nugent, K. M. Nugent, A. Odasso, D. O’Keeffe, A. Oksanen, J. M. O’Meara, A. Ordasi, H. Osborn, J. J. Ott, J. R. Parks, D. Rodriguez Perez, V. Petriew, R. Pickard, A. Pál, P. Plavchan, D. Pollacco, F. Pozo Nuñez, F. J. Pozuelos, S. Rau, S. Redfield, H. Relles, I. Ribas, J. Richards, J. L. O. Saario, E. J. Safron, J. M. Sallai, K. Sárneczky, B. E. Schaefer, C. F. Schumer, M. Schwartzendruber, M. H. Siegel, A. P. V. Siemion, B. D. Simmons, J. D. Simon, S. Simón-Díaz, M. L. Sitko, H. Socas-Navarro, A. Sodor, D. Starkey, I. A. Steele, G. Stone, K. G. Strassmeier, R. A. Street, T. Sullivan, J. Suomela, J. J. Swift, G. M. Szabó, R. Szabó, R. Szakáts, T. Szalai, A. M. Tanner, B. Toledo-Padrón, T. Tordai, A. H. M. J. Triaud, J. D. Turner, J. H. Ulowetz, M. Urbanik, S. Vanaverbeke, A. Vanderburg, K. Vida, B. P. Vietje, J. Vinkó, K. von Braun, E. O. Waagen, D. Walsh, C. A. Watson, R. C. Weir, K. Wenzel, C. Westendorp Plaza, M. W. Williamson, J. T. Wright, M. C. Wyatt, W. Zheng, and

- G. Zsidi. The First Post-Kepler Brightness Dips of KIC 8462852. *The Astrophysical Journal Letters*, 853:L8, Jan. 2018. ISSN 0004-637X. doi: [10.3847/2041-8213/aaa405](https://doi.org/10.3847/2041-8213/aaa405). URL <http://adsabs.harvard.edu/abs/2018ApJ...853L...8B>.
- L. Bradley, B. Sipőcz, T. Robitaille, E. Tollerud, Z. Vinícius, C. Deil, K. Barbary, T. J. Wilson, I. Busko, H. M. Günther, M. Cara, S. Conseil, A. Bostroem, M. Droettboom, E. M. Bray, L. A. Bratholm, P. L. Lim, G. Barentsen, M. Craig, S. Pascual, G. Perren, J. Greco, A. Donath, M. de Val-Borro, W. Kerzendorf, Y. P. Bach, B. A. Weaver, F. D'Eugenio, H. Souchereau, and L. Ferreira. *astropy/photutils*: 1.0.0. Sept. 2020. doi: [10.5281/zenodo.4044744](https://doi.org/10.5281/zenodo.4044744). URL <https://doi.org/10.5281/zenodo.4044744>.
- L. Bradley, B. Sipőcz, T. Robitaille, E. Tollerud, Z. Vinícius, C. Deil, K. Barbary, T. J. Wilson, I. Busko, A. Donath, H. M. Günther, M. Cara, P. L. Lim, S. Meßlinger, S. Conseil, A. Bostroem, M. Droettboom, E. M. Bray, L. A. Bratholm, G. Barentsen, M. Craig, S. Rathi, S. Pascual, G. Perren, I. Y. Georgiev, M. de Val-Borro, W. Kerzendorf, Y. P. Bach, B. Quint, and H. Souchereau. *astropy/photutils*: 1.8.0. May 2023. doi: [10.5281/zenodo.7946442](https://doi.org/10.5281/zenodo.7946442). URL <https://doi.org/10.5281/zenodo.7946442>.
- G. M. Brandt, T. D. Brandt, T. J. Dupuy, Y. Li, and D. Michalik. Precise Dynamical Masses and Orbital Fits for beta Pic β and β Pic c. *AJ*, 161(4):179, Apr. 2021. doi: [10.3847/1538-3881/abdc2e](https://doi.org/10.3847/1538-3881/abdc2e).
- T. D. Brandt. The Hipparcos-Gaia Catalog of Accelerations. *The Astrophysical Journal Supplement Series*, 239(2):31, Dec. 2018. ISSN 0067-0049. doi: [10.3847/1538-4365/aaec06](https://doi.org/10.3847/1538-4365/aaec06). URL <http://adsabs.harvard.edu/abs/2018ApJS..239...31B>.
- T. D. Brandt. The Hipparcos-Gaia Catalog of Accelerations: Gaia EDR3 Edition. *ApJs*, 254(2):42, June 2021. doi: [10.3847/1538-4365/abf93c](https://doi.org/10.3847/1538-4365/abf93c).
- T. D. Brandt. Astrometry as a Tool for Discovering and Weighing Faint Companions to Nearby Stars. *arXiv e-prints*, art. arXiv:2406.11593, June 2024. doi: [10.48550/arXiv.2406.11593](https://doi.org/10.48550/arXiv.2406.11593).
- T. D. Brandt, T. J. Dupuy, and B. P. Bowler. Precise Dynamical Masses of Directly Imaged Companions from Relative Astrometry, Radial Velocities, and Hipparcos-Gaia DR2 Acceler-

- ations. *AJ*, 158:140, Oct. 2019. ISSN 0004-6256. doi: [10.3847/1538-3881/ab04a8](https://doi.org/10.3847/1538-3881/ab04a8). URL <http://adsabs.harvard.edu/abs/2019AJ....158..140B>.
- R. Brasser. Some properties of a two-body system under the influence of the Galactic tidal field. *MNRAS*, 324(4):1109–1116, July 2001. doi: [10.1046/j.1365-8711.2001.04400.x](https://doi.org/10.1046/j.1365-8711.2001.04400.x).
- A. Bressan, P. Marigo, L. Girardi, B. Salasnich, C. Dal Cero, S. Rubele, and A. Nanni. PARSEC: stellar tracks and isochrones with the PAdova and TRieste Stellar Evolution Code. *MNRAS*, 427(1):127–145, Nov. 2012. doi: [10.1111/j.1365-2966.2012.21948.x](https://doi.org/10.1111/j.1365-2966.2012.21948.x).
- M. G. Brouwers, A. Bonsor, and U. Malamud. A road-map to white dwarf pollution: Tidal disruption, eccentric grind-down, and dust accretion. *Mon. Not. R. Astron. Soc.*, 509:2404–2422, Jan. 2022. ISSN 0035-8711. doi: [10.1093/mnras/stab3009](https://doi.org/10.1093/mnras/stab3009).
- M. L. Bryan, B. P. Bowler, H. A. Knutson, A. L. Kraus, S. Hinkley, D. Mawet, E. L. Nielsen, and S. C. Blunt. Searching for Scatterers: High-Contrast Imaging of Young Stars Hosting Wide-Separation Planetary-Mass Companions. *The Astrophysical Journal*, 827:100, Aug. 2016. ISSN 0004-637X. doi: [10.3847/0004-637X/827/2/100](https://doi.org/10.3847/0004-637X/827/2/100). URL <http://adsabs.harvard.edu/abs/2016ApJ...827..100B>.
- M. L. Bryan, H. A. Knutson, E. J. Lee, B. J. Fulton, K. Batygin, H. Ngo, and T. Meshkat. An Excess of Jupiter Analogs in Super-Earth Systems. *AJ*, 157(2):52, Feb. 2019. doi: [10.3847/1538-3881/aaf57f](https://doi.org/10.3847/1538-3881/aaf57f).
- M. L. Bryan, E. Chiang, B. P. Bowler, C. V. Morley, S. Millholland, S. Blunt, K. B. Ashok, E. Nielsen, H. Ngo, D. Mawet, and H. A. Knutson. Obliquity Constraints on an Extrasolar Planetary-mass Companion. *The Astronomical Journal*, 159:181, Apr. 2020. ISSN 0004-6256. doi: [10.3847/1538-3881/ab76c6](https://doi.org/10.3847/1538-3881/ab76c6). URL <http://adsabs.harvard.edu/abs/2020AJ....159..181B>.
- J. Cadman, C. Hall, C. Fontanive, and K. Rice. Binary companions triggering fragmentation in self-gravitating discs. *MNRAS*, Jan. 2022. doi: [10.1093/mnras/stac033](https://doi.org/10.1093/mnras/stac033).
- K. L. Cahoy, M. S. Marley, and J. J. Fortney. Exoplanet Albedo Spectra and Colors as a Function of Planet Phase, Separation, and Metallicity. *The Astrophysical Journal*, 724:189–214, Nov.

2010. ISSN 0004-637X. doi: [10.1088/0004-637X/724/1/189](https://doi.org/10.1088/0004-637X/724/1/189). URL <https://ui.adsabs.harvard.edu/abs/2010ApJ...724..189C>. ADS Bibcode: 2010ApJ...724..189C.
- K. L. Cahoy, M. S. Marley, and J. Fortney. Erratum: “Exoplanet Albedo Spectra and Colors as a Function of Planet Phase, Separation, and Metallicity” (2010, ApJ, 724, 189). *The Astrophysical Journal*, 844:89, July 2017. ISSN 0004-637X. doi: [10.3847/1538-4357/aa79f7](https://doi.org/10.3847/1538-4357/aa79f7). URL <https://ui.adsabs.harvard.edu/abs/2017ApJ...844...89C>. ADS Bibcode: 2017ApJ...844...89C.
- A. J. Cannon and E. C. Pickering. VizieR Online Data Catalog: Henry Draper Catalogue and Extension (Cannon+ 1918-1924; ADC 1989). art. III/135A, Oct. 1993.
- A. Cassan, D. Kubas, J. P. Beaulieu, M. Dominik, K. Horne, J. Greenhill, J. Wambsganss, J. Menzies, A. Williams, U. G. Jørgensen, A. Udalski, D. P. Bennett, M. D. Albrow, V. Batista, S. Brilliant, J. A. R. Caldwell, A. Cole, C. Coutures, K. H. Cook, S. Dieters, D. Dominis Prester, J. Donatowicz, P. Fouqué, K. Hill, N. Kains, S. Kane, J. B. Marquette, R. Martin, K. R. Pollard, K. C. Sahu, C. Vinter, D. Warren, B. Watson, M. Zub, T. Sumi, M. K. Szymański, M. Kubiak, R. Poleski, I. Soszynski, K. Ulaczyk, G. Pietrzyński, and Ł. Wyrzykowski. One or more bound planets per Milky Way star from microlensing observations. *Nature*, 481(7380):167–169, Jan. 2012. doi: [10.1038/nature10684](https://doi.org/10.1038/nature10684).
- C. O. Chandler, I. McDonald, and S. R. Kane. The Catalog of Earth-Like Exoplanet Survey Targets (CELESTA): A Database of Habitable Zones Around Nearby Stars. *AJ*, 151(3):59, Mar. 2016. doi: [10.3847/0004-6256/151/3/59](https://doi.org/10.3847/0004-6256/151/3/59).
- G. Chauvin, A. M. Lagrange, M. Bonavita, B. Zuckerman, C. Dumas, M. S. Bessell, J. L. Beuzit, M. Bonnefoy, S. Desidera, J. Farihi, P. Lowrance, D. Mouillet, and I. Song. Deep imaging survey of young, nearby austral stars . VLT/NACO near-infrared Lyot-coronagraphic observations. *A&A*, 509:A52, Jan. 2010. doi: [10.1051/0004-6361/200911716](https://doi.org/10.1051/0004-6361/200911716).
- Y. Chen, L. Girardi, X. Fu, A. Bressan, B. Aringer, P. Dal Tio, G. Pastorelli, P. Marigo, G. Costa, and X. Zhang. YBC: a stellar bolometric corrections database with variable extinction coefficients. Application to PARSEC isochrones. *A&A*, 632:A105, Dec. 2019. doi: [10.1051/0004-6361/201936612](https://doi.org/10.1051/0004-6361/201936612).

- J. Choi, A. Dotter, C. Conroy, M. Cantiello, B. Paxton, and B. D. Johnson. Mesa Isochrones and Stellar Tracks (MIST). I. Solar-scaled Models. *ApJ*, 823(2):102, June 2016. doi: [10.3847/0004-637X/823/2/102](https://doi.org/10.3847/0004-637X/823/2/102).
- S. Christian, A. Vanderburg, J. Becker, D. A. Yahalomi, L. Pearce, G. Zhou, K. A. Collins, A. L. Kraus, K. G. Stassun, Z. de Beurs, G. R. Ricker, R. K. Vanderspek, D. W. Latham, J. N. Winn, S. Seager, J. M. Jenkins, L. Abe, K. Agabi, P. J. Amado, D. Baker, K. Barkaoui, Z. Benkhaldoun, P. Benni, J. Berberian, P. Berlind, A. Bieryla, E. Esparza-Borges, M. Bowen, P. Brown, L. A. Buchhave, C. J. Burke, M. Buttu, C. Cadieux, D. A. Caldwell, D. Charbonneau, N. Chazov, S. Chimaladinne, K. I. Collins, D. Combs, D. M. Conti, N. Crouzet, J. P. de Leon, S. Deljookorani, B. Diamond, R. Doyon, D. Dragomir, G. Dransfield, Z. Essack, P. Evans, A. Fukui, T. Gan, G. A. Esquerdo, M. Gillon, E. Girardin, P. Guerra, T. Guillot, E. K. K. Habich, A. Henriksen, N. Hoch, K. I. Isogai, E. Jehin, E. L. N. Jensen, M. C. Johnson, J. H. Livingston, J. F. Kielkopf, K. Kim, K. Kawauchi, V. Krushinsky, V. Kunzle, D. Laloum, D. Leger, P. Lewin, F. Mallia, B. Massey, M. Mori, K. K. McLeod, D. Mékarnia, I. Mireles, N. Mishevskiy, M. Tamura, F. Murgas, N. Narita, R. Naves, P. Nelson, H. P. Osborn, E. Palle, H. Parviainen, P. Plavchan, F. J. Pozuelos, M. Rabus, H. M. Relles, C. Rodríguez López, S. N. Quinn, F.-X. Schmider, J. E. Schlieder, R. P. Schwarz, A. Shporer, L. Sibbald, G. Srdoc, C. Stibbards, H. Stickler, O. Suarez, C. Stockdale, T.-G. Tan, Y. Terada, A. Triaud, R. Tronsgaard, W. C. Waalkes, G. Wang, N. Watanabe, M.-S. Wenceslas, G. Wingham, J. Wittrock, and C. Ziegler. A Possible Alignment Between the Orbits of Planetary Systems and their Visual Binary Companions. *arXiv e-prints*, art. arXiv:2202.00042, Jan. 2022.
- C. Cifuentes, J. A. Caballero, M. Cortés-Contreras, D. Montes, F. J. Abellán, R. Dorda, G. Holgado, M. R. Zapatero Osorio, J. C. Morales, P. J. Amado, V. M. Passegger, A. Quirrenbach, A. Reiners, I. Ribas, J. Sanz-Forcada, A. Schweitzer, W. Seifert, and E. Solano. CARMENES input catalogue of M dwarfs. V. Luminosities, colours, and spectral energy distributions. *A&A*, 642:A115, Oct. 2020. doi: [10.1051/0004-6361/202038295](https://doi.org/10.1051/0004-6361/202038295).
- C. J. Clarke. The distribution of relative proper motions of wide binaries in Gaia DR2: MOND or multiplicity? *MNRAS*, 491(1):L72–L75, Jan. 2020. doi: [10.1093/mnras/516/1](https://doi.org/10.1093/mnras/516/1).

- D. P. Clemens, K. Maheshwari, R. Jagani, J. Montgomery, A. M. El Batal, T. G. Ellis, and J. T. Wright. Proper Motion of the Faint Star near KIC 8462852 (Boyajian's Star)—Not a Binary System. *The Astrophysical Journal Letters*, 856:L8, Mar. 2018. ISSN 0004-637X. doi: [10.3847/2041-8213/aab492](https://doi.org/10.3847/2041-8213/aab492). URL <http://adsabs.harvard.edu/abs/2018ApJ...856L...8C>.
- J. B. Climent, J. P. Berger, J. C. Guirado, J. M. Marcaide, I. Martí-Vidal, A. Mérand, E. Tognelli, and M. Wittkowski. Evidence of a Substellar Companion to AB Dor C. *ApJL*, 886(1):L9, Nov. 2019. doi: [10.3847/2041-8213/ab5065](https://doi.org/10.3847/2041-8213/ab5065).
- L. M. Close. MaxProtoPlanetS Survey XRP Proposal. 2020.
- L. M. Close, R. Lenzen, J. C. Guirado, E. L. Nielsen, E. E. Mamajek, W. Brandner, M. Hartung, C. Lidman, and B. Biller. A dynamical calibration of the mass-luminosity relation at very low stellar masses and young ages. *Nature*, 433(7023):286–289, Jan. 2005. doi: [10.1038/nature03225](https://doi.org/10.1038/nature03225).
- L. M. Close, J. R. Males, K. Morzinski, D. Kopon, K. Follette, T. J. Rodigas, P. Hinz, Y.-L. Wu, A. Puglisi, S. Esposito, A. Riccardi, E. Pinna, M. Xompero, R. Briguglio, A. Uomoto, and T. Hare. Diffraction-limited Visible Light Images of Orion Trapezium Cluster with the Magellan Adaptive Secondary Adaptive Optics System (MagAO). *The Astrophysical Journal*, 774:94, Sept. 2013. ISSN 0004-637X. doi: [10.1088/0004-637X/774/2/94](https://doi.org/10.1088/0004-637X/774/2/94). URL <http://adsabs.harvard.edu/abs/2013ApJ...774...94C>.
- L. M. Close, K. B. Follette, J. R. Males, A. Puglisi, M. Xompero, D. Apai, J. Najita, A. J. Weinberger, K. Morzinski, T. J. Rodigas, P. Hinz, V. Bailey, and R. Briguglio. Discovery of H α Emission from the Close Companion inside the Gap of Transitional Disk HD 142527. *ApJL*, 781(2):L30, Feb. 2014. doi: [10.1088/2041-8205/781/2/L30](https://doi.org/10.1088/2041-8205/781/2/L30).
- L. M. Close, J. R. Males, O. Durney, C. Sauve, M. Kautz, A. Hedglen, L. Schatz, J. Lumbres, K. Miller, K. Van Gorkom, M. Jean, and V. Gasho. Optical and mechanical design of the extreme AO coronagraphic instrument MagAO-X. In L. M. Close, L. Schreiber, and D. Schmidt, editors, *Adaptive Optics Systems VI*, volume 10703 of *Society of Photo-Optical Instrumentation Engineers (SPIE) Conference Series*, page 107034Y, July 2018. doi: [10.1117/12.2312280](https://doi.org/10.1117/12.2312280).

- B. F. Collins and R. Sari. Lévy Flights of Binary Orbits due to Impulsive Encounters. *AJ*, 136(6): 2552–2562, Dec. 2008. doi: [10.1088/0004-6256/136/6/2552](https://doi.org/10.1088/0004-6256/136/6/2552).
- C. J. Corbally. Close visual binaries. IMK classifications. *The Astrophysical Journal Supplement Series*, 55:657–677, Aug. 1984. ISSN 0067-0049. doi: [10.1086/190973](https://doi.org/10.1086/190973). URL <https://ui.adsabs.harvard.edu/abs/1984ApJS...55..657C>. ADS Bibcode: 1984ApJS...55..657C.
- J. A. Correa-Otto and R. A. Gil-Hutton. Galactic perturbations on the population of wide binary stars with exoplanets. *Astronomy and Astrophysics*, 608:A116, Dec. 2017. ISSN 0004-6361. doi: [10.1051/0004-6361/201731229](https://doi.org/10.1051/0004-6361/201731229). URL <http://adsabs.harvard.edu/abs/2017A%26A...608A.116C>.
- J. A. Correa-Otto, M. F. Calandra, and R. A. Gil-Hutton. A new insight into the Galactic potential: A simple secular model for the evolution of binary systems in the solar neighbourhood. *A&A*, 600:A59, Apr. 2017. doi: [10.1051/0004-6361/201629679](https://doi.org/10.1051/0004-6361/201629679).
- A. C. M. Correia, J. Couetdic, J. Laskar, X. Bonfils, M. Mayor, J. L. Bertaux, F. Bouchy, X. Delfosse, T. Forveille, C. Lovis, F. Pepe, C. Perrier, D. Queloz, and S. Udry. The HARPS search for southern extra-solar planets. XIX. Characterization and dynamics of the GJ 876 planetary system. *A&A*, 511:A21, Feb. 2010. doi: [10.1051/0004-6361/200912700](https://doi.org/10.1051/0004-6361/200912700).
- S. Correia, H. Zinnecker, T. Ratzka, and M. F. Sterzik. A VLT/NACO survey for triple and quadruple systems among visual pre-main sequence binaries. *Astronomy and Astrophysics*, 459(3):909–926, Dec. 2006. ISSN 0004-6361. doi: [10.1051/0004-6361:20065545](https://doi.org/10.1051/0004-6361:20065545). URL <http://adsabs.harvard.edu/abs/2006A%26A...459..909C>.
- A. R. Costa Silva, E. Delgado Mena, and M. Tsantaki. Chemical abundances of 1111 FGK stars from the HARPS-GTO planet search sample. III. Sulfur. *Astron. & Astrophys*, 634:A136, Feb. 2020. doi: [10.1051/0004-6361/201936523](https://doi.org/10.1051/0004-6361/201936523).
- T. Currie, M. Fukagawa, C. Thalmann, S. Matsumura, and P. Plavchan. Direct Detection and Orbital Analysis of the Exoplanets HR 8799 bcd from Archival 2005 Keck/NIRC2 Data. *ApJL*, 755(2):L34, Aug. 2012. doi: [10.1088/2041-8205/755/2/L34](https://doi.org/10.1088/2041-8205/755/2/L34).
- T. Currie, O. Guyon, N. J. Kasdin, T. Brandt, T. Groff, J. Lozi, J. Chilcote, T. Uyama, E. Nielsen, S. Blunt, C. Marois, N. Jovanovic, M. Kuzuhara, and M. Tamura. Direct Imaging and Spectral

- Characterization of Extrasolar Planets with the SCEXAO/CHARIS. In *American Astronomical Society Meeting Abstracts #233*, volume 233 of *American Astronomical Society Meeting Abstracts*, page 104.04, Jan. 2019.
- T. Currie, T. Brandt, M. Kuzuhara, J. Chilcote, E. Cashman, R. Y. Liu, K. Lawson, T. Tobin, G. M. Brandt, O. Guyon, J. Lozi, V. Deo, S. Vievard, K. Ahn, and N. Skaf. A New Type of Exoplanet Direct Imaging Search: The SCEXAO/CHARIS Survey of Accelerating Stars. *arXiv e-prints*, art. arXiv:2109.09745, Sept. 2021.
- T. Currie, B. Biller, A. Lagrange, C. Marois, O. Guyon, E. L. Nielsen, M. Bonnefoy, and R. J. De Rosa. Direct Imaging and Spectroscopy of Extrasolar Planets. In S. Inutsuka, Y. Aikawa, T. Muto, K. Tomida, and M. Tamura, editors, *Protostars and Planets VII*, volume 534 of *Astronomical Society of the Pacific Conference Series*, page 799, July 2023. doi: [10.48550/arXiv.2205.05696](https://doi.org/10.48550/arXiv.2205.05696).
- R. M. Cutri, M. F. Skrutskie, S. van Dyk, C. A. Beichman, J. M. Carpenter, T. Chester, L. Cambresy, T. Evans, J. Fowler, J. Gizis, E. Howard, J. Huchra, T. Jarrett, E. L. Kopan, J. D. Kirkpatrick, R. M. Light, K. A. Marsh, H. McCallon, S. Schneider, R. Stiening, M. Sykes, M. Weinberg, W. A. Wheaton, S. Wheelock, and N. Zacarias. VizieR Online Data Catalog: 2MASS All-Sky Catalog of Point Sources (Cutri+ 2003). *VizieR Online Data Catalog*, art. II/246, June 2003.
- R. M. Cutri, E. L. Wright, T. Conrow, J. Bauer, D. Benford, H. Brandenburg, J. Dailey, P. R. M. Eisenhardt, T. Evans, S. Fajardo-Acosta, J. Fowler, C. Gelino, C. Grillmair, M. Harbut, D. Hoffman, T. Jarrett, J. D. Kirkpatrick, D. Leisawitz, W. Liu, A. Mainzer, K. Marsh, F. Masci, H. McCallon, D. Padgett, M. E. Ressler, D. Royer, M. F. Skrutskie, S. A. Stanford, P. L. Wyatt, D. Tholen, C. W. Tsai, S. Wachter, S. L. Wheelock, L. Yan, R. Alles, R. Beck, T. Grav, J. Masiero, B. McCollum, P. McGehee, M. Papin, and M. Wittman. Explanatory Supplement to the WISE All-Sky Data Release Products. Explanatory Supplement to the WISE All-Sky Data Release Products, Mar. 2012.
- T. J. David and L. A. Hillenbrand. The Ages of Early-type Stars: Strömgren Photometric Methods Calibrated, Validated, Tested, and Applied to Hosts and Prospective Hosts of Directly Im-

- aged Exoplanets. *The Astrophysical Journal*, 804:146, May 2015. ISSN 0004-637X. doi: 10.1088/0004-637X/804/2/146. URL <http://adsabs.harvard.edu/abs/2015ApJ...804..146D>.
- N. R. Deacon and A. L. Kraus. Wide binaries are rare in open clusters. *arXiv:2006.06679 [astro-ph]*, June 2020. URL <http://arxiv.org/abs/2006.06679>. arXiv: 2006.06679.
- N. R. Deacon, A. L. Kraus, A. W. Mann, E. A. Magnier, K. C. Chambers, R. J. Wainscoat, J. L. Tonry, N. Kaiser, C. Waters, H. Flewelling, K. W. Hodapp, and W. S. Burgett. A Pan-STARRS 1 study of the relationship between wide binarity and planet occurrence in the Kepler field. *Monthly Notices of the Royal Astronomical Society*, 455:4212–4230, Feb. 2016. ISSN 0035-8711. doi: 10.1093/mnras/stv2132. URL <http://adsabs.harvard.edu/abs/2016MNRAS.455.4212D>.
- J. H. Debes and S. Sigurdsson. Are There Unstable Planetary Systems around White Dwarfs? *Astrophys. J.*, 572:556–565, June 2002. ISSN 0004-637X. doi: 10.1086/340291.
- J. H. Debes, K. J. Walsh, and C. Stark. The Link between Planetary Systems, Dusty White Dwarfs, and Metal-polluted White Dwarfs. *Astrophys. J.*, 747:148, Mar. 2012. ISSN 0004-637X. doi: 10.1088/0004-637X/747/2/148.
- E. Delgado Mena, A. Moya, V. Adibekyan, M. Tsantaki, J. I. González Hernández, G. Israelian, G. R. Davies, W. J. Chaplin, S. G. Sousa, A. C. S. Ferreira, and N. C. Santos. Abundance to age ratios in the HARPS-GTO sample with Gaia DR2. Chemical clocks for a range of [Fe/H]. *A&A*, 624:A78, Apr. 2019. doi: 10.1051/0004-6361/201834783.
- J. Dommagnet and O. Nys. The visual double stars observed by the Hipparcos satellite. *A&A*, 363: 991–994, Nov. 2000.
- A. Dotter. MESA Isochrones and Stellar Tracks (MIST) 0: Methods for the Construction of Stellar Isochrones. *ApJs*, 222(1):8, Jan. 2016. doi: 10.3847/0067-0049/222/1/8.
- T. J. Dupuy, K. M. Kratter, A. L. Kraus, H. Isaacson, A. W. Mann, M. J. Ireland, A. W. Howard, and D. Huber. Orbital Architectures of Planet-hosting Binaries. I. Forming Five Small Planets in the Truncated Disk of Kepler-444A. *The Astrophysical Journal*, 817:80, Jan. 2016. ISSN

- 0004-637X. doi: [10.3847/0004-637X/817/1/80](https://doi.org/10.3847/0004-637X/817/1/80). URL <http://adsabs.harvard.edu/abs/2016ApJ...817...80D>.
- T. J. Dupuy, A. L. Kraus, K. M. Kratter, A. C. Rizzuto, A. W. Mann, D. Huber, and M. J. Ireland. Orbital Architectures of Planet-Hosting Binaries II. Low Mutual Inclinations Between Planetary and Stellar Orbits. *arXiv e-prints*, art. arXiv:2202.00013, Jan. 2022.
- U. Dyudina, X. Zhang, L. Li, P. Kopparla, A. P. Ingersoll, L. Dones, A. Verbiscer, and Y. L. Yung. Reflected Light Curves, Spherical and Bond Albedos of Jupiter- and Saturn-like Exoplanets. *ApJ*, 822(2):76, May 2016. doi: [10.3847/0004-637X/822/2/76](https://doi.org/10.3847/0004-637X/822/2/76).
- S. Ekström, C. Georgy, P. Eggenberger, G. Meynet, N. Mowlavi, A. Wyttenbach, A. Granada, T. Decressin, R. Hirschi, U. Frischknecht, C. Charbonnel, and A. Maeder. Grids of stellar models with rotation. I. Models from 0.8 to 120 M_{\odot} at solar metallicity ($Z = 0.014$). *A&A*, 537: A146, Jan. 2012. doi: [10.1051/0004-6361/201117751](https://doi.org/10.1051/0004-6361/201117751).
- K. El-Badry. Gaia's binary star renaissance. *arXiv e-prints*, art. arXiv:2403.12146, Mar. 2024. doi: [10.48550/arXiv.2403.12146](https://doi.org/10.48550/arXiv.2403.12146).
- K. El-Badry, H.-W. Rix, and T. M. Heintz. A million binaries from Gaia eDR3: sample selection and validation of Gaia parallax uncertainties. *arXiv e-prints*, 2101:arXiv:2101.05282, Jan. 2021. URL <http://adsabs.harvard.edu/abs/2021arXiv210105282E>.
- P. Elliott, A. Bayo, C. H. F. Melo, C. A. O. Torres, M. Sterzik, and G. R. Quast. Search for associations containing young stars (SACY). V. Is multiplicity universal? Tight multiple systems. *A&A*, 568:A26, Aug. 2014. doi: [10.1051/0004-6361/201423856](https://doi.org/10.1051/0004-6361/201423856).
- . Esa. VizieR Online Data Catalog: The Hipparcos and Tycho Catalogues (ESA 1997). *VizieR Online Data Catalog*, art. I/239, Feb. 1997.
- ESA, editor. *The HIPPARCOS and TYCHO catalogues. Astrometric and photometric star catalogues derived from the ESA HIPPARCO Space Astrometry Mission*, volume 1200 of *ESA Special Publication*, Jan. 1997.

- C. Fabricius, E. Høg, V. V. Makarov, B. D. Mason, G. L. Wycoff, and S. E. Urban. The Tycho double star catalogue. *A&A*, 384:180–189, Mar. 2002. doi: [10.1051/0004-6361:20011822](https://doi.org/10.1051/0004-6361:20011822).
- J. K. Faherty, A. R. Riedel, K. L. Cruz, J. Gagne, J. C. Filippazzo, E. Lambrides, H. Fica, A. Weinberger, J. R. Thorstensen, C. G. Tinney, V. Baldassare, E. Lemonier, and E. L. Rice. Population Properties of Brown Dwarf Analogs to Exoplanets. *ApJs*, 225(1):10, July 2016. doi: [10.3847/0067-0049/225/1/10](https://doi.org/10.3847/0067-0049/225/1/10).
- J. P. Faria, A. Suárez Mascareño, P. Figueira, A. M. Silva, M. Damasso, O. Demangeon, F. Pepe, N. C. Santos, R. Rebolo, S. Cristiani, V. Adibekyan, Y. Alibert, R. Allart, S. C. C. Barros, A. Cabral, V. D’Odorico, P. Di Marcantonio, X. Dumusque, D. Ehrenreich, J. I. González Hernández, N. Hara, J. Lillo-Box, G. Lo Curto, C. Lovis, C. J. A. P. Martins, D. Mégevand, A. Mehner, G. Micela, P. Molaro, N. J. Nunes, E. Pallé, E. Poretti, S. G. Sousa, A. Sozzetti, H. Taberner, S. Udry, and M. R. Zapatero Osorio. A candidate short-period sub-Earth orbiting Proxima Centauri. *A&A*, 658:A115, Feb. 2022. doi: [10.1051/0004-6361/202142337](https://doi.org/10.1051/0004-6361/202142337).
- J. Farihi. Circumstellar debris and pollution at white dwarf stars. *New Astron. Rev.*, 71:9–34, Apr. 2016. ISSN 1387-6473. doi: [10.1016/j.newar.2016.03.001](https://doi.org/10.1016/j.newar.2016.03.001).
- J. Farihi, B. T. Gänsicke, P. R. Steele, J. Girven, M. R. Burleigh, E. Breedt, and D. Koester. A trio of metal-rich dust and gas discs found orbiting candidate white dwarfs with K-band excess. *MNRAS*, 421(2):1635–1643, Apr. 2012. doi: [10.1111/j.1365-2966.2012.20421.x](https://doi.org/10.1111/j.1365-2966.2012.20421.x).
- J. Farihi, B. T. Gänsicke, and D. Koester. Evidence for Water in the Rocky Debris of a Disrupted Extrasolar Minor Planet. *Science*, 342(6155):218–220, Oct. 2013. ISSN 0036-8075. doi: [10.1126/science.1239447](https://doi.org/10.1126/science.1239447).
- Y. K. Feng, T. D. Robinson, J. J. Fortney, R. E. Lupu, M. S. Marley, N. K. Lewis, B. Macintosh, and M. R. Line. Characterizing Earth Analogs in Reflected Light: Atmospheric Retrieval Studies for Future Space Telescopes. *The Astronomical Journal*, 155:200, May 2018. ISSN 0004-6256. doi: [10.3847/1538-3881/aab95c](https://doi.org/10.3847/1538-3881/aab95c). URL <https://ui.adsabs.harvard.edu/abs/2018AJ....155..200F>. ADS Bibcode: 2018AJ....155..200F.

- R. B. Fernandes, G. D. Mulders, I. Pascucci, C. Mordasini, and A. Emsenhuber. Hints for a Turnover at the Snow Line in the Giant Planet Occurrence Rate. *ApJ*, 874(1):81, Mar. 2019. doi: [10.3847/1538-4357/ab0300](https://doi.org/10.3847/1538-4357/ab0300).
- L. Ferrario. Constraints on the pairing properties of main-sequence stars from observations of white dwarfs in binary systems. *MNRAS*, 426(3):2500–2506, Nov. 2012. doi: [10.1111/j.1365-2966.2012.21836.x](https://doi.org/10.1111/j.1365-2966.2012.21836.x).
- R. Ferrer-Chávez, J. J. Wang, and S. Blunt. Biases in Orbital Fitting of Directly Imaged Exoplanets with Small Orbital Coverage. *AJ*, 161(5):241, May 2021. doi: [10.3847/1538-3881/abf0a8](https://doi.org/10.3847/1538-3881/abf0a8).
- U. Finkenzeller and R. Mundt. The Herbig Ae/Be stars associated with nebulosity. *A&As*, 55: 109–141, Jan. 1984.
- S. Fitton, B. M. Tofflemire, and A. L. Kraus. Disk Material Inflates Gaia RUWE Values in Single Stars. *Research Notes of the American Astronomical Society*, 6(1):18, Jan. 2022. doi: [10.3847/2515-5172/ac4bb7](https://doi.org/10.3847/2515-5172/ac4bb7).
- C. Flammarion. The Companion of Sirius. *Astronomical register*, 15:186–189, Jan. 1877.
- K. B. Follette. An Introduction to High Contrast Differential Imaging of Exoplanets and Disks. *PASP*, 135(1051):093001, Sept. 2023. doi: [10.1088/1538-3873/aceb31](https://doi.org/10.1088/1538-3873/aceb31).
- C. Fontanive, K. Rice, M. Bonavita, E. Lopez, Mužić, K. , and B. Biller. A high binary fraction for the most massive close-in giant planets and brown dwarf desert members. *MNRAS*, 485(4): 4967–4996, June 2019. doi: [10.1093/mnras/stz671](https://doi.org/10.1093/mnras/stz671).
- D. Foreman-Mackey, D. W. Hogg, D. Lang, and J. Goodman. emcee: The MCMC Hammer. *PASP*, 125(925):306, Mar. 2013. doi: [10.1086/670067](https://doi.org/10.1086/670067).
- M. Fouchard, C. Froeschlé, J. J. Matese, and G. B. Valsecchi. Comparison between different models of galactic tidal effects on cometary orbits. *Celestial Mechanics and Dynamical Astronomy*, 96(3-4):341–344, Nov. 2006. doi: [10.1007/s10569-006-9055-4](https://doi.org/10.1007/s10569-006-9055-4).

- K. Franson, B. P. Bowler, T. D. Brandt, T. J. Dupuy, Q. H. Tran, G. M. Brandt, Y. Li, and A. L. Kraus. Dynamical Mass of the Young Substellar Companion HD 984 B. *AJ*, 163(2):50, Feb. 2022. doi: [10.3847/1538-3881/ac35e8](https://doi.org/10.3847/1538-3881/ac35e8).
- S. F. N. Frewen and B. M. S. Hansen. Eccentric planets and stellar evolution as a cause of polluted white dwarfs. *MNRAS*, 439(3):2442–2458, Apr. 2014. doi: [10.1093/mnras/stu097](https://doi.org/10.1093/mnras/stu097).
- B. J. Fulton, J. L. Tonry, H. Flewelling, W. S. Burgett, K. C. Chambers, K. W. Hodapp, M. E. Huber, N. Kaiser, R. J. Wainscoat, and C. Waters. A Search for Planetary Eclipses of White Dwarfs in the Pan-STARRS1 Medium-deep Fields. *ApJ*, 796(2):114, Dec. 2014. doi: [10.1088/0004-637X/796/2/114](https://doi.org/10.1088/0004-637X/796/2/114).
- B. J. Fulton, L. J. Rosenthal, L. A. Hirsch, H. Isaacson, A. W. Howard, C. M. Dedrick, I. A. Sherry, S. C. Blunt, E. A. Petigura, H. A. Knutson, A. Behrmard, A. Chontos, J. R. Crepp, I. J. M. Crossfield, P. A. Dalba, D. A. Fischer, G. W. Henry, S. R. Kane, M. Kosiarek, G. W. Marcy, R. A. Rubenzahl, L. M. Weiss, and J. T. Wright. California Legacy Survey. II. Occurrence of Giant Planets beyond the Ice Line. *ApJs*, 255(1):14, July 2021. doi: [10.3847/1538-4365/abfcc1](https://doi.org/10.3847/1538-4365/abfcc1).
- J. Gagné, E. E. Mamajek, L. Malo, A. Riedel, D. Rodriguez, D. Lafrenière, J. K. Faherty, O. Roy-Loubier, L. Pueyo, A. C. Robin, and R. Doyon. BANYAN. XI. The BANYAN sigma Multivariate Bayesian Algorithm to Identify Members of Young Associations with 150 pc. *The Astrophysical Journal*, 856:23, Mar. 2018. ISSN 0004-637X. doi: [10.3847/1538-4357/aaae09](https://doi.org/10.3847/1538-4357/aaae09). URL <http://adsabs.harvard.edu/abs/2018ApJ...856...23G>.
- Gaia Collaboration, T. Prusti, J. H. J. de Bruijne, A. G. A. Brown, A. Vallenari, C. Babusiaux, C. A. L. Bailer-Jones, U. Bastian, M. Biermann, D. W. Evans, L. Eyer, F. Jansen, C. Jordi, S. A. Klioner, U. Lammers, L. Lindegren, X. Luri, F. Mignard, D. J. Milligan, C. Panem, V. Poinsignon, D. Pourbaix, S. Randich, G. Sarri, P. Sartoretti, H. I. Siddiqui, C. Soubiran, V. Valette, F. van Leeuwen, N. A. Walton, C. Aerts, F. Arenou, M. Cropper, R. Drimmel, E. Høg, D. Katz, M. G. Lattanzi, W. O’Mullane, E. K. Grebel, A. D. Holland, C. Huc, X. Passot, L. Bramante, C. Cacciari, J. Castañeda, L. Chaoul, N. Cheek, F. De Angeli, C. Fabricius, R. Guerra, J. Hernández, A. Jean-Antoine-Piccolo, E. Masana, R. Messineo, N. Mowlavi, K. Nienartowicz, D. Ordóñez Blanco, P. Panuzzo, J. Portell, P. J. Richards, M. Riello, G. M. Seabroke, P. Tanga,

F. Thévenin, J. Torra, S. G. Els, G. Gracia-Abril, G. Comoretto, M. Garcia-Reinaldos, T. Lock, E. Mercier, M. Altmann, R. Andrae, T. L. Astraatmadja, I. Bellas-Velidis, K. Benson, J. Berthier, R. Blomme, G. Busso, B. Carry, A. Cellino, G. Clementini, S. Cowell, O. Creevey, J. Cuypers, M. Davidson, J. De Ridder, A. de Torres, L. Delchambre, A. Dell’Oro, C. Ducourant, Y. Frémat, M. García-Torres, E. Gosset, J.-L. Halbwachs, N. C. Hambly, D. L. Harrison, M. Hauser, D. He-stroffer, S. T. Hodgkin, H. E. Huckle, A. Hutton, G. Jasniewicz, S. Jordan, M. Kontizas, A. J. Korn, A. C. Lanzafame, M. Manteiga, A. Moitinho, K. Muinonen, J. Osinde, E. Pancino, T. Pauwels, J.-M. Petit, A. Recio-Blanco, A. C. Robin, L. M. Sarro, C. Siopis, M. Smith, K. W. Smith, A. Sozzetti, W. Thuillot, W. van Reeve, Y. Viala, U. Abbas, A. Abreu Aramburu, S. Accart, J. J. Aguado, P. M. Allan, W. Allasia, G. Altavilla, M. A. Álvarez, J. Alves, R. I. Anderson, A. H. Andrei, E. Anglada Varela, E. Antiche, T. Antoja, S. Antón, B. Arcay, A. Atzei, L. Ayache, N. Bach, S. G. Baker, L. Balaguer-Núñez, C. Barache, C. Barata, A. Barbier, F. Barblan, M. Baroni, D. Barrado y Navascués, M. Barros, M. A. Barstow, U. Becciani, M. Bellazzini, G. Bellei, A. Bello García, V. Belokurov, P. Bendjoya, A. Berihuete, L. Bianchi, O. Bienaymé, F. Billebaud, N. Blagorodnova, S. Blanco-Cuaresma, T. Boch, A. Bombrun, R. Borrachero, S. Bouquillon, G. Bourda, H. Bouy, A. Bragaglia, M. A. Breddels, N. Brouillet, T. Brüsemeister, B. Bucciarelli, F. Budnik, P. Burgess, R. Burgon, A. Burlacu, D. Busonero, R. Buzzzi, E. Caffau, J. Cambras, H. Campbell, R. Cancelliere, T. Cantat-Gaudin, T. Carlucci, J. M. Carrasco, M. Castellani, P. Charlot, J. Charnas, P. Charvet, F. Chassat, A. Chiavassa, M. Clotet, G. Cocozza, R. S. Collins, P. Collins, G. Costigan, F. Crifo, N. J. G. Cross, M. Crosta, C. Crowley, C. Dafonte, Y. Damerджи, A. Dapergolas, P. David, M. David, P. De Cat, F. de Felice, P. de Laverny, F. De Luise, R. De March, D. de Martino, R. de Souza, J. Debosscher, E. del Pozo, M. Delbo, A. Delgado, H. E. Delgado, F. di Marco, P. Di Matteo, S. Diakite, E. Distefano, C. Dolding, S. Dos Anjos, P. Drazinos, J. Durán, Y. Dzigian, E. Ecale, B. Edvardsson, H. Enke, M. Erdmann, D. Escolar, M. Espina, N. W. Evans, G. Eynard Bontemps, C. Fabre, M. Fabrizio, S. Faigler, A. J. Falcão, M. Farràs Casas, F. Faye, L. Federici, G. Fedorets, J. Fernández-Hernández, P. Fernique, A. Fienga, F. Figueras, F. Filippi, K. Findeisen, A. Fonti, M. Foues-neau, E. Fraile, M. Fraser, J. Fuchs, R. Furnell, M. Gai, S. Galleti, L. Galluccio, D. Garabato, F. García-Sedano, P. Garé, A. Garofalo, N. Garralda, P. Gavras, J. Gerssen, R. Geyer, G. Gilmore, S. Girona, G. Giuffrida, M. Gomes, A. González-Marcos, J. González-Núñez, J. J.

González-Vidal, M. Granvik, A. Guerrier, P. Guillout, J. Guiraud, A. Gúrpide, R. Gutiérrez-Sánchez, L. P. Guy, R. Haignon, D. Hatzidimitriou, M. Haywood, U. Heiter, A. Helmi, D. Hobbs, W. Hofmann, B. Holl, G. Holland, J. A. S. Hunt, A. Hypki, V. Icardi, M. Irwin, G. Jevardat de Fombelle, P. Jofré, P. G. Jonker, A. Jorissen, F. Julbe, A. Karampelas, A. Kochoska, R. Kohley, K. Kolenberg, E. Kontizas, S. E. Kuposov, G. Kordopatis, P. Koubsky, A. Kowalczyk, A. Krone-Martins, M. Kudryashova, I. Kull, R. K. Bachchan, F. Lacoste-Seris, A. F. Lanza, J.-B. Lavigne, C. Le Poncin-Lafitte, Y. Lebreton, T. Lebzelter, S. Leccia, N. Leclerc, I. Lecoeur-Taibi, V. Lemaitre, H. Lenhardt, F. Leroux, S. Liao, E. Licata, H. E. P. Lindstrøm, T. A. Lister, E. Livanou, A. Lobel, W. Löffler, M. López, A. Lopez-Lozano, D. Lorenz, T. Loureiro, I. MacDonald, T. Magalhães Fernandes, S. Managau, R. G. Mann, G. Mantelet, O. Marchal, J. M. Marchant, M. Marconi, J. Marie, S. Marinoni, P. M. Marrese, G. Marschalkó, D. J. Marshall, J. M. Martín-Fleitas, M. Martino, N. Mary, G. Matijević, T. Maze, P. J. McMillan, S. Messina, A. Mestre, D. Michalik, N. R. Millar, B. M. H. Miranda, D. Molina, R. Molinaro, M. Molinaro, L. Molnár, M. Moniez, P. Montegriffo, D. Monteiro, R. Mor, A. Mora, R. Morbidelli, T. Morel, S. Morgenthaler, T. Morley, D. Morris, A. F. Mulone, T. Muraveva, I. Musella, J. Narbonne, G. Nelemans, L. Nicastro, L. Noval, C. Ordénovic, J. Ordieres-Meré, P. Osborne, C. Pagani, I. Pagano, F. Pailler, H. Palacin, L. Palaversa, P. Parsons, T. Paulsen, M. Pecoraro, R. Pedrosa, H. Pentikäinen, J. Pereira, B. Pichon, A. M. Piersimoni, F.-X. Pineau, E. Plachy, G. Plum, E. Poujoulet, A. Prša, L. Pulone, S. Ragaini, S. Rago, N. Rambaux, M. Ramos-Lerate, P. Ranalli, G. Rauw, A. Read, S. Regibo, F. Renk, C. Reylé, R. A. Ribeiro, L. Rimoldini, V. Ripepi, A. Riva, G. Rixon, M. Roelens, M. Romero-Gómez, N. Rowell, F. Royer, A. Rudolph, L. Ruiz-Dern, G. Sadowski, T. Sagristà Sellés, J. Sahlmann, J. Salgado, E. Salguero, M. Sarasso, H. Savietto, A. Schnorhk, M. Schultheis, E. Sciacca, M. Segol, J. C. Segovia, D. Segransan, E. Serpell, I.-C. Shih, R. Smareglia, R. L. Smart, C. Smith, E. Solano, F. Solitto, R. Sordo, S. Soria Nieto, J. Souchay, A. Spagna, F. Spoto, U. Stampa, I. A. Steele, H. Steidelmüller, C. A. Stephenson, H. Stoev, F. F. Suess, M. Süveges, J. Surdej, L. Szabados, E. Szegedi-Elek, D. Tapiador, F. Taris, G. Tauran, M. B. Taylor, R. Teixeira, D. Terrett, B. Tingley, S. C. Trager, C. Turon, A. Ulla, E. Utrilla, G. Valentini, A. van Elteren, E. Van Hemelryck, M. van Leeuwen, M. Varadi, A. Vecchiato, J. Veljanoski, T. Via, D. Vicente, S. Vogt, H. Voss, V. Votruba, S. Voutsinas, G. Walmsley, M. Weiler, K. Weingrill, D. Werner, T. Wevers, G. Whitehead, L. Wyrzykowski, A. Yoldas,

M. Žerjal, S. Zucker, C. Zurbach, T. Zwitter, A. Alecu, M. Allen, C. Allende Prieto, A. Amorim, G. Anglada-Escudé, V. Arsenijevic, S. Azaz, P. Balm, M. Beck, H.-H. Bernstein, L. Bigot, A. Bijaoui, C. Blasco, M. Bonfigli, G. Bono, S. Boudreault, A. Bressan, S. Brown, P.-M. Brunet, P. Bunclark, R. Buonanno, A. G. Butkevich, C. Carret, C. Carrion, L. Chemin, F. Chéreau, L. Corcione, E. Darmigny, K. S. de Boer, P. de Teodoro, P. T. de Zeeuw, C. Delle Luche, C. D. Domingues, P. Dubath, F. Fodor, B. Frézouls, A. Fries, D. Fustes, D. Fyfe, E. Gallardo, J. Gallegos, D. Gardiol, M. Gebran, A. Gomboc, A. Gómez, E. Grux, A. Gueguen, A. Heyrovsky, J. Hoar, G. Iannicola, Y. Isasi Parache, A.-M. Janotto, E. Joliet, A. Jonckheere, R. Keil, D.-W. Kim, P. Klagyivik, J. Klar, J. Knude, O. Kochukhov, I. Kolka, J. Kos, A. Kutka, V. Lainey, D. LeBouquin, C. Liu, D. Loreggia, V. V. Makarov, M. G. Marseille, C. Martayan, O. Martinez-Rubi, B. Massart, F. Meynadier, S. Mignot, U. Munari, A.-T. Nguyen, T. Nordlander, P. Ocvirk, K. S. O’Flaherty, A. Olias Sanz, P. Ortiz, J. Osorio, D. Oszkiewicz, A. Ouzounis, M. Palmer, P. Park, E. Pasquato, C. Peltzer, J. Peralta, F. Péturaud, T. Pieniluoma, E. Pigozzi, J. Poels, G. Prat, T. Prod’homme, F. Raison, J. M. Rebordao, D. Risquez, B. Rocca-Volmerange, S. Rosen, M. I. Ruiz-Fuertes, F. Russo, S. Sembay, I. Serraller Vizcaino, A. Short, A. Siebert, H. Silva, D. Sinachopoulos, E. Slezak, M. Soffel, D. Sosnowska, V. Straižys, M. ter Linden, D. Terrell, S. Theil, C. Tiede, L. Troisi, P. Tsalmantza, D. Tur, M. Vaccari, F. Vachier, P. Valles, W. Van Hamme, L. Veltz, J. Virtanen, J.-M. Wallut, R. Wichmann, M. I. Wilkinson, H. Ziaepour, and S. Zschocke. The Gaia mission. *Astronomy and Astrophysics*, 595:A1, Nov. 2016. ISSN 0004-6361. doi: [10.1051/0004-6361/201629272](https://doi.org/10.1051/0004-6361/201629272). URL <http://adsabs.harvard.edu/abs/2016A%26A...595A...1G>.

Gaia Collaboration, A. G. A. Brown, A. Vallenari, T. Prusti, J. H. J. de Bruijne, C. Babusiaux, C. A. L. Bailer-Jones, M. Biermann, D. W. Evans, L. Eyer, F. Jansen, C. Jordi, S. A. Klioner, U. Lammers, L. Lindegren, X. Luri, F. Mignard, C. Panem, D. Pourbaix, S. Randich, P. Sartoretti, H. I. Siddiqui, C. Soubiran, F. van Leeuwen, N. A. Walton, F. Arenou, U. Bastian, M. Cropper, R. Drimmel, D. Katz, M. G. Lattanzi, J. Bakker, C. Cacciari, J. Castañeda, L. Chaoul, N. Cheek, F. De Angeli, C. Fabricius, R. Guerra, B. Holl, E. Masana, R. Messineo, N. Mowlavi, K. Nienartowicz, P. Panuzzo, J. Portell, M. Riello, G. M. Seabroke, P. Tanga, F. Thévenin, G. Gracia-Abril, G. Comoretto, M. Garcia-Reinaldos, D. Teyssier, M. Altmann,

R. Andrae, M. Audard, I. Bellas-Velidis, K. Benson, J. Berthier, R. Blomme, P. Burgess, G. Busso, B. Carry, A. Cellino, G. Clementini, M. Clotet, O. Creevey, M. Davidson, J. De Ridder, L. Delchambre, A. Dell’Oro, C. Ducourant, J. Fernández-Hernández, M. Fouesneau, Y. Frémat, L. Galluccio, M. García-Torres, J. González-Núñez, J. J. González-Vidal, E. Gosset, L. P. Guy, J. L. Halbwachs, N. C. Hambly, D. L. Harrison, J. Hernández, D. Hestroffer, S. T. Hodgkin, A. Hutton, G. Jasniewicz, A. Jean-Antoine-Piccolo, S. Jordan, A. J. Korn, A. Krone-Martins, A. C. Lanzafame, T. Lebzelter, W. Löffler, M. Manteiga, P. M. Marrese, J. M. Martín-Fleitas, A. Moitinho, A. Mora, K. Muinonen, J. Osinde, E. Pancino, T. Pauwels, J. M. Petit, A. Recio-Blanco, P. J. Richards, L. Rimoldini, A. C. Robin, L. M. Sarro, C. Siopis, M. Smith, A. Sozzetti, M. Süveges, J. Torra, W. van Reeve, U. Abbas, A. Abreu Aramburu, S. Accart, C. Aerts, G. Altavilla, M. A. Álvarez, R. Alvarez, J. Alves, R. I. Anderson, A. H. Andrei, E. Anglada Varela, E. Antiche, T. Antoja, B. Arcay, T. L. Astraatmadja, N. Bach, S. G. Baker, L. Balaguer-Núñez, P. Balm, C. Barache, C. Barata, D. Barbato, F. Barblan, P. S. Barklem, D. Barrado, M. Barros, M. A. Barstow, S. Bartholomé Muñoz, J. L. Bassilana, U. Bacci, M. Bellazzini, A. Berihuete, S. Bertone, L. Bianchi, O. Bienaymé, S. Blanco-Cuaresma, T. Boch, C. Boeche, A. Bombrun, R. Borrachero, D. Bossini, S. Bouquillon, G. Bourda, A. Bragaglia, L. Bramante, M. A. Breddels, A. Bressan, N. Brouillet, T. Brüsemeister, E. Brugaletta, B. Bucciarelli, A. Burlacu, D. Busonero, A. G. Butkevich, R. Buzzì, E. Caffau, R. Cancelliere, G. Cannizzaro, T. Cantat-Gaudin, R. Carballo, T. Carlucci, J. M. Carrasco, L. Casamiquela, M. Castellani, A. Castro-Ginard, P. Charlot, L. Chemin, A. Chiavassa, G. Cocozza, G. Costigan, S. Cowell, F. Crifo, M. Crosta, C. Crowley, J. Cuypers, C. Dafonte, Y. Damerdjì, A. Dapergolas, P. David, M. David, P. de Laverny, F. De Luise, R. De March, D. de Martino, R. de Souza, A. de Torres, J. Debosscher, E. del Pozo, M. Delbo, A. Delgado, H. E. Delgado, P. Di Matteo, S. Diakite, C. Diener, E. Distefano, C. Dolding, P. Drazinos, J. Durán, B. Edvardsson, H. Enke, K. Eriksson, P. Esquej, G. Eynard Bontemps, C. Fabre, M. Fabrizio, S. Faigler, A. J. Falcão, M. Farràs Casas, L. Federici, G. Fedorets, P. Fernique, F. Figueras, F. Filippi, K. Findenisen, A. Fonti, E. Fraile, M. Fraser, B. Frézouls, M. Gai, S. Galletti, D. Garabato, F. García-Sedano, A. Garofalo, N. Garralda, A. Gavel, P. Gavras, J. Gerssen, R. Geyer, P. Giacobbe, G. Gilmore, S. Girona, G. Giuffrida, F. Glass, M. Gomes, M. Granvik, A. Gueguen, A. Guerrier, J. Guiraud, R. Gutiérrez-Sánchez, R. Haignon, D. Hatzidimitriou, M. Hauser, M. Haywood,

U. Heiter, A. Helmi, J. Heu, T. Hilger, D. Hobbs, W. Hofmann, G. Holland, H. E. Huckle, A. Hypki, V. Icardi, K. Janßen, G. Jevardat de Fombelle, P. G. Jonker, Á. L. Juhász, F. Julbe, A. Karampelas, A. Kewley, J. Klar, A. Kochoska, R. Kohley, K. Kolenberg, M. Kontizas, E. Kontizas, S. E. Koposov, G. Kordopatis, Z. Kostrzewa-Rutkowska, P. Koubsky, S. Lambert, A. F. Lanza, Y. Lasne, J. B. Lavigne, Y. Le Fustec, C. Le Poncin-Lafitte, Y. Lebreton, S. Leccia, N. Leclerc, I. Lecoeur-Taibi, H. Lenhardt, F. Leroux, S. Liao, E. Licata, H. E. P. Lindstrøm, T. A. Lister, E. Livanou, A. Lobel, M. López, S. Managau, R. G. Mann, G. Mantelet, O. Marchal, J. M. Marchant, M. Marconi, S. Marinoni, G. Marschalkó, D. J. Marshall, M. Martino, G. Marton, N. Mary, D. Massari, G. Matijević, T. Mazeh, P. J. McMillan, S. Messina, D. Michalik, N. R. Millar, D. Molina, R. Molinaro, L. Molnár, P. Montegriffo, R. Mor, R. Morbidelli, T. Morel, D. Morris, A. F. Mulone, T. Muraveva, I. Musella, G. Nelemans, L. Nicastrò, L. Noval, W. O'Mullane, C. Ordénovic, D. Ordóñez-Blanco, P. Osborne, C. Pagani, I. Pagano, F. Pailler, H. Palacin, L. Palaversa, A. Panahi, M. Pawlak, A. M. Piersimoni, F. X. Pineau, E. Plachy, G. Plum, E. Poggio, E. Poujoulet, A. Prša, L. Pulone, E. Racero, S. Ragaini, N. Rambaux, M. Ramos-Lerate, S. Regibo, C. Reylé, F. Riclet, V. Ripepi, A. Riva, A. Rivard, G. Rixon, T. Roegiers, M. Roelens, M. Romero-Gómez, N. Rowell, F. Royer, L. Ruiz-Dern, G. Sadowski, T. Sagristà Sellés, J. Sahlmann, J. Salgado, E. Salguero, N. Sanna, T. Santana-Ros, M. Sarasso, H. Savietto, M. Schultheis, E. Sciacca, M. Segol, J. C. Segovia, D. Ségransan, I. C. Shih, L. Siltala, A. F. Silva, R. L. Smart, K. W. Smith, E. Solano, F. Solitro, R. Sordo, S. Soria Nieto, J. Souchay, A. Spagna, F. Spoto, U. Stampa, I. A. Steele, H. Steidelmüller, C. A. Stephenson, H. Stoev, F. F. Suess, J. Surdej, L. Szabados, E. Szegedi-Elek, D. Tapiador, F. Taris, G. Tauran, M. B. Taylor, R. Teixeira, D. Terrett, P. Teyssandier, W. Thuillot, A. Titarenko, F. Torra Clotet, C. Turon, A. Ulla, E. Utrilla, S. Uzzi, M. Vaillant, G. Valentini, V. Valette, A. van Elteren, E. Van Hemelryck, M. van Leeuwen, M. Vaschetto, A. Vecchiato, J. Veljanoski, Y. Viala, D. Vicente, S. Vogt, C. von Essen, H. Voss, V. Votruba, S. Voutsinas, G. Walmsley, M. Weiler, O. Wertz, T. Wevers, Ł. Wyrzykowski, A. Yoldas, M. Žerjal, H. Ziaeeypour, J. Zorec, S. Zschocke, S. Zucker, C. Zurbach, and T. Zwitter. Gaia Data Release 2. Summary of the contents and survey properties. *Astron. & Astrophys*, 616:A1, Aug. 2018. doi: [10.1051/0004-6361/201833051](https://doi.org/10.1051/0004-6361/201833051).

Gaia Collaboration, A. G. A. Brown, A. Vallenari, T. Prusti, J. H. J. de Bruijne, C. Babusiaux, M. Biermann, O. L. Creevey, D. W. Evans, L. Eyer, A. Hutton, F. Jansen, C. Jordi, S. A. Klioner, U. Lammers, L. Lindegren, X. Luri, F. Mignard, C. Panem, D. Pourbaix, S. Randich, P. Sartoretti, C. Soubiran, N. A. Walton, F. Arenou, C. A. L. Bailer-Jones, U. Bastian, M. Cropper, R. Drimmel, D. Katz, M. G. Lattanzi, F. van Leeuwen, J. Bakker, C. Cacciari, J. Castañeda, F. De Angeli, C. Ducourant, C. Fabricius, M. Fouesneau, Y. Frémat, R. Guerra, A. Guerrier, J. Guiraud, A. Jean-Antoine Piccolo, E. Masana, R. Messineo, N. Mowlavi, C. Nicolas, K. Nienartowicz, F. Pailler, P. Panuzzo, F. Riclet, W. Roux, G. M. Seabroke, R. Sordo, P. Tanga, F. Thévenin, G. Gracia-Abril, J. Portell, D. Teyssier, M. Altmann, R. Andrae, I. Bellas-Velidis, K. Benson, J. Berthier, R. Blomme, E. Brugaletta, P. W. Burgess, G. Busso, B. Carry, A. Cellino, N. Cheek, G. Clementini, Y. Damerddji, M. Davidson, L. Delchambre, A. Dell’Oro, J. Fernández-Hernández, L. Galluccio, P. García-Lario, M. Garcia-Reinaldos, J. González-Núñez, E. Gosset, R. Haigron, J. L. Halbwachs, N. C. Hambly, D. L. Harrison, D. Hatzidimitriou, U. Heiter, J. Hernández, D. Hestroffer, S. T. Hodgkin, B. Holl, K. Janßen, G. Jevardat de Fombelle, S. Jordan, A. Krone-Martins, A. C. Lanzafame, W. Löffler, A. Lorca, M. Manteiga, O. Marchal, P. M. Marrese, A. Moitinho, A. Mora, K. Muinonen, P. Osborne, E. Pancino, T. Pauwels, J. M. Petit, A. Recio-Blanco, P. J. Richards, M. Riello, L. Rimoldini, A. C. Robin, T. Roegiers, J. Rybizki, L. M. Sarro, C. Siopis, M. Smith, A. Sozzetti, A. Ulla, E. Utrilla, M. van Leeuwen, W. van Reeven, U. Abbas, A. Abreu Aramburu, S. Accart, C. Aerts, J. J. Aguado, M. Ajaj, G. Altavilla, M. A. Álvarez, J. Álvarez Cid-Fuentes, J. Alves, R. I. Anderson, E. Anglada Varela, T. Antoja, M. Audard, D. Baines, S. G. Baker, L. Balaguer-Núñez, E. Balbinot, Z. Balog, C. Barache, D. Barbato, M. Barros, M. A. Barstow, S. Bartolomé, J. L. Bassilana, N. Bauchet, A. Baudesson-Stella, U. Becciani, M. Bellazzini, M. Bernet, S. Bertone, L. Bianchi, S. Blanco-Cuaresma, T. Boch, A. Bombrun, D. Bossini, S. Bouquillon, A. Bragaglia, L. Bramante, E. Breedt, A. Bressan, N. Brouillet, B. Bucciarelli, A. Burlacu, D. Busonero, A. G. Butkevich, R. Buzzzi, E. Caffau, R. Cancelliere, H. Cánovas, T. Cantat-Gaudin, R. Carballo, T. Carlucci, M. I. Carnerero, J. M. Carrasco, L. Casamiquela, M. Castellani, A. Castro-Ginard, P. Castro Sampol, L. Chaoul, P. Charlot, L. Chemin, A. Chiavassa, M. R. L. Cioni, G. Comoretto, W. J. Cooper, T. Cornez, S. Cowell, F. Crifo, M. Crosta, C. Crowley, C. Dafonte, A. Dapergolas, M. David, P. David, P. de Laverny, F. De Luise, R. De March, J. De Ridder, R. de Souza, P. de Teodoro, A. de Torres, E. F.

del Peloso, E. del Pozo, M. Delbo, A. Delgado, H. E. Delgado, J. B. Delisle, P. Di Matteo, S. Diakite, C. Diener, E. Distefano, C. Dolding, D. Eappachen, B. Edvardsson, H. Enke, P. Esquej, C. Fabre, M. Fabrizio, S. Faigler, G. Fedorets, P. Fernique, A. Fienga, F. Figueras, C. Fouron, F. Fragkoudi, E. Fraile, F. Franke, M. Gai, D. Garabato, A. Garcia-Gutierrez, M. García-Torres, A. Garofalo, P. Gavras, E. Gerlach, R. Geyer, P. Giacobbe, G. Gilmore, S. Girona, G. Giuffrida, R. Gomel, A. Gomez, I. Gonzalez-Santamaria, J. J. González-Vidal, M. Granvik, R. Gutiérrez-Sánchez, L. P. Guy, M. Hauser, M. Haywood, A. Helmi, S. L. Hidalgo, T. Hilger, N. Hładczuk, D. Hobbs, G. Holland, H. E. Huckle, G. Jasniewicz, P. G. Jonker, J. Juaristi Campillo, F. Julbe, L. Karbevaska, P. Kervella, S. Khanna, A. Kochoska, M. Kontizas, G. Kordopatis, A. J. Korn, Z. Kostrzewa-Rutkowska, K. Kruszyńska, S. Lambert, A. F. Lanza, Y. Lasne, J. F. Le Campion, Y. Le Fustec, Y. Lebreton, T. Lebzelter, S. Leccia, N. Leclerc, I. Lecoœur-Taibi, S. Liao, E. Licata, E. P. Lindstrøm, T. A. Lister, E. Livanou, A. Lobel, P. Madrero Pardo, S. Managau, R. G. Mann, J. M. Marchant, M. Marconi, M. M. S. Marcos Santos, S. Marinoni, F. Marocco, D. J. Marshall, L. Martin Polo, J. M. Martín-Fleitas, A. Masip, D. Massari, A. Mastrobuono-Battisti, T. Mazeh, P. J. McMillan, S. Messina, D. Michalik, N. R. Millar, A. Mints, D. Molina, R. Molinaro, L. Molnár, P. Montegriffo, R. Mor, R. Morbidelli, T. Morel, D. Morris, A. F. Mulone, D. Munoz, T. Muraveva, C. P. Murphy, I. Musella, L. Noval, C. Ordénovic, G. Orrù, J. Osinde, C. Pagani, I. Pagano, L. Palaversa, P. A. Palicio, A. Panahi, M. Pawlak, X. Peñalosa Esteller, A. Penttilä, A. M. Piersimoni, F. X. Pineau, E. Plachy, G. Plum, E. Poggio, E. Poretti, E. Poujoulet, A. Prša, L. Pulone, E. Racero, S. Ragaini, M. Rainer, C. M. Raiteri, N. Rambaux, P. Ramos, M. Ramos-Lerate, P. Re Fiorentin, S. Regibo, C. Reylé, V. Ripepi, A. Riva, G. Rixon, N. Robichon, C. Robin, M. Roelens, L. Rohrbasser, M. Romero-Gómez, N. Rowell, F. Royer, K. A. Rybicki, G. Sadowski, A. Sagristà Sellés, J. Sahlmann, J. Salgado, E. Salguero, N. Samaras, V. Sanchez Gimenez, N. Sanna, R. Santoveña, M. Sarasso, M. Schultheis, E. Sciacca, M. Segol, J. C. Segovia, D. Ségransan, D. Semeux, S. Shahaf, H. I. Siddiqui, A. Siebert, L. Siltala, E. Slezak, R. L. Smart, E. Solano, F. Solitro, D. Souami, J. Souchay, A. Spagna, F. Spoto, I. A. Steele, H. Steidelmüller, C. A. Stephenson, M. Süveges, L. Szabados, E. Szegedi-Elek, F. Taris, G. Tauran, M. B. Taylor, R. Teixeira, W. Thuillot, N. Tonello, F. Torra, J. Torra, C. Turon, N. Unger, M. Vaillant, E. van Dillen, O. Vanel, A. Vecchiato, Y. Viala, D. Vicente, S. Voutsinas, M. Weiler, T. Wevers, Ł. Wyrzykowski, A. Yoldas, P. Yvard, H. Zhao, J. Zorec,

S. Zucker, C. Zurbach, and T. Zwitter. Gaia Early Data Release 3. Summary of the contents and survey properties. *A&A*, 649:A1, May 2021. doi: [10.1051/0004-6361/202039657](https://doi.org/10.1051/0004-6361/202039657).

Gaia Collaboration, A. Vallenari, A. G. A. Brown, T. Prusti, J. H. J. de Bruijne, F. Arenou, C. Babusiaux, M. Biermann, O. L. Creevey, C. Ducourant, D. W. Evans, L. Eyer, R. Guerra, A. Hutton, C. Jordi, S. A. Klioner, U. L. Lammers, L. Lindegren, X. Luri, F. Mignard, C. Panem, D. Pourbaix, S. Randich, P. Sartoretti, C. Soubiran, P. Tanga, N. A. Walton, C. A. L. Bailer-Jones, U. Bastian, R. Drimmel, F. Jansen, D. Katz, M. G. Lattanzi, F. van Leeuwen, J. Bakker, C. Cacciari, J. Castañeda, F. De Angeli, C. Fabricius, M. Fouesneau, Y. Frémat, L. Galluccio, A. Guerrier, U. Heiter, E. Masana, R. Messineo, N. Mowlavi, C. Nicolas, K. Nienartowicz, F. Pailler, P. Panuzzo, F. Riclet, W. Roux, G. M. Seabroke, R. Sordo, F. Thévenin, G. Gracia-Abril, J. Portell, D. Teyssier, M. Altmann, R. Andrae, M. Audard, I. Bellas-Velidis, K. Benson, J. Berthier, R. Blomme, P. W. Burgess, D. Busonero, G. Busso, H. Cánovas, B. Carry, A. Cellino, N. Cheek, G. Clementini, Y. Damerджи, M. Davidson, P. de Teodoro, M. Nuñez Campos, L. Delchambre, A. Dell’Oro, P. Esquej, J. Fernández-Hernández, E. Fraile, D. Garabato, P. García-Lario, E. Gosset, R. Haignon, J. L. Halbwachs, N. C. Hambly, D. L. Harrison, J. Hernández, D. Hestroffer, S. T. Hodgkin, B. Holl, K. Janßen, G. Jevardat de Fombelle, S. Jordan, A. Krone-Martins, A. C. Lanzafame, W. Löffler, O. Marchal, P. M. Marrese, A. Moitinho, K. Muinonen, P. Osborne, E. Pancino, T. Pauwels, A. Recio-Blanco, C. Reylé, M. Riello, L. Rimoldini, T. Roegiers, J. Rybizki, L. M. Sarro, C. Siopis, M. Smith, A. Sozzetti, E. Utrilla, M. van Leeuwen, U. Abbas, P. Abraham, A. Abreu Aramburu, C. Aerts, J. J. Aguado, M. Ajaj, F. Aldea-Montero, G. Altavilla, M. A. Álvarez, J. Alves, F. Anders, R. I. Anderson, E. Anglada Varela, T. Antoja, D. Baines, S. G. Baker, L. Balaguer-Núñez, E. Balbinot, Z. Balog, C. Barache, D. Barbato, M. Barros, M. A. Barstow, S. Bartolomé, J. L. Bassilana, N. Bauchet, U. Beciani, M. Bellazzini, A. Berihuete, M. Bernet, S. Bertone, L. Bianchi, A. Binnenfeld, S. Blanco-Cuaresma, A. Blazere, T. Boch, A. Bombrun, D. Bossini, S. Bouquillon, A. Bragaglia, L. Bramante, E. Breedt, A. Bressan, N. Brouillet, E. Brugaletta, B. Bucciarelli, A. Burlacu, A. G. Butkevich, R. Buzzi, E. Caffau, R. Cancelliere, T. Cantat-Gaudin, R. Carballo, T. Carlucci, M. I. Carnerero, J. M. Carrasco, L. Casamiquela, M. Castellani, A. Castro-Ginard, L. Chaoul, P. Charlot, L. Chemin, V. Chiaramida, A. Chiavassa, N. Chornay, G. Comoretto, G. Contursi,

W. J. Cooper, T. Cornez, S. Cowell, F. Crifo, M. Cropper, M. Crosta, C. Crowley, C. Dafonte, A. Dapergolas, M. David, P. David, P. de Laverny, F. De Luise, R. De March, J. De Ridder, R. de Souza, A. de Torres, E. F. del Peloso, E. del Pozo, M. Delbo, A. Delgado, J. B. Delisle, C. Demouchy, T. E. Dharmawardena, P. Di Matteo, S. Diakite, C. Diener, E. Distefano, C. Dolding, B. Edvardsson, H. Enke, C. Fabre, M. Fabrizio, S. Faigler, G. Fedorets, P. Fernique, A. Fienga, F. Figueras, Y. Fournier, C. Fouron, F. Fragkoudi, M. Gai, A. Garcia-Gutierrez, M. Garcia-Reinaldos, M. García-Torres, A. Garofalo, A. Gavel, P. Gavras, E. Gerlach, R. Geyer, P. Giacobbe, G. Gilmore, S. Girona, G. Giuffrida, R. Gomel, A. Gomez, J. González-Núñez, I. González-Santamaría, J. J. González-Vidal, M. Granvik, P. Guillout, J. Guiraud, R. Gutiérrez-Sánchez, L. P. Guy, D. Hatzidimitriou, M. Hauser, M. Haywood, A. Helmer, A. Helmi, M. H. Sarmiento, S. L. Hidalgo, T. Hilger, N. Hładczuk, D. Hobbs, G. Holland, H. E. Huckle, K. Jardine, G. Jasniewicz, A. Jean-Antoine Piccolo, Ó. Jiménez-Arranz, A. Jorissen, J. Juaristi Campillo, F. Julbe, L. Karbevská, P. Kervella, S. Khanna, M. Kontizas, G. Kordopatis, A. J. Korn, Á. Kóspál, Z. Kostrzewa-Rutkowska, K. Kruszyńska, M. Kun, P. Laizeau, S. Lambert, A. F. Lanza, Y. Lasne, J. F. Le Campion, Y. Lebreton, T. Lebzelter, S. Leccia, N. Leclerc, I. Lecoœur-Taïbi, S. Liao, E. L. Licata, H. E. P. Lindstrøm, T. A. Lister, E. Livanou, A. Lobel, A. Lorca, C. Loup, P. Madrero Pardo, A. Magdaleno Romeo, S. Managau, R. G. Mann, M. Manteiga, J. M. Marchant, M. Marconi, J. Marcos, M. M. S. Marcos Santos, D. Marín Pina, S. Marinoni, F. Marocco, D. J. Marshall, L. Martin Polo, J. M. Martín-Fleitas, G. Marton, N. Mary, A. Masip, D. Massari, A. Mastrobuono-Battisti, T. Mazeh, P. J. McMillan, S. Messina, D. Michalik, N. R. Millar, A. Mints, D. Molina, R. Molinaro, L. Molnár, G. Monari, M. Monguió, P. Montegriffo, A. Montero, R. Mor, A. Mora, R. Morbidelli, T. Morel, D. Morris, T. Muraveva, C. P. Murphy, I. Musella, Z. Nagy, L. Noval, F. Ocaña, A. Ogden, C. Ordenovic, J. O. Osinde, C. Pagani, I. Pagano, L. Palaversa, P. A. Palicio, L. Pallas-Quintela, A. Panahi, S. Payne-Wardenaar, X. Peñalosa Esteller, A. Penttilä, B. Pichon, A. M. Piersimoni, F. X. Pineau, E. Plachy, G. Plum, E. Poggio, A. Prša, L. Pulone, E. Racero, S. Ragaini, M. Rainer, C. M. Raiteri, N. Rambaux, P. Ramos, M. Ramos-Lerate, P. Re Fiorentin, S. Regibo, P. J. Richards, C. Rios Diaz, V. Ripepi, A. Riva, H. W. Rix, G. Rixon, N. Robichon, A. C. Robin, C. Robin, M. Roelens, H. R. O. Rogues, L. Rohrbasser, M. Romero-Gómez, N. Rowell, F. Royer, D. Ruz Mieres, K. A. Rybicki, G. Sadowski, A. Sáez Núñez, A. Sagristà

- Sellés, J. Sahlmann, E. Salguero, N. Samaras, V. Sanchez Gimenez, N. Sanna, R. Santoveña, M. Sarasso, M. Schultheis, E. Sciacca, M. Segol, J. C. Segovia, D. Ségransan, D. Semeux, S. Shahaf, H. I. Siddiqui, A. Siebert, L. Siltala, A. Silvelo, E. Slezak, I. Slezak, R. L. Smart, O. N. Snaith, E. Solano, F. Solitro, D. Souami, J. Souchay, A. Spagna, L. Spina, F. Spoto, I. A. Steele, H. Steidelmüller, C. A. Stephenson, M. Süveges, J. Surdej, L. Szabados, E. Szegedi-Elek, F. Taris, M. B. Taylor, R. Teixeira, L. Tolomei, N. Tonello, F. Torra, J. Torra, G. Torralba Elipe, M. Trabucchi, A. T. Tsounis, C. Turon, A. Ulla, N. Unger, M. V. Vaillant, E. van Dillen, W. van Reeven, O. Vanel, A. Vecchiato, Y. Viala, D. Vicente, S. Voutsinas, M. Weiler, T. Wevers, Ł. Wyrzykowski, A. Yoldas, P. Yvard, H. Zhao, J. Zorec, S. Zucker, and T. Zwitter. Gaia Data Release 3. Summary of the content and survey properties. *A&A*, 674:A1, June 2023. doi: [10.1051/0004-6361/202243940](https://doi.org/10.1051/0004-6361/202243940).
- R. Galicher, C. Marois, B. Macintosh, B. Zuckerman, T. Barman, Q. Konopacky, I. Song, J. Patience, D. Lafrenière, R. Doyon, and E. L. Nielsen. The International Deep Planet Survey. II. The frequency of directly imaged giant exoplanets with stellar mass. *A&A*, 594:A63, Oct. 2016. doi: [10.1051/0004-6361/201527828](https://doi.org/10.1051/0004-6361/201527828).
- B. T. Gänsicke, T. R. Marsh, J. Southworth, and A. Rebassa-Mansergas. A Gaseous Metal Disk Around a White Dwarf. *Science*, 314(5807):1908, Dec. 2006. doi: [10.1126/science.1135033](https://doi.org/10.1126/science.1135033).
- B. T. Gänsicke, D. Koester, T. R. Marsh, A. Rebassa-Mansergas, and J. Southworth. SDSSJ084539.17+225728.0: the first DBZ white dwarf with a metal-rich gaseous debris disc. *MNRAS*, 391(1):L103–L107, Nov. 2008. doi: [10.1111/j.1745-3933.2008.00565.x](https://doi.org/10.1111/j.1745-3933.2008.00565.x).
- B. T. Gänsicke, D. Koester, J. Farihi, J. Girven, S. G. Parsons, and E. Breedt. The chemical diversity of exo-terrestrial planetary debris around white dwarfs. *Mon. Not. R. Astron. Soc.*, 424:333–347, July 2012. ISSN 0035-8711. doi: [10.1111/j.1365-2966.2012.21201.x](https://doi.org/10.1111/j.1365-2966.2012.21201.x).
- P. Gao, M. S. Marley, and A. S. Ackerman. Sedimentation Efficiency of Condensation Clouds in Substellar Atmospheres. *The Astrophysical Journal*, 855:86, Mar. 2018. ISSN 0004-637X. doi: [10.3847/1538-4357/aab0a1](https://doi.org/10.3847/1538-4357/aab0a1). URL <https://ui.adsabs.harvard.edu/abs/2018ApJ...855...86G>. ADS Bibcode: 2018ApJ...855...86G.

- A. Gáspár, G. H. Rieke, and Z. Balog. The Collisional Evolution of Debris Disks. *ApJ*, 768(1):25, May 2013. doi: [10.1088/0004-637X/768/1/25](https://doi.org/10.1088/0004-637X/768/1/25).
- N. P. Gentile Fusillo, P. E. Tremblay, E. Cukanovaite, A. Vorontseva, R. Lallement, M. Hollands, B. T. Gänsicke, K. B. Burdge, J. McCleery, and S. Jordan. A catalogue of white dwarfs in Gaia EDR3. *MNRAS*, 508(3):3877–3896, Dec. 2021. doi: [10.1093/mnras/stab2672](https://doi.org/10.1093/mnras/stab2672).
- C. Georgy, S. Ekström, A. Granada, G. Meynet, N. Mowlavi, P. Eggenberger, and A. Maeder. Populations of rotating stars. I. Models from 1.7 to 15 M_{\odot} at $Z = 0.014$, 0.006, and 0.002 with Ω/Ω_{crit} between 0 and 1. *A&A*, 553:A24, May 2013. doi: [10.1051/0004-6361/201220558](https://doi.org/10.1051/0004-6361/201220558).
- M. Gillon, A. H. M. J. Triaud, B.-O. Demory, E. Jehin, E. Agol, K. M. Deck, S. M. Lederer, J. de Wit, A. Burdanov, J. G. Ingalls, E. Bolmont, J. Leconte, S. N. Raymond, F. Selsis, M. Turbet, K. Barkaoui, A. Burgasser, M. R. Burleigh, S. J. Carey, A. Chaushev, C. M. Copperwheat, L. Delrez, C. S. Fernandes, D. L. Holdsworth, E. J. Kotze, V. Van Grootel, Y. Almeleaky, Z. Benkhaldoun, P. Magain, and D. Queloz. Seven temperate terrestrial planets around the nearby ultracool dwarf star TRAPPIST-1. *Nature*, 542(7642):456–460, Feb. 2017. doi: [10.1038/nature21360](https://doi.org/10.1038/nature21360).
- J. E. Gizis. M-Subdwarfs: Spectroscopic Classification and the Metallicity Scale. *AJ*, 113:806–822, Feb. 1997. doi: [10.1086/118302](https://doi.org/10.1086/118302).
- R. M. Goody and Y. L. Yung. *Atmospheric radiation : theoretical basis*. 1989.
- R. O. Gray and R. F. Garrison. The Early A-Type Stars: Refined MK Classification, Confrontation with Stroemgren Photometry, and the Effects of Rotation. *ApJs*, 65:581, Dec. 1987. doi: [10.1086/191237](https://doi.org/10.1086/191237).
- R. O. Gray, C. J. Corbally, R. F. Garrison, M. T. McFadden, E. J. Bubar, C. E. McGahee, A. A. O’Donoghue, and E. R. Knox. Contributions to the Nearby Stars (NStars) Project: Spectroscopy of Stars Earlier than M0 within 40 pc-The Southern Sample. *The Astronomical Journal*, 132:161–170, July 2006. ISSN 0004-6256. doi: [10.1086/504637](https://doi.org/10.1086/504637). URL <http://adsabs.harvard.edu/abs/2006AJ....132..161G>.

- T. Guillot. On the radiative equilibrium of irradiated planetary atmospheres. *Astronomy and Astrophysics*, 520:A27, Sept. 2010. ISSN 0004-6361. doi: [10.1051/0004-6361/200913396](https://doi.org/10.1051/0004-6361/200913396). URL <https://ui.adsabs.harvard.edu/abs/2010A&A...520A..27G>. ADS Bibcode: 2010A&A...520A..27G.
- S. Y. Haffert, A. J. Bohn, J. de Boer, I. A. G. Snellen, J. Brinchmann, J. H. Girard, C. U. Keller, and R. Bacon. Two accreting protoplanets around the young star PDS 70. *Nature Astronomy*, 3: 749–754, June 2019. doi: [10.1038/s41550-019-0780-5](https://doi.org/10.1038/s41550-019-0780-5).
- J. Hagelberg, N. Engler, C. Fontanive, S. Daemgen, S. P. Quanz, J. Kühn, M. Reggiani, M. Meyer, R. Jayawardhana, and V. Kostov. VIBES: Visual Binary Exoplanet survey with SPHERE. Upper limits on wide S-planet and S-BD frequencies, triple system discovery, and astrometric confirmation of 20 stellar binaries and three triple systems. *A&A*, 643:A98, Nov. 2020. doi: [10.1051/0004-6361/202039173](https://doi.org/10.1051/0004-6361/202039173).
- J.-L. Halbwachs, D. Pourbaix, F. Arenou, L. Galluccio, P. Guillout, N. Bauchet, O. Marchal, G. Sadowski, and D. Teyssier. Gaia Data Release 3. Astrometric binary star processing. *A&A*, 674:A9, June 2023. doi: [10.1051/0004-6361/202243969](https://doi.org/10.1051/0004-6361/202243969).
- A. S. Hamers. Hints for Hidden Planetary Companions to Hot Jupiters in Stellar Binaries. *ApJL*, 835(2):L24, Feb. 2017. doi: [10.3847/2041-8213/835/2/L24](https://doi.org/10.3847/2041-8213/835/2/L24).
- A. S. Hamers. Secular dynamics of hierarchical multiple systems composed of nested binaries, with an arbitrary number of bodies and arbitrary hierarchical structure - II. External perturbations: flybys and supernovae. *MNRAS*, 476(3):4139–4161, May 2018. doi: [10.1093/mnras/sty428](https://doi.org/10.1093/mnras/sty428).
- A. S. Hamers and S. F. Portegies Zwart. White dwarf pollution by planets in stellar binaries. *Mon. Not. R. Astron. Soc.*, 462:L84–L87, Oct. 2016. ISSN 0035-8711. doi: [10.1093/mnras/1slw134](https://doi.org/10.1093/mnras/1slw134).
- A. S. Hamers and S. Tremaine. Hot Jupiters Driven by High-eccentricity Migration in Globular Clusters. *AJ*, 154(6):272, Dec. 2017. doi: [10.3847/1538-3881/aa9926](https://doi.org/10.3847/1538-3881/aa9926).

- R. J. Harris, S. M. Andrews, D. J. Wilner, and A. L. Kraus. A Resolved Census of Millimeter Emission from Taurus Multiple Star Systems. *ApJ*, 751(2):115, June 2012. doi: [10.1088/0004-637X/751/2/115](https://doi.org/10.1088/0004-637X/751/2/115).
- W. I. Hartkopf, B. D. Mason, C. T. Finch, N. Zacharias, G. L. Wycoff, and D. Hsu. Double Stars in the USNO CCD Astrographic Catalog. *AJ*, 146(4):76, Oct. 2013. doi: [10.1088/0004-6256/146/4/76](https://doi.org/10.1088/0004-6256/146/4/76).
- A. N. Heinze, P. M. Hinz, S. Sivanandam, M. Kenworthy, M. Meyer, and D. Miller. Constraints on Long-period Planets from an L'- and M-band Survey of Nearby Sun-like Stars: Observations. *ApJ*, 714(2):1551–1569, May 2010. doi: [10.1088/0004-637X/714/2/1551](https://doi.org/10.1088/0004-637X/714/2/1551).
- J. Heisler and S. Tremaine. The influence of the Galactic tidal field on the Oort comet cloud. *Icarus*, 65(1):13–26, Jan. 1986. doi: [10.1016/0019-1035\(86\)90060-6](https://doi.org/10.1016/0019-1035(86)90060-6).
- G. J. Herczeg and L. A. Hillenbrand. An Optical Spectroscopic Study of T Tauri Stars. I. Photospheric Properties. *The Astrophysical Journal*, 786(2):97, May 2014. ISSN 0004-637X. doi: [10.1088/0004-637X/786/2/97](https://doi.org/10.1088/0004-637X/786/2/97). URL <http://adsabs.harvard.edu/abs/2014ApJ...786...97H>.
- M. K. Herman, W. Zhu, and Y. Wu. Revisiting the Long-period Transiting Planets from Kepler. *AJ*, 157(6):248, June 2019. doi: [10.3847/1538-3881/ab1f70](https://doi.org/10.3847/1538-3881/ab1f70).
- J. Hernández, N. Calvet, L. Hartmann, C. Briceño, A. Sicilia-Aguilar, and P. Berlind. Herbig Ae/Be Stars in nearby OB Associations. *AJ*, 129(2):856–871, Feb. 2005. doi: [10.1086/426918](https://doi.org/10.1086/426918).
- M. Hjorth, S. Albrecht, T. Hirano, J. N. Winn, R. I. Dawson, J. J. Zanzizzi, E. Knudstrup, and B. Sato. A backward-spinning star with two coplanar planets. *Proceedings of the National Academy of Science*, 118(8):2017418118, Feb. 2021. doi: [10.1073/pnas.2017418118](https://doi.org/10.1073/pnas.2017418118).
- J. B. Holberg. What fraction of white dwarfs are members of binary systems? In *Journal of Physics Conference Series*, volume 172 of *Journal of Physics Conference Series*, page 012022. IOP, June 2009. doi: [10.1088/1742-6596/172/1/012022](https://doi.org/10.1088/1742-6596/172/1/012022).
- J. B. Holberg and P. Bergeron. Calibration of Synthetic Photometry Using DA White Dwarfs. *Astronomical Journal*, 132(3):1221–1233, Sept. 2006. doi: [10.1086/505938](https://doi.org/10.1086/505938).

- J. B. Holberg, E. M. Sion, T. Oswalt, G. P. McCook, S. Foran, and J. P. Subasavage. A New Look at the Local White Dwarf Population. *AJ*, 135(4):1225–1238, Apr. 2008. doi: [10.1088/0004-6256/135/4/1225](https://doi.org/10.1088/0004-6256/135/4/1225).
- J. B. Holberg, T. D. Oswalt, E. M. Sion, M. A. Barstow, and M. R. Burleigh. Where are all the Sirius-like binary systems? *MNRAS*, 435(3):2077–2091, Nov. 2013. doi: [10.1093/mnras/stt1433](https://doi.org/10.1093/mnras/stt1433).
- J. B. Holberg, T. D. Oswalt, E. M. Sion, and G. P. McCook. The 25 parsec local white dwarf population. *MNRAS*, 462(3):2295–2318, Nov. 2016. doi: [10.1093/mnras/stw1357](https://doi.org/10.1093/mnras/stw1357).
- M. J. Holman and P. A. Wiegert. Long-Term Stability of Planets in Binary Systems. *AJ*, 117(1):621–628, Jan. 1999. doi: [10.1086/300695](https://doi.org/10.1086/300695).
- R. Hoogerwerf. OB association members in the ACT and TRC catalogues. *MNRAS*, 313(1):43–65, Mar. 2000. doi: [10.1046/j.1365-8711.2000.03192.x](https://doi.org/10.1046/j.1365-8711.2000.03192.x).
- H. G. Horak and S. J. Little. Calculations of Planetary Reflection. *ApJs*, 11:373, June 1965. doi: [10.1086/190119](https://doi.org/10.1086/190119).
- N. Houk. *Michigan catalogue of two-dimensional spectral types for the HD stars*. 1978.
- N. Houk and A. P. Cowley. *University of Michigan Catalogue of two-dimensional spectral types for the HD stars. Volume I. Declinations -90_ to -53_f0*. 1975.
- N. Houk and C. Swift. Michigan catalogue of two-dimensional spectral types for the HD Stars, Vol. 5. *Michigan Spectral Survey*, 5:0, Jan. 1999.
- R. Hu, B. L. Ehlmann, and S. Seager. THEORETICAL SPECTRA OF TERRESTRIAL EXOPLANET SURFACES. *ApJ*, 752(1):7, May 2012. ISSN 0004-637X. doi: [10.1088/0004-637X/752/1/7](https://doi.org/10.1088/0004-637X/752/1/7). URL <https://dx.doi.org/10.1088/0004-637X/752/1/7>. Publisher: The American Astronomical Society.
- D. Huber, J. Zinn, M. Bojsen-Hansen, M. Pinsonneault, C. Sahlholdt, A. Serenelli, V. Silva Aguirre, K. Stassun, D. Stello, J. Tayar, F. Bastien, T. R. Bedding, L. A. Buchhave, W. J. Chaplin, G. R. Davies, R. A. García, D. W. Latham, S. Mathur, B. Mosser, and S. Sharma.

- Asteroseismology and Gaia: Testing Scaling Relations Using 2200 Kepler Stars with TGAS Parallaxes. *ApJ*, 844(2):102, Aug. 2017. doi: [10.3847/1538-4357/aa75ca](https://doi.org/10.3847/1538-4357/aa75ca).
- F. M. Jiménez-Esteban, S. Torres, A. Rebassa-Mansergas, P. Cruz, R. Murillo-Ojeda, E. Solano, C. Rodrigo, and M. E. Camisassa. Spectral classification of the 100 pc white dwarf population from Gaia-DR3 and the virtual observatory. *MNRAS*, 518(4):5106–5122, Feb. 2023. doi: [10.1093/mnras/stac3382](https://doi.org/10.1093/mnras/stac3382).
- E. Jofré, R. Petrucci, C. Saffe, L. Saker, E. Artur de la Villarmois, C. Chavero, M. Gómez, and P. J. D. Mauas. Stellar parameters and chemical abundances of 223 evolved stars with and without planets. *A&A*, 574:A50, Feb. 2015. doi: [10.1051/0004-6361/201424474](https://doi.org/10.1051/0004-6361/201424474).
- J. H. Joseph, W. J. Wiscombe, and J. A. Weinman. The delta-Eddington approximation for radiative flux transfer. *Journal of the Atmospheric Sciences*, 33:2452–2459, Dec. 1976. doi: [10.1175/1520-0469\(1976\)033<2452:TDEAFR>2.0.CO;2](https://doi.org/10.1175/1520-0469(1976)033<2452:TDEAFR>2.0.CO;2).
- M. Jura. Pollution of Single White Dwarfs by Accretion of Many Small Asteroids. *Astron. J.*, 135:1785–1792, May 2008. ISSN 0004-6256. doi: [10.1088/0004-6256/135/5/1785](https://doi.org/10.1088/0004-6256/135/5/1785).
- N. A. Kaib, S. N. Raymond, and M. Duncan. Planetary system disruption by Galactic perturbations to wide binary stars. *Nature*, 493(7432):381–384, Jan. 2013. doi: [10.1038/nature11780](https://doi.org/10.1038/nature11780). URL <http://adsabs.harvard.edu/abs/2013Natur.493..381K>.
- M. Kasper, D. Apai, M. Janson, and W. Brandner. A novel L-band imaging search for giant planets in the Tucana and β Pictoris moving groups. *A&A*, 472(1):321–327, Sept. 2007. doi: [10.1051/0004-6361:20077646](https://doi.org/10.1051/0004-6361:20077646).
- B. Katz, S. Dong, and D. Kushnir. Luminosity function suggests up to 100 white dwarfs within 20 pc may be hiding in multiple systems. *arXiv e-prints*, art. arXiv:1402.7083, Feb. 2014. doi: [10.48550/arXiv.1402.7083](https://doi.org/10.48550/arXiv.1402.7083).
- M. A. Kenworthy, J. L. Codona, P. M. Hinz, J. R. P. Angel, A. Heinze, and S. Sivanandam. First On-Sky High-Contrast Imaging with an Apodizing Phase Plate. *ApJ*, 660(1):762–769, May 2007. doi: [10.1086/513596](https://doi.org/10.1086/513596).

- P. Kervella, F. Arenou, F. Mignard, and F. Thévenin. Stellar and substellar companions of nearby stars from *Gaia* DR2: Binarity from proper motion anomaly. *A&A*, 623:A72, Mar. 2019. ISSN 0004-6361, 1432-0746. doi: [10.1051/0004-6361/201834371](https://doi.org/10.1051/0004-6361/201834371). URL <https://www.aanda.org/10.1051/0004-6361/201834371>.
- P. Kervella, F. Arenou, and F. Thévenin. Stellar and substellar companions from Gaia EDR3. Proper-motion anomaly and resolved common proper-motion pairs. *A&A*, 657:A7, Jan. 2022. ISSN 0004-6361. doi: [10.1051/0004-6361/202142146](https://doi.org/10.1051/0004-6361/202142146). URL <https://ui.adsabs.harvard.edu/abs/2022A%26A...657A...7K/abstract>.
- N. V. Kharchenko. All-sky compiled catalogue of 2.5 million stars. *Kinematika i Fizika Nebesnykh Tel*, 17(5):409–423, Oct. 2001.
- W. Knapp and J. Nanson. Estimating Visual Magnitudes for Wide Double Stars with Missing or Suspect WDS Values. *Journal of Double Star Observations*, 14(3):503–520, July 2018.
- H. A. Knutson, B. J. Fulton, B. T. Montet, M. Kao, H. Ngo, A. W. Howard, J. R. Crepp, S. Hinkley, G. Á. Bakos, K. Batygin, J. A. Johnson, T. D. Morton, and P. S. Muirhead. Friends of Hot Jupiters. I. A Radial Velocity Search for Massive, Long-period Companions to Close-in Gas Giant Planets. *ApJ*, 785(2):126, Apr. 2014. doi: [10.1088/0004-637X/785/2/126](https://doi.org/10.1088/0004-637X/785/2/126).
- D. Koester. Accretion and diffusion in white dwarfs. New diffusion timescales and applications to GD 362 and G 29-38. *Astron. Astrophys. Vol. 498 Issue 2 2009 Pp517-525*, 498(2):517, May 2009. ISSN 0004-6361. doi: [10.1051/0004-6361/200811468](https://doi.org/10.1051/0004-6361/200811468).
- D. Koester. White dwarf spectra and atmosphere models. *Mem. Della Soc. Astron. Ital.*, 81:921–931, Jan. 2010. ISSN 0037-8720.
- D. Koester. White Dwarf Stars. In T. D. Oswalt and M. A. Barstow, editors, *Planets, Stars and Stellar Systems. Volume 4: Stellar Structure and Evolution*, volume 4, page 559. 2013. doi: [10.1007/978-94-007-5615-1_11](https://doi.org/10.1007/978-94-007-5615-1_11).
- D. Koester and D. Wilken. The accretion-diffusion scenario for metals in cool white dwarfs. *A&A*, 453(3):1051–1057, July 2006. doi: [10.1051/0004-6361:20064843](https://doi.org/10.1051/0004-6361:20064843).

- D. Koester, B. T. Gänsicke, and J. Farihi. The frequency of planetary debris around young white dwarfs. *Astron. Astrophys.*, 566:A34, June 2014. ISSN 0004-6361. doi: [10.1051/0004-6361/201423691](https://doi.org/10.1051/0004-6361/201423691).
- Y. Kozai. Secular perturbations of asteroids with high inclination and eccentricity. *The Astronomical Journal*, 67:591–598, Nov. 1962. ISSN 0004-6256. doi: [10.1086/108790](https://doi.org/10.1086/108790). URL <http://adsabs.harvard.edu/abs/1962AJ.....67..591K>.
- K. M. Kratter and H. B. Perets. Star Hoppers: Planet Instability and Capture in Evolving Binary Systems. *ApJ*, 753(1):91, July 2012. doi: [10.1088/0004-637X/753/1/91](https://doi.org/10.1088/0004-637X/753/1/91).
- A. L. Kraus, E. L. Shkolnik, K. N. Allers, and M. C. Liu. A Stellar Census of the Tucana-Horologium Moving Group. *The Astronomical Journal*, 147:146, June 2014. ISSN 0004-6256. doi: [10.1088/0004-6256/147/6/146](https://doi.org/10.1088/0004-6256/147/6/146). URL <http://adsabs.harvard.edu/abs/2014AJ....147..146K>.
- A. L. Kraus, M. J. Ireland, D. Huber, A. W. Mann, and T. J. Dupuy. The Impact of Stellar Multiplicity on Planetary Systems. I. The Ruinous Influence of Close Binary Companions. *The Astronomical Journal*, 152(1):8, July 2016. ISSN 0004-6256. doi: [10.3847/0004-6256/152/1/8](https://doi.org/10.3847/0004-6256/152/1/8). URL <http://adsabs.harvard.edu/abs/2016AJ....152....8K>.
- J. R. Kuhn, D. Potter, and B. Parise. Imaging Polarimetric Observations of a New Circumstellar Disk System. *ApJL*, 553(2):L189–L191, June 2001. doi: [10.1086/320686](https://doi.org/10.1086/320686).
- D. Lafrenière, C. Marois, R. Doyon, D. Nadeau, and É. Artigau. A New Algorithm for Point-Spread Function Subtraction in High-Contrast Imaging: A Demonstration with Angular Differential Imaging. *ApJ*, 660(1):770–780, May 2007. ISSN 0004-637X. doi: [10.1086/513180](https://doi.org/10.1086/513180). URL <http://adsabs.harvard.edu/abs/2007ApJ...660..770L>.
- D. Lafrenière, R. Jayawardhana, M. H. van Kerkwijk, A. Brandeker, and M. Janson. An Adaptive Optics Multiplicity Census of Young Stars in Upper Scorpius. *ApJ*, 785(1):47, Apr. 2014. doi: [10.1088/0004-637X/785/1/47](https://doi.org/10.1088/0004-637X/785/1/47).
- S. Lalitha, B. Fuhrmeister, U. Wolter, J. H. M. M. Schmitt, D. Engels, and M. H. Wieringa. A multi-wavelength view of AB Doradus outer atmosphere . Simultaneous X-ray and optical spectroscopy at high cadence. *A&A*, 560:A69, Dec. 2013. doi: [10.1051/0004-6361/201321419](https://doi.org/10.1051/0004-6361/201321419).

- J. Lannier, P. Delorme, A. M. Lagrange, S. Borgniet, J. Rameau, J. E. Schlieder, J. Gagné, M. A. Bonavita, L. Malo, G. Chauvin, M. Bonnefoy, and J. H. Girard. MASSIVE: A Bayesian analysis of giant planet populations around low-mass stars. *A&A*, 596:A83, Dec. 2016. doi: [10.1051/0004-6361/201628237](https://doi.org/10.1051/0004-6361/201628237).
- S. Lépine, R. M. Rich, and M. M. Shara. Revised Metallicity Classes for Low-Mass Stars: Dwarfs (dM), Subdwarfs (sdM), Extreme Subdwarfs (esdM), and Ultrasubdwarfs (usdM). *ApJ*, 669(2): 1235–1247, Nov. 2007. doi: [10.1086/521614](https://doi.org/10.1086/521614).
- M. L. Lidov. The evolution of orbits of artificial satellites of planets under the action of gravitational perturbations of external bodies. *Planetary and Space Science*, 9:719–759, Oct. 1962. ISSN 0032-0633. doi: [10.1016/0032-0633\(62\)90129-0](https://doi.org/10.1016/0032-0633(62)90129-0). URL <http://adsabs.harvard.edu/abs/1962P%26SS....9..719L>.
- L. Lindegren. Re-normalising the astrometric chi-square in gaia dr2. GAIA-C3-TN-LU-LL-124, August 2018a. URL <http://www.rssd.esa.int/doc%5Ffetch.php?id=3757412>.
- L. Lindegren. Re-normalising the astrometric chi-square in Gaia dr2, Aug. 2018b. URL <http://www.rssd.esa.int/doc%5Ffetch.php?id=3757412>. institution={Lund Observatory} note={GAIA-C3-TN-LU-LL-124}, type={Technical Note}.
- L. Lindegren, J. Hernández, A. Bombrun, S. Klioner, U. Bastian, M. Ramos-Lerate, A. de Torres, H. Steidelmüller, C. Stephenson, D. Hobbs, U. Lammers, M. Biermann, R. Geyer, T. Hilger, D. Michalik, U. Stampa, P. J. McMillan, J. Castañeda, M. Clotet, G. Comoretto, M. Davidson, C. Fabricius, G. Gracia, N. C. Hambly, A. Hutton, A. Mora, J. Portell, F. van Leeuwen, U. Abbas, A. Abreu, M. Altmann, A. Andrei, E. Anglada, L. Balaguer-Núñez, C. Barache, U. Becciani, S. Bertone, L. Bianchi, S. Bouquillon, G. Bourda, T. Brüsemeister, B. Bucciarelli, D. Busonero, R. Buzzzi, R. Cancelliere, T. Carlucci, P. Charlot, N. Cheek, M. Crosta, C. Crowley, J. de Bruijne, F. de Felice, R. Drimmel, P. Esquej, A. Fienga, E. Fraile, M. Gai, N. Garralda, J. J. González-Vidal, R. Guerra, M. Hauser, W. Hofmann, B. Holl, S. Jordan, M. G. Lattanzi, H. Lenhardt, S. Liao, E. Licata, T. Lister, W. Löffler, J. Marchant, J.-M. Martin-Fleitas, R. Messineo, F. Mignard, R. Morbidelli, E. Poggio, A. Riva, N. Rowell, E. Salguero, M. Sarasso, E. Sciacca, H. Siddiqui, R. L. Smart, A. Spagna, I. Steele, F. Taris, J. Torra, A. van Elteren, W. van

- Reeven, and A. Vecchiato. Gaia Data Release 2. The astrometric solution. *Astronomy and Astrophysics*, 616:A2, Aug. 2018. ISSN 0004-6361. doi: [10.1051/0004-6361/201832727](https://doi.org/10.1051/0004-6361/201832727). URL <http://adsabs.harvard.edu/abs/2018A%26A...616A...2L>.
- L. Lindegren, S. A. Klioner, J. Hernández, A. Bombrun, M. Ramos-Lerate, H. Steidelmüller, U. Bastian, M. Biermann, A. de Torres, E. Gerlach, R. Geiger, T. Hilger, D. Hobbs, U. Lammers, P. J. McMillan, C. A. Stephenson, J. Castañeda, M. Davidson, C. Fabricius, G. Gracia-Abril, J. Portell, N. Rowell, D. Teyssier, F. Torra, S. Bartolomé, M. Clotet, N. Garralda, J. J. González-Vidal, J. Torra, U. Abbas, M. Altmann, E. Anglada Varela, L. Balaguer-Núñez, Z. Balog, C. Barache, U. Becciani, M. Bernet, S. Bertone, L. Bianchi, S. Bouquillon, A. G. A. Brown, B. Bucciarelli, D. Busonero, A. G. Butkevich, R. Buzzi, R. Cancelliere, T. Carlucci, P. Charlot, M. R. L. Cioni, M. Crosta, C. Crowley, E. F. del Peloso, E. del Pozo, R. Drimmel, P. Esquej, A. Fienga, E. Fraile, M. Gai, M. Garcia-Reinaldos, R. Guerra, N. C. Hambly, M. Hauser, K. Janßen, S. Jordan, Z. Kostrzewa-Rutkowska, M. G. Lattanzi, S. Liao, E. Licata, T. A. Lister, W. Löffler, J. M. Marchant, A. Masip, F. Mignard, A. Mints, D. Molina, A. Mora, R. Morbidelli, C. P. Murphy, C. Pagani, P. Panuzzo, X. Peñalosa Esteller, E. Poggio, P. Re Fiorentin, A. Riva, A. Sagristà Sellés, V. Sanchez Gimenez, M. Sarasso, E. Sciacca, H. I. Siddiqui, R. L. Smart, D. Souami, A. Spagna, I. A. Steele, F. Taris, E. Utrilla, W. van Reeve, and A. Vecchiato. Gaia Early Data Release 3. The astrometric solution. *A&A*, 649:A2, May 2021. ISSN 0004-6361. doi: [10.1051/0004-6361/202039709](https://doi.org/10.1051/0004-6361/202039709). URL <https://ui.adsabs.harvard.edu/abs/2021A%26A...649A...2L/abstract>.
- C. M. Lisse, M. L. Sitko, and M. Marengo. IRTF/SPeX Observations of the Unusual Kepler Light Curve System KIC8462852. *The Astrophysical Journal Letters*, 815:L27, Dec. 2015. ISSN 0004-637X. doi: [10.1088/2041-8205/815/2/L27](https://doi.org/10.1088/2041-8205/815/2/L27). URL <http://adsabs.harvard.edu/abs/2015ApJ...815L..27L>.
- J. D. Long, J. R. Males, S. Y. Haffert, L. Pearce, M. S. Marley, K. M. Morzinski, L. M. Close, G. P. P. L. Otten, F. Snik, M. A. Kenworthy, C. U. Keller, P. Hinz, J. D. Monnier, A. Weinberger, and V. Tolls. Improved Companion Mass Limits for Sirius A with Thermal Infrared Coronagraphy Using a Vector-apodizing Phase Plate and Time-domain Starlight-subtraction Techniques. *AJ*, 165(5):216, May 2023. doi: [10.3847/1538-3881/acbd4b](https://doi.org/10.3847/1538-3881/acbd4b).

- S. D. Lord. Nasa technical memorandum 103957: A new software tool for computing earth's atmospheric transmission of near- and far-infrared radiation. Technical report, NASA Ames Research Center Moffett Field, CA, United States, 1992. URL <https://ntrs.nasa.gov/citations/19930010877>.
- K. L. Luhman, J. R. Stauffer, and E. E. Mamajek. The Age of AB Doradus. *ApJL*, 628(1):L69–L72, July 2005. doi: [10.1086/432617](https://doi.org/10.1086/432617).
- J. I. Lunine, D. Fischer, H. Hammel, T. Henning, L. Hillenbrand, J. Kasting, G. Laughlin, B. Macintosh, M. Marley, G. Melnick, D. Monet, C. Noecker, S. Peale, A. Quirrenbach, S. Seager, and J. Winn. Worlds Beyond: A Strategy for the Detection and Characterization of Exoplanets. *arXiv e-prints*, art. arXiv:0808.2754, Aug. 2008.
- R. E. Lupu, M. S. Marley, N. Lewis, M. Line, W. A. Traub, and K. Zahnle. Developing Atmospheric Retrieval Methods for Direct Imaging Spectroscopy of Gas Giants in Reflected Light I: Methane Abundances and Basic Cloud Properties. *AJ*, 152(6):217, Dec. 2016. ISSN 1538-3881. doi: [10.3847/0004-6256/152/6/217](https://doi.org/10.3847/0004-6256/152/6/217). URL <http://arxiv.org/abs/1604.05370>. arXiv:1604.05370 [astro-ph].
- B. Macintosh, J. R. Graham, P. Ingraham, Q. Konopacky, C. Marois, M. Perrin, L. Poyneer, B. Bauman, T. Barman, A. S. Burrows, A. Cardwell, J. Chilcote, R. J. De Rosa, D. Dillon, R. Doyon, J. Dunn, D. Erikson, M. P. Fitzgerald, D. Gavel, S. Goodsell, M. Hartung, P. Higon, P. Kalas, J. Larkin, J. Maire, F. Marchis, M. S. Marley, J. McBride, M. Millar-Blanchaer, K. Morzinski, A. Norton, B. R. Oppenheimer, D. Palmer, J. Patience, L. Pueyo, F. Rantakyro, N. Sadakuni, L. Saddlemyer, D. Savransky, A. Serio, R. Soummer, A. Sivaramakrishnan, I. Song, S. Thomas, J. K. Wallace, S. Wiktorowicz, and S. Wolff. First light of the Gemini Planet Imager. *Proceedings of the National Academy of Science*, 111(35):12661–12666, Sept. 2014. doi: [10.1073/pnas.1304215111](https://doi.org/10.1073/pnas.1304215111).
- N. Madhusudhan. C/O Ratio as a Dimension for Characterizing Exoplanetary Atmospheres. *The Astrophysical Journal*, 758:36, Oct. 2012. ISSN 0004-637X. doi: [10.1088/0004-637X/758/1/36](https://doi.org/10.1088/0004-637X/758/1/36). URL <https://ui.adsabs.harvard.edu/abs/2012ApJ...758...36M>. ADS Bibcode: 2012ApJ...758...36M.

- J. R. Males and O. Guyon. Ground-based adaptive optics coronagraphic performance under closed-loop predictive control. *Journal of Astronomical Telescopes, Instruments, and Systems*, 4:019001, Jan. 2018. doi: [10.1117/1.JATIS.4.1.019001](https://doi.org/10.1117/1.JATIS.4.1.019001).
- J. R. Males, A. J. Skemer, and L. M. Close. Direct Imaging in the Habitable Zone and the Problem of Orbital Motion. *The Astrophysical Journal*, 771(1):10, July 2013. ISSN 0004-637X. doi: [10.1088/0004-637X/771/1/10](https://doi.org/10.1088/0004-637X/771/1/10). URL <https://ui.adsabs.harvard.edu/abs/2013ApJ...771...10M>. ADS Bibcode: 2013ApJ...771...10M.
- J. R. Males, M. P. Fitzgerald, R. Belikov, and O. Guyon. The Mysterious Lives Of Speckles. I. Residual atmospheric speckle lifetimes in ground-based coronagraphs. *arXiv:2107.04604 [astro-ph]*, 133(1028):104504, July 2021. doi: [10.1088/1538-3873/ac0f0c](https://doi.org/10.1088/1538-3873/ac0f0c). URL <http://arxiv.org/abs/2107.04604>. arXiv: 2107.04604.
- J. R. Males, L. M. Close, S. Haffert, J. D. Long, A. D. Hedglen, L. Pearce, A. J. Weinberger, O. Guyon, J. M. Knight, A. McLeod, M. Kautz, K. Van Gorkom, J. Lumbres, L. Schatz, A. Rodack, V. Gasho, J. Kueny, and W. Foster. MagAO-X: current status and plans for Phase II. In L. Schreiber, D. Schmidt, and E. Vernet, editors, *Adaptive Optics Systems VIII*, volume 12185 of *Society of Photo-Optical Instrumentation Engineers (SPIE) Conference Series*, page 1218509, Aug. 2022. doi: [10.1117/12.2630584](https://doi.org/10.1117/12.2630584).
- E. E. Mamajek and L. A. Hillenbrand. Improved Age Estimation for Solar-Type Dwarfs Using Activity-Rotation Diagnostics. *ApJ*, 687(2):1264–1293, Nov. 2008. doi: [10.1086/591785](https://doi.org/10.1086/591785).
- A. W. Mann, G. A. Feiden, E. Gaidos, T. Boyajian, and K. von Braun. How to Constrain Your M Dwarf: Measuring Effective Temperature, Bolometric Luminosity, Mass, and Radius. *ApJ*, 804(1):64, May 2015. doi: [10.1088/0004-637X/804/1/64](https://doi.org/10.1088/0004-637X/804/1/64).
- A. W. Mann, T. Dupuy, A. L. Kraus, E. Gaidos, M. Ansdell, M. Ireland, A. C. Rizzuto, C.-L. Hung, J. Dittmann, S. Factor, G. Feiden, R. A. Martinez, D. Ruíz-Rodríguez, and P. C. Thao. How to Constrain Your M Dwarf. II. The Mass-Luminosity-Metallicity Relation from 0.075 to 0.70 Solar Masses. *The Astrophysical Journal*, 871:63, Jan. 2019. ISSN 0004-637X. doi: [10.3847/1538-4357/aaf3bc](https://doi.org/10.3847/1538-4357/aaf3bc). URL <http://adsabs.harvard.edu/abs/2019ApJ...871...63M>.

- C. J. Manser, B. T. Gänsicke, D. Koester, T. R. Marsh, and J. Southworth. Another one grinds the dust: variability of the planetary debris disc at the white dwarf SDSS J104341.53+085558.2. *MNRAS*, 462(2):1461–1469, Oct. 2016. doi: [10.1093/mnras/stw1760](https://doi.org/10.1093/mnras/stw1760).
- M. Marengo, A. Hulsebus, and S. Willis. KIC 8462852: The Infrared Flux. *The Astrophysical Journal Letters*, 814:L15, Nov. 2015. ISSN 0004-637X. doi: [10.1088/2041-8205/814/1/L15](https://doi.org/10.1088/2041-8205/814/1/L15). URL <http://adsabs.harvard.edu/abs/2015ApJ...814L..15M>.
- M. S. Marley, C. Gelino, D. Stephens, J. I. Lunine, and R. Freedman. Reflected Spectra and Albedos of Extrasolar Giant Planets. I. Clear and Cloudy Atmospheres. *ApJ*, 513(2):879–893, Mar. 1999. doi: [10.1086/306881](https://doi.org/10.1086/306881).
- M. S. Marley, D. Saumon, C. Visscher, R. Lupu, R. Freedman, C. Morley, J. J. Fortney, C. Seay, A. J. R. W. Smith, D. J. Teal, and R. Wang. The Sonora Brown Dwarf Atmosphere and Evolution Models. I. Model Description and Application to Cloudless Atmospheres in Rainout Chemical Equilibrium. *ApJ*, 920(2):85, Oct. 2021. ISSN 0004-637X. doi: [10.3847/1538-4357/ac141d](https://doi.org/10.3847/1538-4357/ac141d). URL <https://ui.adsabs.harvard.edu/abs/2021ApJ...920...85M>. ADS Bibcode: 2021ApJ...920...85M.
- C. Marois, R. Doyon, R. Racine, and D. Nadeau. Efficient Speckle Noise Attenuation in Faint Companion Imaging. *PASP*, 112(767):91–96, Jan. 2000. doi: [10.1086/316492](https://doi.org/10.1086/316492).
- C. Marois, D. Lafrenière, R. Doyon, B. Macintosh, and D. Nadeau. Angular Differential Imaging: A Powerful High-Contrast Imaging Technique. *The Astrophysical Journal*, 641(1):556–564, Apr. 2006. ISSN 0004-637X. doi: [10.1086/500401](https://doi.org/10.1086/500401). URL <http://adsabs.harvard.edu/abs/2006ApJ...641..556M>.
- C. Marois, C. Correia, R. Galicher, P. Ingraham, B. Macintosh, T. Currie, and R. De Rosa. GPI PSF subtraction with TLOCI: the next evolution in exoplanet/disk high-contrast imaging. In E. Marchetti, L. M. Close, and J.-P. Vran, editors, *Adaptive Optics Systems IV*, volume 9148 of *Society of Photo-Optical Instrumentation Engineers (SPIE) Conference Series*, page 91480U, July 2014. doi: [10.1117/12.2055245](https://doi.org/10.1117/12.2055245).

- C. Martin, F. Mignard, and M. Froeschle. Mass determination of astrometric binaries with Hipparcos. I. Theory and simulation. *A&As*, 122:571–580, May 1997. doi: [10.1051/aas:1997339](https://doi.org/10.1051/aas:1997339).
- M. J. Martínez González, C. González-Fernández, A. Asensio Ramos, H. Socas-Navarro, C. Westendorp Plaza, T. S. Boyajian, J. T. Wright, A. Collier Cameron, J. I. González Hernández, G. Holgado, G. M. Kennedy, T. Masseron, E. Molinari, J. Saario, S. Simón-Díaz, and B. Toledo-Adrón. High-resolution spectroscopy of Boyajian’s star during optical dimming events. *Monthly Notices of the Royal Astronomical Society*, 486(1):236–244, June 2019. ISSN 0035-8711. doi: [10.1093/mnras/stz850](https://doi.org/10.1093/mnras/stz850). URL <http://adsabs.harvard.edu/abs/2019MNRAS.486..236M>.
- B. D. Mason, G. L. Wycoff, W. I. Hartkopf, G. G. Douglass, and C. E. Worley. The 2001 US Naval Observatory Double Star CD-ROM. I. The Washington Double Star Catalog. *The Astronomical Journal*, 122(6):3466–3471, Dec. 2001. ISSN 0004-6256. doi: [10.1086/323920](https://doi.org/10.1086/323920). URL <http://adsabs.harvard.edu/abs/2001AJ....122.3466M>.
- D. Mawet, L. Pueyo, P. Lawson, L. Mugnier, W. Traub, A. Boccaletti, J. T. Trauger, S. Gladysz, E. Serabyn, J. Milli, R. Belikov, M. Kasper, P. Baudoz, B. Macintosh, C. Marois, B. Oppenheimer, H. Barrett, J.-L. Beuzit, N. Devaney, J. Girard, O. Guyon, J. Krist, B. Mennesson, D. Mouillet, N. Murakami, L. Poyneer, D. Savransky, C. Véraud, and J. K. Wallace. Review of small-angle coronagraphic techniques in the wake of ground-based second-generation adaptive optics systems. In M. C. Clampin, G. G. Fazio, H. A. MacEwen, and J. Oschmann, Jacobus M., editors, *Space Telescopes and Instrumentation 2012: Optical, Infrared, and Millimeter Wave*, volume 8442 of *Society of Photo-Optical Instrumentation Engineers (SPIE) Conference Series*, page 844204, Sept. 2012. doi: [10.1117/12.927245](https://doi.org/10.1117/12.927245).
- D. Mawet, J. Milli, Z. Wahhaj, D. Pelat, O. Absil, C. Delacroix, A. Boccaletti, M. Kasper, M. Kenworthy, C. Marois, B. Mennesson, and L. Pueyo. Fundamental Limitations of High Contrast Imaging Set by Small Sample Statistics. *ApJ*, 792(2):97, Sept. 2014. doi: [10.1088/0004-637X/792/2/97](https://doi.org/10.1088/0004-637X/792/2/97).
- J. Maíz Apellániz, M. Pantaleoni González, and R. H. Barbá. Validation of the accuracy and precision of Gaia EDR3 parallaxes with globular clusters. *A&A*, Volume 649, id.A13, 10 pp.,

- 649:A13, May 2021. ISSN 0004-6361. doi: [10.1051/0004-6361/202140418](https://doi.org/10.1051/0004-6361/202140418). URL <https://ui.adsabs.harvard.edu/abs/2021A%26A...649A..13M/abstract>.
- K. McCarthy and R. J. White. The Sizes of the Nearest Young Stars. *AJ*, 143(6):134, June 2012. doi: [10.1088/0004-6256/143/6/134](https://doi.org/10.1088/0004-6256/143/6/134).
- I. McDonald, A. A. Zijlstra, and M. L. Boyer. Fundamental parameters and infrared excesses of Hipparcos stars. *Monthly Notices of the Royal Astronomical Society*, 427:343–357, Nov. 2012. ISSN 0035-8711. doi: [10.1111/j.1365-2966.2012.21873.x](https://doi.org/10.1111/j.1365-2966.2012.21873.x). URL <http://adsabs.harvard.edu/abs/2012MNRAS.427..343M>.
- C. P. McKay, J. B. Pollack, and R. Courtin. The thermal structure of Titan’s atmosphere. *Icarus*, 80(1):23–53, July 1989. doi: [10.1016/0019-1035\(89\)90160-7](https://doi.org/10.1016/0019-1035(89)90160-7).
- C. Melis, P. Dufour, J. Farihi, J. Bochanski, A. J. Burgasser, S. G. Parsons, B. T. Gänsicke, D. Koester, and B. J. Swift. Gaseous Material Orbiting the Polluted, Dusty White Dwarf HE 1349-2305. *ApJL*, 751(1):L4, May 2012. doi: [10.1088/2041-8205/751/1/L4](https://doi.org/10.1088/2041-8205/751/1/L4).
- T. Meshkat, D. Mawet, M. L. Bryan, S. Hinkley, B. P. Bowler, K. R. Stapelfeldt, K. Batygin, D. Padgett, F. Y. Morales, E. Serabyn, V. Christiaens, T. D. Brandt, and Z. Wahhaj. A Direct Imaging Survey of Spitzer-detected Debris Disks: Occurrence of Giant Planets in Dusty Systems. *AJ*, 154(6):245, Dec. 2017. doi: [10.3847/1538-3881/aa8e9a](https://doi.org/10.3847/1538-3881/aa8e9a).
- S. Messina, A. C. Lanzafame, G. A. Feiden, M. Millward, S. Desidera, A. Buccino, I. Curtis, E. Jofré, P. Kehusmaa, B. J. Medhi, B. Monard, and R. Petrucci. The rotation-lithium depletion correlation in the beta Pictoris association and the LDB age determination. *Astronomy and Astrophysics*, 596:A29, Nov. 2016. ISSN 0004-6361. doi: [10.1051/0004-6361/201628524](https://doi.org/10.1051/0004-6361/201628524). URL <http://adsabs.harvard.edu/abs/2016A%26A...596A..29M>.
- S. Messina, A. C. Lanzafame, L. Malo, S. Desidera, A. Buccino, L. Zhang, S. Artemenko, M. Millward, and F.-J. Hamsch. The beta Pictoris association low-mass members: Membership assessment, rotation period distribution, and dependence on multiplicity. *Astronomy and Astrophysics*, 607:A3, Oct. 2017. ISSN 0004-6361. doi: [10.1051/0004-6361/201730444](https://doi.org/10.1051/0004-6361/201730444). URL <http://adsabs.harvard.edu/abs/2017A%26A...607A...3M>.

- R. Mewe, J. S. Kaastra, S. M. White, and R. Pallavicini. Simultaneous EUVE & ASCA observations of AB Doradus: temperature structure and abundances of the quiescent corona. *A&A*, 315: 170–178, Nov. 1996.
- D. Michalik, L. Lindegren, and D. Hobbs. The Tycho-Gaia astrometric solution . How to get 2.5 million parallaxes with less than one year of Gaia data. *A&A*, 574:A115, Feb. 2015. doi: [10.1051/0004-6361/201425310](https://doi.org/10.1051/0004-6361/201425310).
- T. Mittal, C. H. Chen, H. Jang-Condell, P. Manoj, B. A. Sargent, D. M. Watson, and C. M. Lisse. The Spitzer Infrared Spectrograph Debris Disk Catalog. II. Silicate Feature Analysis of Unresolved Targets. *ApJ*, 798(2):87, Jan. 2015. doi: [10.1088/0004-637X/798/2/87](https://doi.org/10.1088/0004-637X/798/2/87).
- S. Modak and C. Hamilton. Eccentricity dynamics of wide binaries - I. The effect of Galactic tides. *MNRAS*, 524(2):3102–3115, Sept. 2023. doi: [10.1093/mnras/stad2073](https://doi.org/10.1093/mnras/stad2073).
- M. Moe and K. M. Kratter. Impact of Binary Stars on Planet Statistics – I. Planet Occurrence Rates, Trends with Stellar Mass, and Wide Companions to Hot Jupiter Hosts. *arXiv e-prints*, 1912: arXiv:1912.01699, Dec. 2019. URL <http://adsabs.harvard.edu/abs/2019arXiv191201699M>.
- B. T. Montet and J. D. Simon. KIC 8462852 Faded throughout the Kepler Mission. *The Astrophysical Journal Letters*, 830:L39, Oct. 2016. ISSN 0004-637X. doi: [10.3847/2041-8205/830/2/L39](https://doi.org/10.3847/2041-8205/830/2/L39). URL <http://adsabs.harvard.edu/abs/2016ApJ...830L..39M>.
- K. M. Morzinski, J. R. Males, A. J. Skemer, L. M. Close, P. M. Hinz, T. J. Rodigas, A. Puglisi, S. Esposito, A. Riccardi, E. Pinna, M. Xompero, R. Briguglio, V. P. Bailey, K. B. Follette, D. Kopon, A. J. Weinberger, and Y.-L. Wu. Magellan Adaptive Optics First-light Observations of the Exoplanet beta Pic b. II. 3-5 μm Direct Imaging with MagAO+Clio, and the Empirical Bolometric Luminosity of a Self-luminous Giant Planet. *The Astrophysical Journal*, 815:108, Dec. 2015. ISSN 0004-637X. doi: [10.1088/0004-637X/815/2/108](https://doi.org/10.1088/0004-637X/815/2/108). URL <http://adsabs.harvard.edu/abs/2015ApJ...815..108M>.
- L. R. Mudryk and Y. Wu. Resonance Overlap Is Responsible for Ejecting Planets in Binary Systems. *ApJ*, 639(1):423–431, Mar. 2006. doi: [10.1086/499347](https://doi.org/10.1086/499347).

- S. Mukherjee, J. J. Fortney, N. E. Batalha, T. Karalidi, M. S. Marley, C. Visscher, B. E. Miles, and A. J. I. Skemer. Probing the Extent of Vertical Mixing in Brown Dwarf Atmospheres with Disequilibrium Chemistry. *The Astrophysical Journal*, 938:107, Oct. 2022. ISSN 0004-637X. doi: [10.3847/1538-4357/ac8dfb](https://doi.org/10.3847/1538-4357/ac8dfb). URL <https://ui.adsabs.harvard.edu/abs/2022ApJ...938..107M>. ADS Bibcode: 2022ApJ...938..107M.
- S. Mukherjee, N. E. Batalha, J. J. Fortney, and M. S. Marley. PICASO 3.0: A One-dimensional Climate Model for Giant Planets and Brown Dwarfs. *The Astrophysical Journal*, 942:71, Jan. 2023. ISSN 0004-637X. doi: [10.3847/1538-4357/ac9f48](https://doi.org/10.3847/1538-4357/ac9f48). URL <https://ui.adsabs.harvard.edu/abs/2023ApJ...942...71M>. ADS Bibcode: 2023ApJ...942...71M.
- A. J. Mustill and E. Villaver. Foretellings of Ragnarök: World-engulfing Asymptotic Giants and the Inheritance of White Dwarfs. *Astrophys. J.*, 761:121, Dec. 2012. ISSN 0004-637X. doi: [10.1088/0004-637X/761/2/121](https://doi.org/10.1088/0004-637X/761/2/121).
- A. J. Mustill, M. B. Davies, S. Blunt, and A. Howard. Dynamical orbital evolution scenarios of the wide-orbit eccentric planet HR 5183b. *arXiv e-prints*, art. arXiv:2102.06031, Feb. 2021.
- A. J. Mustill, M. B. Davies, S. Blunt, and A. Howard. Dynamical orbital evolution scenarios of the wide-orbit eccentric planet HR 5183b. *MNRAS*, 509(3):3616–3625, Jan. 2022. doi: [10.1093/mnras/stab3174](https://doi.org/10.1093/mnras/stab3174).
- National Academies of Sciences, Engineering, and Medicine. *Pathways to Discovery in Astronomy and Astrophysics for the 2020s*. 2021. doi: [10.17226/26141](https://doi.org/10.17226/26141).
- M.-E. Naud, É. Artigau, R. Doyon, L. Malo, J. Gagné, D. Lafrenière, C. Wolf, and E. A. Magnier. PSYM-WIDE: A Survey for Large-separation Planetary-mass Companions to Late Spectral Type Members of Young Moving Groups. *AJ*, 154(3):129, Sept. 2017. doi: [10.3847/1538-3881/aa826b](https://doi.org/10.3847/1538-3881/aa826b).
- M. Nayak, R. Lupu, M. S. Marley, J. J. Fortney, T. Robinson, and N. Lewis. Atmospheric Retrieval for Direct Imaging Spectroscopy of Gas Giants in Reflected Light. II. Orbital Phase and Planetary Radius. *Publications of the Astronomical Society of the Pacific*, 129:034401, Mar.

2017. ISSN 0004-6280. doi: [10.1088/1538-3873/129/973/034401](https://doi.org/10.1088/1538-3873/129/973/034401). URL <http://adsabs.harvard.edu/abs/2017PASP..129c4401N>.
- P. K. Nayak, A. Ganguly, and S. Chatterjee. Hunting down white dwarf-main sequence binaries using multiwavelength observations. *MNRAS*, 527(3):6100–6109, Jan. 2024. doi: [10.1093/mnras/stad3580](https://doi.org/10.1093/mnras/stad3580).
- B. E. Nelson, P. M. Robertson, M. J. Payne, S. M. Pritchard, K. M. Deck, E. B. Ford, J. T. Wright, and H. T. Isaacson. An empirically derived three-dimensional Laplace resonance in the Gliese 876 planetary system. *MNRAS*, 455(3):2484–2499, Jan. 2016. doi: [10.1093/mnras/stv2367](https://doi.org/10.1093/mnras/stv2367).
- E. R. Newton, A. W. Mann, B. M. Tofflemire, L. Pearce, A. C. Rizzuto, A. Vanderburg, R. A. Martinez, J. J. Wang, J.-B. Ruffio, A. L. Kraus, M. C. Johnson, P. C. Thao, M. L. Wood, R. Rampalli, E. L. Nielsen, K. A. Collins, D. Dragomir, C. Hellier, D. R. Anderson, T. Barclay, C. Brown, G. Feiden, R. Hart, G. Isopi, J. F. Kielkopf, F. Mallia, P. Nelson, J. E. Rodriguez, C. Stockdale, I. A. Waite, D. J. Wright, J. J. Lissauer, G. R. Ricker, R. Vanderspek, D. W. Latham, S. Seager, J. N. Winn, J. M. Jenkins, L. G. Bouma, C. J. Burke, M. Davies, M. Fausnaugh, J. Li, R. L. Morris, K. Mukai, J. Villaseñor, S. Villeneuve, R. J. De Rosa, B. Macintosh, M. W. Mengel, J. Okumura, and R. A. Wittenmyer. TESS Hunt for Young and Maturing Exoplanets (THYME): A Planet in the 45 Myr Tucana-Horologium Association. *The Astrophysical Journal Letters*, 880:L17, July 2019. ISSN 0004-637X. doi: [10.3847/2041-8213/ab2988](https://doi.org/10.3847/2041-8213/ab2988). URL <http://adsabs.harvard.edu/abs/2019ApJ...880L..17N>.
- E. R. Newton, A. W. Mann, A. L. Kraus, J. H. Livingston, A. Vanderburg, J. L. Curtis, P. C. Thao, K. Hawkins, M. L. Wood, A. C. Rizzuto, A. Soubkiou, B. M. Tofflemire, G. Zhou, I. J. M. Crossfield, L. A. Pearce, K. A. Collins, D. M. Conti, T.-G. Tan, S. Villeneuve, A. Spencer, D. Dragomir, S. N. Quinn, E. L. N. Jensen, K. I. Collins, C. Stockdale, R. Cloutier, C. Hellier, Z. Benkhaldoun, C. Ziegler, C. Briceño, N. Law, B. Benneke, J. L. Christiansen, V. Gorjian, S. R. Kane, L. Kreidberg, F. Y. Morales, M. W. Werner, J. D. Twicken, A. M. Levine, D. R. Ciardi, N. M. Guerrero, K. Hesse, E. V. Quintana, B. Shiao, J. C. Smith, G. Torres, G. R. Ricker, R. Vanderspek, S. Seager, J. N. Winn, J. M. Jenkins, and D. W. Latham. TESS Hunt for Young

- and Maturing Exoplanets (THYME). IV. Three Small Planets Orbiting a 120 Myr Old Star in the Pisces-Eridanus Stream. *AJ*, 161(2):65, Feb. 2021. doi: [10.3847/1538-3881/abccc6](https://doi.org/10.3847/1538-3881/abccc6).
- H. Ngo, H. A. Knutson, S. Hinkley, J. R. Crepp, E. B. Bechter, K. Batygin, A. W. Howard, J. A. Johnson, T. D. Morton, and P. S. Muirhead. Friends of Hot Jupiters. II. No Correspondence between Hot-jupiter Spin-Orbit Misalignment and the Incidence of Directly Imaged Stellar Companions. *ApJ*, 800(2):138, Feb. 2015. doi: [10.1088/0004-637X/800/2/138](https://doi.org/10.1088/0004-637X/800/2/138).
- H. Ngo, H. A. Knutson, S. Hinkley, M. Bryan, J. R. Crepp, K. Batygin, I. Crossfield, B. Hansen, A. W. Howard, J. A. Johnson, D. Mawet, T. D. Morton, P. S. Muirhead, and J. Wang. Friends of Hot Jupiters. IV. Stellar Companions Beyond 50 au Might Facilitate Giant Planet Formation, but Most are Unlikely to Cause Kozai-Lidov Migration. *ApJ*, 827(1):8, Aug. 2016. doi: [10.3847/0004-637X/827/1/8](https://doi.org/10.3847/0004-637X/827/1/8).
- E. L. Nielsen, R. J. De Rosa, B. Macintosh, J. J. Wang, J.-B. Ruffio, E. Chiang, M. S. Marley, D. Saumon, D. Savransky, S. M. Ammons, V. P. Bailey, T. Barman, C. Blain, J. Bulger, A. Burrows, J. Chilcote, T. Cotten, I. Czekala, R. Doyon, G. Duchêne, T. M. Esposito, D. Fabrycky, M. P. Fitzgerald, K. B. Follette, J. J. Fortney, B. L. Gerard, S. J. Goodsell, J. R. Graham, A. Z. Greenbaum, P. Higon, S. Hinkley, L. A. Hirsch, J. Hom, L.-W. Hung, R. I. Dawson, P. Ingraham, P. Kalas, Q. Konopacky, J. E. Larkin, E. J. Lee, J. W. Lin, J. Maire, F. Marchis, C. Marois, S. Metchev, M. A. Millar-Blanchaer, K. M. Morzinski, R. Oppenheimer, D. Palmer, J. Patience, M. Perrin, L. Poyneer, L. Pueyo, R. R. Rafikov, A. Rajan, J. Rameau, F. T. Rantakyro, B. Ren, A. C. Schneider, A. Sivaramakrishnan, I. Song, R. Sommer, M. Tallis, S. Thomas, K. Ward-Duong, and S. Wolff. The Gemini Planet Imager Exoplanet Survey: Giant Planet and Brown Dwarf Demographics from 10 to 100 au. *The Astronomical Journal*, 158:13, July 2019. ISSN 0004-6256. doi: [10.3847/1538-3881/ab16e9](https://doi.org/10.3847/1538-3881/ab16e9). URL <http://adsabs.harvard.edu/abs/2019AJ....158...13N>.
- H. T. Noor, J. Farihi, M. Hollands, and S. Toonen. White dwarf pollution: one star or two? *MNRAS*, 529(3):2910–2917, Apr. 2024. doi: [10.1093/mnras/stae731](https://doi.org/10.1093/mnras/stae731).
- M. W. O’Brien, P. E. Tremblay, B. L. Klein, D. Koester, C. Melis, A. Bédard, E. Cukanovaite, T. Cunningham, A. E. Doyle, B. T. Gänsicke, N. P. Gentile Fusillo, M. A. Hollands, J. McCleery,

- I. Pelisoli, S. Toonen, A. J. Weinberger, and B. Zuckerman. The 40 pc sample of white dwarfs from Gaia. *MNRAS*, 527(3):8687–8705, Jan. 2024. doi: [10.1093/mnras/stad3773](https://doi.org/10.1093/mnras/stad3773).
- C. E. O’Connor, J. Teyssandier, and D. Lai. Secular chaos in white dwarf planetary systems: Origins of metal pollution and short-period planetary companions. *Mon. Not. R. Astron. Soc.*, 513:4178–4195, July 2022. ISSN 0035-8711. doi: [10.1093/mnras/stac1189](https://doi.org/10.1093/mnras/stac1189).
- H. P. Osborn, M. Ansdell, Y. Ioannou, M. Sasdelli, D. Angerhausen, D. Caldwell, J. M. Jenkins, C. Räissi, and J. C. Smith. Rapid classification of TESS planet candidates with convolutional neural networks. *A&A*, 633:A53, Jan. 2020. doi: [10.1051/0004-6361/201935345](https://doi.org/10.1051/0004-6361/201935345).
- G. P. P. L. Otten, F. Snik, M. A. Kenworthy, M. N. Miskiewicz, and M. J. Escuti. Performance characterization of a broadband vector Apodizing Phase Plate coronagraph. *Optics Express*, 22(24):30287, Dec. 2014. doi: [10.1364/OE.22.030287](https://doi.org/10.1364/OE.22.030287).
- S. G. Parsons, A. Rebassa-Mansergas, M. R. Schreiber, B. T. Gänsicke, M. Zorotovic, and J. J. Ren. The white dwarf binary pathways survey - I. A sample of FGK stars with white dwarf companions. *MNRAS*, 463(2):2125–2136, Dec. 2016. doi: [10.1093/mnras/stw2143](https://doi.org/10.1093/mnras/stw2143).
- B. Paxton, L. Bildsten, A. Dotter, F. Herwig, P. Lesaffre, and F. Timmes. Modules for Experiments in Stellar Astrophysics (MESA). *ApJs*, 192(1):3, Jan. 2011. doi: [10.1088/0067-0049/192/1/3](https://doi.org/10.1088/0067-0049/192/1/3).
- B. Paxton, M. Cantiello, P. Arras, L. Bildsten, E. F. Brown, A. Dotter, C. Mankovich, M. H. Montgomery, D. Stello, F. X. Timmes, and R. Townsend. Modules for Experiments in Stellar Astrophysics (MESA): Planets, Oscillations, Rotation, and Massive Stars. *ApJs*, 208(1):4, Sept. 2013. doi: [10.1088/0067-0049/208/1/4](https://doi.org/10.1088/0067-0049/208/1/4).
- B. Paxton, P. Marchant, J. Schwab, E. B. Bauer, L. Bildsten, M. Cantiello, L. Dessart, R. Farmer, H. Hu, N. Langer, R. H. D. Townsend, D. M. Townsley, and F. X. Timmes. Modules for Experiments in Stellar Astrophysics (MESA): Binaries, Pulsations, and Explosions. *ApJs*, 220(1):15, Sept. 2015. doi: [10.1088/0067-0049/220/1/15](https://doi.org/10.1088/0067-0049/220/1/15).
- M. J. Payne, D. Veras, M. J. Holman, and B. T. Gänsicke. Liberating exomoons in white dwarf planetary systems. *MNRAS*, 457(1):217–231, Mar. 2016. doi: [10.1093/mnras/stv2966](https://doi.org/10.1093/mnras/stv2966).

- L. A. Pearce, A. L. Kraus, T. J. Dupuy, M. J. Ireland, A. C. Rizzuto, B. P. Bowler, E. K. Birchall, and A. L. Wallace. Orbital Motion of the Wide Planetary-mass Companion GSC 6214-210 b: No Evidence for Dynamical Scattering. *The Astronomical Journal*, 157(2):71, Feb. 2019. ISSN 0004-6256. doi: [10.3847/1538-3881/aafacb](https://doi.org/10.3847/1538-3881/aafacb). URL <http://adsabs.harvard.edu/abs/2019AJ....157..71P>.
- L. A. Pearce, A. L. Kraus, T. J. Dupuy, A. W. Mann, E. R. Newton, B. M. Tofflemire, and A. Vanderburg. Orbital Parameter Determination for Wide Stellar Binary Systems in the Age of Gaia. *The Astrophysical Journal*, 894(2):115, May 2020. ISSN 0004-637X. doi: [10.3847/1538-4357/ab8389](https://doi.org/10.3847/1538-4357/ab8389). URL <http://adsabs.harvard.edu/abs/2020ApJ...894..115P>.
- L. A. Pearce, A. L. Kraus, T. J. Dupuy, A. W. Mann, and D. Huber. Boyajian’s Star B: The Co-moving Companion to KIC 8462852 A. *ApJ*, 909(2):216, Mar. 2021. ISSN 0004-637X. doi: [10.3847/1538-4357/abdd33](https://doi.org/10.3847/1538-4357/abdd33). URL <https://doi.org/10.3847/1538-4357/abdd33>. Publisher: American Astronomical Society.
- L. A. Pearce, J. R. Males, A. J. Weinberger, J. D. Long, K. M. Morzinski, L. M. Close, and P. M. Hinz. Companion mass limits for 17 binary systems obtained with binary differential imaging and MagAO/Clio. *MNRAS*, 515(3):4487–4504, Sept. 2022. doi: [10.1093/mnras/stac2056](https://doi.org/10.1093/mnras/stac2056).
- L. A. Pearce, J. R. Males, S. Y. Haffert, L. M. Close, J. D. Long, A. L. McLeod, J. M. Knight, A. D. Hedglen, A. J. Weinberger, O. Guyon, M. Kautz, K. Van Gorkom, J. Lumbres, L. Schatz, A. Rodack, V. Gasho, J. Kueny, W. Foster, K. M. Morzinski, and P. M. Hinz. HIP 67506 C: MagAO-X confirmation of a new low-mass stellar companion to HIP 67506 A. *MNRAS*, 521(3):4775–4784, May 2023. doi: [10.1093/mnras/stad859](https://doi.org/10.1093/mnras/stad859).
- M. J. Pecaut and E. E. Mamajek. Intrinsic Colors, Temperatures, and Bolometric Corrections of Pre-main-sequence Stars. *The Astrophysical Journal Supplement Series*, 208(1):9, Sept. 2013. ISSN 0067-0049. doi: [10.1088/0067-0049/208/1/9](https://doi.org/10.1088/0067-0049/208/1/9). URL <http://adsabs.harvard.edu/abs/2013ApJS..208....9P>.
- M. J. Pecaut, E. E. Mamajek, and E. J. Bubar. A Revised Age for Upper Scorpius and the Star Formation History among the F-type Members of the Scorpius-Centaurus OB Association.

- tion. *The Astrophysical Journal*, 746:154, Feb. 2012. ISSN 0004-637X. doi: [10.1088/0004-637X/746/2/154](https://doi.org/10.1088/0004-637X/746/2/154). URL <http://adsabs.harvard.edu/abs/2012ApJ...746..154P>.
- Z. Penoyre, V. Belokurov, N. Wyn Evans, A. Everall, and S. E. Koposov. Binary deviations from single object astrometry. *MNRAS*, 495(1):321–337, June 2020. doi: [10.1093/mnras/staa1148](https://doi.org/10.1093/mnras/staa1148).
- Z. Penoyre, V. Belokurov, and N. W. Evans. Astrometric Identification of Nearby Binary Stars I: Predicted Astrometric Signals. *arXiv e-prints*, art. arXiv:2111.10380, Nov. 2021.
- H. B. Perets. Planets in Evolved Binary Systems. In S. Schuh, H. Drechsel, and U. Heber, editors, *Planetary Systems Beyond the Main Sequence*, volume 1331 of *American Institute of Physics Conference Series*, pages 56–75, Mar. 2011. doi: [10.1063/1.3556185](https://doi.org/10.1063/1.3556185).
- M. A. C. Perryman, L. Lindegren, J. Kovalevsky, E. Hoeg, U. Bastian, P. L. Bernacca, M. Cr ez e, F. Donati, M. Grenon, M. Grewing, F. van Leeuwen, H. van der Marel, F. Mignard, C. A. Murray, R. S. Le Poole, H. Schrijver, C. Turon, F. Arenou, M. Froeschl e, and C. S. Petersen. The HIPPARCOS Catalogue. *A&A*, 323:L49–L52, July 1997.
- C. Petrovich and D. J. Mu noz. Planetary Engulfment as a Trigger for White Dwarf Pollution. *Astrophys. J.*, 834:116, Jan. 2017. ISSN 0004-637X. doi: [10.3847/1538-4357/834/2/116](https://doi.org/10.3847/1538-4357/834/2/116).
- A. J. Pickles. A Stellar Spectral Flux Library: 1150-25000  . *PASP*, 110(749):863–878, July 1998. doi: [10.1086/316197](https://doi.org/10.1086/316197).
- D. Piskorz, H. A. Knutson, H. Ngo, P. S. Muirhead, K. Batygin, J. R. Crepp, S. Hinkley, and T. D. Morton. Friends of Hot Jupiters. III. An Infrared Spectroscopic Search for Low-mass Stellar Companions. *ApJ*, 814(2):148, Dec. 2015. doi: [10.1088/0004-637X/814/2/148](https://doi.org/10.1088/0004-637X/814/2/148).
- C. Pittordis and W. Sutherland. Testing modified gravity with wide binaries in Gaia DR2. *MNRAS*, 488(4):4740–4752, Oct. 2019. doi: [10.1093/mnras/stz1898](https://doi.org/10.1093/mnras/stz1898).
- R. Poleski, J. Skowron, P. Mr oz, A. Udalski, M. K. Szyma nski, P. Pietrukowicz, K. Ulaczyk, K. Rybicki, P. Iwanek, M. Wrona, and M. Gromadzki. Wide-Orbit Exoplanets are Common. Analysis of Nearly 20 Years of OGLE Microlensing Survey Data. *Acta Astronomica*, 71(1): 1–23, Mar. 2021. doi: [10.32023/0001-5237/71.1.1](https://doi.org/10.32023/0001-5237/71.1.1).

- D. Pourbaix, A. A. Tokovinin, A. H. Batten, F. C. Fekel, W. I. Hartkopf, H. Levato, N. I. Morrell, G. Torres, and S. Udry. S_B^9 : The ninth catalogue of spectroscopic binary orbits. *A&A*, 424: 727–732, Sept. 2004. doi: [10.1051/0004-6361:20041213](https://doi.org/10.1051/0004-6361:20041213).
- L. Pueyo. Detection and Characterization of Exoplanets using Projections on Karhunen-Loève Eigenimages: Forward Modeling. *ApJ*, 824(2):117, June 2016. doi: [10.3847/0004-637X/824/2/117](https://doi.org/10.3847/0004-637X/824/2/117).
- R. Racine, G. A. H. Walker, D. Nadeau, R. Doyon, and C. Marois. Speckle Noise and the Detection of Faint Companions. *PASP*, 111(759):587–594, May 1999. doi: [10.1086/316367](https://doi.org/10.1086/316367).
- D. Raghavan, H. A. McAlister, T. J. Henry, D. W. Latham, G. W. Marcy, B. D. Mason, D. R. Gies, R. J. White, and T. A. ten Brummelaar. A Survey of Stellar Families: Multiplicity of Solar-type Stars. *The Astrophysical Journal Supplement Series*, 190:1–42, Sept. 2010. ISSN 0067-0049. doi: [10.1088/0067-0049/190/1/1](https://doi.org/10.1088/0067-0049/190/1/1). URL <http://adsabs.harvard.edu/abs/2010ApJS..190....1R>.
- J. Rameau, G. Chauvin, A. M. Lagrange, A. L. Maire, A. Boccaletti, and M. Bonnefoy. Detection limits with spectral differential imaging data. *A&A*, 581:A80, Sept. 2015. doi: [10.1051/0004-6361/201525879](https://doi.org/10.1051/0004-6361/201525879).
- A. Rebassa-Mansergas, E. Solano, F. M. Jiménez-Esteban, S. Torres, C. Rodrigo, A. Ferrer-Burjachs, L. M. Calcaferro, L. G. Althaus, and A. H. Córscico. White dwarf-main-sequence binaries from Gaia EDR3: the unresolved 100 pc volume-limited sample. *MNRAS*, 506(4): 5201–5211, Oct. 2021. doi: [10.1093/mnras/stab2039](https://doi.org/10.1093/mnras/stab2039).
- J. J. Ren, R. Raddi, A. Rebassa-Mansergas, M. S. Hernandez, S. G. Parsons, P. Irawati, P. Rittipruk, M. R. Schreiber, B. T. Gänsicke, S. Torres, H. J. Wang, J. B. Zhang, Y. Zhao, Y. T. Zhou, Z. W. Han, B. Wang, C. Liu, X. W. Liu, Y. Wang, J. Zheng, J. F. Wang, F. Zhao, K. M. Cui, J. R. Shi, and H. Tian. The White Dwarf Binary Pathways Survey. V. The Gaia White Dwarf Plus AFGK Binary Sample and the Identification of 23 Close Binaries. *ApJ*, 905(1):38, Dec. 2020. doi: [10.3847/1538-4357/abc017](https://doi.org/10.3847/1538-4357/abc017).
- B. Riaz, J. E. Gizis, and J. Harvin. Identification of New M Dwarfs in the Solar Neighborhood. *The Astronomical Journal*, 132(2):866–872, Aug. 2006. ISSN 0004-6256. doi: [10.1086/5071111](https://doi.org/10.1086/5071111).

10.1086/505632. URL <https://ui.adsabs.harvard.edu/abs/2006AJ....132..866R>. ADS Bibcode: 2006AJ....132..866R.

T. Richey-Yowell, E. L. Shkolnik, A. C. Schneider, E. Osby, T. Barman, and V. S. Meadows. HAZMAT. V. The Ultraviolet and X-Ray Evolution of K Stars. *ApJ*, 872(1):17, Feb. 2019. doi: [10.3847/1538-4357/aafa74](https://doi.org/10.3847/1538-4357/aafa74).

G. R. Ricker, J. N. Winn, R. Vanderspek, D. W. Latham, G. Á. Bakos, J. L. Bean, Z. K. Bertan-Thompson, T. M. Brown, L. Buchhave, N. R. Butler, R. P. Butler, W. J. Chaplin, D. Charbonneau, J. Christensen-Dalsgaard, M. Clampin, D. Deming, J. Doty, N. De Lee, C. Dressing, E. W. Dunham, M. Endl, F. Fressin, J. Ge, T. Henning, M. J. Holman, A. W. Howard, S. Ida, J. M. Jenkins, G. Jernigan, J. A. Johnson, L. Kaltenegger, N. Kawai, H. Kjeldsen, G. Laughlin, A. M. Levine, D. Lin, J. J. Lissauer, P. MacQueen, G. Marcy, P. R. McCullough, T. D. Morton, N. Narita, M. Paegert, E. Palte, F. Pepe, J. Pepper, A. Quirrenbach, S. A. Rinehart, D. Sasselov, B. Sato, S. Seager, A. Sozzetti, K. G. Stassun, P. Sullivan, A. Szentgyorgyi, G. Torres, S. Udry, and J. Villaseñor. Transiting Exoplanet Survey Satellite (TESS). *Journal of Astronomical Telescopes, Instruments, and Systems*, 1:014003, Jan. 2015. doi: [10.1117/1.JATIS.1.1.014003](https://doi.org/10.1117/1.JATIS.1.1.014003).

E. L. Rickman, W. Ceva, E. C. Matthews, D. Ségransan, B. P. Bowler, T. Forveille, K. Franson, J. Hagelberg, S. Udry, and A. Vigan. The discovery of two new benchmark brown dwarfs with precise dynamical masses at the stellar-substellar boundary. *A&A*, 684:A88, Apr. 2024. doi: [10.1051/0004-6361/202347906](https://doi.org/10.1051/0004-6361/202347906).

E. J. Rivera, G. Laughlin, R. P. Butler, S. S. Vogt, N. Haghighipour, and S. Meschiari. The Lick-Carnegie Exoplanet Survey: a Uranus-Mass Fourth Planet for GJ 876 in an Extrasolar Laplace Configuration. *The Astrophysical Journal*, 719(1):890–899, Aug. 2010. ISSN 0004-637X. doi: [10.1088/0004-637X/719/1/890](https://doi.org/10.1088/0004-637X/719/1/890). URL <https://ui.adsabs.harvard.edu/abs/2010ApJ...719..890R>. ADS Bibcode: 2010ApJ...719..890R.

T. J. Rodigas, A. Weinberger, E. E. Mamajek, J. R. Males, L. M. Close, K. Morzinski, P. M. Hinz, and N. Kaib. Direct Exoplanet Detection with Binary Differential Imaging. *The Astrophysical Journal*, 811:157, Oct. 2015. ISSN 0004-637X. doi: [10.1088/0004-637X/811/2/157](https://doi.org/10.1088/0004-637X/811/2/157). URL <http://adsabs.harvard.edu/abs/2015ApJ...811..157R>.

- C. M. Rooney, N. E. Batalha, and M. S. Marley. Spherical Harmonics for the 1D Radiative Transfer Equation. I. Reflected Light. *ApJ*, 950(1):22, June 2023. doi: [10.3847/1538-4357/acca79](https://doi.org/10.3847/1538-4357/acca79).
- L. J. Rosenthal, B. J. Fulton, L. A. Hirsch, H. T. Isaacson, A. W. Howard, C. M. Dédrick, I. A. Sherstyuk, S. C. Blunt, E. A. Petigura, H. A. Knutson, A. Behmard, A. Chontos, J. R. Crepp, I. J. M. Crossfield, P. A. Dalba, D. A. Fischer, G. W. Henry, S. R. Kane, M. Kosiarek, G. W. Marcy, R. A. Rubenzahl, L. M. Weiss, and J. T. Wright. The California Legacy Survey. I. A Catalog of 178 Planets from Precision Radial Velocity Monitoring of 719 Nearby Stars over Three Decades. *ApJs*, 255(1):8, July 2021. doi: [10.3847/1538-4365/abe23c](https://doi.org/10.3847/1538-4365/abe23c).
- G. Ruane, H. Ngo, D. Mawet, O. Absil, É. Choquet, T. Cook, C. Gomez Gonzalez, E. Huby, K. Matthews, T. Meshkat, M. Reggiani, E. Serabyn, N. Wallack, and W. J. Xuan. Reference Star Differential Imaging of Close-in Companions and Circumstellar Disks with the NIRC2 Vortex Coronagraph at the W. M. Keck Observatory. *AJ*, 157(3):118, Mar. 2019. doi: [10.3847/1538-3881/aafee2](https://doi.org/10.3847/1538-3881/aafee2).
- D. Ruz-Mieres and zuzannakr. gaia-dpci/gaiaxy: Gaiaxy v2.1.0. Aug. 2023. doi: [10.5281/zenodo.8239995](https://doi.org/10.5281/zenodo.8239995). URL <https://doi.org/10.5281/zenodo.8239995>.
- A. Salvador, T. D. Robinson, J. J. Fortney, and M. S. Marley. Influence of Orbit and Mass Constraints on Reflected Light Characterization of Directly Imaged Rocky Exoplanets. *arXiv e-prints*, art. arXiv:2406.07749, June 2024. doi: [10.48550/arXiv.2406.07749](https://doi.org/10.48550/arXiv.2406.07749).
- M. Samland, J. Bouwman, D. W. Hogg, W. Brandner, T. Henning, and M. Janson. TRAP: a temporal systematics model for improved direct detection of exoplanets at small angular separations. *A&A*, 646:A24, Feb. 2021. doi: [10.1051/0004-6361/201937308](https://doi.org/10.1051/0004-6361/201937308).
- N. N. Samus', V. P. Goranskii, O. V. Durevich, A. V. Zharova, E. V. Kazarovets, N. N. Kireeva, E. N. Pastukhova, D. B. Williams, and M. L. Hazen. An Electronic Version of the Second Volume of the General Catalogue of Variable Stars with Improved Coordinates. *Astronomy Letters*, 29:468–479, July 2003. doi: [10.1134/1.1589864](https://doi.org/10.1134/1.1589864).

- A. Sanghi, Y. Zhou, and B. P. Bowler. Efficiently Imaging Accreting Protoplanets from Space: Reference Star Differential Imaging of the PDS 70 Planetary System using the HST/WFC3 Archival PSF Library. *arXiv e-prints*, art. arXiv:2112.10777, Dec. 2021.
- A. Sanghi, Y. Zhou, and B. P. Bowler. Efficiently Imaging Accreting Protoplanets from Space: Reference Star Differential Imaging of the PDS 70 Planetary System Using the HST/WFC3 Archival PSF Library. *AJ*, 163(3):119, Mar. 2022. doi: [10.3847/1538-3881/ac477e](https://doi.org/10.3847/1538-3881/ac477e).
- E. L. Schatzman. *White dwarfs*. 1958.
- K. C. Schlafman and G. Laughlin. A physically-motivated photometric calibration of M dwarf metallicity. *Astronomy and Astrophysics*, 519:A105, Sept. 2010. ISSN 0004-6361. doi: [10.1051/0004-6361/201015016](https://doi.org/10.1051/0004-6361/201015016). URL <https://ui.adsabs.harvard.edu/abs/2010A&A...519A.105S>. ADS Bibcode: 2010A&A...519A.105S.
- A. Schneider, C. Melis, and I. Song. TW HYA Association Membership and New WISE-detected Circumstellar Disks. *ApJ*, 754(1):39, July 2012. doi: [10.1088/0004-637X/754/1/39](https://doi.org/10.1088/0004-637X/754/1/39).
- G. Schneider, C. A. Grady, D. C. Hines, C. C. Stark, J. H. Debes, J. Carson, M. J. Kuchner, M. D. Perrin, A. J. Weinberger, J. P. Wisniewski, M. D. Silverstone, H. Jang-Condell, T. Henning, B. E. Woodgate, E. Serabyn, A. Moro-Martin, M. Tamura, P. M. Hinz, and T. J. Rodigas. Probing for Exoplanets Hiding in Dusty Debris Disks: Disk Imaging, Characterization, and Exploration with HST/STIS Multi-roll Coronagraphy. *AJ*, 148(4):59, Oct. 2014. doi: [10.1088/0004-6256/148/4/59](https://doi.org/10.1088/0004-6256/148/4/59).
- D. Sebastian, M. Gillon, E. Ducrot, F. J. Pozuelos, L. J. Garcia, M. N. Günther, L. Delrez, D. Queloz, B. O. Demory, A. H. M. J. Triaud, A. Burgasser, J. de Wit, A. Burdanov, G. Dransfield, E. Jehin, J. McCormac, C. A. Murray, P. Niraula, P. P. Pedersen, B. V. Rackham, S. Sohy, S. Thompson, and V. Van Grootel. SPECULOOS: Ultracool dwarf transit survey. Target list and strategy. *A&A*, 645:A100, Jan. 2021. doi: [10.1051/0004-6361/202038827](https://doi.org/10.1051/0004-6361/202038827).
- A. G. Sepulveda and B. P. Bowler. Dynamical Mass of the Exoplanet Host Star HR 8799. *AJ*, 163(2):52, Feb. 2022. doi: [10.3847/1538-3881/ac3bb5](https://doi.org/10.3847/1538-3881/ac3bb5).

- M. Service, J. R. Lu, R. Campbell, B. N. Sitarski, A. M. Ghez, and J. Anderson. A New Distortion Solution for NIRC2 on the Keck II Telescope. *Publications of the Astronomical Society of the Pacific*, 128:095004, Sept. 2016. ISSN 0004-6280. doi: [10.1088/1538-3873/128/967/095004](https://doi.org/10.1088/1538-3873/128/967/095004). URL <http://adsabs.harvard.edu/abs/2016PASP..128i5004S>.
- J. D. Simon, B. J. Shappee, G. Pojmański, B. T. Montet, C. S. Kochanek, J. van Saders, T. W.-S. Holoiën, and A. A. Henden. Where Is the Flux Going? The Long-term Photometric Variability of Boyajian's Star. *The Astrophysical Journal*, 853:77, Jan. 2018. ISSN 0004-637X. doi: [10.3847/1538-4357/aaa0c1](https://doi.org/10.3847/1538-4357/aaa0c1). URL <http://adsabs.harvard.edu/abs/2018ApJ...853...77S>.
- M. F. Skrutskie, R. M. Cutri, R. Stiening, M. D. Weinberg, S. Schneider, J. M. Carpenter, C. Beichman, R. Capps, T. Chester, J. Elias, J. Huchra, J. Liebert, C. Lonsdale, D. G. Monet, S. Price, P. Seitzer, T. Jarrett, J. D. Kirkpatrick, J. E. Gizis, E. Howard, T. Evans, J. Fowler, L. Fullmer, R. Hurt, R. Light, E. L. Kopan, K. A. Marsh, H. L. McCallon, R. Tam, S. Van Dyk, and S. Wheelock. The Two Micron All Sky Survey (2MASS). *The Astronomical Journal*, 131:1163–1183, Feb. 2006. ISSN 0004-6256. doi: [10.1086/498708](https://doi.org/10.1086/498708). URL <http://adsabs.harvard.edu/abs/2006AJ....131.1163S>.
- J. L. Smallwood, R. G. Martin, M. Livio, and S. H. Lubow. White dwarf pollution by asteroids from secular resonances. *MNRAS*, 480(1):57–67, Oct. 2018. doi: [10.1093/mnras/sty1819](https://doi.org/10.1093/mnras/sty1819).
- B. A. Smith and R. J. Terrile. A Circumstellar Disk around β Pictoris. *Science*, 226(4681):1421–1424, Dec. 1984. doi: [10.1126/science.226.4681.1421](https://doi.org/10.1126/science.226.4681.1421).
- K. J. Snook. Optical properties and radiative heating effects of dust suspended in the Mars atmosphere. Nov. 1999.
- V. V. Sobolev. *Light scattering in planetary atmospheres*. 1975.
- R. Soummer, L. Pueyo, and J. Larkin. Detection and Characterization of Exoplanets and Disks Using Projections on Karhunen-Loève Eigenimages. *The Astrophysical Journal Letters*, 755(2):L28, Aug. 2012. ISSN 0004-637X. doi: [10.1088/2041-8205/755/2/L28](https://doi.org/10.1088/2041-8205/755/2/L28). URL <http://adsabs.harvard.edu/abs/2012ApJ...755L..28S>.

- H. Spencer Jones and J. Jackson. *Catalogue of 20554 faint stars in the Cape Astrographic Zone -40 deg. to -52 deg. For the equinox of 1900.0 giving positions, precessions, proper motions and photographic magnitudes*. Her Majesty's Stationary Office (HMSO), 1939.
- K. G. Stassun and G. Torres. Parallax Systematics and Photocenter Motions of Benchmark Eclipsing Binaries in Gaia EDR3. *ApJL*, 907(2):L33, Feb. 2021. ISSN 0004-637X. doi: 10.3847/2041-8213/abdaad. URL <https://ui.adsabs.harvard.edu/abs/2021ApJ...907L..33S>. ADS Bibcode: 2021ApJ...907L..33S.
- J. Stegmann, A. Vigna-Gómez, A. Rantala, T. Wagg, L. Zwick, M. Renzo, L. A. C. van Son, S. E. de Mink, and S. D. M. White. Close Encounters of Wide Binaries Induced by the Galactic Tide: Implications for Stellar Mergers and Gravitational-Wave Sources. *arXiv e-prints*, art. arXiv:2405.02912, May 2024.
- A. P. Stephan, S. Naoz, and B. Zuckerman. Throwing Icebergs at White Dwarfs. *ApJL*, 844(2): L16, Aug. 2017. doi: 10.3847/2041-8213/aa7cf3.
- P. B. Stetson. DAOPHOT: A Computer Program for Crowded-Field Stellar Photometry. *PASP*, 99: 191, Mar. 1987. doi: 10.1086/131977.
- STScI Development Team. pysynphot: Synthetic photometry software package. art. ascl:1303.023, Mar. 2013.
- N. Tetzlaff, R. Neuhauser, and M. M. Hohle. A catalogue of young runaway Hipparcos stars within 3 kpc from the Sun. *Monthly Notices of the Royal Astronomical Society*, 410:190–200, Jan. 2011. ISSN 0035-8711. doi: 10.1111/j.1365-2966.2010.17434.x. URL <http://adsabs.harvard.edu/abs/2011MNRAS.410..190T>.
- C. Thalmann, S. Desidera, M. Bonavita, M. Janson, T. Usuda, T. Henning, R. Köhler, J. Carson, A. Boccaletti, C. Bergfors, W. Brandner, M. Feldt, M. Goto, H. Klahr, F. Marzari, and C. Mordasini. SPOTS: The Search for Planets Orbiting Two Stars. I. Survey description and first observations. *A&A*, 572:A91, Dec. 2014. doi: 10.1051/0004-6361/201424581.
- M. A. Thompson, P. Scicluna, F. Kemper, J. E. Geach, M. M. Dunham, O. Morata, S. Ertel, P. T. P. Ho, J. Dempsey, I. Coulson, G. Petitpas, and L. E. Kristensen. Constraints on the circumstellar

- dust around KIC 8462852. *Monthly Notices of the Royal Astronomical Society*, 458:L39–L43, May 2016. ISSN 0035-8711. doi: 10.1093/mnras/slw008. URL <http://adsabs.harvard.edu/abs/2016MNRAS.458L..39T>.
- T. Tobal. Mesures d'étoiles doubles visuelles. *Observations et Travaux*, 52:67–72, Jan. 2000.
- O. B. Toon, C. P. McKay, T. P. Ackerman, and K. Santhanam. Rapid calculation of radiative heating rates and photodissociation rates in inhomogeneous multiple scattering atmospheres. *Journal of Geophysical Research*, 94:16287–16301, Nov. 1989. doi: 10.1029/JD094iD13p16287.
- C. A. O. Torres, L. da Silva, G. R. Quast, R. de la Reza, and E. Jilinski. A New Association of Post-T Tauri Stars near the Sun. *The Astronomical Journal*, 120:1410–1425, Sept. 2000. ISSN 0004-6256. doi: 10.1086/301539. URL <http://adsabs.harvard.edu/abs/2000AJ....120.1410T>.
- C. A. O. Torres, G. R. Quast, L. da Silva, R. de La Reza, C. H. F. Melo, and M. Sterzik. Search for associations containing young stars (SACY). I. Sample and searching method. *Astronomy and Astrophysics*, 460(3):695–708, Dec. 2006. ISSN 0004-6361. doi: 10.1051/0004-6361:20065602. URL <http://adsabs.harvard.edu/abs/2006A%26A...460..695T>.
- T. Trifonov, M. Kürster, M. Zechmeister, L. Tal-Or, J. A. Caballero, A. Quirrenbach, P. J. Amado, I. Ribas, A. Reiners, S. Reffert, S. Dreizler, A. P. Hatzes, A. Kaminski, R. Launhardt, T. Henning, D. Montes, V. J. S. Béjar, R. Mundt, A. Pavlov, J. H. M. M. Schmitt, W. Seifert, J. C. Morales, G. Nowak, S. V. Jeffers, C. Rodríguez-López, C. del Burgo, G. Anglada-Escudé, J. López-Santiago, R. J. Mathar, M. Ammler-von Eiff, E. W. Guenther, D. Barrado, J. I. González Hernández, L. Mancini, J. Stürmer, M. Abril, J. Aceituno, F. J. Alonso-Floriano, R. Antona, H. Anwand-Heerwart, B. Arroyo-Torres, M. Azzaro, D. Baroch, F. F. Bauer, S. Becerril, D. Benítez, Z. M. Berdiñas, G. Bergond, M. Blümcke, M. Brinkmüller, J. Cano, M. C. Cárdenas Vázquez, E. Casal, C. Cifuentes, A. Claret, J. Colomé, M. Cortés-Contreras, S. Czesla, E. Díez-Alonso, C. Feiz, M. Fernández, I. M. Ferro, B. Fuhrmeister, D. Galadí-Enríquez, A. Garcia-Piquer, M. L. García Vargas, L. Gesa, V. Gómez Galera, R. González-Peinado, U. Grözing, S. Grohnert, J. Guàrdia, A. Guijarro, E. de Guindos, J. Gutiérrez-Soto, H. J. Hagen, P. H. Hauschildt, R. P. Hedrosa, J. Helmling, I. Hermelo, R. Hernández Arabí, L. Hernández Castaño, F. Hernández Hernando, E. Herrero, A. Huber, P. Huke, E. Johnson, E. de

- Juan, M. Kim, R. Klein, J. Klüter, A. Klutsch, M. Lafarga, M. Lampón, L. M. Lara, W. Laun, U. Lemke, R. Lenzen, M. López del Fresno, M. J. López-González, M. López-Puertas, J. F. López Salas, R. Luque, H. Magán Madinabeitia, U. Mall, H. Mandel, E. Marfil, J. A. Marín Molina, D. Maroto Fernández, E. L. Martín, S. Martín-Ruiz, C. J. Marvin, E. Mirabet, A. Moya, M. E. Moreno-Raya, E. Nagel, V. Naranjo, L. Nortmann, A. Ofir, R. Oreiro, E. Pallé, J. Panduro, J. Pascual, V. M. Passegger, S. Pedraz, A. Pérez-Calpena, D. Pérez Medialdea, M. Perger, M. A. C. Perryman, M. Pluto, O. Rabaza, A. Ramón, R. Rebolo, P. Redondo, S. Reinhardt, P. Rhode, H. W. Rix, F. Rodler, E. Rodríguez, A. Rodríguez Trinidad, R. R. Rohloff, A. Rosich, S. Sadegi, E. Sánchez-Blanco, M. A. Sánchez Carrasco, A. Sánchez-López, J. Sanz-Forcada, P. Sarkis, L. F. Sarmiento, S. Schäfer, J. Schiller, P. Schöfer, A. Schweitzer, E. Solano, O. Stahl, J. B. P. Strachan, J. C. Suárez, H. M. Tabernero, M. Tala, S. M. Tulloch, G. Veredas, J. I. Vico Linares, F. Vilardell, K. Wagner, J. Winkler, V. Wolthoff, W. Xu, F. Yan, and M. R. Zapatero Osorio. The CARMENES search for exoplanets around M dwarfs . First visual-channel radial-velocity measurements and orbital parameter updates of seven M-dwarf planetary systems. *A&A*, 609:A117, Feb. 2018. doi: [10.1051/0004-6361/201731442](https://doi.org/10.1051/0004-6361/201731442).
- M. Tsantaki, S. G. Sousa, V. Z. Adibekyan, N. C. Santos, A. Mortier, and G. Israelian. Deriving precise parameters for cool solar-type stars. Optimizing the iron line list. *A&A*, 555:A150, July 2013. doi: [10.1051/0004-6361/201321103](https://doi.org/10.1051/0004-6361/201321103).
- M. C. Turnbull. ExoCat-1: The Nearby Stellar Systems Catalog for Exoplanet Imaging Missions. *arXiv e-prints*, art. arXiv:1510.01731, Oct. 2015. doi: [10.48550/arXiv.1510.01731](https://doi.org/10.48550/arXiv.1510.01731).
- F. van Leeuwen. Validation of the new Hipparcos reduction. *A&A*, 474(2):653–664, Nov. 2007. doi: [10.1051/0004-6361:20078357](https://doi.org/10.1051/0004-6361:20078357).
- A. Vanderburg, J. A. Johnson, S. Rappaport, A. Bieryla, J. Irwin, J. A. Lewis, D. Kipping, W. R. Brown, P. Dufour, D. R. Ciardi, R. Angus, L. Schaefer, D. W. Latham, D. Charbonneau, C. Beichman, J. Eastman, N. McCrady, R. A. Wittenmyer, and J. T. Wright. A disintegrating minor planet transiting a white dwarf. *Nature*, 526(7574):546–549, Oct. 2015. doi: [10.1038/nature15527](https://doi.org/10.1038/nature15527).

- A. Vanderburg, C. X. Huang, J. E. Rodriguez, J. C. Becker, G. R. Ricker, R. K. Vanderspek, D. W. Latham, S. Seager, J. N. Winn, J. M. Jenkins, B. Addison, A. Bieryla, C. Briceño, B. P. Bowler, T. M. Brown, C. J. Burke, J. A. Burt, D. A. Caldwell, J. T. Clark, I. Crossfield, J. A. Dittmann, S. Dynes, B. J. Fulton, N. Guerrero, D. Harbeck, J. Horner, S. R. Kane, J. Kielkopf, A. L. Kraus, L. Kreidberg, N. Law, A. W. Mann, M. W. Mengel, T. D. Morton, J. Okumura, L. A. Pearce, P. Plavchan, S. N. Quinn, M. Rabus, M. E. Rose, P. Rowden, A. Shporer, R. J. Siverd, J. C. Smith, K. Stassun, C. G. Tinney, R. Wittenmyer, D. J. Wright, H. Zhang, G. Zhou, and C. A. Ziegler. TESS Spots a Compact System of Super-Earths around the Naked-eye Star HR 858. *The Astrophysical Journal Letters*, 881:L19, Aug. 2019. ISSN 0004-637X. doi: [10.3847/2041-8213/ab322d](https://doi.org/10.3847/2041-8213/ab322d). URL <http://adsabs.harvard.edu/abs/2019ApJ...881L..19V>.
- A. Vanderburg, S. A. Rappaport, S. Xu, I. J. M. Crossfield, J. C. Becker, B. Gary, F. Murgas, S. Blouin, T. G. Kaye, E. Palte, C. Melis, B. M. Morris, L. Kreidberg, V. Gorjian, C. V. Morley, A. W. Mann, H. Parviainen, L. A. Pearce, E. R. Newton, A. Carrillo, B. Zuckerman, L. Nelson, G. Zeimann, W. R. Brown, R. Tronsgaard, B. Klein, G. R. Ricker, R. K. Vanderspek, D. W. Latham, S. Seager, J. N. Winn, J. M. Jenkins, F. C. Adams, B. Benneke, D. Berardo, L. A. Buchhave, D. A. Caldwell, J. L. Christiansen, K. A. Collins, K. D. Colón, T. Daylan, J. Doty, A. E. Doyle, D. Dragomir, C. Dressing, P. Dufour, A. Fukui, A. Glidden, N. M. Guerrero, X. Guo, K. Heng, A. I. Henriksen, C. X. Huang, L. Kaltenegger, S. R. Kane, J. A. Lewis, J. J. Lissauer, F. Morales, N. Narita, J. Pepper, M. E. Rose, J. C. Smith, K. G. Stassun, and L. Yu. A giant planet candidate transiting a white dwarf. *Nature*, 585(7825):363–367, Sept. 2020. ISSN 1476-4687. doi: [10.1038/s41586-020-2713-y](https://doi.org/10.1038/s41586-020-2713-y). URL <https://www.nature.com/articles/s41586-020-2713-y>. Number: 7825 Publisher: Nature Publishing Group.
- A. Venner, A. Vanderburg, and L. A. Pearce. True Masses of the Long-period Companions to HD 92987 and HD 221420 from Hipparcos–Gaia Astrometry. *AJ*, 162(1):12, June 2021. ISSN 1538-3881. doi: [10.3847/1538-3881/abf932](https://doi.org/10.3847/1538-3881/abf932). URL <https://doi.org/10.3847/1538-3881/abf932>. Publisher: American Astronomical Society.
- D. Veras and N. W. Evans. Exoplanets beyond the Solar neighbourhood: Galactic tidal perturbations. *MNRAS*, 430(1):403–415, Mar. 2013. doi: [10.1093/mnras/sts647](https://doi.org/10.1093/mnras/sts647).

- D. Veras, N. W. Evans, M. C. Wyatt, and C. A. Tout. The great escape - III. Placing post-main-sequence evolution of planetary and binary systems in a Galactic context. *Mon. Not. R. Astron. Soc.*, 437:1127–1140, Jan. 2014. ISSN 0035-8711. doi: [10.1093/mnras/stt1905](https://doi.org/10.1093/mnras/stt1905).
- D. Veras, A. J. Mustill, B. T. Gänsicke, S. Redfield, N. Georgakarakos, A. B. Bowler, and M. J. S. Lloyd. Full-lifetime simulations of multiple unequal-mass planets across all phases of stellar evolution. *MNRAS*, 458(4):3942–3967, June 2016. doi: [10.1093/mnras/stw476](https://doi.org/10.1093/mnras/stw476).
- D. Veras, N. Georgakarakos, I. Dobbs-Dixon, and B. T. Gänsicke. Binary star influence on post-main-sequence multi-planet stability. *Mon. Not. R. Astron. Soc.*, 465:2053–2059, Feb. 2017. ISSN 0035-8711. doi: [10.1093/mnras/stw2699](https://doi.org/10.1093/mnras/stw2699).
- D. Veras, S. Xu, and A. Rebassa-Mansergas. The critical binary star separation for a planetary system origin of white dwarf pollution. *Mon. Not. R. Astron. Soc.*, 473:2871–2880, Jan. 2018. ISSN 0035-8711. doi: [10.1093/mnras/stx2141](https://doi.org/10.1093/mnras/stx2141).
- L. Vican. Age Determination for 346 Nearby Stars in the Herschel DEBRIS Survey. *AJ*, 143(6): 135, June 2012. doi: [10.1088/0004-6256/143/6/135](https://doi.org/10.1088/0004-6256/143/6/135).
- A. Vigan, C. Fontanive, M. Meyer, B. Biller, M. Bonavita, M. Feldt, S. Desidera, G. D. Marleau, A. Emsenhuber, R. Galicher, K. Rice, D. Forgan, C. Mordasini, R. Gratton, H. Le Coroller, A. L. Maire, F. Cantalloube, G. Chauvin, A. Cheetham, J. Hagelberg, A. M. Lagrange, M. Langlois, M. Bonnefoy, J. L. Beuzit, A. Boccaletti, V. D’Orazi, P. Delorme, C. Dominik, T. Henning, M. Janson, E. Lagadec, C. Lazzoni, R. Ligi, F. Menard, D. Mesa, S. Messina, C. Moutou, A. Müller, C. Perrot, M. Samland, H. M. Schmid, T. Schmidt, E. Sissa, M. Turatto, S. Udry, A. Zurlo, L. Abe, J. Antichi, R. Asensio-Torres, A. Baruffolo, P. Baudoz, J. Baudrand, A. Bazzon, P. Blanchard, A. J. Bohn, S. Brown Sevilla, M. Carbillet, M. Carle, E. Cascone, J. Char-ton, R. Claudi, A. Costille, V. De Caprio, A. Delboulbé, K. Dohlen, N. Engler, D. Fantinel, P. Feautrier, T. Fusco, P. Gigan, J. H. Girard, E. Giro, D. Gisler, L. Gluck, C. Gry, N. Hubin, E. Hugot, M. Jaquet, M. Kasper, D. Le Mignant, M. Llored, F. Madec, Y. Magnard, P. Martinez, D. Maurel, O. Möller-Nilsson, D. Mouillet, T. Moulin, A. Origné, A. Pavlov, D. Perret, C. Petit, J. Pragt, P. Puget, P. Rabou, J. Ramos, E. L. Rickman, F. Rigal, S. Rochat, R. Roelfsema, G. Rousset, A. Roux, B. Salasnich, J. F. Sauvage, A. Sevin, C. Soenke, E. Stadler, M. Suarez,

- Z. Wahhaj, L. Weber, and F. Wildi. The SPHERE infrared survey for exoplanets (SHINE). III. The demographics of young giant exoplanets below 300 au with SPHERE. *A&A*, 651:A72, July 2021. doi: [10.1051/0004-6361/202038107](https://doi.org/10.1051/0004-6361/202038107).
- O. Vilhu and J. L. Linsky. Detection of X-ray emission from the young low-mass star Rossiter 137B. *PASP*, 99:1071–1075, Oct. 1987. doi: [10.1086/132079](https://doi.org/10.1086/132079).
- P. Virtanen, R. Gommers, T. E. Oliphant, M. Haberland, T. Reddy, D. Cournapeau, E. Burovski, P. Peterson, W. Weckesser, J. Bright, S. J. van der Walt, M. Brett, J. Wilson, K. J. Millman, N. Mayorov, A. R. J. Nelson, E. Jones, R. Kern, E. Larson, C. J. Carey, I. Polat, Y. Feng, E. W. Moore, J. VanderPlas, D. Laxalde, J. Perktold, R. Cimrman, I. Henriksen, E. A. Quintero, C. R. Harris, A. M. Archibald, A. H. Ribeiro, F. Pedregosa, and P. van Mulbregt. SciPy 1.0: fundamental algorithms for scientific computing in Python. *Nature Methods*, 17(3):261–272, Mar. 2020. ISSN 1548-7105. doi: [10.1038/s41592-019-0686-2](https://doi.org/10.1038/s41592-019-0686-2). URL <https://www.nature.com/articles/s41592-019-0686-2>. Number: 3 Publisher: Nature Publishing Group.
- K. von Braun, T. S. Boyajian, G. T. van Belle, S. R. Kane, J. Jones, C. Farrington, G. Schaefer, N. Vargas, N. Scott, T. A. ten Brummelaar, M. Kephart, D. R. Gies, D. R. Ciardi, M. López-Morales, C. Mazingue, H. A. McAlister, S. Ridgway, P. J. Goldfinger, N. H. Turner, and L. Sturmann. Stellar diameters and temperatures - V. 11 newly characterized exoplanet host stars. *MNRAS*, 438(3):2413–2425, Mar. 2014. doi: [10.1093/mnras/stt2360](https://doi.org/10.1093/mnras/stt2360).
- H. von Zeipel. Sur l'application des séries de M. Lindstedt à l'étude du mouvement des comètes périodiques. *Astronomische Nachrichten*, 183(22):345, Mar. 1910. doi: [10.1002/asna.19091832202](https://doi.org/10.1002/asna.19091832202).
- K. Wagner, K. B. Follete, L. M. Close, D. Apai, A. Gibbs, M. Keppler, A. Müller, T. Henning, M. Kasper, Y.-L. Wu, J. Long, J. Males, K. Morzinski, and M. McClure. Magellan Adaptive Optics Imaging of PDS 70: Measuring the Mass Accretion Rate of a Young Giant Planet within a Gapped Disk. *ApJL*, 863(1):L8, Aug. 2018. doi: [10.3847/2041-8213/aad695](https://doi.org/10.3847/2041-8213/aad695).
- J. J. Wang, J.-B. Ruffio, R. J. De Rosa, J. Aguilar, S. G. Wolff, and L. Pueyo. pyKLIP: PSF Subtraction for Exoplanets and Disks. art. ascl:1506.001, June 2015.

- M. Wenger, F. Ochsenbein, D. Egret, P. Dubois, F. Bonnarel, S. Borde, F. Genova, G. Jasniewicz, S. Laloë, S. Lesteven, and R. Monier. The SIMBAD astronomical database. The CDS reference database for astronomical objects. *A&As*, 143:9–22, Apr. 2000. doi: [10.1051/aas:2000332](https://doi.org/10.1051/aas:2000332).
- B. Willems and U. Kolb. Detached white dwarf main-sequence star binaries. *A&A*, 419:1057–1076, June 2004. doi: [10.1051/0004-6361:20040085](https://doi.org/10.1051/0004-6361:20040085).
- D. J. Wilson, B. T. Gänsicke, D. Koester, R. Raddi, E. Breedt, J. Southworth, and S. G. Parsons. Variable emission from a gaseous disc around a metal-polluted white dwarf. *MNRAS*, 445(2): 1878–1884, Dec. 2014. doi: [10.1093/mnras/stu1876](https://doi.org/10.1093/mnras/stu1876).
- T. G. Wilson, J. Farihi, B. T. Gänsicke, and A. Swan. The unbiased frequency of planetary signatures around single and binary white dwarfs using Spitzer and Hubble. *MNRAS*, 487(1): 133–146, July 2019. doi: [10.1093/mnras/stz1050](https://doi.org/10.1093/mnras/stz1050).
- P. Wizinowich, D. S. Acton, C. Shelton, P. Stomski, J. Gathright, K. Ho, W. Lupton, K. Tsubota, O. Lai, C. Max, J. Brase, J. An, K. Avicola, S. Olivier, D. Gavel, B. Macintosh, A. Ghez, and J. Larkin. First Light Adaptive Optics Images from the Keck II Telescope: A New Era of High Angular Resolution Imagery. *Publications of the Astronomical Society of the Pacific*, 112: 315–319, Mar. 2000. doi: [10.1086/316543](https://doi.org/10.1086/316543).
- J. T. Wright and S. Sigurdsson. Families of Plausible Solutions to the Puzzle of Boyajian’s Star. *The Astrophysical Journal Letters*, 829:L3, Sept. 2016. ISSN 0004-637X. doi: [10.3847/2041-8205/829/1/L3](https://doi.org/10.3847/2041-8205/829/1/L3). URL <http://adsabs.harvard.edu/abs/2016ApJ...829L...3W>.
- J. T. Wright, K. M. S. Cartier, M. Zhao, D. Jontof-Hutter, and E. B. Ford. The Search for Extraterrestrial Civilizations with Large Energy Supplies. IV. The Signatures and Information Content of Transiting Megastructures. *The Astrophysical Journal*, 816:17, Jan. 2016. ISSN 0004-637X. doi: [10.3847/0004-637X/816/1/17](https://doi.org/10.3847/0004-637X/816/1/17). URL <http://adsabs.harvard.edu/abs/2016ApJ...816...17W>.
- M. C. Wyatt, J. Farihi, J. E. Pringle, and A. Bonsor. Stochastic accretion of planetesimals on to white dwarfs: constraints on the mass distribution of accreted material from atmospheric pollution. *MNRAS*, 439(4):3371–3391, Apr. 2014. doi: [10.1093/mnras/stu183](https://doi.org/10.1093/mnras/stu183).

- M. C. Wyatt, R. van Lieshout, G. M. Kennedy, and T. S. Boyajian. Modelling the KIC8462852 light curves: compatibility of the dips and secular dimming with an exocomet interpretation. *Monthly Notices of the Royal Astronomical Society*, 473:5286–5307, Feb. 2018. ISSN 0035-8711. doi: [10.1093/mnras/stx2713](https://doi.org/10.1093/mnras/stx2713). URL <http://adsabs.harvard.edu/abs/2018MNRAS.473.5286W>.
- J. W. Xuan and M. C. Wyatt. Evidence for a high mutual inclination between the cold Jupiter and transiting super Earth orbiting π Men. *arXiv:2007.01871 [astro-ph]*, July 2020. URL <http://arxiv.org/abs/2007.01871>. arXiv: 2007.01871.
- J. W. Xuan, G. M. Kennedy, M. C. Wyatt, and B. Yelverton. Mutual inclinations between giant planets and their debris discs in HD 113337 and HD 38529. *MNRAS*, 499(4):5059–5074, Dec. 2020. doi: [10.1093/mnras/staa3155](https://doi.org/10.1093/mnras/staa3155).
- N. Yamaguchi, K. El-Badry, N. Rees, S. Shahaf, T. Mazeh, and R. Andrae. Wide post-common envelope binaries from Gaia: orbit validation and formation models. *arXiv e-prints*, art. arXiv:2405.06020, May 2024.
- S. Yelda, J. R. Lu, A. M. Ghez, W. Clarkson, J. Anderson, T. Do, and K. Matthews. Improving Galactic Center Astrometry by Reducing the Effects of Geometric Distortion. *The Astrophysical Journal*, 725:331–352, Dec. 2010. ISSN 0004-637X. doi: [10.1088/0004-637X/725/1/331](https://doi.org/10.1088/0004-637X/725/1/331). URL <http://adsabs.harvard.edu/abs/2010ApJ...725..331Y>.
- N. Zacharias, C. T. Finch, T. M. Girard, A. Henden, J. L. Bartlett, D. G. Monet, and M. I. Zacharias. VizieR Online Data Catalog: UCAC4 Catalogue (Zacharias+, 2012). *VizieR Online Data Catalog*, art. I/322A, July 2012.
- N. L. Zakamska and S. Tremaine. Excitation and Propagation of Eccentricity Disturbances in Planetary Systems. *The Astronomical Journal*, 128(2):869–877, Aug. 2004. doi: [10.1086/422023](https://doi.org/10.1086/422023). URL <http://adsabs.harvard.edu/abs/2004AJ....128..869Z>.
- H. Zhang, T. D. Brandt, R. Kiman, A. Venner, Q. An, M. Chen, and Y. Li. Dynamical masses and ages of Sirius-like systems. *MNRAS*, 524(1):695–715, Sept. 2023. doi: [10.1093/mnras/stad1849](https://doi.org/10.1093/mnras/stad1849).

- C. Ziegler, A. Tokovinin, C. Briceño, J. Mang, N. Law, and A. W. Mann. SOAR TESS Survey. I. Sculpting of TESS Planetary Systems by Stellar Companions. *The Astronomical Journal*, 159: 19, Jan. 2020. ISSN 0004-6256. doi: [10.3847/1538-3881/ab55e9](https://doi.org/10.3847/1538-3881/ab55e9). URL <http://adsabs.harvard.edu/abs/2020AJ....159...19Z>.
- J. C. Zinn, M. H. Pinsonneault, D. Huber, and D. Stello. Confirmation of the Gaia DR2 Parallax Zero-point Offset Using Asteroseismology and Spectroscopy in the Kepler Field. *ApJ*, 878(2): 136, June 2019. doi: [10.3847/1538-4357/ab1f66](https://doi.org/10.3847/1538-4357/ab1f66).
- S. Zúñiga-Fernández, A. Bayo, P. Elliott, C. Zamora, G. Corvalán, X. Haubois, J. M. Corral-Santana, J. Olofsson, N. Huélamo, M. F. Sterzik, C. A. O. Torres, G. R. Quast, and C. H. F. Melo. Search for associations containing young stars (SACY). VIII. An updated census of spectroscopic binary systems exhibiting hints of non-universal multiplicity among their associations. *A&A*, 645:A30, Jan. 2021. doi: [10.1051/0004-6361/202037830](https://doi.org/10.1051/0004-6361/202037830).
- B. Zuckerman. The Occurrence of Wide-orbit Planets in Binary Star Systems. *Astrophys. J.*, 791: L27, Aug. 2014. ISSN 0004-637X. doi: [10.1088/2041-8205/791/2/L27](https://doi.org/10.1088/2041-8205/791/2/L27).
- B. Zuckerman. The Nearby, Young, Argus Association: Membership, Age, and Dusty Debris Disks. *The Astrophysical Journal*, 870(1):27, Jan. 2019. ISSN 0004-637X. doi: [10.3847/1538-4357/aaee66](https://doi.org/10.3847/1538-4357/aaee66). URL <http://adsabs.harvard.edu/abs/2019ApJ...870...27Z>.
- B. Zuckerman, D. Koester, I. N. Reid, and M. Hüensch. Metal Lines in DA White Dwarfs. *Astrophys. J.*, 596:477–495, Oct. 2003. ISSN 0004-637X. doi: [10.1086/377492](https://doi.org/10.1086/377492).
- B. Zuckerman, D. Koester, C. Melis, B. M. Hansen, and M. Jura. The Chemical Composition of an Extrasolar Minor Planet. *ApJ*, 671(1):872–877, Dec. 2007. doi: [10.1086/522223](https://doi.org/10.1086/522223).
- B. Zuckerman, C. Melis, B. Klein, D. Koester, and M. Jura. Ancient Planetary Systems are Orbiting a Large Fraction of White Dwarf Stars. *Astrophys. J.*, 722:725–736, Oct. 2010. ISSN 0004-637X. doi: [10.1088/0004-637X/722/1/725](https://doi.org/10.1088/0004-637X/722/1/725).
- B. Zuckerman, L. Vican, I. Song, and A. Schneider. Young Stars near Earth: The Octans-Near Association and Castor Moving Group. *The Astrophysical Journal*, 778:5, Nov. 2013. ISSN

0004-637X. doi: 10.1088/0004-637X/778/1/5. URL <http://adsabs.harvard.edu/abs/2013ApJ...778....5Z>.